

A FIRST SEARCH FOR COHERENT ELASTIC
NEUTRINO-NUCLEUS SCATTERING WITH LIQUID ARGON

Matthew R. Heath

Submitted to the faculty of the University Graduate School

in partial fulfillment of the requirements

for the degree

Doctor of Philosophy

in the Department of Department of Physics,

Indiana University

May 2019

Accepted by the Graduate Faculty, Indiana University, in partial fulfillment of the requirements
for the degree of Doctor of Philosophy.

Doctoral Committee

Rex Tayloe, Ph. D.

Charles Horowitz, Ph. D.

Chen-Yu Liu, Ph. D.

Joshua Long, Ph. D.

Jon Urheim, Ph. D.

April 26, 2019

Copyright © 2019

Matthew R. Heath

ACKNOWLEDGMENTS

This work would not have been possible without the help and support of many people. First I would like to thank my parents for always supporting me and pushing me to achieve my goals. My wife, Haley, has been so understanding and encouraging as I have completed my degree and I can't put into words how grateful I am.

I am thankful for my advisor, Dr. Rex Tayloe. He was always ready with suggestions when I needed help, and taught me how to think like a physicist. It has been a privilege and a pleasure to work with him for the past six years. I want to thank Robert Cooper for being patient with me when I was a young graduate student and teaching me how to calibrate and commission detectors in the field. I also want to acknowledge Tyler Thornton whose programming skills and understanding of ROOT and **Geant4** are unparalleled and proved invaluable as I worked through the analysis of my thesis project.

I want to thank the Physics Department at Indiana University for their support throughout my graduate studies. I also want to thank the friends I have made during my time at IU, in particular Andrew, Blake, Braden, and Matt.

A big thank you to Jonghee Yoo and Fermilab for their work in designing and building the CENNS-10 detector. Without them this measurement would not have been possible. I want to thank Oak Ridge National Lab and the Spallation Neutron source for hosting the COHERENT collaboration's suite of detector systems. Everyone from the COHERENT collaboration deserves my thanks. In particular I want to thank Jason Newby, who always had helpful advice when I was stationed in Oak Ridge and whose experience with and knowledge of working with lab management is unparalleled.

Finally I would like to thank my committee—Charles Horowitz, Chen-Yu Liu, Joshua Long, and Jon Urheim—for their time, support, and evaluation of my work.

Matthew R. Heath

A FIRST SEARCH FOR COHERENT ELASTIC NEUTRINO-NUCLEUS SCATTERING
WITH LIQUID ARGON

First proposed by Freedman in 1974, coherent elastic neutrino-nucleus scattering (CEvNS) is the dominant low energy neutrino coupling and provides a window to many interesting areas of physics research: nuclear structure, physics beyond the Standard Model, and supernovae evolution and detection. The COHERENT collaboration recently observed CEvNS with a low background 14.6kg CsI[Na] crystal at the Spallation Neutron Source (SNS) at Oak Ridge National Lab. A primary goal of COHERENT is to measure the N^2 dependence of the CEvNS cross section. To that end, COHERENT has deployed the single-phase liquid argon detector CENNS-10 to provide a low N measurement of the cross section. CENNS-10 completed an Engineering Run in the spring of 2017. From this analysis, a vital in-situ measurement of the beam-related neutron flux in liquid argon, relevant for future measurements, was made and a limit on the CEvNS cross section on argon, consistent with the Standard Model prediction, was placed. Finally, implications for non-standard neutrino interactions were investigated.

Rex Tayloe, Ph. D.

Charles Horowitz, Ph. D.

Chen-Yu Liu, Ph. D.

Joshua Long, Ph. D.

Jon Urheim, Ph. D.

CONTENTS

1	Coherent Elastic Neutrino-Nucleus Scattering	1
1.1	Cross section	3
1.2	Physics Beyond the Standard Model	4
1.3	Neutrino floor	6
1.4	Supernovae Dynamics	7
1.5	Nuclear Structure	8
1.6	Prior and Ongoing CEvNS Searches	9
2	COHERENT at the Spallation ‘Neutrino’ Source	11
2.1	The Spallation Neutron Source	11
2.1.1	The SNS as a Neutrino Source	12
2.1.2	Neutrino Time and Energy Spectra	13
2.2	The COHERENT Experiment	15
2.2.1	First Measurement of CEvNS with CsI[Na]	19
3	Background Measurements at the SNS	21
3.1	Beam-Unrelated Backgrounds	21
3.1.1	Neutrino Alley Beam-Unrelated Backgrounds	22
3.1.2	Detector-Specific Beam-Unrelated Backgrounds	23
3.2	Beam-Related Backgrounds	24
3.2.1	Neutrino-Induced Neutrons	24
3.2.2	Beam-Related Neutrons	25
3.3	The SciBath Measurement	25
3.3.1	The SciBath Detector	27
3.3.2	SNS Run Summary	27

3.3.3	Analysis Methodology	30
3.3.4	Results	48
4	A Liquid Argon CEvNS Search at the SNS	53
4.1	Liquid Argon as a CEvNS Detector Medium	53
4.2	The CENNS-10 Detector	54
4.2.1	Cryogenic System	57
4.2.2	Vacuum System	59
4.2.3	Gas-Handling System	60
4.2.4	Data Acquisition System	61
4.2.5	External Radiation Shield	63
4.3	Liquid Argon Scintillation	64
4.3.1	N ₂ Contamination	67
4.3.2	Nuclear Recoil Quenching	68
4.4	CENNS-10 Engineering Run	69
4.4.1	Triggering Scheme	70
5	CENNS-10 Waveform Analysis and Calibration	73
5.1	daqman	73
5.1.1	Terminology	73
5.1.2	Event Building	74
5.2	Pulse Fitting	76
5.2.1	Fitting Procedure	77
5.3	Single Photoelectron Analysis	77
5.4	Waveform Analysis	80
5.4.1	Shift and Scale	80
5.4.2	Subtract	80

5.5	Energy Calibration	82
5.6	Pulse Shape Discrimination	84
5.7	CENNS-10 Simulations	85
5.7.1	Geometry	86
5.7.2	Simulation Tuning	87
5.7.3	Detector Simulation	90
5.7.4	Beam-Unrelated Background Simulations	90
5.7.5	Beam-Related Neutron Simulations	93
5.7.6	CEvNS Simulation	94
5.8	Efficiencies	95
5.8.1	Data Quality Cuts	95
5.8.2	Dark Rate Inefficiencies	97
6	CENNS-10 Shielding Studies	99
6.1	Run Summary	99
6.2	PSD Cut Optimization	100
6.2.1	Figure of Merit	100
6.2.2	Beam-Related Neutron Predictions	101
6.3	Pre-Beam and Delayed Time Regions	103
6.4	Beam-Related Neutron Signal	104
6.4.1	No PSD Cut	104
6.4.2	PSD Cut	104
7	A CEvNS Search with CENNS-10	109
7.1	Run Summary	109
7.1.1	Analysis Summary	109
7.1.2	Strobe Trigger Investigations	110

7.2	Signal Predictions	112
7.2.1	CEvNS Signal	113
7.2.2	Beam-Related Neutron Signal	113
7.2.3	Systematics	115
7.3	Counting Experiment	117
7.3.1	Maximizing \mathcal{F}	117
7.3.2	Pre-Beam Subtraction	118
7.3.3	Prompt Beam Events	120
7.3.4	Delayed Events	124
7.4	3D Likelihood Analysis	125
7.4.1	Neutron PDF PSD Shape Correction	126
7.4.2	Likelihood Fitting	127
7.4.3	Beam-Related Neutron Result	129
7.4.4	CEvNS Analysis	130
7.4.5	CEvNS Cross Section Limit	133
7.5	Implications for Non-Standard Neutrino Interactions	135
8	Conclusions	137
	Bibliography	138
A	SciBath Capture Simulation Re-weighting	152
B	CENNS-10 N₂ Doping Test	154
B.1	Motivation	154
B.2	Procedure	155
B.2.1	N ₂ Levels	155
B.2.2	Test Preparation	156

B.2.3	Tests Performed	156
B.2.4	N ₂ Introduction	158
B.3	Results	158
B.3.1	Pre N ₂ Doping	158
B.3.2	Post N ₂ Doping	159
B.4	Conclusions	160
C	Least Squares Fitting	161
C.1	Least Squares Method	161
C.2	Parabola Fit	163
D	Monte Carlo Tuned Optical Parameters	166
	Curriculum Vitae	

LIST OF FIGURES

1.1	The CEvNS process	2
1.2	CEvNS cross section N^2 dependence and typical CEvNS recoil spectra	3
1.3	Current non-standard neutrino interaction constraints	5
1.4	WIMP parameter space demonstrating the ‘Neutrino Floor’	7
2.1	Average protons-on-target trace at the SNS	12
2.2	Neutrino production mechanism and timing spectrum	13
2.3	Characteristic stopped-pion neutrino energy spectra	14
2.4	Current COHERENT detector siting at the SNS	16
2.5	Planned future COHERENT detector siting at the SNS	16
2.6	Neutron flux throughout the SNS target building	17
2.7	Integrated protons-on-target for COHERENT detectors	18
2.8	First measurement of CEvNS with CsI[Na] detector	20
3.1	Comparison of hot off-gas rate and beam power.	23
3.2	Schematic of the SciBath detector	26
3.3	SciBath siting in Neutrino Alley	28
3.4	SciBath beam-related event rates	29
3.5	Single photoelectron spectrum in SciBath neutron detector	30
3.6	Fiber-to-fiber calibration results	31
3.7	Cosmic-muon response in SciBath	32
3.8	SciBath event display	34
3.9	SciBath particle identification capabilities	35
3.10	Tuning SciBath simulation light output	37
3.11	Pictorial representation of SciBath Geant4 muon simulation starting point generation	39

3.12	Scibath response to fast neutrons	40
3.13	SciBath response to thermal neutrons	41
3.14	Cosmic-muon rate measurement systematic error	43
3.15	Expansion coefficients from fast-neutron spectral unfolding	44
3.16	Comparison of the n-p elastic cross sections from various cross section libraries to those used by Geant4	46
3.17	Scibath cosmic-muon angular distribution	48
3.18	SciBath prompt-neutron spectrum	49
3.19	Unfolded SciBath prompt-neutron spectrum	50
3.20	Delayed-neutron energy spectrum	51
4.1	Layout of the CENNS-10 Detector	55
4.2	CENNS-10 plumbing diagram	56
4.3	CENNS-10 fiducial volume mockup	58
4.4	Engineering drawing of CENNS-10 inner detector volume	59
4.5	CENNS-10 gas-handling rack	60
4.6	Trigger setup for Engineering Run	61
4.7	Snapshot of CENNS-10 Slow Monitoring Display	63
4.8	CENNS-10 detector siting in Neutrino Alley	64
4.9	Liquid argon scintillation process	65
4.10	Pulse-shape discrimination in liquid argon	66
4.11	Electronic and nuclear recoil band behavior as a function of energy	66
4.12	Global liquid argon quenching factor data	68
4.13	Timeline of CENNS-10 liquid argon fill at the SNS	70
4.14	Engineering Run integrated beam power totals	71
4.15	CENNS-10 beam trigger schematic	72

5.1	Pulse-finding algorithm schematic	74
5.2	Waveform baseline issues	76
5.3	Average single photoelectron shapes	78
5.4	Single photoelectron response throughout the Engineering Run	79
5.5	Example waveform fit	81
5.6	Reconstructed ^{137}Cs energy spectrum	82
5.7	^{137}Cs photopeak stability throughout the Engineering Run.	83
5.8	^{137}Cs photopeak as a function of position and integration threshold	84
5.9	Low energy nuclear recoil pulse-shape distributions	86
5.10	CENNS-10 Geant4 simulation detector geometry	87
5.11	Tuning CENNS-10 Geant4 simulation optical properties	88
5.12	Relevant surface optical properties in the CENNS-10 simulation	89
5.13	Tuning CENNS-10 Geant4 pulse shape behavior to match calibration data	90
5.14	Expected beam-off background simulations	91
5.15	Expected beam-on beam-unrelated backgrounds	92
5.16	Comparison of CENNS-10 event rates with HOG rate	93
5.17	Example events failing quality cuts	95
5.18	Energy-dependent event detection efficiency	96
5.19	PMT singles rate throughout the run	97
6.1	Optimized no-shielding PSD cut	102
6.2	Predicted beam-unrelated background and beam-related neutron spectra for the no-shielding dataset	103
6.3	No-shielding beam residuals before and after beam on target	104
6.4	No-shielding time spectrum and prompt energy spectra with no pulse-shape-discrimination cut	105

6.5	No-shielding time spectrum and prompt energy spectra with pulse shape discrimination cut	106
6.6	Fit of beam-related neutron prediction to the no-shielding prompt beam-related excess	107
6.7	Beam-related neutron mean energy vs arrival time	108
7.1	Strobe time spectrum fit	111
7.2	Comparison of energy and PSD spectra for different time windows within strobe triggers	111
7.3	Expected CEvNS recoil spectra	112
7.4	Two-dimensional CEvNS energy:PSD pdfs	113
7.5	Efficiency of fast neutrons to reach the CENNS-10 detector	114
7.6	Optimized PSD cut for the full-shielded Counting Experiment analysis	117
7.7	Predicted beam-unrelated background and beam-related neutron spectra for the full-shielded dataset	118
7.8	Nuclear recoil detection efficiency with all cuts applied	119
7.9	Full-shielded dataset pre-beam subtraction	120
7.10	Full-shielded time and prompt energy spectra with no PSD cut	121
7.11	Full-shielded energy and time spectra after optimized PSD cut	122
7.12	Correlation matrix and running χ^2 between the full-shielded beam excess and the predicted beam-related neutron spectrum	123
7.13	Full-shielded delayed energy spectrum with PSD cut	124
7.14	PSD shape correction for beam-related neutron likelihood pdf	127
7.15	Likelihood pdfs in energy, PSD and time	128
7.16	One-dimensional projections of global best-fit to Engineering Run data	129
7.17	Beam-related neutron profile-likelihood fit results	130
7.18	Sensitivity calculation following SensMethod1	131
7.19	Sensitivity calculation following SensMethod2	132

7.20	Placing a limit on the CEvNS cross section	134
7.21	NSI constraints from the Engineering Run results	136
8.1	CEvNS cross section as a function of neutron number	138
B.11	Shift of electronic recoil PSD band during purification	155
B.22	Plumbing used for gas quality tests	157
B.33	Change in average waveforms due to N ₂ doping	159

LIST OF TABLES

3.1	Beam-unrelated background fluxes characteristic to Neutrino Alley	24
3.2	A summary of SciBath data cuts	36
3.3	Summary of fast-neutron simulation systematic excursions	47
3.4	Summary of background measurement results from the SciBath run	52
4.1	CENNS-10 Engineering Run timeline	71
5.1	Summary of pulse-finding settings	75
5.2	Detected photon yield calculation	85
5.3	Event efficiencies not included in the CENNS-10 Geant4 simulation	98
6.1	Timing regions used for no-shielding beam analysis	100
6.2	Summary of pre and post-beam event rates for no-shielding dataset	103
6.3	Predicted and observed no-shielding prompt event rates summary	105
7.1	Summary of analysis-specific cuts used for full-shielded analysis	110
7.2	Expected rates in the full-shielded dataset	115
7.3	Systematics on the signal predictions considered for the CEvNS search at the SNS	116
7.4	Observed event rates from the counting experiment	125
7.5	Summary of likelihood fit results	135
B.21	Summary of LD8000 N ₂ monitor readings from N ₂ doping tests	158
B.42	Measured triplet lifetimes during N ₂ doping tests	160
C.21	Summary of notation used in the Least Squares Fit	163
D.01	Summary of liquid argon scintillation properties in the CENNS-10 Geant4 simulation	166
D.02	A summary of surface optical properties used in the CENNS-10 Geant4 simulation	166

CHAPTER 1

COHERENT ELASTIC NEUTRINO-NUCLEUS SCATTERING

Shortly after the first observation of neutrino-nucleus scattering via the neutral weak current [1], Daniel Freedman first proposed Coherent Elastic Neutrino-Nucleus Scattering (CEvNS) in which the neutrino scatters coherently off the nucleus as a whole [2]. Typically when a neutrino scatters off a nucleus, the scattering is via a complicated interaction between the neutrino and the individual nucleons. However, if the wavelength of the momentum transfer between the neutrino and the nucleus is larger than the size of the nucleus, relevant for low energy (\sim few MeV) neutrinos, the neutrino can not see the individual nucleons. In this ‘coherent scattering’ regime, the neutrino exchanges a Z_0 boson with the entire nucleus as seen in Fig. 1.1a. This coherence condition leads to an enhancement of the scattering cross section, which roughly scales with the number of neutrons in the nucleus squared due to the small weak charge of the proton. This results in a scattering cross section orders of magnitude larger than the other more traditional neutrino scattering channels at low energy as seen in Fig. 1.1b.

Due to the (relatively) large cross section, it may be surprising that CEvNS was only recently observed by the COHERENT collaboration with a CsI[Na] target [3]. However, when the difficult requirements of observing CEvNS are considered, it is not surprise! Freedman himself considered the attempt to measure CEvNS an ‘...act of hubris...’ [2]. While the cross section is large, the coherence condition requires neutrinos with energy $E_\nu \lesssim 50$ MeV. By kinematics, the maximum recoil energy possible for a given neutrino energy is given by $T_{max} = \frac{2E_\nu^2}{M+2E_\nu}$ which, for a ~ 50 MeV

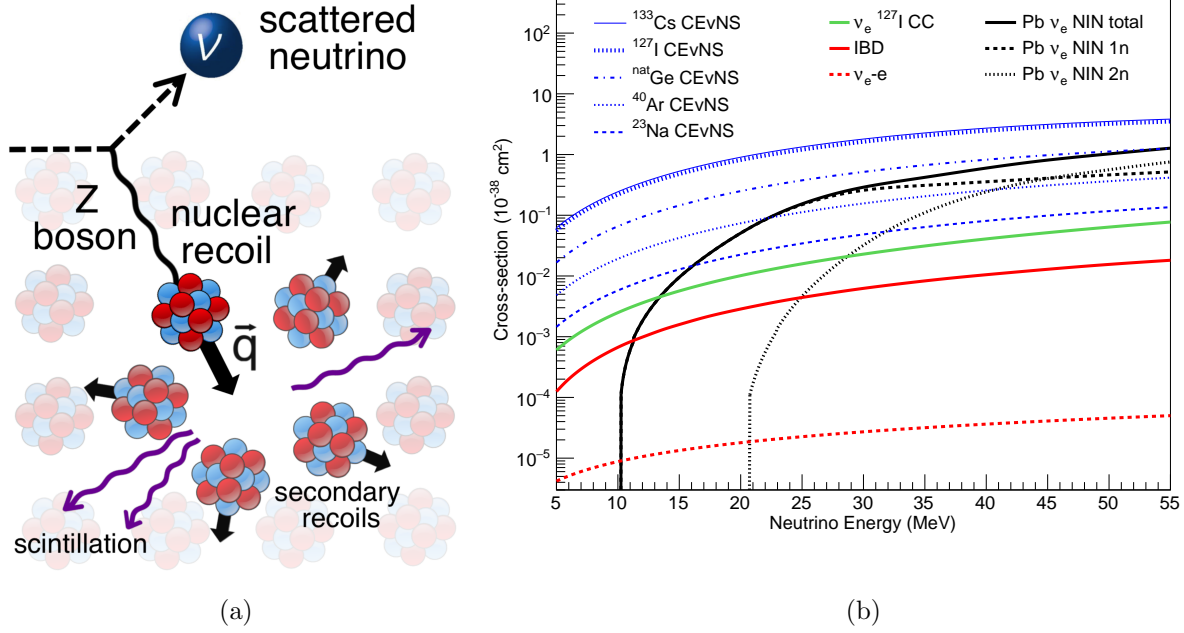


Figure 1.1: (a) A schematic of Coherent Elastic Neutrino-Nucleus Scattering (CEvNS). For sufficiently small momentum transfer (q), the Z_0 boson exchanged between the neutrino and the recoiling nucleus sees the nucleus as a whole rather than its constituent parts. From [3]. (b) A comparison of various neutrino cross sections as a function of energy. The CEvNS cross section is an order of magnitude higher than other neutrino interactions at low energy. From [4].

neutrino on a medium-sized nucleus, is on the order of a few 10s of keV.

As CEvNS is an elastic neutral current process, the only detectable signature is a low energy nuclear recoil on the order of 10s of keV_{nr}, where the nr implies nuclear recoil as seen in Fig. 1.2a. Due to the different dE/dx characteristics of electronic and nuclear recoils, nuclear recoils tend to deposit a noticeable fraction of their energy in channels other than scintillation. In other words, the light output is quenched relative to an electronic recoil of the same energy. To distinguish between the two recoil types, energies are generally given with either the suffix nr (as defined above), or with the suffix ee (electron equivalent). The energy deposit in ee corresponds to the electromagnetic recoil energy that would produce the same light output as a given nuclear recoil in the detector. CEvNS remained undetected for so long due to the combination of the quenching of nuclear recoil light, and the low energy recoil signature.

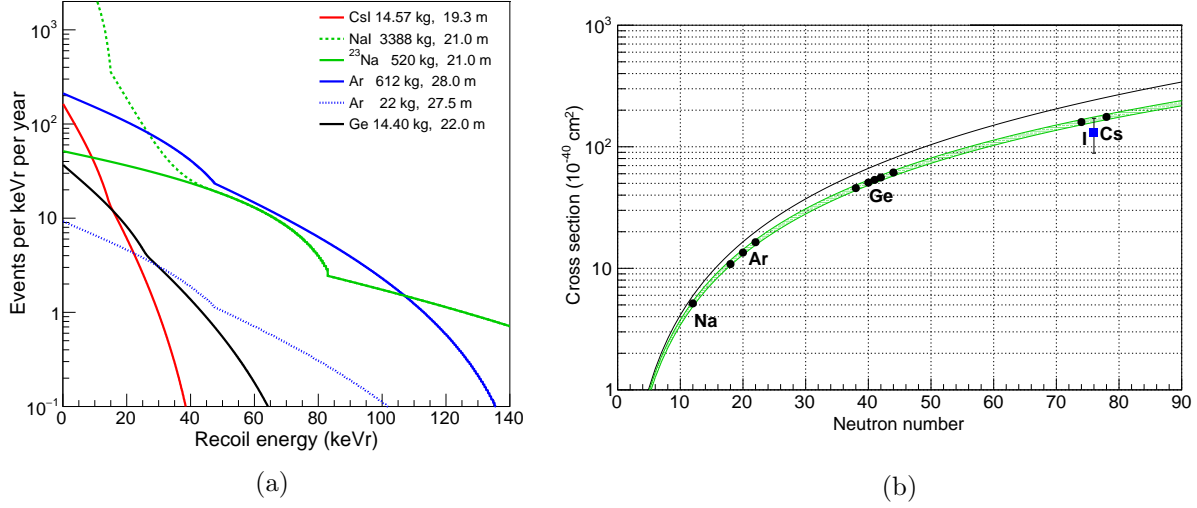


Figure 1.2: (a) Expected CEvNS recoil spectra from a stopped-pion source for some selected target nuclei. (b) The dependence of the stopped-pion flux-averaged CEvNS cross section on the number of neutrons N . The solid black curve represents a pure N^2 dependence (ie a unity form-factor). The green band shows the effect of an assumed form factor (similar effects from [5], [6], and [7], with the latter assumed in [3]). The width represents a 3% uncertainty on the neutron radius in the Helm parameterization. The black dots represent isotopes of interest to the COHERENT collaboration. The blue square shows the flux-averaged cross section from the result in [3]. Plot from [4].

1.1 CROSS SECTION

The differential CEvNS cross section can be written as [8]:

$$\frac{d\sigma}{dT_{coh}} = \frac{G_F^2 M}{2\pi} \left[(G_V + G_A)^2 + (G_V - G_A)^2 \left(1 - \frac{T}{E_\nu}\right)^2 - (G_V^2 - G_A^2) \frac{MT}{E_\nu^2} \right] \quad (1.1)$$

where M is the mass of the nucleus, G_F is Fermi's constant, T is the recoil energy, and E_ν is the neutrino energy. G_V and G_A are given below:

$$\begin{aligned} G_V &= (g_V^p Z + g_V^n N) F_{nuc}^V(Q^2) \\ G_A &= (g_A^p (Z_+ - Z_-) + g_A^n (N_+ - N_-)) F_{nuc}^A(Q^2) \end{aligned} \quad (1.2)$$

where Z is the number of protons in the target nucleus, N is the number of neutrons, Z_\pm and N_\pm are the number of spin up/down protons and neutrons, and $F(Q^2)$ are the form factors as a

function of the momentum transfer $Q = \sqrt{2MT}$. The form factors are point-like for low energy interactions ($\lesssim 10$ MeV neutrinos) and suppress the cross section as the neutrino energy increases, or as the size of the target nucleus increases, as seen in Fig. 1.2b. The vector couplings in G_V and G_A are written as

$$\begin{aligned} g_V^p &= \rho_{\nu N}^{NC} \left(\frac{1}{2} - \hat{\kappa}_{\nu N} \sin^2 \theta_W \right) + 2\lambda^{uL} + 2\lambda^{uR} + \lambda^{dL} + \lambda^{dR} \\ g_V^n &= -\frac{1}{2}\rho_{\nu N}^{NC} + \lambda^{uL} + \lambda^{uR} + 2\lambda^{dL} + 2\lambda^{dR} \end{aligned} \quad (1.3)$$

where $\rho_{\nu N}^{NC}$ and $\hat{\kappa}_{\nu N}$ are electroweak parameters, θ_W is the weak mixing angle, and the λ parameters are radiative corrections as given in [8, 9].

The N^2 dependence of the cross section becomes much clearer when considering the total coherent scattering cross section for a spin-0 nucleus [10]:

$$\sigma_{\nu A} \simeq \frac{4}{\pi} E_\nu^2 [Zw_p + Nw_n]^2 \quad (1.4)$$

Here w_n and w_p are the weak charges of the neutron and proton respectively. w_p is proportional to $(4\sin^2 \theta_W - 1)$. $\sin^2 \theta_W$ has been measured to be $0.23867 \pm 0.00016 \approx 1/4$ [11], resulting in the cross section being proportional to N^2 rather than A^2 . Recently, information on the neutron radius using the recent COHERENT result [12] has been used to re-interpret the measurement of the weak mixing angle at low Q^2 from atomic parity violating (APV) experiments on ^{133}Cs [13]. While not yet competitive with purely APV measurements, this demonstrates the feasibility of using the results from CEvNS measurements to investigate $\sin^2 \theta_W$ at low Q values.

1.2 PHYSICS BEYOND THE STANDARD MODEL

New physics specific to neutrino-nucleon interactions is quite poorly constrained. Because the CEvNS cross section is so cleanly predicted within the Standard Model, any deviations from the prediction could be indicative of physics beyond the Standard Model. Among other possibilities,

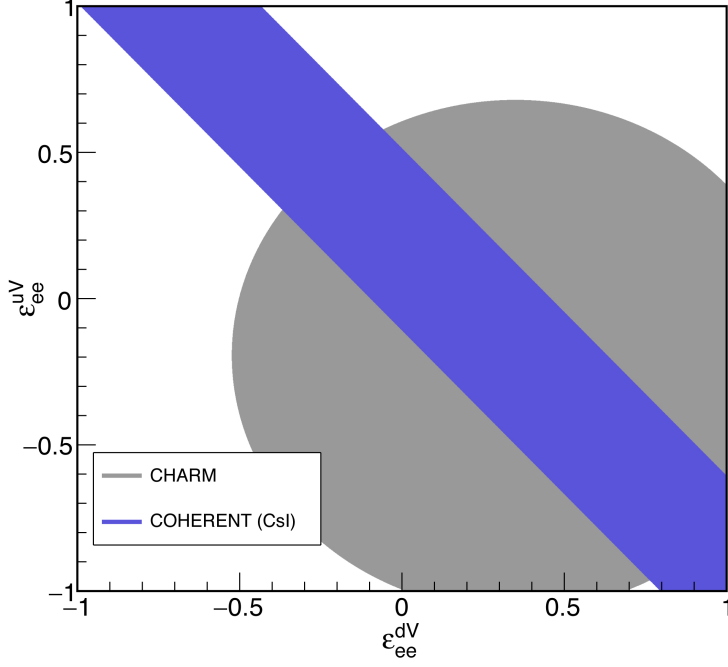


Figure 1.3: 90 % confidence limits on NSI parameters from [3] assuming all other ϵ s are 0 and from the CHARM experiment [21].

these include sensitivity to flavor changing neutral currents [8, 14–16], possible Z' bosons [14–16], and probes of the weak nuclear charge sensitive to radiative corrections above the weak scale [17].

In particular, so-called ‘Non-Standard Interactions’ (NSI) can confuse the mass ordering determination by long baseline neutrino experiments [18, 19] such as DUNE. Constraining these interactions by scattering experiments is very important for the global neutrino physics program and CEvNS provides an opportunity to do so.

A model-independent parameterization of non-standard contributions to the neutrino-quark interactions can be added to the SM Lagrangian in the following form (following [8, 20]):

$$\begin{aligned} \mathcal{L}_{\nu H}^{NSI} = & -\frac{G_F}{\sqrt{2}} \sum_{\substack{f,g=e,\mu,\tau \\ q=u,d}} \left[\bar{\nu}_f \gamma^\mu (1 - \gamma^5) \nu_g \right] \times \\ & \left[\epsilon_{fg}^{qL} \left(\bar{q} \gamma_\mu (1 - \gamma^5) q \right) + \epsilon_{fg}^{qR} \left(\bar{q} \gamma_\mu (1 + \gamma^5) q \right) \right] \end{aligned} \quad (1.5)$$

Here the ϵ parameters describe non-standard interactions that are either ‘non-universal’ ($f = g$) or ‘flavor-changing’ ($f \neq g$).

With the inclusion of these NSI couplings, G_V and G_A (Eq. 1.1) are modified [8, 14, 22]:

$$\begin{aligned} G_V &= \left[\left(g_V^p + 2\epsilon_{ee}^{uV} + \epsilon_{ee}^{dV} \right) Z + \left(g_V^n + \epsilon_{ee}^{uV} + 2\epsilon_{ee}^{dV} \right) N \right] F_{nuc}^V(Q^2) \\ G_A &= \left[\left(g_A^p + 2\epsilon_{ee}^{uA} + \epsilon_{ee}^{dA} \right) (Z_+ - Z_-) + \left(g_A^n + \epsilon_{ee}^{uA} + 2\epsilon_{ee}^{dA} \right) (N_+ - N_-) \right] F_{nuc}^A(Q^2) \end{aligned} \quad (1.6)$$

As the axial couplings for most targets are small, the axial ϵ s can be assumed to be zero. For coherent scattering, where the recoil energies are much smaller than the incident neutrino energies, the effect of NSI couplings is an overall scale factor to the cross section, rather than a spectral shape distortion.

The ϵ_{ee} couplings are poorly constrained (on the order of unity [20]) and the parameter space (Fig. 1.3) has already been further constrained with the first observation of CEvNS on CsI[Na] [3]. Additional target nuclei will help to further constrain the NSI parameter space, with larger variations of $\frac{A+N}{A+Z}$ between targets increasing the parameter space rejection capabilities from CEvNS [4, 22, 23]. A joint analysis of the recent COHERENT result and global neutrino oscillation data has already been used to exclude the NSI degeneracy effecting DUNE at greater than 3σ [24].

1.3 NEUTRINO FLOOR

Weakly Interacting Massive Particles (WIMPs) are a popular dark matter candidate. Many theories allow for an interaction of the ‘dark sector’ and the Standard Model via a similar interaction as CEvNS: coherent scattering from a nucleus [26]. This means that the signature of a WIMP interaction cannot be separated from CEvNS via the normal means: event topology, pulse shape discrimination, etc. Combined with a lack of directional information due to the low energies of the recoiling nuclei, CEvNS recoils from atmospheric neutrinos (e.g. the sun) and cosmological sources (e.g. the Diffuse Supernova Background) will result in an irreducible ‘Neutrino Floor’ for

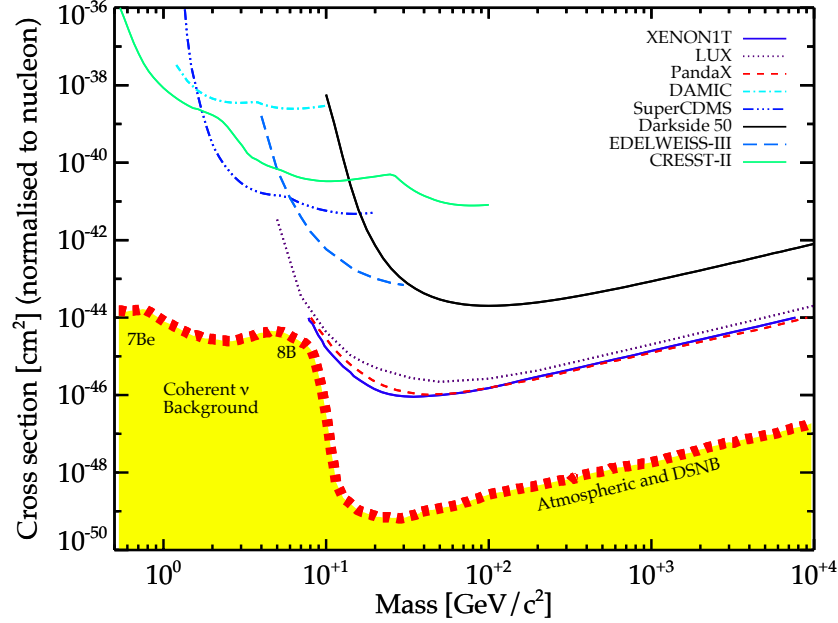


Figure 1.4: WIMP parameter space demonstrating the ‘Neutrino Floor’ from the CEvNS of solar, atmospheric, and diffuse relic neutrinos. Plot courtesy of L. Strigari and updated from [25].

next-generation dark matter experiments [25]. It is therefore important to characterize the CEvNS cross section to learn where the Neutrino Floor lies in the WIMP parameter space (Fig. 1.4).

1.4 SUPERNOVAE DYNAMICS

One important application of CEvNS physics, recognized by Freedman in his initial paper on CEvNS [2], is in the modeling and understanding of supernovae explosions. When a star undergoes core collapse, approximately 1×10^{53} erg ($\sim 99\%$ of its gravitational potential energy) is carried away by neutrinos [27]. Within the first 0.1s after the collapse begins, the core density is so high, $\sim 1 \times 10^{12}$ g cm³, that neutrinos can no longer freely escape the core [28]. For the few MeV neutrinos produced, the dominant interaction is coherent scattering from the heavy nuclei in the core. It is therefore very important to understand the CEvNS cross section to properly model the core-collapse process.

CEvNS also opens up a new channel to observe supernovae neutrinos. As CEvNS is the

dominant neutrino cross section for the few MeV neutrinos produced by supernovae, a detector sensitive to CEvNS could observe a few events per ton from a galactic supernova at 10 kpc [29]. Such a detector can provide information of the ν_e and ν_x flux and spectrum from supernovae ($\nu_x = \nu_\mu, \bar{\nu}_\mu, \nu_\tau$, and $\bar{\nu}_\tau$). While a CEvNS detector would not be able to distinguish between ν_e and ν_x neutrinos, when coupled with supernovae observables providing spectral information about ν_e and $\bar{\nu}_e$, CEvNS could be used to measure the ν_x energy spectrum and possibly provide information about $\nu_x \rightarrow \nu_e$ oscillations [29].

1.5 NUCLEAR STRUCTURE

One of the outstanding questions in nuclear physics is the distribution of neutrons in the nucleus. While the distribution of protons can be relatively easily measured with electron elastic scattering (due to the electrical charge of the proton) [30], the lack of electrical charge carried by the neutron makes a similar measurement much harder to perform. There is considerable interest in measurements of the neutron distribution as they can provide valuable input for nuclear structure models [31]. Through the dependence of the cross section on the form factors, CEvNS provides such a method. In fact, the neutron radius of Cs and I has already been constrained to 18 % using the 2017 CsI result in [12], although they did not include effects from the spectral-shape uncertainties. A better understanding of the structure of neutron-rich nuclei can inform the neutron equation of state and help constrain existing neutron star models [31–33].

In 2008, CEvNS was recognized as a new channel to measure neutron form factors [34]. The form factors are simply the Fourier transform of the nuclear matter distribution. This raises the possibility that with a precision CEvNS measurement, the form factor shape could be unfolded from the CEvNS recoil spectrum. While not competitive with more recent parity violating measurements of the neutron distribution, such as that by PREX [35], CEvNS will provide a new channel with entirely different systematics to measure the neutron distribution.

1.6 PRIOR AND ONGOING CEVNS SEARCHES

With the advances in detector technology over the past few decades, largely driven by dark matter and $0\nu\beta\beta$ -decay experiments, the low thresholds required for CEvNS observation are now attainable. There are many experiments currently running and proposed that hope to measure CEvNS.

While the first experimental proposal to measure CEvNS was published in the 1980s [36], it was not until the past decade that a significant attempt to measure CEvNS was under way. The two most common neutrino sources used to search for coherent scattering are nuclear reactors [37–40] and stopped-pion sources [3, 10].

While the neutrino flux from reactors is several orders of magnitude higher than at a stopped-pion source, the neutrinos are relatively low energy, $\mathcal{O}(1\text{ MeV})$. In order to observe CEvNS with these low energy neutrinos, detectors with sub-keV energy thresholds are required. A variety of detector technologies have been proposed or are currently running to measure CEvNS at a reactor. Among others, Ricochet has proposed low-temperature bolometers [37], CONNIE has proposed an array of charge-coupled devices [38, 41, 42], MINER is planning to use cryogenic germanium and silicon detectors [39], and ν -cleus is proposing to use calorimeters [40]. The first hint of CEvNS from a reactor-neutrino source was recently observed by the CONUS experiment with p-type point contact HPGe detectors [43], but there has yet to be a definitive measurement.

The major advantage of a stopped-pion source lies in the higher energy neutrinos produced. These neutrinos come from pion decay-at-rest and are $\mathcal{O}(10\text{ MeV})$, producing more energetic nuclear recoils that are more easily seen. The CENNS collaboration [10] proposed to run a ton-scale liquid argon detector off-axis near the Booster Neutrino Beamline target at Fermilab. COHERENT [3] on the other hand, is located at the Spallation Neutron Source at Oak Ridge National Lab, and is planning CEvNS measurements on a variety of $\sim 10\text{ kg}$ detectors to map out the N^2 dependence of the cross section. COHERENT observed CEvNS for the first time in 2017 [3]. Stopped-pion sources and the COHERENT collaboration are discussed in more detail in Chapter 2.

The topic of this thesis is a first search for CEvNS on argon by the COHERENT collaboration. Chapter 2 centers on the Spallation Neutron Source as a neutrino source and describes ongoing measurements by the COHERENT experiment. Relevant backgrounds at the SNS, and the campaign to measure them, are covered in Chapter 3. Chapters 4-5 cover liquid argon as a target for CEvNS, and in particular the CENNS-10 detector, as well as the calibration of CENNS-10. Chapters 6-7 cover the analysis of the CENNS-10 Engineering Run data at the SNS, and I conclude with Chapter 8.

CHAPTER 2

COHERENT AT THE SPALLATION ‘NEUTRINO’ SOURCE

In this chapter I discuss the efforts of the COHERENT collaboration to detect CEvNS at the Spallation Neutron Source (SNS) at Oak Ridge National Lab. I begin with a discussion of the SNS as a neutrino source. I follow with an overview of the COHERENT experiment and a brief summary of the exciting first detection of CEvNS using a CsI[Na] detector.

2.1 THE SPALLATION NEUTRON SOURCE

The Spallation Neutron Source (SNS) at Oak Ridge National Lab (ORNL) is the most intense pulsed-neutron source in the world. It is used for neutron scattering research by researchers in fields ranging from biology to chemistry to fundamental physics [44, 45].

At the SNS, a 1 GeV proton beam impinges on a liquid mercury target. The interaction of the beam with the target spallates neutrons that are directed to experiments at various target stations. Of greater interest to COHERENT is the fact that the proton beam is narrow in time (with a full width at half max of ~ 380 ns resulting in most of the pulse arriving within an $1 \mu\text{s}$ window as seen in Fig. 2.1) and is pulsed at 60 Hz. This reduces the effect from steady-state backgrounds by a factor of $\mathcal{O}(1 \times 10^{-4})$ while also providing the opportunity to characterize these backgrounds by measuring them outside of the beam window. Within the past year, the SNS has reached its design power of 1.4 MW resulting in a beam luminosity of $\mathcal{O}(1 \times 10^{16}$ protons/s).

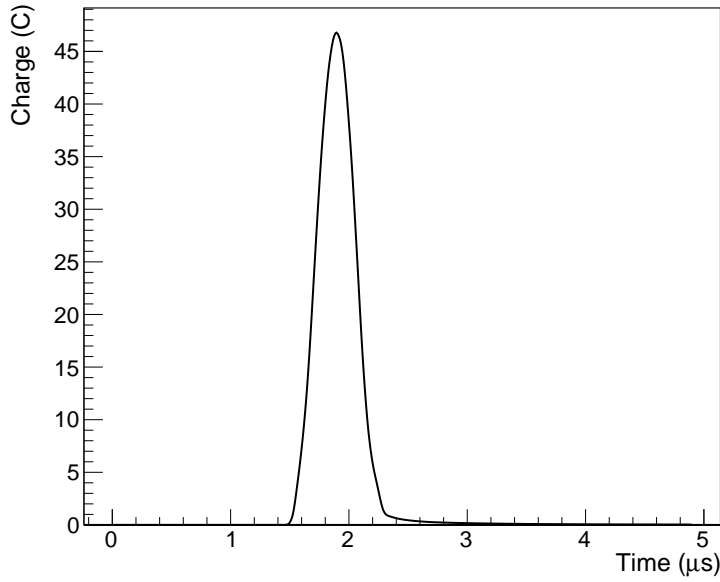


Figure 2.1: Average protons-on-target trace at the SNS. The beam pulse at the SNS is almost entirely contained within a $1\text{ }\mu\text{s}$ time window reducing the effect of steady-state backgrounds and allowing them to be measured outside of the beam-timing window.

2.1.1 THE SNS AS A NEUTRINO SOURCE

When the protons impact the mercury target, a number of charged pions (π^\pm) are produced. While the π^- are mostly re-captured by the mercury, the majority of the π^+ thermalize and decay at rest (DAR) with a lifetime of 26 ns. An individual π^+ decays to a muon neutrino (ν_μ) and a positive muon (μ^+). The μ^+ then decays with a lifetime of 2.2 μs to a positron (e^+), an anti-muon neutrino ($\bar{\nu}_\mu$), and an electron neutrino (ν_e). The neutrino production mechanism can be seen in Fig. 2.2a. These neutrinos have well-understood time and energy spectra which can be used by a neutrino experiment at a stopped-pion source.

To characterize the neutrino flux at the SNS, a **Geant4** simulation [46, 47] of the liquid mercury target, including the target and target-hall geometries, was carried out. In this simplified simulation, a 1 GeV beam of protons impinged on a liquid mercury target and the neutrino flux and spectra were measured 20 m from the target. An average of $0.08\text{ }\nu/\text{flavor}/\text{POT}$ ($\pm 10\%$) were found to be produced isotropically at the target, with some dependence on the actual beam energy on the order of 2% [3]. The uncertainty in the neutrino yield is largely driven by the uncertainties

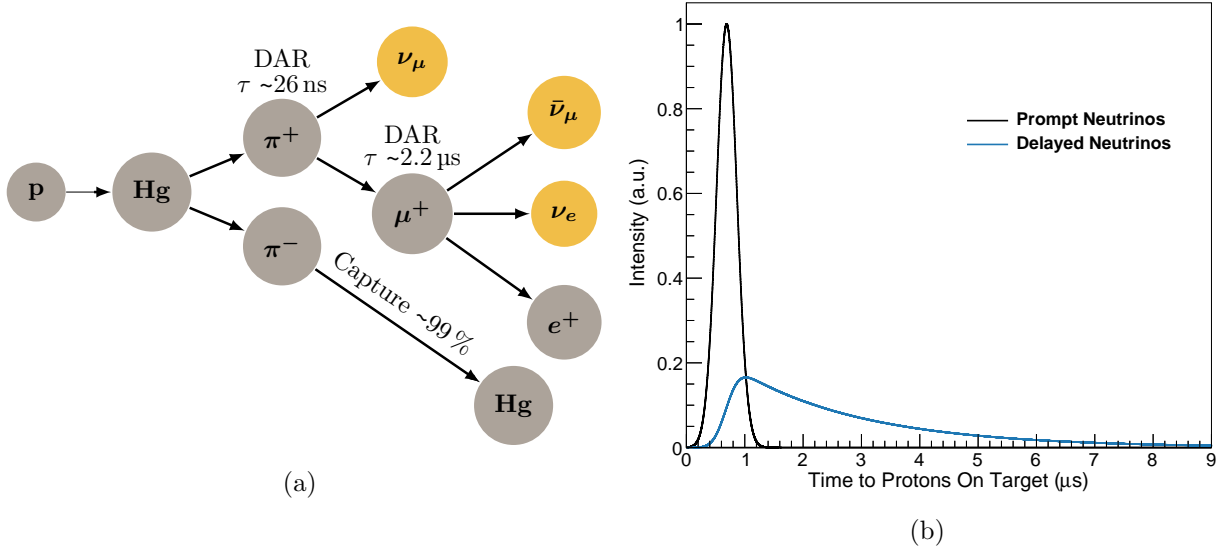


Figure 2.2: (a) A schematic of stopped-pion neutrino production. Most π^- are captured by the target before decaying. π^+ decay into a muon neutrino and a positive muon which subsequently decays to a positron, a ν_e , and a $\bar{\nu}_\mu$. A total of $0.08 \nu/\text{flavor}/\text{POT}$ are produced. (b) The timing spectrum of neutrinos produced at a stopped-pion source. The prompt ν_μ arrive within a ~ 1 μ s time window and follow the beam time profile. The characteristic 2.2 μ s lifetime of muon decay is seen in the delayed neutrino time spectrum. A beam-related signal with such a lifetime is an indication that it is neutrino related.

in pion production and nucleon-nucleon cross sections.

Contamination of the stopped-pion neutrino spectrum from neutrinos produced via decay-in-flight and μ -capture is small (see Fig. 2.3), and this contamination is two orders of magnitude smaller at the SNS than at similar stopped-pion neutrino sources such as the Fermilab Booster Neutrino Beam [10] and JPARC [48,49]. In addition, the contribution to the CEvNS signal from these high energy neutrinos ($\gtrsim 50$ MeV) is $< 1\%$. The neutrino flux at the SNS is also ~ 80 times higher than at the BNB at the same distance from the target. The SNS provides the best combination of beam power and background suppression of any stopped-pion source in the world.

2.1.2 NEUTRINO TIME AND ENERGY SPECTRA

The ν_μ produced via π^+ decay occur via a two-body process which results in a well-defined energy

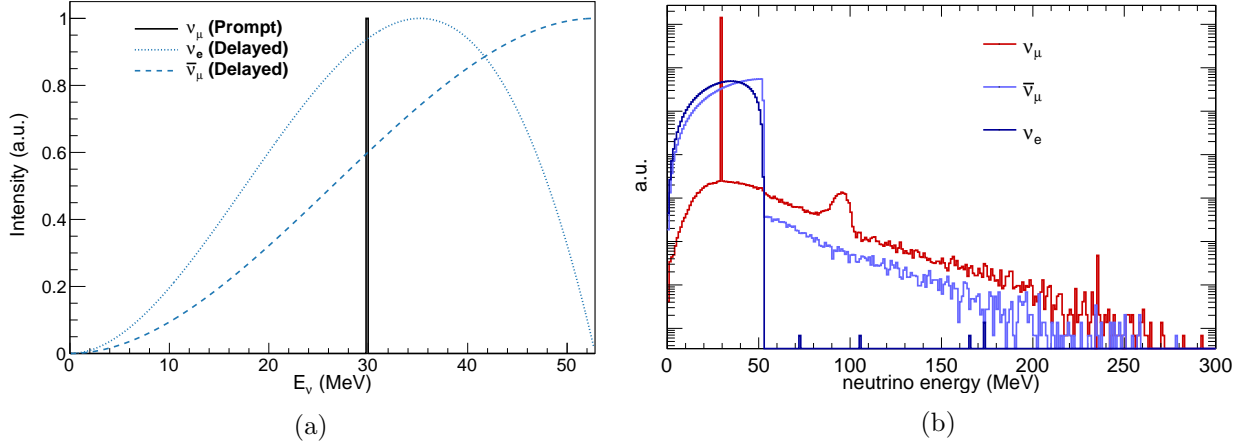


Figure 2.3: Characteristic neutrino energy spectra from a stopped-pion source. (a) Idealized analytical energy distributions. The ν_μ come from π^+ decay and arrive roughly in time with the beam. The ν_e and $\bar{\nu}_\mu$ are due to muon decay at rest and exhibit the characteristic energy spectra expected for Michel decays. (b) Realistic spectra expected in Neutrino Alley. These are based on a **Geant4** simulations including the geometry of the SNS target and the target building. Contamination from higher energy neutrinos due to decay-in-flight is seen to be down by orders of magnitude from the decay-at-rest spectra. The feature at ~ 100 MeV is due to muon capture.

dependent on the mass difference between the original pion and the resulting muon:

$$f_{\nu_\mu}(E_{\nu_\mu}) = \delta\left(E_{\nu_\mu} - \frac{m_\pi^2 - m_\mu^2}{2m_\pi}\right) \quad (2.1)$$

$$\rightarrow E_{\nu_\mu} \equiv 29.8 \text{ MeV}$$

The $\bar{\nu}_\mu$ and ν_e on the other hand are produced via a three-body decay resulting in a continuum of possible energies. The distribution of the $\bar{\nu}_\mu$ and ν_e energies follows from the well understood Michel spectrum which can be parameterized as in [34, 50]:

$$f_{\nu_e}(E_{\nu_e}) = \frac{96}{m_\mu^4} E_{\nu_e}^2 (m_\mu - 2E_{\nu_e}) dE_{\nu_e} \quad (2.2)$$

$$f_{\bar{\nu}_\mu}(E_{\bar{\nu}_\mu}) = \frac{16}{m_\mu^4} E_{\bar{\nu}_\mu}^2 (3m_\mu - 4E_{\bar{\nu}_\mu}) dE_{\bar{\nu}_\mu}$$

The maximum energy from this decay is ~ 52.8 MeV, roughly half the mass of the muon. These idealized energy spectra can be seen in Fig. 2.3. Also shown in Fig. 2.3 are more realistic neutrino energy spectra predicted by the **Geant4** target simulation discussed in Sec. 2.1.1. There is consid-

erable overlap of the energy spectrum from a stopped-pion source and theoretical predictions of supernovae neutrino spectra which follow a Fermi-Dirac distribution [51]. Thus, a measurement of CEvNS at a stopped-pion source can validate coherent-scattering effects from neutrinos produced in supernovae (Section 1.4).

The pulsed nature of the SNS, as well as the short timescales required for neutrino production (as seen in Fig. 2.2), allows for considerable reduction of the steady-state beam-unrelated background on the order of $(1-10) \times 10^{-5}$. Due to the localized nature in time of the SNS beam pulses, these backgrounds can be well-characterized with beam-off measurements and then subtracted making stopped-pion sources (and in particular the SNS) ideal for measuring the CEvNS process.

The neutrino energies at a stopped-pion source are sufficiently low to maintain the coherence condition of CEvNS. At the same time, they are higher than the energies of reactor neutrinos and therefore result in higher energy recoils which are easier to detect. Thus, even though the total neutrino flux at a stopped-pion source like the SNS is lower than a typical reactor source, there are some advantages due to the neutrino energy and timing characteristics at a stopped-pion source.

2.2 THE COHERENT EXPERIMENT

The COHERENT collaboration is an international group of roughly 100 researchers from 20 institutions coming together at the SNS to search for CEvNS. The characteristics of the SNS beam in particular and a stopped-pion neutrino source in general provide a few significant features to unambiguously measure CEvNS:

1. Beam-related signal: The pulsed nature of the SNS allows for the ability to show that a signal is beam-related. The beam pulses are short enough that the separation of a ‘beam window’ and a ‘strobe window’ anticoincident with the beam are possible.
2. Neutrino-related signal: Even within a beam window, the time profile of neutrinos from π -DAR can be used to show the signal is due to neutrinos rather than some other beam signature such as beam-related neutrons. The delayed neutrinos in particular have a well

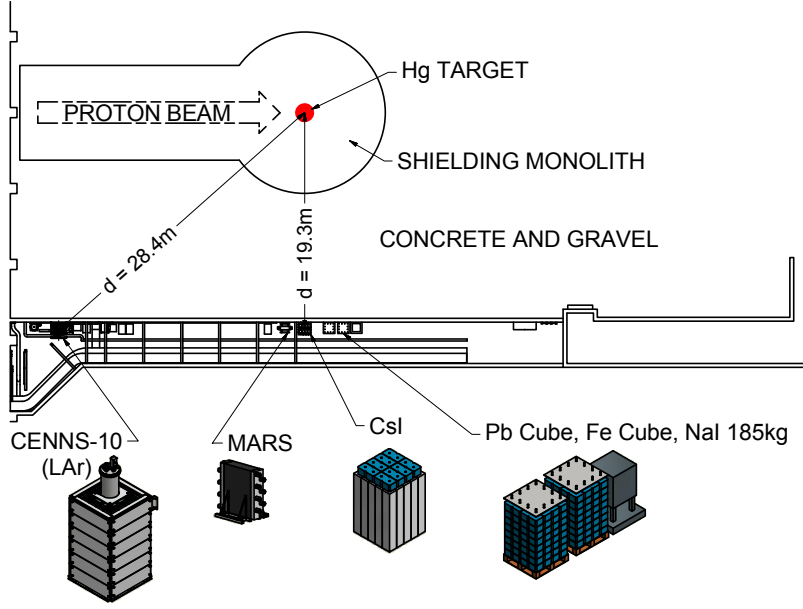


Figure 2.4: Current COHERENT detector siting at the SNS. CENNS-10 and the CsI[Na] detectors are sensitive to CEvNS. MARS is intended to monitor the beam-related neutron rate in ‘Neutrino Alley’ discussed further in Ch. 3. The Pb and Fe Cubes are sensitive to neutrino-induced neutrons, an important beam-related signal that is interesting in its own right and discussed in Sec. 3.2.1. NaI 185 kg is sensitive to charged-current interactions on I and is a prototype of a planned 2 t NaI CEvNS detector seen in Fig. 2.5.

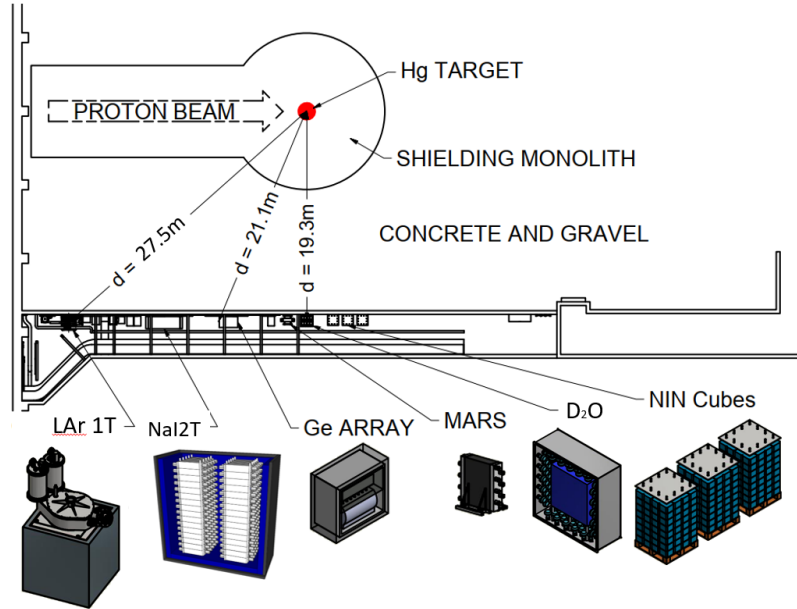


Figure 2.5: Planned future COHERENT detector siting in Neutrino Alley. Tonne-scale detectors, as well as PPC Ge detectors, will allow for precision measurements of the CEvNS cross section. A heavy water detector (D_2O) is planned to reduce the systematic uncertainty on the neutrino flux from the target by taking advantage of the small theoretical uncertainty for the charged-current $\nu_e + d \rightarrow p + p + e^-$ reaction [52, 53].

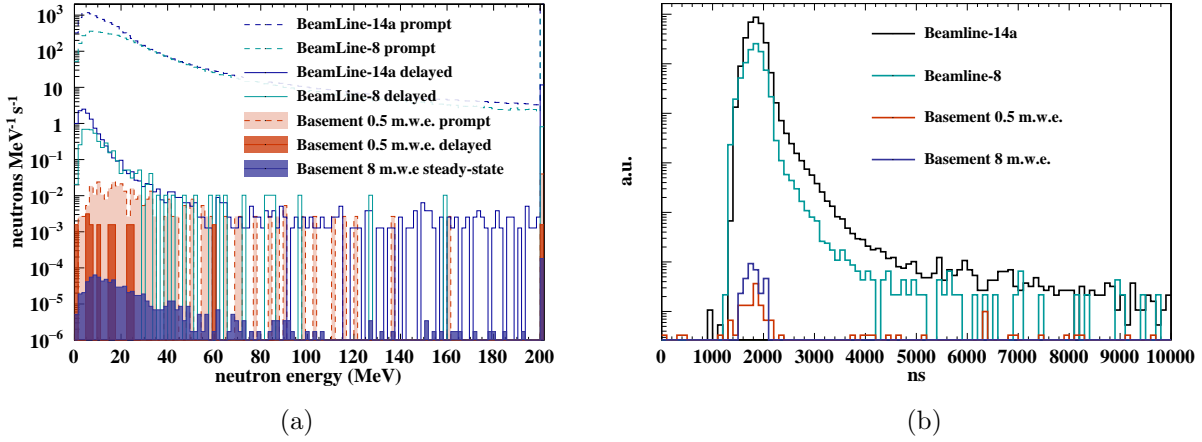


Figure 2.6: The neutron flux throughout the SNS target building as measured by the Sandia Neutron Scatter Camera [54]. The beam-related flux in ‘Neutrino Alley’ is four orders of magnitude lower than on the target floor. (a) Fast-neutron energy spectra taken at various locations in the SNS target building. ‘Basement 8 mwe’ was taken in Neutrino Alley. (b) Fast-neutron timing spectra. In Neutrino Alley there is no indication of fast neutrons in the ‘delayed’ window.

known 2.2 μ s lifetime.

3. N^2 cross section: A measurement of the N^2 dependence of the cross section can be used to show that the events are due to CEvNS rather than some other neutrino interaction.

Beginning in 2013, the COHERENT collaboration undertook a background measurement campaign to measure beam-related neutrons (BRNs) at the SNS. BRNs are a non-negligible background for a CEvNS measurement and are discussed further in Chapter 3. Through this search, COHERENT identified ‘Neutrino Alley,’ a basement corridor in the SNS target building shown in Fig. 2.4. Neutrino Alley is located (20-29) m from the SNS target. The volume between the target and the alley is filled with engineered backfill, cutting down on the beam-related neutron flux considerably (by more than four orders of magnitude relative to the target floor) as seen in Fig. 2.6. In addition, Neutrino Alley provides an overburden of 8 mwe to reduce the cosmic ray flux. Meter water equivalent (mwe) represents the depth of water required to achieve a comparable reduction in the cosmic-ray rate at a given location.

Since the identification of Neutrino Alley, the fast beam-related neutron background has been further mapped out at various locations in the alley by the Sandia Neutron Scatter Camera [54]

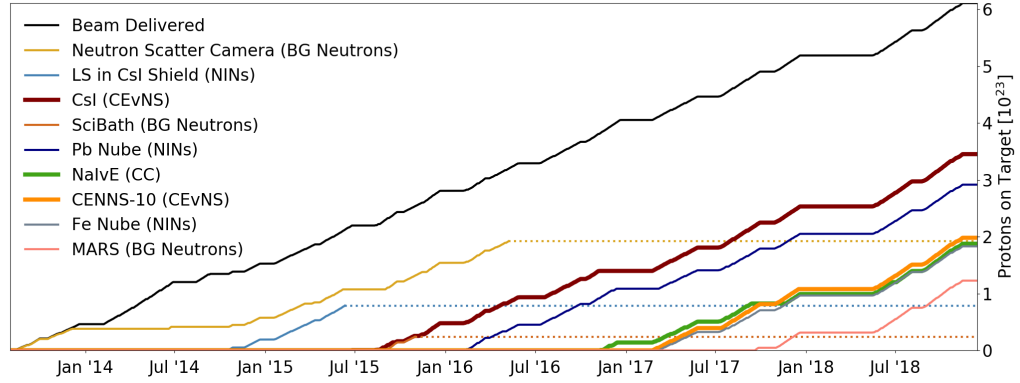


Figure 2.7: The total integrated protons-on-target for past and current COHERENT detectors in Neutrino Alley. Detectors sensitive to neutrino interactions have bolded lines (CsI[Na], CENNS-10, and NaIvE). Horizontal dashed lines indicate the detector is no longer taking data in Neutrino Alley. Figure is accurate as of the SNS winter shutdown in December 2018.

and by the Indiana University owned SciBath detector [10, 55, 56]. The Scibath measurement is further discussed in Chapter 3.

A primary goal of the collaboration is to measure the N^2 dependence of the CEvNS cross section. To do so, measurements are planned with a variety of detector media spanning the N parameter space. To date, COHERENT has deployed a CsI[Na] detector [3], a liquid argon detector (described in Chapter 4), and 185 kg of NaI[Tl]. A first measurement of CEvNS was made with the CsI[Na] detector in 2017 [3]. The total integrated protons-on-target seen by past and current COHERENT detectors in Neutrino Alley can be seen in Fig 2.7.

Future planned measurements with p-type point contact germanium and tonne-scale liquid argon and NaI detectors will allow for precision measurements of the CEvNS cross section [4] as well as provide opportunities for physics beyond a CEvNS search. A tonne-scale liquid argon detector in particular will provide opportunities to search for accelerator-produced dark matter [57–60] as well as measure charged-current cross sections relevant for DUNE that are currently poorly measured [52]. Fig. 2.5 shows the planned future detectors in Neutrino Alley as well as their expected locations in the hallway.

2.2.1 FIRST MEASUREMENT OF CEVNS WITH CsI[Na]

After the identification of Neutrino Alley, but prior to the installation of the CsI[Na] detector, a liquid scintillator cell was installed at the planned CsI[Na] location to characterize the beam-related neutron flux, as well as constrain the flux of neutrino-induced neutrons [61,62]. This measurement showed that the CEvNS signal should dominate over any beam-related backgrounds with sufficient shielding [3].

CsI[Na] was the first CEvNS-sensitive detector commissioned in Neutrino Alley. As a target, CsI[Na] offered many advantages for a CEvNS search. As Cs and I are relatively heavy with a large number of neutrons, the CEvNS cross section is quite large. Their similar mass results in a nearly identical response to CEvNS recoils and the high light yield of CsI[Na] (~ 64 photoelectrons/keVee) allows for a sufficiently low threshold to detect the low-energy nuclear recoils from CEvNS. CsI[Na] has a much shorter afterglow than is characteristic in Cs[Tl] [63] which is important when searching for low-energy signals in a surface experiment. Finally, low-background CsI[Na] crystals can be commercially produced and are relatively inexpensive at $\sim \$1 \text{ g}^{-1}$.

At the time of [3], the CsI[Na] detector had acquired data for a total of fifteen months. As seen in Fig. 2.8, by comparing beam-on to beam-off time windows, a significant beam excess was found that followed the expected CEvNS signature very closely. The excess agrees with the Standard Model prediction within one-sigma and rejects the null hypothesis at the 6.7σ level. This first measurement has already been used for a wealth of new physics, from constraining non-standard neutrino interactions [3,16,24], to constraining the neutron radius [12], and searching for accelerator produced dark matter [59]. The integrated beam exposure of the CsI[Na] detector has doubled since the result in [3].

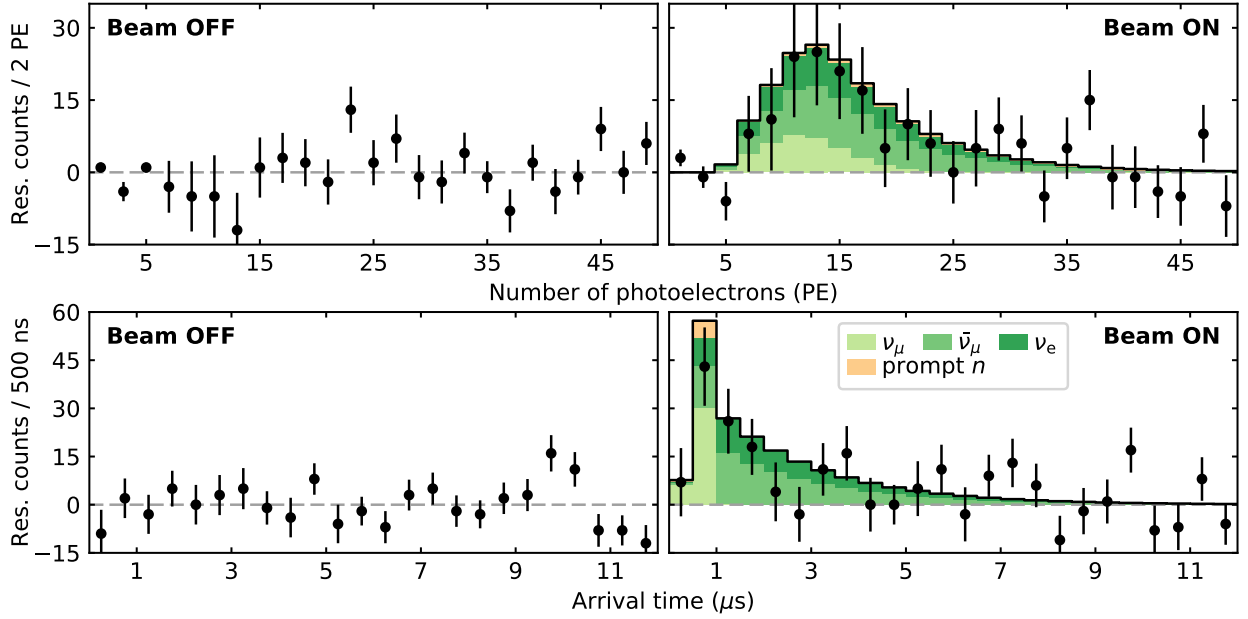


Figure 2.8: The result from a first measurement of CEvNS by the COHERENT collaboration using a CsI[Na] detector. These show the residuals between CsI[Na] signals in the $12\text{ }\mu\text{s}$ following beam triggers and those in a similar $12\text{ }\mu\text{s}$ time window with no beam trigger for 7.48 GWhr of beam data ($\sim 1.76 \times 10^{23}$ protons on target). The top panel shows the residual energy spectra and the bottom panel shows the time spectra. The beam-related excess is seen to closely follow the standard model CEvNS prediction. From [3].

CHAPTER 3

BACKGROUND MEASUREMENTS AT THE SNS

Due to the low energy recoils characteristic of CEvNS, a detailed understanding of the expected backgrounds is required for any CEvNS experiment. To that end, prior to the installation of any CEvNS detectors, measurements were made of the various background sources present in Neutrino Alley. Broadly speaking, there are two categories of backgrounds to be concerned with in Neutrino Alley: (1) beam-unrelated or steady-state backgrounds and (2) beam-related backgrounds.

In this chapter, I cover the important backgrounds for a CEvNS measurement in Neutrino Alley. I concentrate on the beam-related neutron measurement by the SciBath detector taken in the Fall of 2015 in the planned location of the CENNS-10 liquid argon detector.

3.1 BEAM-UNRELATED BACKGROUNDS

Any background unassociated with the SNS beam pulse is classified as a beam-unrelated background (BUB). These backgrounds are always present which means that their effect can be greatly reduced by making use of the SNS duty factor (the fraction of the time when the beam is actually on target). Because they are steady-state, they can be well-measured by making use of the pulsed nature of the SNS beam and subtracted for any sort of beam-related analysis.

The beam-unrelated background measurements discussed here were useful in characterizing the backgrounds in Neutrino Alley and helped inform detector-shielding designs. However, the actual rates and spectra of BUB sources for a beam analysis are measured in-situ with beam-off windows.

3.1.1 NEUTRINO ALLEY BEAM-UNRELATED BACKGROUNDS

There are two main sources of steady-state backgrounds in Neutrino Alley:

1. Natural radioactivity in the concrete walls and floors
2. The ‘Hot Off-Gas Pipe’ running down Neutrino Alley

Measurements to characterize these backgrounds were made using an Ortec Detective-100T HPGe germanium crystal detector [64] enclosed by a lead shield by M. Swinney of ORNL in 2014.

NATURAL RADIOACTIVITY The dominant source of natural radioactivity in Neutrino Alley is the concrete in the walls and floor. This radiation predominantly comes from ^{40}K and the ^{238}U and ^{232}Th decay chains.

HOT OFF-GAS The Hot Off-Gas (HOG) Pipe that runs down Neutrino Alley is a part of the SNS target exhaust system. While the target exhaust is passed through a variety of filtration systems [65], the HOG still contains a variety of radioisotopes that can be seen with a sensitive detector. The largest concentration of isotopes in the HOG passing the filtration systems are ^{11}C , ^{13}N , and ^{15}O all of which decay via positron emission, ultimately leading to a flux of 511 keV gamma rays in Neutrino Alley. While there is no health concern from the radioactivity of the HOG as it passes through Neutrino Alley, the rate is high enough that it leads to a noticeable gamma ray flux that can be seen with a sensitive detector.

BACKGROUND RATES To unfold any detector effects from the measurements made with the germanium detector, and unfold the actual rates of these sources, various MCNP [66] simulations were run by J. Zettlemoyer of Indiana University. Details of those simulations can be found in [67]. A summary of the expected rates can be found in Table 3.1. The rates from the concrete are expected to, for all practical purposes, remain constant. The HOG rate on the other hand, can change depending on the conditions of the SNS target-exhaust system, independent of the beam

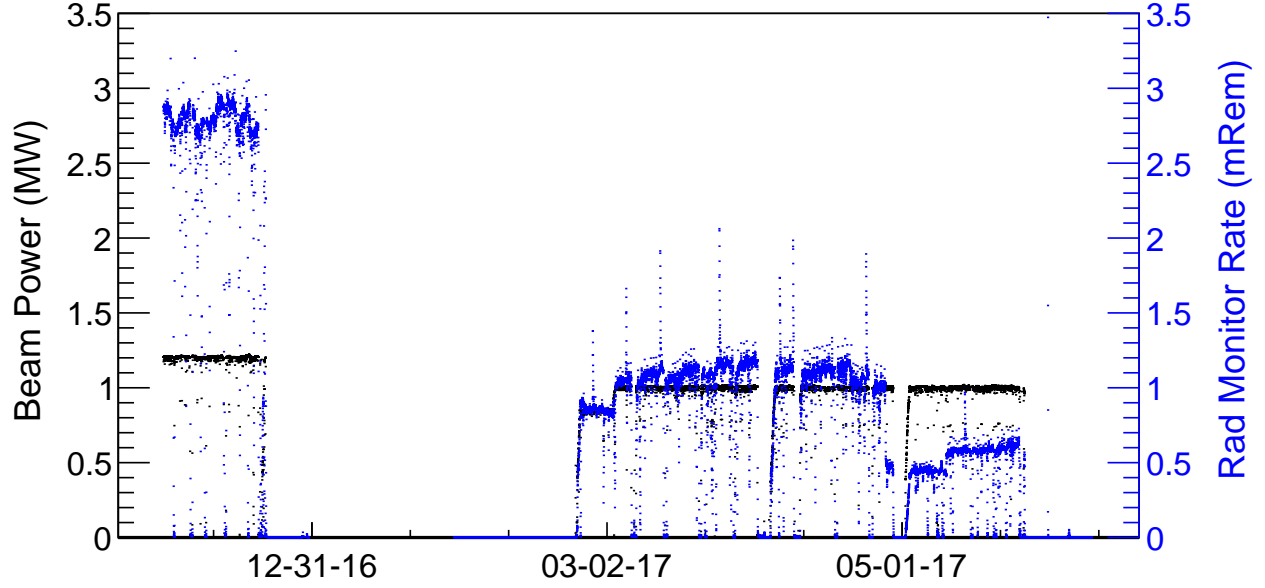


Figure 3.1: The hot off-gas (HOG) rate as measured by a radiation monitor on the HOG pipe (blue points) is seen to vary significantly (by a factor of $\mathcal{O}(3)$) as a function of time independent of the beam power (black points). Therefore the flux quoted in Table 3.1 should be used as a ‘starting point’ when calculating expected rates.

power, as seen in Fig. 3.1. As such, the rate of 511 keV gamma rays in Table 3.1 should be taken as a nominal value useful for, e.g. shielding design, and not assumed to be constant.

3.1.2 DETECTOR-SPECIFIC BEAM-UNRELATED BACKGROUNDS

In addition to the beam-unrelated backgrounds characteristic of Neutrino Alley, every CENNS detector also has detector-specific backgrounds. For the CENNS-10 liquid argon detector, the dominant detector-specific background is due to ^{39}Ar .

^{39}Ar is a naturally-occurring isotope of argon produced by cosmic rays in the atmosphere. It is inherent in any type of argon detector using an atmospheric source of argon. ^{39}Ar beta decays to ^{39}K with an endpoint of 535 keV at a rate of roughly 1 Bq kg^{-1} . It has half life of 269 years [68].

There has been some effort recently, especially among the dark matter community, to utilize underground sources of argon [69]. The ^{39}Ar contamination of these underground sources of argon is down by over a factor of 100 relative to atmospheric argon sources [70, 71], and the use of

Measured Flux	
HOG	$25 \gamma/\text{cm}^2/\text{s}$
Concrete (Wall)	$0.9 \gamma/\text{cm}^2/\text{s}$
Concrete (Floor)	$1.0 \gamma/\text{cm}^2/\text{s}$
^{39}Ar	1 Bq kg^{-1}

Table 3.1: Fluxes for some characteristic backgrounds in neutrino alley. Assumed errors are 10 % for the concrete and hot off-gas (HOG) environmental-gamma backgrounds. The HOG rate changes in time (see Fig. 3.1), and the value above can be used as a nominal rate when calculating expected background rates in a given detector. It is based on a single measurement from 2014. ^{39}Ar is a background inherent to argon detectors and is produced by cosmic rays in the atmosphere. It is only relevant for the CENNS-10 liquid argon detector.

underground argon is being considered for use in CENNS-10.

3.2 BEAM-RELATED BACKGROUNDS

Beam-related backgrounds are particularly tricky to characterize as their arrival time is correlated with the SNS beam pulse. This means that they both can not be reduced by using the beam duty factor and can not be measured outside of the beam window. For this reason, it is very important to measure these backgrounds with auxiliary detectors before any sort of CEvNS measurement can be made.

3.2.1 NEUTRINO-INDUCED NEUTRONS

Neutrino-Induced Neutrons (NINs) can be produced by the SNS neutrinos interacting with the radiation shielding of a detector, in particular with any Pb shielding [72, 73]. These neutrons are produced via the charged and neutral current interactions $^{208}\text{Pb}(\nu_e, e^- \text{xn})$ and $^{208}\text{Pb}(\nu_x, \nu_x \text{yn})$ where ‘x’ and ‘y’ represent the neutron multiplicity. These NINs have the same time signature as CEvNS and can mimic the CEvNS signal. Currently, the NIN cross section is only estimated theoretically to within a factor of ~ 3 [74–76].

NINs are an interesting physics topic in their own right and are the neutrino-detection mechanism used by the HALO supernova neutrino detection experiment [77, 78]. The spallation of

neutrons from heavy elements is also expected to influence nucleosynthesis during supernovae explosions [79, 80]. COHERENT is making a dedicated measurement of the NIN cross section on multiple materials (currently Pb and Fe). These measurements will be used to evaluate the NIN background for COHERENT as well as an independent physics measurement.

A non-zero NIN signal was found in [3], but it suggests a smaller cross section than theoretically predicted.

3.2.2 BEAM-RELATED NEUTRONS

A particularly tricky background to understand is beam-related neutrons (BRNs). Beam-related neutrons can elastically scatter and mimic the CEvNS neutral current signal. The time structure of CEvNS events should help separate the CEvNS signal from any sort of beam-related neutron signal, but before that can be done, the BRN flux in both energy and time needs to be understood.

While the beam-related neutron rate in Neutrino Alley is quite low (Sec 2.2), it is still important to measure the BRN rate in the exact location a CEvNS detector will run. To that end, the SciBath detector [10, 55, 56] was deployed to Neutrino Alley in the Fall of 2015 at the planned location of CENNS-10 to monitor the beam-related neutron flux. This measurement demonstrated the beam-related neutron rates were low enough to perform a CEvNS measurement and provided energy and timing information about the BRN flux, informing the shielding design for CENNS-10.

3.3 THE SCIBATH MEASUREMENT

SciBath is a fast-neutron detector first used to measure the cosmic ray muon flux deep underground in the NuMI cavern at Fermilab [56] and then later to measure beam-related neutrons for the CENNS collaboration at the Booster Neutrino Beam target at Fermilab [10].

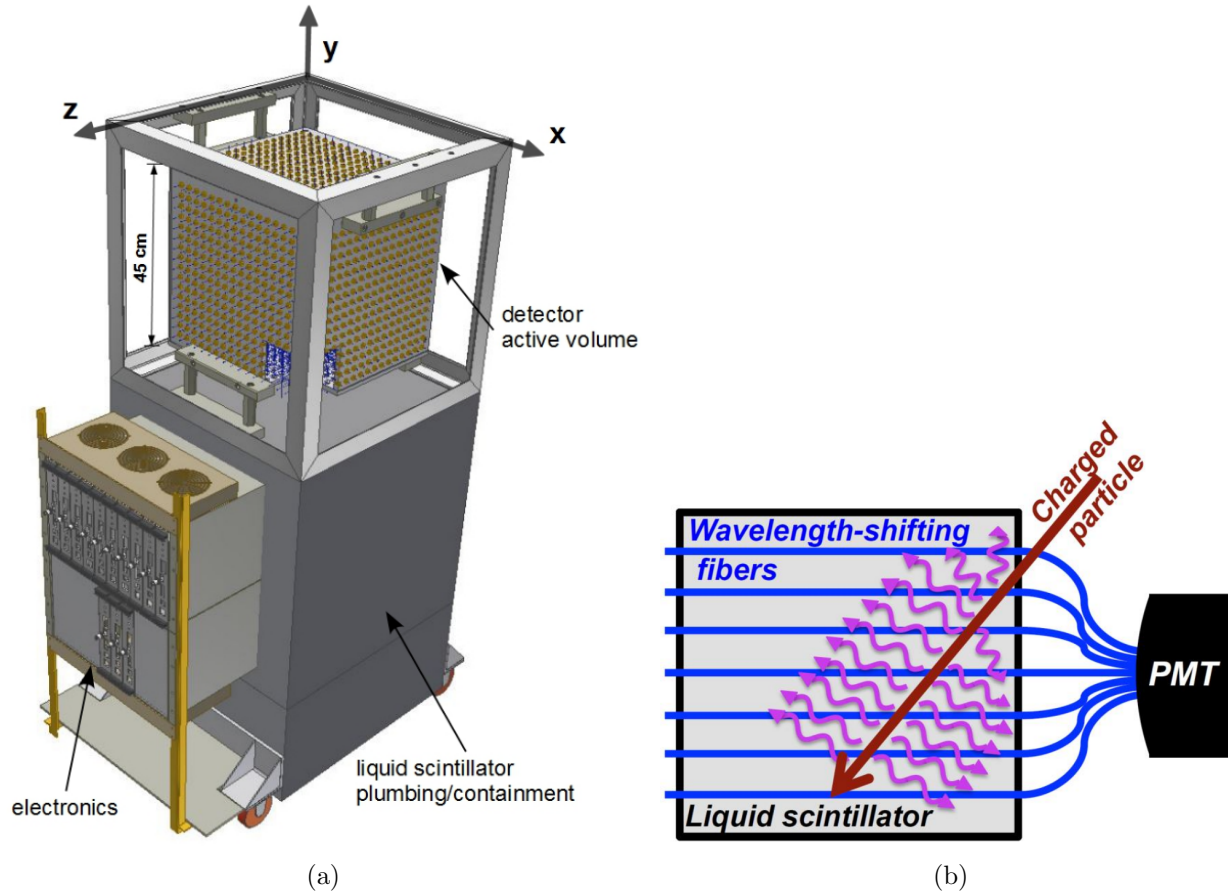


Figure 3.2: The SciBath detector. (a) SciBath schematic. The active volume contains 82l of liquid scintillator with 768 wavelength-shifting (WLS) fibers woven through it in a 3D grid. (b) SciBath operating principle. Charged particles pass through the detector and induce scintillation light. The light is captured and wavelength shifted by the wavelength-shifting fibers and then carried to the photomultiplier tubes (PMTs).

3.3.1 THE SCIBATH DETECTOR

As seen in Fig. 3.2, SciBath is a cubical 821 liquid scintillator detector. Event topology and tracking is done by a 3D grid of 768 wavelength-shifting (WLS) fibers which couple to twelve R6400 Hamamatsu 64-channel photomultiplier tubes (PMTs). The fibers shift the UV scintillation light to blue light which is more efficiently detected by the PMTs [56]. Each PMT is read out by a custom-built Integrated Readout Module (IRM).

Each IRM records the PMT pulses with an onboard 12-bit 20 MS/s flash ADC. In addition, an onboard FPGA provides some elementary data analysis. The IRMs are externally powered and readout via 1 Gbit Ethernet ports. SciBath also has a 13th Break-in-Board (BIB) which can be used to run auxiliary detectors, but is typically used to read out accelerator timing signals to mark beam-related/unrelated events.

For the 2015 run at the SNS, a fresh mixture of mineral oil-based liquid scintillator was made. The mixture was broken up as follows:

1. 80.25 l of mineral oil (MO)
2. 19.9 l of pseudocumene (PC)
3. 477 g of 2,5-Diphenyloxazole (PPO)

This gave a final mixture of 99.5 l of scintillator at 4.8 g l^{-1} of PPO and 20 % PC. This scintillator makeup was similar to the commercially available products EJ-321L [81] and BC-517 H [82]. The scintillator was continuously circulated between the detector and a reservoir volume under a N_2 environment to prevent oxygen poisoning and keep the light output consistent throughout the run. For the SNS run, the scintillator was continually bubbled with N_2 as a degradation in the light yield had been observed near the end of previous runs.

3.3.2 SNS RUN SUMMARY

As seen in Fig. 3.3, SciBath ran in the alcove at the end of Neutrino Alley. This is the current location of CENNS-10. It was $\sim 3.2 \text{ m}$ from the end of the hallway and $\sim 28 \text{ m}$ from the SNS target

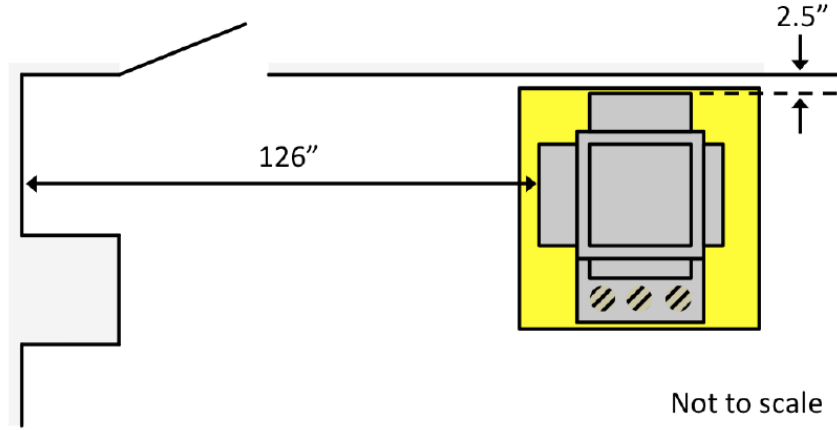


Figure 3.3: Siting of the SciBath detector for the 2015 beam-related neutron measurement in Neutrino Alley. This is roughly the same location CENNS-10 is currently running in (see Chapter 4).

as seen in Fig. 2.4.

TIMELINE

SciBath began running on Sep. 2, 2015. The beam was off Sep. 8-9 so an LED calibration run was performed to characterize the single-photoelectron (SPE) response for each PMT channel. The SNS resumed running on Sep. 10th at 1300 kW and ran until Sep. 25 when the SNS target failed. A second LED calibration was taken on Oct. 6 and the beam turned back on Oct. 8. At this time the beam was running at $\sim 2/3$ power (~ 850 kW) and it continued running at 850 kW until the winter shutdown on Nov. 2.

The SNS beam runs more or less continuously with the exception of minor repairs and ‘Accelerator Physics’ studies every Tuesday. Throughout the run, the beam nominally fired at 60 Hz (see Fig. 3.4a) at an average beam power of 1.0 MW.

TRIGGER

For this measurement campaign, SciBath made use of two SNS accelerator signals: ‘Event 39’ and ‘Event 61.’ Evt. 61 precedes the beam by some milliseconds and signifies that the next beam pulse actually contains beam. Evt. 39 constantly runs at 60 Hz regardless of whether or not there

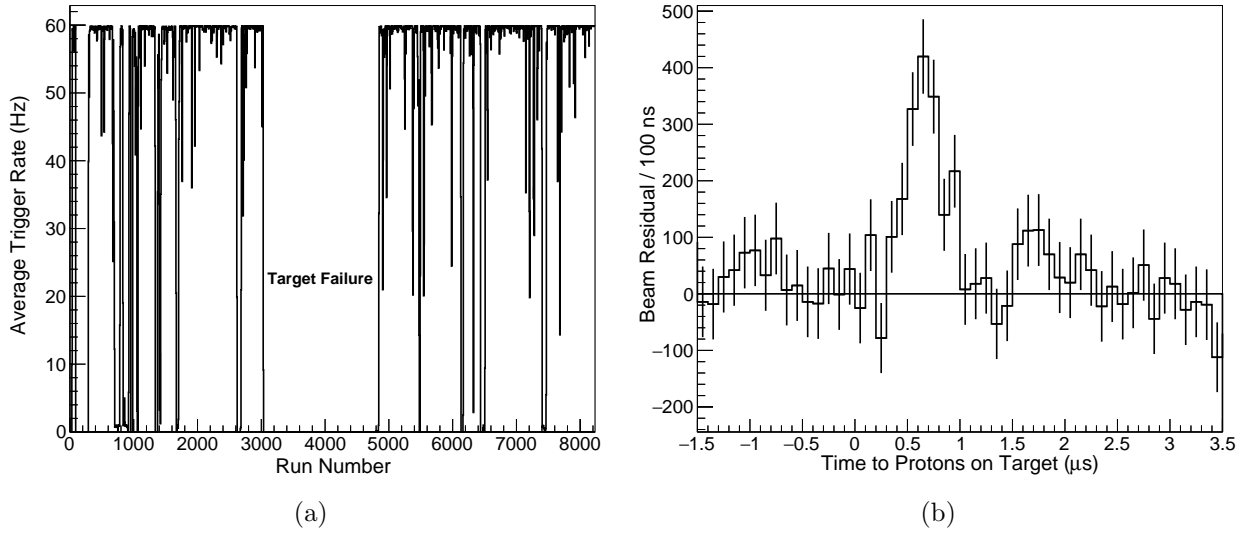


Figure 3.4: (a) SciBath triggered on the SNS ‘Event 61’ which signals that a proton pulse is imminent. This leads to a trigger rate that effectively monitored the SNS beam repetition rate, a nominal 60 Hz. There is some down time every Tuesday for minor repairs and ‘Accelerator Physics’ studies. The SNS suffered a target failure mid-run on Sept. 25, and resumed neutron production on Oct. 8. (b) Background-subtracted time spectrum of events relative to protons-on-target. The beam-related fast neutron events can be seen occurring at $t = 0 \mu\text{s}$.

is beam. It corresponds to the extract signal for the kicker magnets in the proton accumulator ring at the SNS [83] and is therefore very stable in time with respect to protons-on-target. The combination of these signals serves to provide information about whether beam is coming and when it is on target.

SciBath was externally triggered on a version of Evt. 61 delayed to come in time with the beam. However, the timing of Evt. 39 (and therefore beam-on-target) relative to Evt. 61 can move around depending on the beam energy. Therefore, Evt. 39 was also input into the data stream via the BIB to timestamp exactly when the beam was on target.

A trigger opened a $200 \mu\text{s}$ data acquisition (DAQ) window centered on the beam. The prompt beam pulse can be clearly seen in Fig. 3.4b. A $1/3$ photoelectron (PE) zero suppression threshold was implemented on each fiber to reduce the data rate.

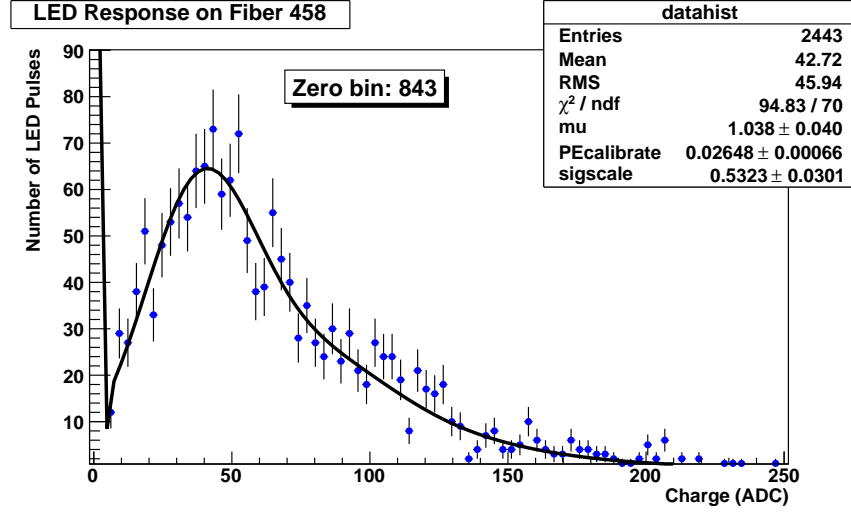


Figure 3.5: Typical single photoelectron spectrum in SciBath. The SPE calibration in ADC/PE is the reciprocal of ‘PEcalibrate.’ The PMT high voltages are tuned so that this value is ~ 30 ADC/PE.

3.3.3 ANALYSIS METHODOLOGY

The analysis methodology for SciBath can be roughly outlined as follows with details for each step later in this section. First, the response of SciBath to incident particles is characterized with the combination of LED calibrations, cosmic muons, and simulations. Second, event interactions are characterized and particle-identification cuts are placed. Then, through comparison to Monte Carlo simulations, the true particle rates and, in some cases, energy spectra are unfolded.

ENERGY CALIBRATION

The optical properties of the SciBath detector are characterized with a combination of pulsed low-light LEDs (one per fiber) and the use of cosmic ray muons. The low-light LEDs are used to find the single photoelectron (SPE) response for each fiber. As seen in Fig. 3.5, in SciBath the photomultiplier tube (PMT) voltages are tuned so that a single PE has a pulse height of ~ 30 ADCs (the reciprocal of ‘PEcalibrate’).

During an LED calibration, each fiber is pulsed with a low-light LED at a rate of 10 Hz for a total of 3 min. Three different LED brightnesses are used for each fiber to ensure that the single photoelectron peak is well characterized. In 2015, SciBath was used in multiple measurement

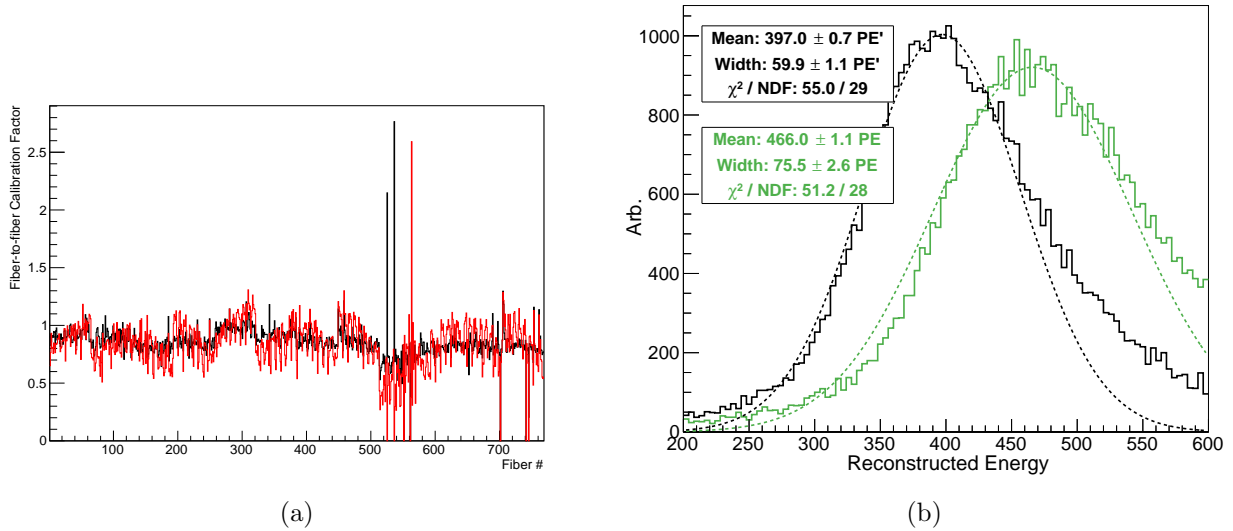


Figure 3.6: (a) Fiber-to-fiber calibration values. Red is Fall 2015 Booster Neutrino Beam (BNB), black is NuMI (2011). Evidence of additional dead fibers can be seen in the BNB data. (b) Fiber-to-fiber calibration effect on the muon peak. Solid histograms are muon spectra with (black) and without (green) the fiber-to-fiber calibration applied. Dotted curves are gaussian fits to the peak. The fiber-to-fiber calibration causes a small improvement in the energy resolution on the order of 1 %.

campaigns, with a separate LED calibration taken for each measurement. Due to the consistency in PMT gain throughout these runs, a single SPE value was used for all 2015 datasets. This value came from a dataset taken at Fermilab along the Booster Neutrino Beam on Dec. 1 2015, and serves as a good average for the entire fall. During the course of the LED calibrations, seven dead fibers were identified and incorporated into the SciBath Monte Carlo.

In addition, for this run, a fiber-to-fiber calibration was implemented to account for individual fiber differences (variations in coupling, fiber degradation etc.). The fiber-to-fiber calibration was done using a previous SciBath measurement from 2011 [56], although the calibration was not implemented in that analysis. For this calibration, only events with total PE between (250-500) PEs were used to isolate cosmic-muon events. The average number of PEs for each fiber was found for both data and a muon Monte Carlo (MC) simulation. For each fiber, the MC prediction was divided by the data. This value is the “fiber-to-fiber calibration factor” as shown in Fig. 3.6a. While overall normalization is NOT conserved, the fiber-to-fiber calibration improves energy

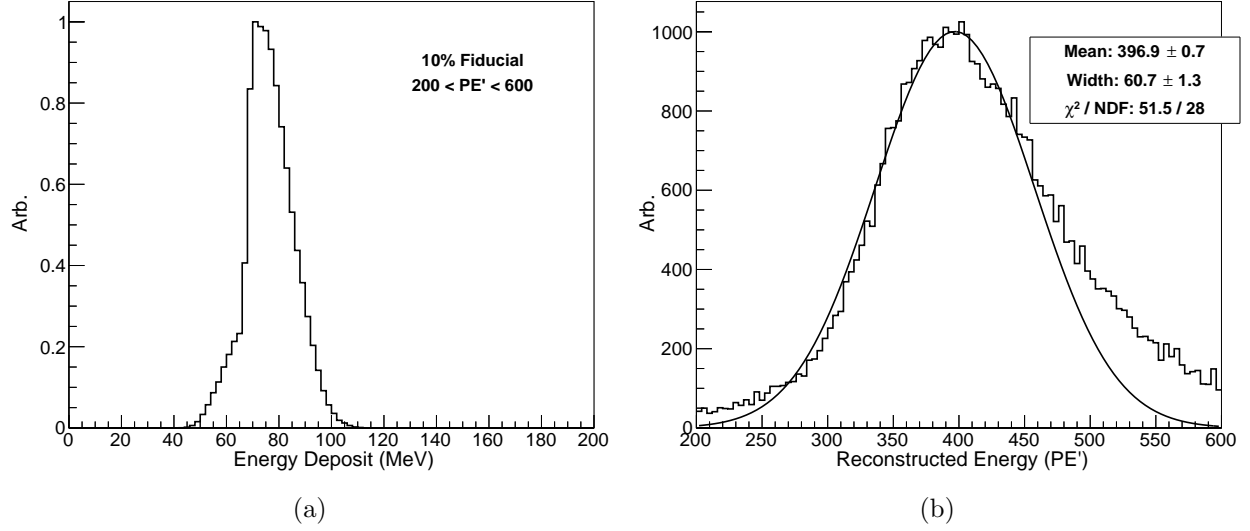


Figure 3.7: (a) Expected energy deposit from cosmic ray muons in SciBath from the SciBath **Geant4** simulation. (b) Reconstructed cosmic ray muon peak in the SNS dataset. Cosmic ray muons are minimally ionizing particles in SciBath and deposit a known energy (76.5 MeV) in the detector volume. A spherical fiducial volume cut of only the inner 10 % of the detector is imposed to remove the effect of ‘corner clippers’ that do not deposit the full 76.5 MeV in the detector volume. The combination of these plots can be used to find the detected photon yield in SciBath: $5.2 \text{ PE}'/\text{MeV}\mu e$.

resolution by roughly 1 % seen in Fig. 3.6b. The application of the fiber-to-fiber calibration results in a reconstructed energy scale called PE'.

Muons are minimal ionizing particles (MIPs) in SciBath and deposit a known amount of energy. The combination of the LED calibration and cosmic muons allows us to convert from the induced ADC counts to an energy scale (MeV μe or MeV muon-equivalent). Cosmic ray muons passing through SciBath deposit 76.5 MeV of energy in the scintillator (Fig. 3.7a). Knowing both the energy deposit, and the number of photoelectrons seen for minimally ionizing muons (Fig. 3.7b), it is possible to evaluate the detected photon yield Y in SciBath:

$$Y \equiv \frac{396.8 \text{ PE}'}{76.5 \text{ MeV}\mu e} \approx 5.2 \text{ PE}'/\text{MeV}\mu e \quad (3.1)$$

EVENT SELECTION AND PARTICLE IDENTIFICATION

The SciBath detector is sensitive to a variety of particles over a wide energy range (eg. 1 eV thermal

neutrons through the 2.2 MeV capture gamma from the $n(p, d)\gamma$ reaction up to ~ 1 GeV cosmic ray muons). Therefore some sophisticated particle-tracking algorithms were developed as a form of particle identification (PID).

A Principle Component Analysis (PCA) is performed on the distribution of fiber hits in an event to indicate how point or track-like a particle interaction was [56]. This PCA is analogous to performing a moment of inertia calculation for a solid body:

$$\det(T - \lambda I) = 0 \quad (3.2)$$

where the light seen by each fiber is substituted for the mass in the calculation. In other words, the inertia tensor T is

$$T = \begin{bmatrix} \overline{y^2} + \overline{z^2} & -\overline{xy} & -\overline{xz} \\ -\overline{xy} & \overline{x^2} + \overline{z^2} & -\overline{yz} \\ -\overline{xz} & -\overline{yz} & \overline{x^2} + \overline{y^2} \end{bmatrix} \quad (3.3)$$

where

$$\overline{x_i x_j} \equiv \frac{\sum_{\alpha} [(PE_{\alpha})^2 x_{\alpha,i} x_{\alpha,j}]}{\sum_{\alpha} (PE_{\alpha})^2}, \quad \overline{x_i^2} \equiv \overline{x_i x_i}, \quad x_i = x, y, \text{ or } z \quad (3.4)$$

where PE_{α} represents the corrected photoelectron response of a given fiber and the sum is over all fibers registering a hit for a given event. The resulting eigenvalues contain information about how cigar-shaped (track-like) or circular (point-like) a given particle interaction was. The eigenvectors contain information about the track direction, but this information is typically lost for point-like events. This PCA is performed for each event.

Neutrons tend to produce localized scatters and therefore look more point-like in SciBath. As muons are charged, they tend to interact and ionize along the entire track in the detector, producing more track-like interactions in SciBath as is seen in Fig. 3.8. By placing a cut on the largest eigenvalue for a given particle interaction, we can differentiate between neutrons and

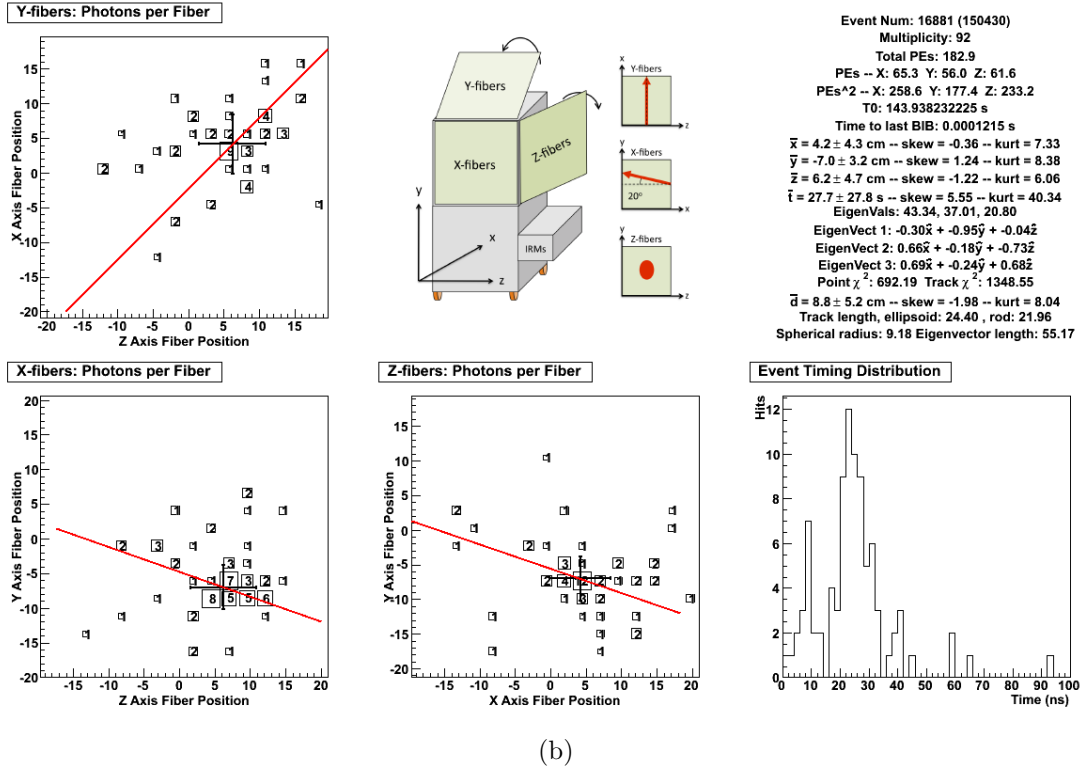
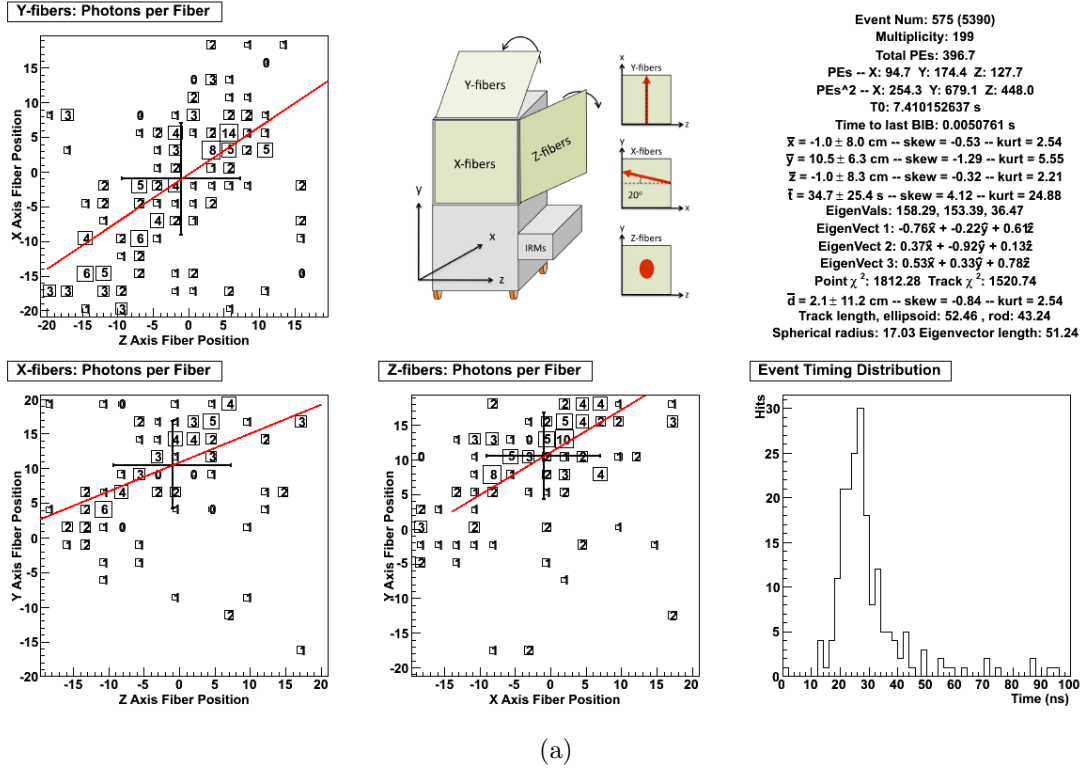


Figure 3.8: SciBath event display showing (a) a typical muon event and (b) a typical neutron event in SciBath with similar reconstructed energies. Muons are seen to be more track-like whereas neutrons are more point-like.

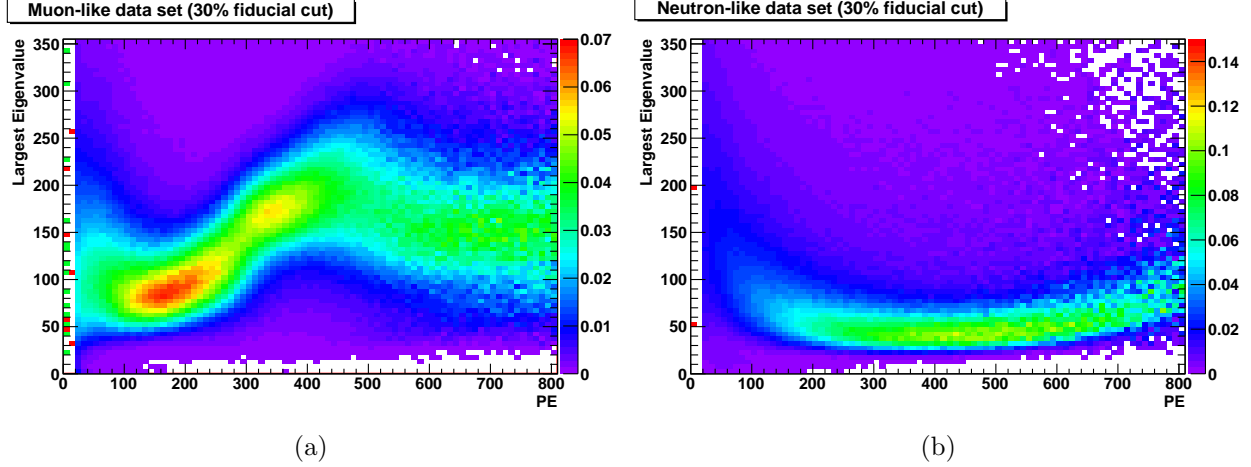


Figure 3.9: SciBath particle identification capabilities showing how point or track-like an event was as a function of energy. Larger eigenvalues indicate a more track-like event. (a) Muon dominated dataset taken in the NuMI cavern in 2011 [56]. (b) Neutrons from the 2012 MI12 dataset [10]. Muons are seen to be more track-like than similar energy neutron events. The particle ID cut only works at high energies and was only implemented to measure the cosmic-muon rate in Neutrino Alley.

muons. Unfortunately this PID cut only works at high energies as muons that aren’t minimally ionizing (ie corner clippers) produce point-like interactions.

This PID cut was developed during the 2011-2012 NuMI and MI-12 analyses [10, 56] as seen in Fig. 3.9. The NuMI run was underground in the NuMI cavern at Fermilab, and therefore the events were dominated by cosmic ray muons. The MI-12 data run was taken off-axis at the Booster Neutrino Beam (BNB) target, again at Fermilab, and provided an incredibly neutron-rich dataset.

For the SNS run, the beam-related excess was too low energy for the PID cut to be applied. Due to this, it was assumed that every excess event occurring right on the beam was due to a beam-related neutron. PID cuts were only imposed on the “pre-beam” data where the cosmic-muon rate was measured. There were data quality cuts placed on both the cosmic-muon data and the beam-related neutron data which are summarized below and in Table 3.2.

COSMIC-MUON DATA CUTS For the cosmic-muon analysis, “pre-beam” data was used to minimize the risk of any sort of beam-related contamination. This meant that an event came in $(5-90) \mu\text{s}$ before the beam as marked by Event 39. A minimum reconstructed energy cut of $250 \text{ PE}'$

	Muons	Prompt Neutrons	Delayed Neutrons
Timing Cut (μs)	$-90 < t < -5$	$0 < t < 1$	$1 < t < 86$
Energy Cut	250 PE'	1 MeV μe	1 MeV μe
Fiducial Cut (%)	26 (Sphere)	50 (Box)	50 (Box)
Minimum Fiber Hits	6	6	6
Max σ_t^{hit} (ns)	100	100	100
Eigenvalue Cut	> 115	NA	NA

Table 3.2: A summary of SciBath data cuts. Note that the timing cut is made relative to beam on target (SNS Event 39).

(~ 48 MeV) was implemented. More than six fibers were required to be hit and the standard deviation of the fiber hit times was required to be less than 100 ns. A spherical fiducial-volume cut on the average reconstructed position of 26 % was imposed to reduce the effect of corner-clipping muons. The largest eigenvalue from the PCA was required to be larger than 115 to ensure the event was track-like.

BEAM-RELATED NEUTRON (PROMPT AND DELAYED) DATA CUTS Only data quality cuts were imposed on the neutron data to help remove the effects from PMT noise and the large 511 keV gamma rate in the corridor. Neutron events were required to have a reconstructed energy greater than 1 MeV μe . This is about the minimum energy threshold of SciBath and is above all but the tail of the 511 keV gamma flux from the HOG. A box-like 50 % fiducial volume cut was also imposed to help remove any photon contamination in the neutron signal. External gamma rays typically interact on the edges of the detector. Like the muon sample, a minimum of six fiber hits and an average hit time standard deviation of less than 100 ns were required.

For the beam-related neutron measurement, two different neutron fluxes were characterized: prompt and delayed. For prompt neutrons arriving in time with the beam, a timing cut of (0-1) μs around the beam was implemented. To measure the delayed neutrons, which straggle behind the beam on the order of a few μs , a timing cut of (1-86) μs after the beam was used.

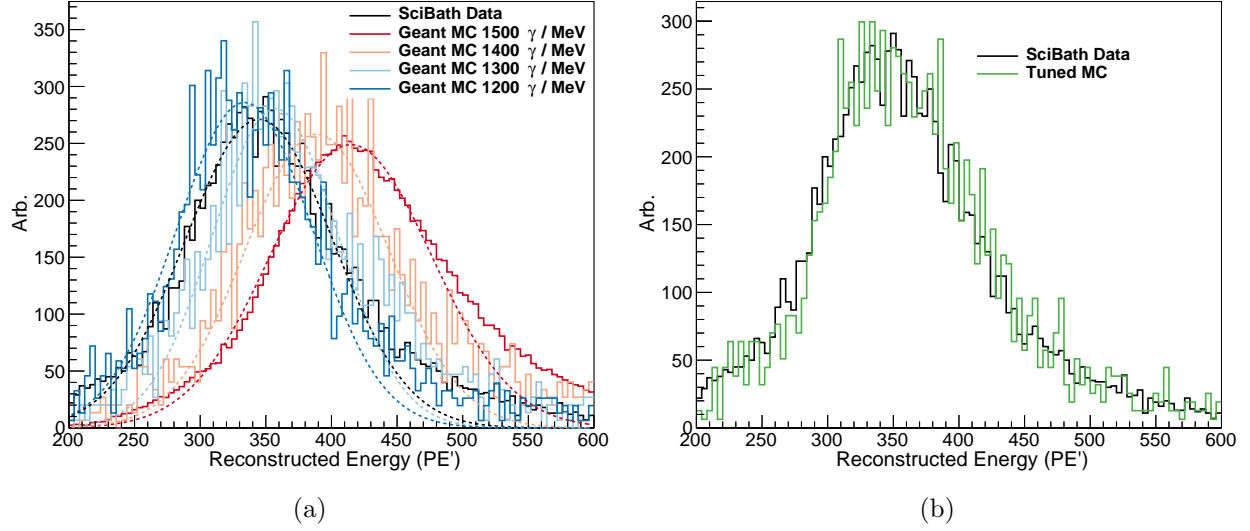


Figure 3.10: (a) Tuning the effective scintillation yield in the SciBath **Geant4** simulation. Dashed lines are gaussian fits to the histogram peaks of the same color. (b) Comparison of tuned MC to MI12 data. As stated in Sec. 3.3.3, the calibration for the 2015 MI12 run was used for all 2015 runs. The muon peak from the SNS run (Fig. 3.7) is within 5 % of the muon peak location during the MI12 run.

SIMULATIONS

In order to convert the observed rates from Scibath into an absolute flux measurement, an unfolding of the detector response needs to be done. A combination of the **Geant4** [46, 47] and **MCNP-Polimi** [84] simulation packages was used to do so. **Geant4** is very useful for simulating detector response to gamma rays, muons and fast neutrons, but suffers in simulating thermal neutrons. **MCNP-Polimi** on the other hand suffers at simulating detector response, but does an excellent job with thermal neutron transport and capture. The combination of these two simulation packages enables every particle interaction of interest for the SNS measurement to be simulated.

The physics package used for the SciBath **Geant4** simulations was **QGSP_BERT_HP**. The detector itself was simulated as a $(43.2 \times 44.5 \times 43.2)$ cm cube of mineral oil (CH_2 , density 0.86 g cm^{-3} , index of refraction $n = 1.46$), surrounded by 1.3 cm of Al. Quenching of light for particles with high dE/dx is done with a Birks' Law response [85]. To minimize computer time, the number of photons produced at each particle step (found to be $1350 \gamma/\text{MeV}$ deposited by comparison to muon data as seen in Fig. 3.10), was reduced by the WLS fiber optical-photon capture probability

(2.5 %) times the photomultiplier tube (PMT) quantum efficiency (20 %). Any remaining photons that hit a fiber were assumed to be detected. A separate ‘Detector Simulation’ was then run to replicate the photon detection response of the PMTs (single photoelectron smearing etc.).

COSMIC-MUON SIMULATION The SciBath muon simulation made use of the `Geant4` simulation package. This simulation was used to both find the cosmic-muon rate and to tune the light output of the scintillator for later beam-related neutron simulations. Implementing the fiber-to-fiber calibration required a re-tuning of the light output in the simulation. The simulation light output was tuned to the muon peak from the Fall 2015 run at MI12 and was found to be (for this and all remaining simulations) $1350 \gamma/\text{MeV}$. 1×10^6 muons were simulated with a Miyake [86] angular distribution (at the surface) on a “rotated disk” (see Fig. 3.11) with a flat energy spectrum from (1-100) GeV.

A first order cosmic-muon rate calculation was performed using the results from an older simulation used for the 2011 NuMI analysis [56]. The only difference in the simulations was the scintillator light output (previously $1500 \gamma/\text{MeV}$). This effective light yield matched the muon peak prior to the implementation of the fiber-to-fiber calibration, when the initial analysis was performed. The muon analysis was not repeated after implementing this calibration.

FAST NEUTRON SIMULATION `Geant4` was also used to characterize the response of SciBath to fast neutrons. This simulation consisted of an inward flux of neutrons until 1×10^6 neutrons induced at least one fiber hit in the detector. The neutrons had a flat energy spectrum from (1-300) MeV and were generated on the surface of a sphere with a radius of 40 cm centered on the detector. These neutrons had a cosine angular distribution. The detector response of SciBath to fast neutrons for this central value (CV) simulation, with the light yield tuned to the muon peak, can be seen in Fig. 3.12.

- 1) Randomly pick $\eta = (1, \cos\theta, \varphi)$
- 2) Randomly chose point inside of circle of radius r at $y = 0$ (red plane)
- 3) Rotate red plane by angle α so that the new plane is tangent to sphere point η . (blue plane)
- 4) Translate blue plane by $r*\eta$ so center is located at $r*\eta$ (green plane)
- 5) This is starting position for event.
- 6) $-p*\eta$ is used for generating the momentum for the event

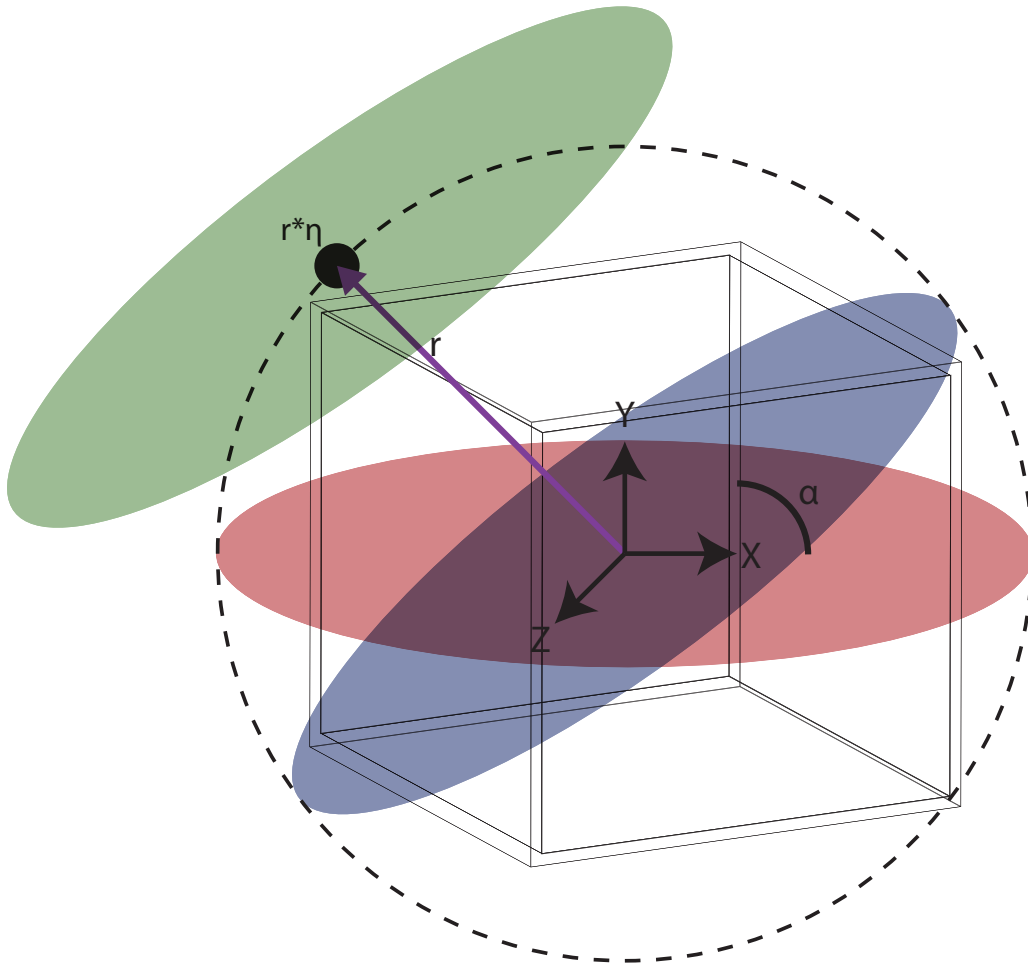


Figure 3.11: Pictorial representation of SciBath **Geant4** muon simulation starting point generation.

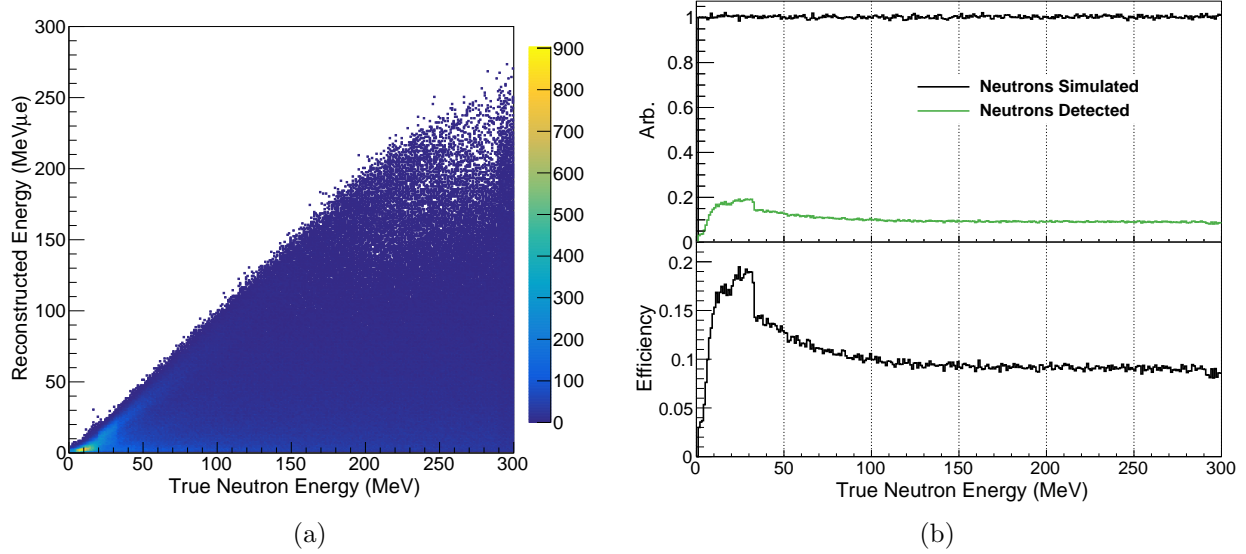


Figure 3.12: SciBath detector response to fast neutron scatters. (a) Reconstructed energy vs incident neutron energy. The effects of bin migration due to escaping energy can be seen. (b) SciBath detection efficiency as a function of neutron energy. Geometric effects (e.g. neutrons generated on a path that will not hit the detector) have not been factored out. The kink at ~ 30 MeV is due to an issue in the neutron libraries used by **Geant4** and is discussed in Sec. 3.3.3.

THERMAL NEUTRONS MCNP Polimi was used to simulate thermal neutrons due to its analog simulation probabilities for neutron captures. Neutrons were generated uniformly along the surface of a sphere ($r = 45$ cm) with a cosine angular distribution to represent a uniform thermal neutron flux. As in the **Geant4** simulations, the detector was represented by a cube of liquid scintillator ($43.2 \times 44.5 \times 43.2$ cm) surrounded by 1.3 cm of Al. A variety of monoenergetic neutron sources, from 25 meV to 1 MeV, were simulated due to the uncertainty in the exact energy of the incident thermal neutron flux. The location of and efficiency for detection of the modeled thermal neutron captures is shown in Fig. 3.13.

GAMMAS A variety of gamma ray simulations were performed using the **Geant4** simulation package. The first simulation, in which 1×10^6 2.22 MeV gamma rays were simulated uniformly throughout the detector with an isotropic angular distribution, was performed to characterize the efficiency for SciBath to detect capture gammas from the $n(p,d)\gamma$ reaction. As most neutron captures occur near the edges of the detector, as seen in Fig. 3.13, this simulation was then

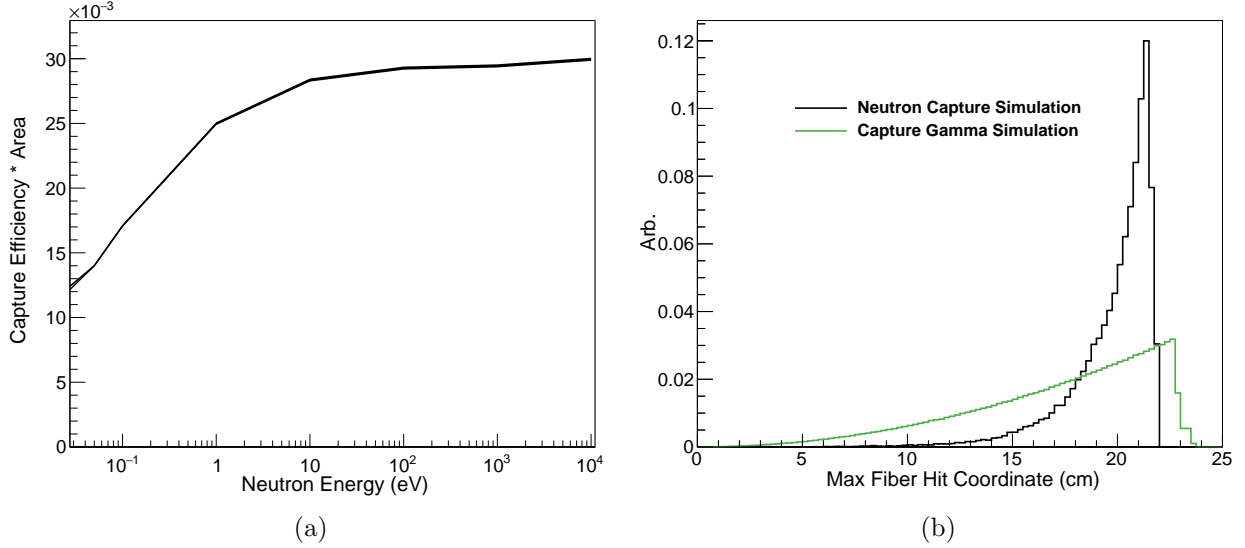


Figure 3.13: SciBath response to thermal neutrons. (a) Neutron capture efficiency vs incident neutron energy. A variety of neutron energies were simulated as the exact thermal neutron energy in Neutrino Alley is unknown. (b) Comparing maximum coordinate ($\max(x, y, z)$) of thermal neutron capture locations in SciBath (from 25 meV simulation) to a simulation of 2.2 MeV gammas generated uniformly throughout the detector volume showing the necessity of reweighting the capture gamma simulation. External thermal neutrons preferentially capture near the edge of the detector.

re-weighted with the results of the MCNP-Polimi thermal neutron simulation described in Sec. 3.3.3. This re-weighting procedure is discussed in App. A. In addition, simulations of photons from neutron captures on C (throughout the scintillator) and Al (only in the detector walls) were performed.

An additional simulation was run with a spherical external 511 keV gamma ray source to examine the efficiency for SciBath to detect them after data quality cuts were made. SciBath was determined not to be sensitive to gamma rays at such a low energy.

SPECTRUM UNFOLDING

Whenever a detector measures a spectrum b (a vector with n_b bins), the measurement is subject to detector effects (detector resolution, efficiency etc.). To convert to any sort of absolute measurement, these effects need to be “unfolded.” If we have some estimate of what the “true” underlying spectrum, x (a vector with n_x bins) is, we can relate the two spectra easily through the following

linear system of equations

$$Ax = b. \quad (3.5)$$

Here A is an $n_x \times n_b$ matrix describing the detector response typically found via Monte Carlo simulations. The more general case where the errors on the measured vector b vary from bin to bin can be expressed as the weighted-least-square problem:

$$(Ax - b)^T B^{-1} (Ax - b) = \min \quad (3.6)$$

where B is the covariance matrix of b .

ROOT TSVDUNFOLD Solving Eq. 3.5 exactly through inversion of A typically leads to solutions for the true spectrum x with large, rapid oscillations due to incomplete knowledge of A and statistical fluctuations in b . Therefore, to unfold the beam-related fast neutron flux measured by SciBath, the built-in ROOT class TSVDUnfold [87] was used.

TSVDUnfold makes use of Singular Value Decomposition (SVD) of the detector response matrix (A) to solve the system in Eq. 3.5 for x . It also introduces a regularization term to suppress the oscillatory nature of the exact solution of Eq. 3.5.

$$\left(\tilde{A}w - \tilde{b}\right)^T \left(\tilde{A}w - \tilde{b}\right) + \tau \cdot (Cw)^T Cw = \min \quad (3.7)$$

Where the covariance matrix B has been absorbed into A and b forming \tilde{A} and \tilde{b} and w is a scaled version of x . τ is the regularization term, and C is a general matrix chosen to help prevent solutions with large curvatures. The appropriate choice for τ varies from problem to problem, and is discussed in more detail later and in [87].

SYSTEMATIC ERRORS: COSMIC MUONS

To find the systematic error on the cosmic-muon flux, the measured flux was found using five

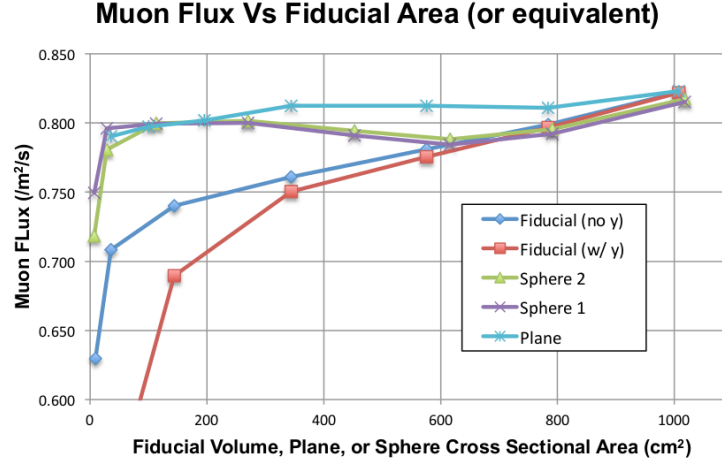


Figure 3.14: The 2011 NuMI cosmic-muon flux vs effective cross sectional area [56]. Five different cross section definitions were considered. “Sphere 2” at 791 cm² was used as the central value.

different definitions of the effective cross sectional area of SciBath (Fig. 3.14). The divergence of the measured flux at low cross sections is due to differences between the different methods for muons with high azimuthal angles. The simulation of these high angle muons does not exactly match the physical spectrum and each fiducial volume definition has a different response to this difference. The “Fiducial (no γ)” method has an additional systematic error because the fiducial volume is not vertically centered on the location of the average energy deposit.

A description of the fiducial volume definitions can be found in [56]. The spread in these results gives a systematic uncertainty of 5 % to apply to the measured cosmic-muon flux. “Sphere 2” at 791 cm² was used as the CV result.

SYSTEMATIC ERRORS: FAST NEUTRONS

The SciBath MC was used to run a variety of systematic excursions to account for any imperfections in the fast-neutron detector simulation. For each simulated excursion, one parameter from the central-value simulation was modified by $\pm 1\sigma$. The excursions considered were the scintillator light yield (LY), quenching (Birks’ coefficient), single PE uncertainty (SPE sigScale), neutron cross section (x-Sec.), and the unfolding regularization parameter (regParam). The systematic excursions considered are summarized in Tab. 3.3.

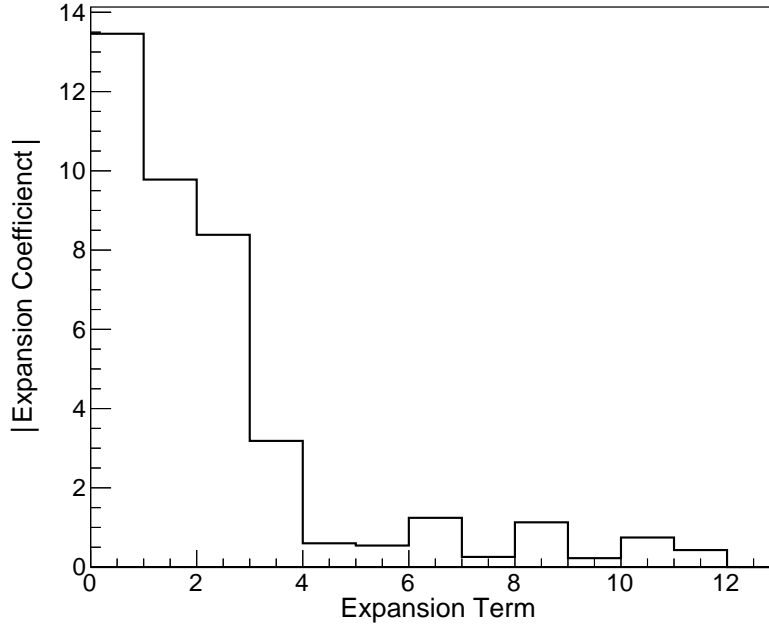


Figure 3.15: Expansion coefficients from the fast-neutron spectral unfolding. Only the first four terms in the expansion were used for the central-value unfolding result. Results keeping three and five terms were used to evaluate systematic errors from the unfolding procedure.

REGPARAM: In the unfolding algorithm, singular value decomposition of the detector response matrix A is used to rotate the system of equations in Eq. 3.5 to a diagonal basis making inversion of A simpler. The number of terms kept in the expansion in this basis depends on the expansion coefficients themselves. When the magnitude of the coefficient values stops decreasing, the remaining terms in the expansion are no longer statistically significant and can be removed. The regularization term τ is defined as the k -th singular value, where k is the last term kept in the expansion [87].

Keeping too many terms results in large oscillations, similar to the result of just inverting the detector response matrix A directly, while keeping too few biases the results to the Monte Carlo truth spectrum. The distribution of these coefficients from unfolding the beam-related excess observed by SciBath can be seen in Fig. 3.15. For the central value, four terms were kept. Due to the ambiguity in the prescription for the number of terms kept in the expansion, the unfolding was also performed keeping three and five terms. These are considered the “unfolding errors.”

LY: The light yield excursions consisted of changing the scintillation yield in the **Geant4** simulations. The scintillation yield varied from $1200 \gamma/\text{MeV}$ to $1500 \gamma/\text{MeV}$. The NuMI analysis made use of the simulation with $1500 \gamma/\text{MeV}$ so the light yield was bounded on the lower side as well.

BIRKS' COEFFICIENT: The central value used for Birks' coefficient (kB) in the **Geant4** simulations was $9.2 \times 10^{-3} \text{ g/cm}^2/\text{MeV}$. This value is from Braizinha et al. [88], and is the value for the commercially available scintillator BC-517H. Braizinha also measured Birks' coefficient for the KamLAND scintillator ($kB = 8.0 \times 10^{-3} \text{ g cm}^{-2} \text{ MeV}^{-1}$), which is 10 % lower than BC-517H. Therefore excursions were run with a Birks' coefficient $\pm 10\%$ from the CV.

SPE SIGSCALE: The SPE fits were done using a Poisson-smeared gaussian. The width of the single photoelectron peak is an indication of the uncertainty in the SPE fit. In the **Geant4** simulation, integer number of photoelectrons are detected. A second "detector simulation" smears these photoelectrons according to the uncertainty in the SPE peak. This smearing is the average gaussian width of the SPE distribution for all 768 fibers. For this excursion, the average error on this width divided by $\sqrt{768}$ was assumed to be the average of how each fiber SPE calibration could shift. This is one standard deviation from the average, and plus/minus this amount was considered as an uncertainty on the SPE response.

X-SEC: An excursion on the neutron cross section was run as there is a discontinuity in the MC-predicted detection efficiency for SciBath to measure fast-neutron scatters at $\sim(20\text{-}30) \text{ MeV}$ in the MC (Fig. 3.12). This issue with detector efficiencies around $(20\text{-}30) \text{ MeV}$ is a known issue with **Geant4**¹, and is due to changing the neutron cross section libraries/models at 30 MeV as seen Fig. 3.16. This issue was not fixed by changing the physics settings as recommended.

In Fig. 3.16, there are discrepancies between the **Geant4** and literature cross sections even beyond this discontinuity. Therefore, we opted to include systematic excursions about the **Geant4**

¹<http://hypernews.slac.stanford.edu/HyperNews/geant4/get/phys-list/849.html?inline=-1>

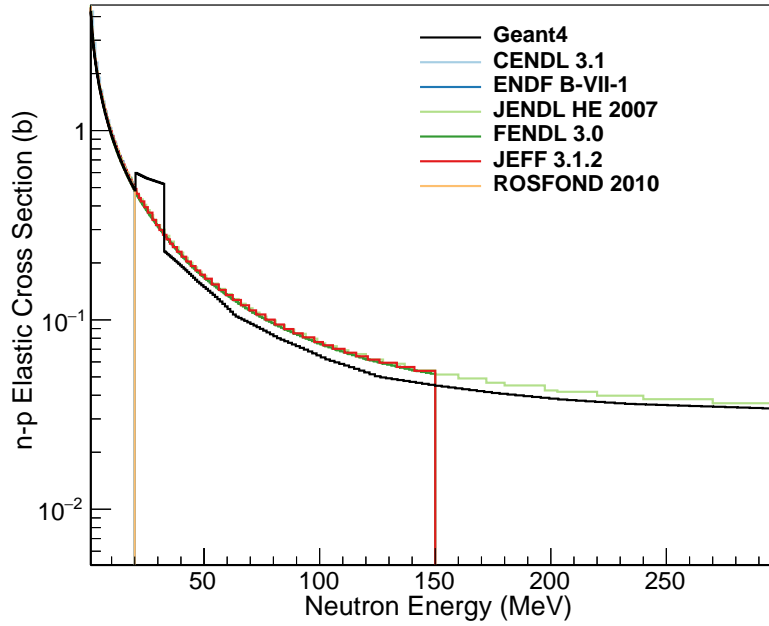


Figure 3.16: Comparison of the n-p elastic cross sections from various cross section libraries to those used by **Geant4**. A significant deviation from the literature values is seen leading to an inclusion of the n-p cross section as a systematic uncertainty on the unfolded neutron flux.

cross sections used for neutron scattering. This was done by applying an energy-dependent re-weighting factor to the fast neutron simulation central-value results. The $\pm 1\sigma$ weighting factor was based on the relative difference (σ_{err}) between the **Geant4** and JENDL HE 2007 cross sections (the only database up to 300 MeV). The excursion consisted of a re-weighted spectrum of $1 \pm \sigma_{err}$ based on the initial neutron energy.

FAST-NEUTRON SYSTEMATIC UNCERTAINTIES To use these excursions to find the systematic errors, the following procedure was used. The measured spectrum (b) was first unfolded using the central value (CV) detector response matrix (A^{CV}) from simulation. The statistical covariance matrix (B) of the measured spectrum was also propagated through the unfolding procedure as a measure of the statistical uncertainty on the unfolded spectrum. This gave the central value “truth” distribution (x_{true}^{data}).

Next the CV MC reconstructed distribution (from the uniform energy spectrum simulated), as well as the reconstructed distributions from the systematic excursions, was also passed through

Table 3.3: Summary of fast-neutron simulation systematic excursions. All excursions were run with a spherical neutron generating source.

	Light Yield (γ/MeV)	Birks Coeff. ($\text{g cm}^{-2} \text{MeV}^{-1}$)	SPE sigScale	Neutron X-Sec.	Reg. Param.
CV	1350	9.2×10^{-3}	0.778	Geant4	4
LY	1350 ± 150	9.2×10^{-3}	0.778	Geant4	4
Birks	1350	$(9.2 \pm 1.2) \times 10^{-3}$	0.778	Geant4	4
SPE	1350	9.2×10^{-3}	0.778 ± 0.004	Geant4	4
X-Sec.	1350	9.2×10^{-3}	0.778	$\text{Geant4} \pm \sigma_{err}$	4
Unf.	1350	9.2×10^{-3}	0.778	Geant4	3, 5

the unfolding algorithm. For each distribution, the reconstructed spectra were unfolded against the central value detector response matrix. This unfolding procedure unfolds back to the flat input energy spectrum with some spread due to the systematic differences. In order to calculate the systematic errors, each unfolded Monte Carlo spectrum needs to be compared to the unfolded data distribution.

A bin-to-bin scaling factor a_i was found to scale the CV simulation unfolded distribution to the unfolded SNS data distribution ($a_i x_{true,unf,i}^{MC} = x_{true,i}^{data}$). This scaling factor was then applied to each unfolded excursion curve giving the family of curves seen in Fig. 3.18b. From these curves, a covariance matrix for the unfolded neutron energy spectrum can be found in the usual way:

$$V_{ij} = \sum_{Excursion} \frac{1}{N} \mathbf{E} \left[(x_i - \mu_i) (x_j - \mu_j) \right] \quad (3.8)$$

where μ_i is the expected value (in this case CV) of the i^{th} bin, x_i is the excursion value of the i^{th} bin and N is the number of that particular excursion considered.

SYSTEMATIC ERRORS: THERMAL NEUTRONS

The largest systematic uncertainty in the thermal neutron measurement is due to the uncertainty in the incident neutron energy and the corresponding detection efficiency for these thermal neutrons. The spread in this efficiency about the assumed CV (1 eV neutrons) is 20 %. Additional systematic

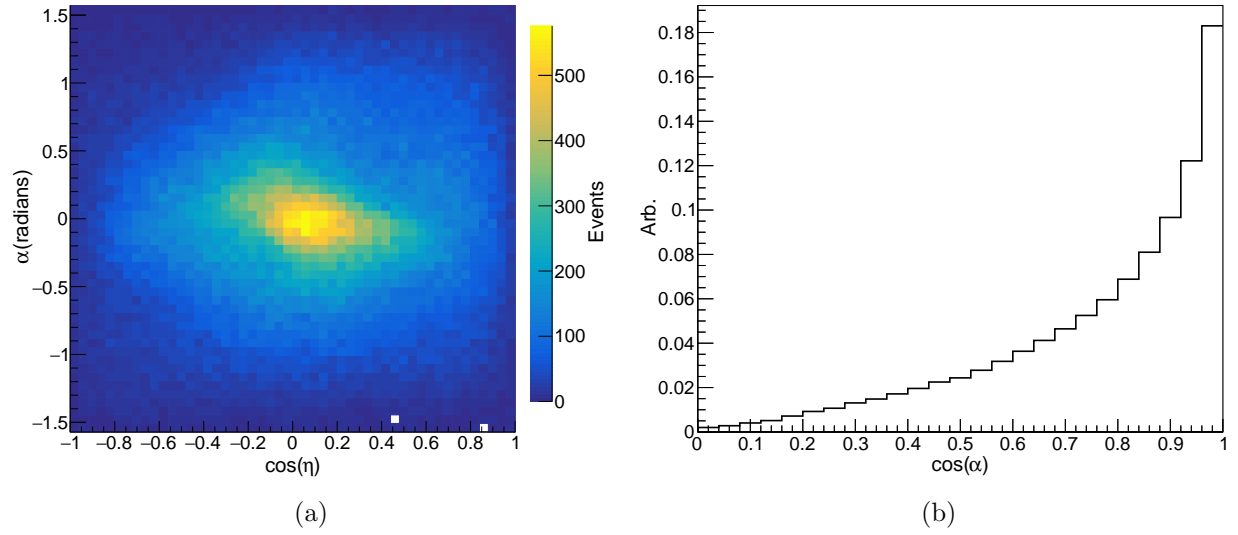


Figure 3.17: SciBath cosmic-muon angular distribution. (a) Cosmic-muon $\cos \eta : \alpha$ angular distribution. Downward going muons are clearly visible at $\cos \eta = \alpha = 0$. (b) Cosmic-muon $\cos \alpha$ distribution. Downward moving muons have $\cos \alpha = 1$. α is the angle from the vertical (y) axis and η is measured in the x-z plane. The axes are defined in Fig. 3.2.

uncertainties due to changes in the unfolded rate from varying the fiducial volume cut, indications of capture gammas from C and Al captures in previous measurements, and a small excess in events near the detector edge when compared to thermal neutron simulations contribute an additional 20 % systematic uncertainty to the thermal neutron flux measurement.

3.3.4 RESULTS

For this run there are two main results: (1) the cosmic-muon rate and (2) the beam-related neutron rate (prompt and delayed).

COSMIC MUONS

To calculate the cosmic-muon flux Φ_μ , the total count rate, N_μ , must be divided by an effective area from simulation (ϵA). This efficiency corrected event number is then normalized by the amount of time the measurement was taken over.

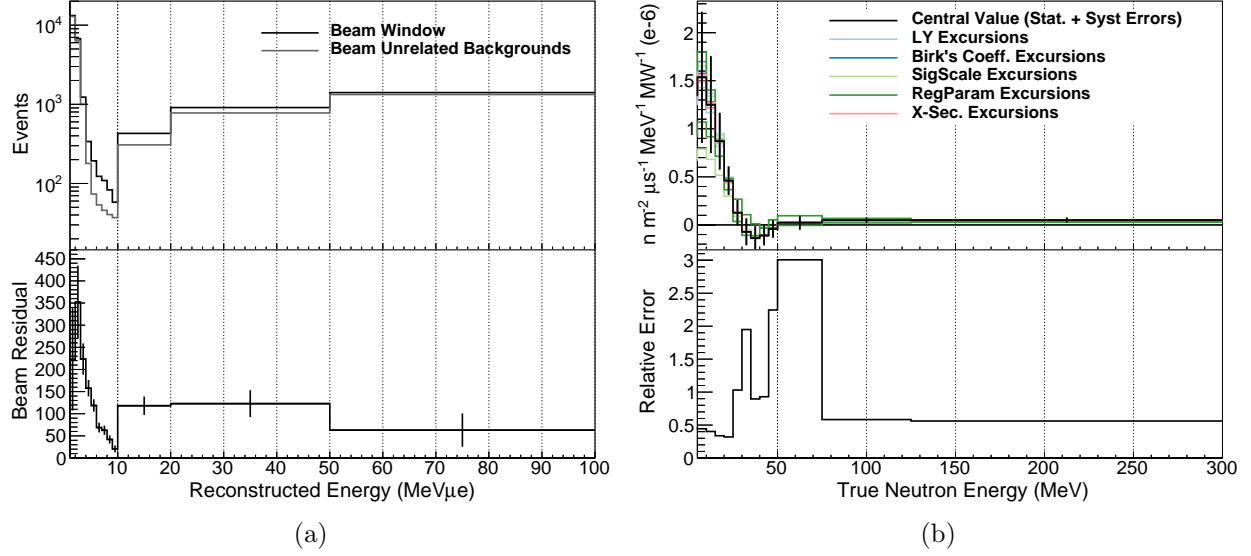


Figure 3.18: SciBath prompt-neutron spectrum. (a) Measured SciBath prompt-neutron spectrum with binning used for spectral unfolding. Top panel shows the energy spectra both for the prompt beam window (in black), and the scaled beam-unrelated background from considering pre-beam data. Bottom panel is the residual with statistical errors shown. (b) Systematic effects on the unfolded fast-neutron spectrum measured by SciBath. Top panel shows the central value result with statistical and systematic errors overlaid with the spectral shapes for different systematic assumptions discussed in the text. Lower panel shows the relative error for each energy bin.

The final flux is then given by

$$\Phi_{\mu} = \frac{N_{\mu}}{(\epsilon A) \overline{T}} \quad (3.9)$$

where \overline{T} is the total observation time.

Throughout the SNS run, SciBath detected 91 628 cosmic muons. These muons were observed over a time period of 16 014 s. Accounting for the detector efficiency, and using Eq. 3.9 gives a cosmic-muon flux of $(60 \pm 3) \mu/\text{m}^2/\text{s}$. This rate is rough agreement with Bogdanova et al. [89] at a depth of 8 m w e .

A check on the angular distribution of identified muon events provides further evidence that these are actually cosmic ray muons. Fig. 3.17 shows that indeed, these events primarily consisted of downward moving particles.

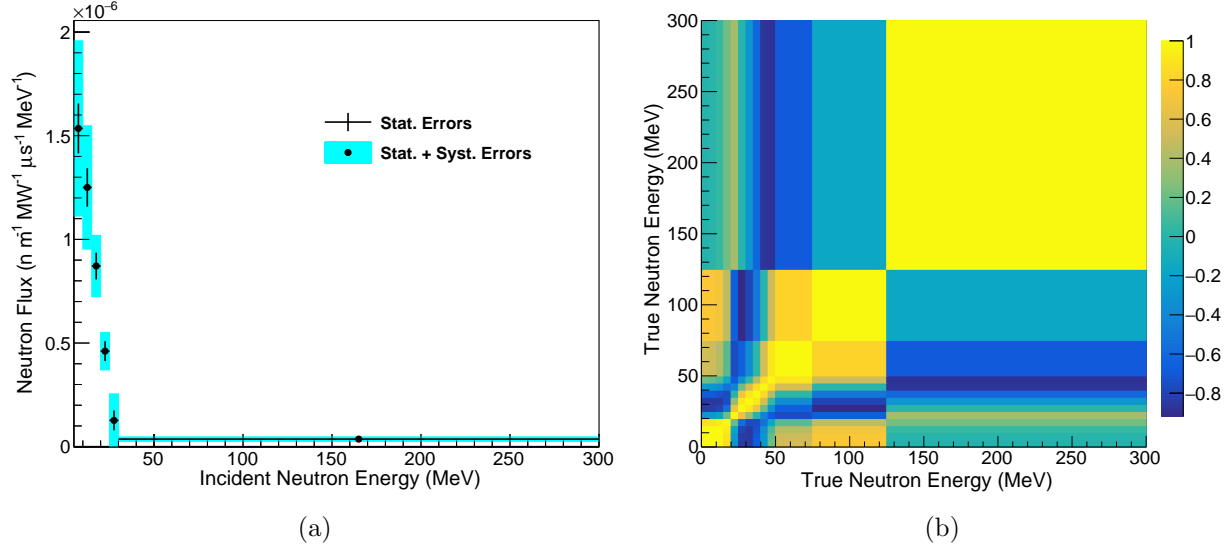


Figure 3.19: Unfolded SciBath prompt neutron spectrum. (a) Unfolded energy spectrum. Systematic errors displayed are only from the diagonal of the covariance matrix. (b) Full correlation matrix after unfolding.

BEAM-RELATED PROMPT NEUTRONS

To characterize the beam-unrelated backgrounds, the same time window used for the cosmic-muon analysis was used for the beam-related neutron analysis. This steady-state spectrum was then normalized to the appropriate amount of time.

SciBath detected a beam-related excess of 1573 events as seen in Fig. 3.18a. The results from unfolding the measured reconstructed spectrum can be seen in Fig. 3.18b. As expected, the greatest uncertainty is near the detector threshold. The unfolded flux, with statistical and systematic errors along with the full correlation matrix can be seen in Fig. 3.19.

As stated in Sec. 3.3.3 the excess events in the prompt beam window were too low energy to apply PID cuts, so the unfolded spectrum is an upper limit assuming all beam related events are due to fast neutrons. Including systematic errors, SciBath detected $(2.1 \pm 0.4) \times 10^{-5}$ n/m²/beam spill from (5-30) MeV. Incorporating our knowledge of the average beam power, during this run (see Sec. 3.3.2) allows us to convert this flux to something more easily compared to other measurements: $(2.1 \pm 0.4) \times 10^{-5}$ n/MW/μs/m².

SciBath is sensitive to neutrons up to a true neutron kinetic energy of 300 MeV. There is some

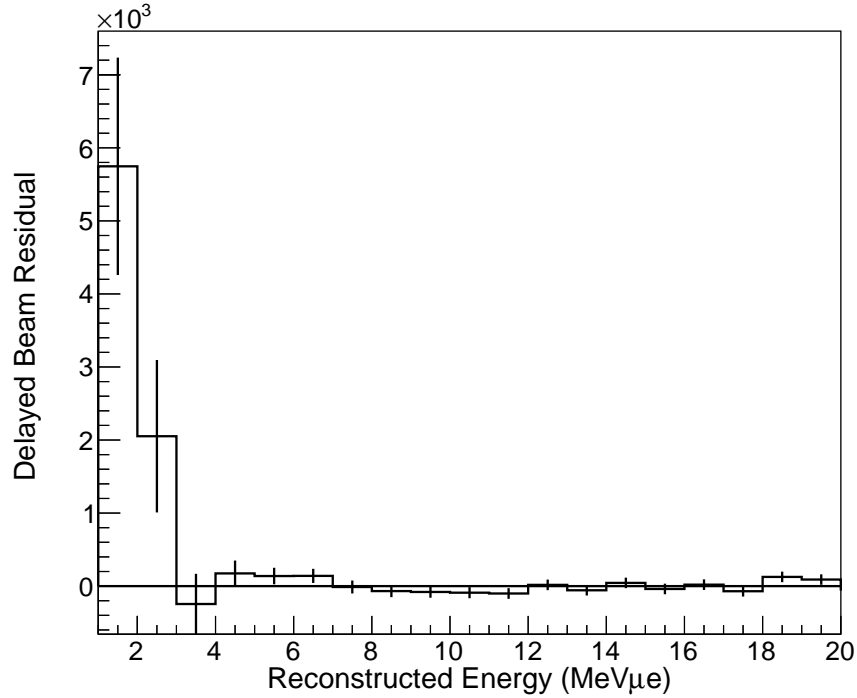


Figure 3.20: Energy spectrum of ‘delayed’ beam-related neutron candidates. The spectrum is consistent with gamma rays from thermal neutron captures. Especially prominent is the 2.2 MeV gamma ray from thermal neutron capture on hydrogen.

indication of an excess up to this high energy, and we are able to place a limit on this neutron flux of $< 1 \times 10^{-5} \text{ n/MW}/\mu\text{s}/\text{m}^2$ for neutrons $> 30 \text{ MeV}$.

The Scatter Camera [54] took a similar measurement near the CENNS-10 detector, but with a more direct line of sight to a doorway near the end of the hallway. This stairway has been hypothesized to be a source of beam-related neutrons in the hallway. The higher flux observed by the Scatter Camera in this position of $\sim 4 \times 10^{-3} \text{ n/cm}^2/\text{MeV/s}$, as well as the lower beam-related neutron flux measured at the CsI[Na] detector location [3] is consistent with this hypothesis.

BEAM-RELATED DELAYED NEUTRONS

SciBath did observe an excess of events in the delayed region ($1 < t < 86 \mu\text{s}$ from the beam) as can be seen in Fig. 3.20. The excess seems to be due to thermal neutron captures. Especially visible is the 2.2 MeV gamma-ray from the $n(p, d)\gamma$ reaction. Therefore the delayed spectrum was divided into two energy regions;

	Cosmic Muons ($\mu/\text{m}^2/\text{s}$)	Prompt Neutron Flux ($\text{n}/\text{MW}/\mu\text{s}/\text{m}^2$)	Delayed Neutron Flux ($\text{n}/\text{MW}/\mu\text{s}/\text{m}^2$)
Total Rate	60 ± 3	$(2.1 \pm 0.4) \times 10^{-5}$	$(1.9 \pm 0.7) \times 10^{-5}$

Table 3.4: Summary of background measurement results from the SciBath run. A limit of the flux of high energy ($> 30 \text{ MeV}$) prompt neutrons of $< 1 \times 10^{-5} \text{ n}/\text{MW}/\mu\text{s}/\text{m}^2$ was also placed. The delayed neutron flux events are all consistent with thermal neutron captures and easily shielded.

1. $1 \text{ MeV}\mu\text{e} < E_{reco} < 6 \text{ MeV}\mu\text{e}$
2. $6 \text{ MeV}\mu\text{e} < E_{reco} < 100 \text{ MeV}\mu\text{e}$

Region (1) is sufficiently wide to cover the tail of the $2.2 \text{ MeV } \gamma$ from the $\text{n(p,d)}\gamma$ reaction as well as effects from thermal neutron captures on C and Al. In this region, (7728 ± 1870) events were detected. Making use of the efficiencies found in the simulations described in Sec. 3.3.3, the total time considered, and the average beam power gives an observed delayed thermal neutron flux of $(1.9 \pm 0.7) \times 10^{-5} \text{ n}/\text{MW}/\mu\text{s}/\text{m}^2$.

In energy region (2), there is no observed beam-related excess. From (6-100) MeVee, a total of (-108 ± 676) events were observed, consistent with zero. There is no significant flux of high energy neutrons in the delayed region.

A summary of the event rates observed by SciBath can be found in Tab. 3.4.

CHAPTER 4

A LIQUID ARGON CEVNS SEARCH AT THE SNS

In this chapter I discuss the use of liquid argon for a CEvNS detector. I first motivate the use of liquid argon as a detector medium. Then I introduce the CENNS-10 detector and give an overview of liquid argon scintillation. Finally, I summarize the CENNS-10 Engineering Run at the SNS.

4.1 LIQUID ARGON AS A CEVNS DETECTOR MEDIUM

Liquid argon (LiqAr) is a natural choice for a detector medium to detect coherent elastic neutrino-nucleus scattering (CEvNS). Following the recent CsI[Na] measurement, the low mass of argon nuclei (with $N = 22$) provides a long lever arm to begin to map out the N^2 dependence of the CEvNS cross section. LiqAr also has many benefits for measuring CEvNS independent of the previous CsI[Na] measurement:

1. The light mass of the argon nuclei results in higher energy nuclear recoils that are (relatively) easy to see.
2. Liquid argon has a high light yield (~ 40 photons/keV [90]) allowing a sufficiently low threshold to observe CEvNS.
3. The quenching factor has been well characterized allowing for good understanding of liquid argon response to nuclear recoils [91–94].
4. Liquid argon provides powerful pulse-shape discrimination capabilities allowing for significant separation of signal and background (up to $\mathcal{O}(1 \times 10^{-8})$ [95–97]).

5. Argon is readily available in the atmosphere and can be bought at a similar cost to liquid nitrogen.

However, there are a few drawbacks to using liquid argon as a detector medium. Liquid argon scintillates at a wavelength of 128 nm which is both not readily detectable by standard photomultiplier tubes and outside the range of most reflective materials. This requires the use of secondary wavelength shifters to shift the scintillation light to a more detectable wavelength.

Atmospheric argon also contains trace amounts of ^{39}Ar , a radioactive isotope produced by cosmogenic muons as they pass through the atmosphere. The effects of this can be mitigated with the pulse-shape discrimination capabilities of liquid argon, and there has been a recent push towards the production and acquisition of underground argon that has a significantly reduced contamination of ^{39}Ar as discussed in Sec. 3.1.2.

4.2 THE CENNS-10 DETECTOR

CENNS-10 is a single-phase, scintillation only, liquid argon system. CENNS-10 was initially designed and built at Fermilab before being shipped to Indiana University for further testing. It was ultimately installed in Neutrino Alley in late 2016 and has been running there ever since. This measurement campaign can be broken up into two run periods: Feb. 2017 - June 2017, called the ‘Engineering Run’ and post-summer 2017 called the ‘Production Run.’ Over the SNS shutdown during the summer of 2017, the detector was disassembled, a light collection upgrade was performed, and additional lead shielding was installed.

Figure 4.1 gives an overview of the detector system which can be broken into five sections discussed in more detail below: (1) Vacuum system, (2) Cryogenic system, (3) Gas-handling system, (4) Data acquisition system, and (5) the External radiation shield.

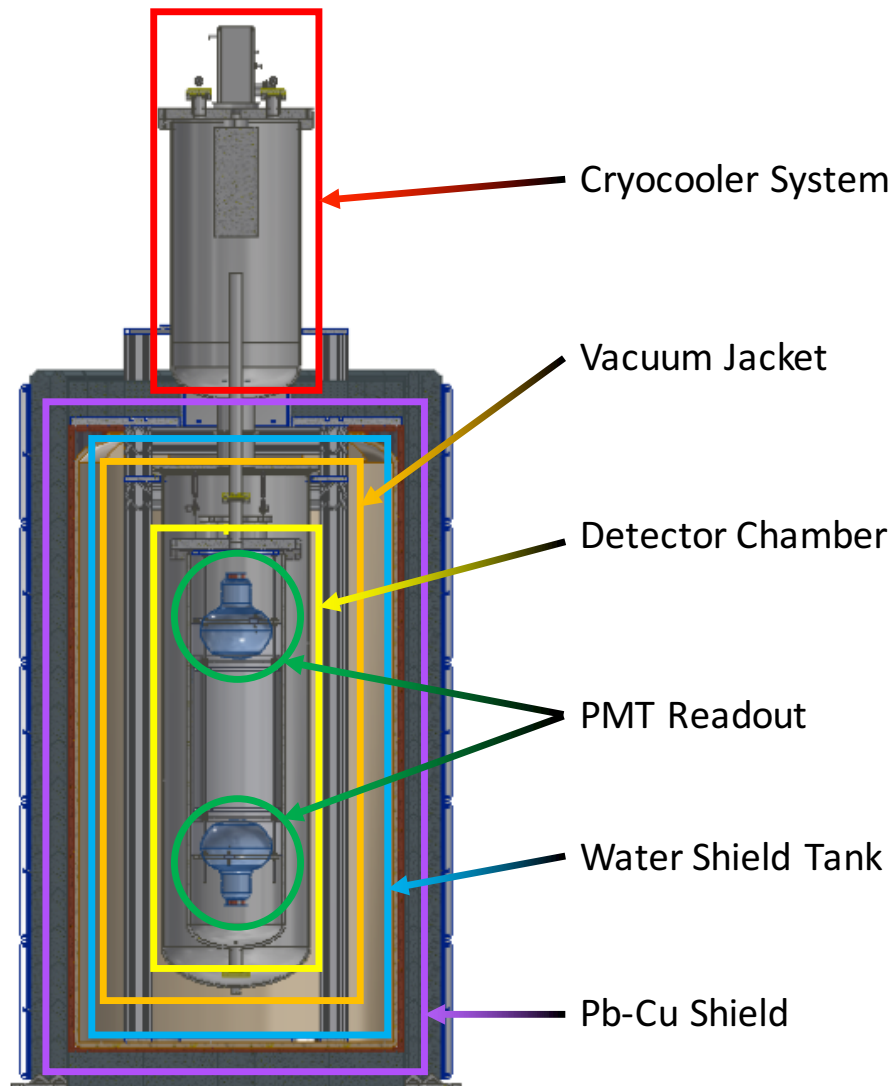
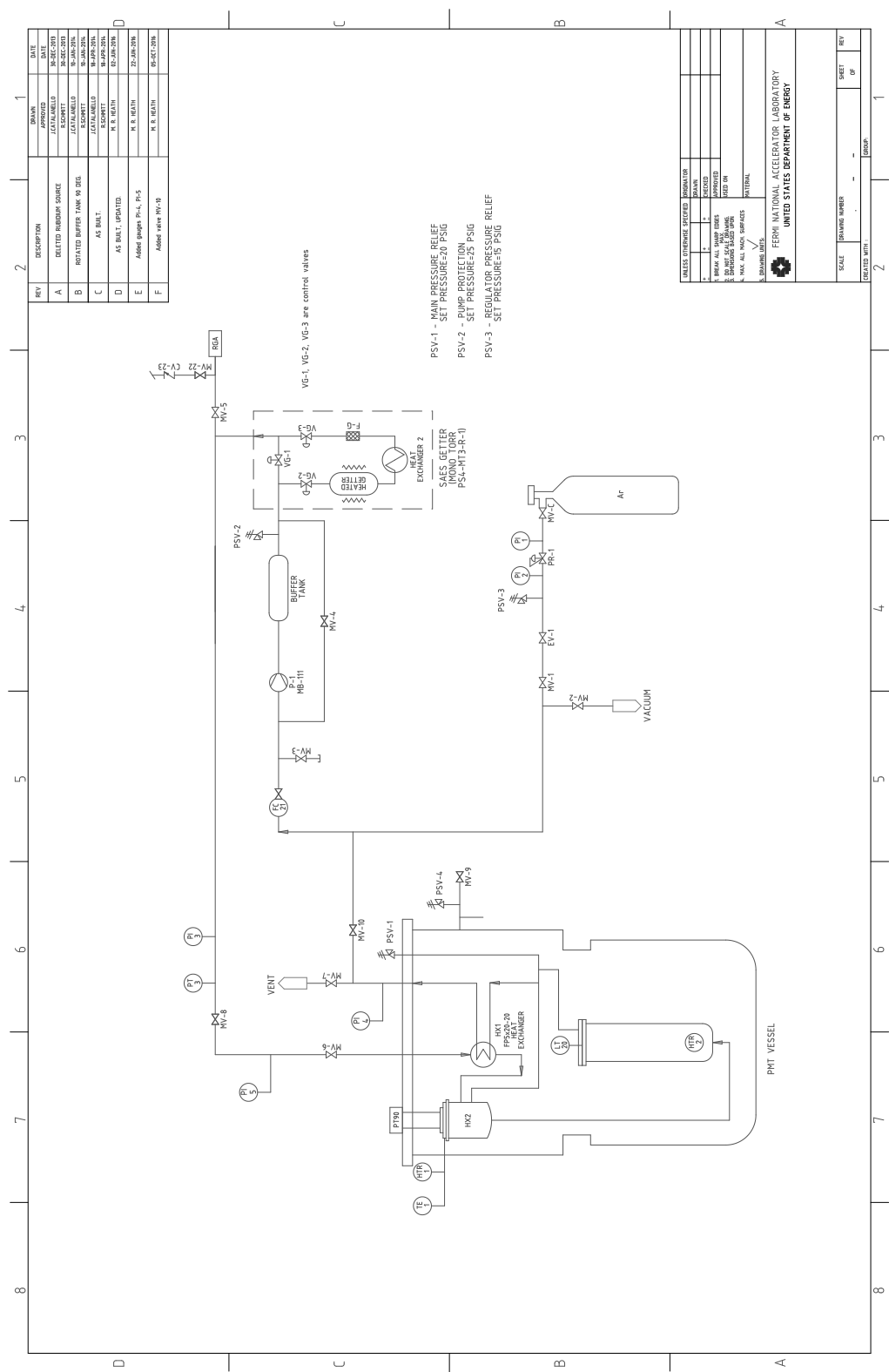


Figure 4.1: Layout of the CENNS-10 Detector. Note that the external lead shielding was not installed until Summer 2017.

Figure 4.2: CENNS-10 plumbing diagram. The cryogenic detector system can be seen on the left side of the diagram inside of the envelope titled 'PMT Vessel.' The gas handling and circulation system used to purify the argon in the system is located on the right side of the diagram.



4.2.1 CRYOGENIC SYSTEM

CRYOSTAT COOLER The detector itself is a vacuum cryostat that uses a Cryomech CP-950 cryocooler to power a PT-90 cold head to cool the detector volume to liquid argon temperatures. Therefore, no additional cryogens (e.g., liquid nitrogen) are needed. At 80 K, the PT-90 supplies 90 W of cooling power [98]. As seen in Fig. 4.2, incoming gaseous argon is pre-cooled by a heat exchanger where it exchanges heat with liquid argon boiloff from the detector. This pre-cooled argon then condenses on a set of copper fins in a cold pot and fills the detector chamber via a pipe to the bottom of the detector volume. A heater mounted on the cold head prevents freezing and is cycled on/off by the CENNS-10 slow control system. The detector is held between (84-88) K and between a relative pressure of (5-8) psig to help prevent impurities from leaking into the system.

DETECTOR VOLUME The main detector volume contains pure liquid argon and is thermally isolated by suspending it from the exterior vacuum vessel with three stainless steel turnbuckles. The total volume of the main detector is 56.8 L. As seen in Figs. 4.3, 4.4, during normal operation, the active detection region is defined by a tetraphenyl-butadiene (TPB) coated acrylic cylinder read out by two Hamamatsu R5912-02MOD photomultiplier tubes (PMT). The volume of the active region is defined by this acrylic cylinder, and it is 20.5 L. The density of liquid argon at atmospheric pressure and 88 K is 1.4 kg L^{-1} giving a total active detector mass of 29.0 kg.

TPB is a widely used wavelength shifter in liquid argon that has a high conversion efficiency of possibly larger than 100 % [99] (although there is some recent evidence that the efficiency is quite a bit lower [100]). Optimizing the TPB-coating thickness is a balancing act between using enough TPB to absorb the scintillation light and re-emit, but not making the coating so thick that the re-emitted visible light is also re-absorbed in the TPB. This is especially a concern in a larger detector where the visible light has the possibility to pass through the TPB coating multiple times before reaching a photo-detector. Generally speaking, a thickness of $(0.1-0.2) \text{ mg cm}^{-2}$ has been found to be optimal [101–103].

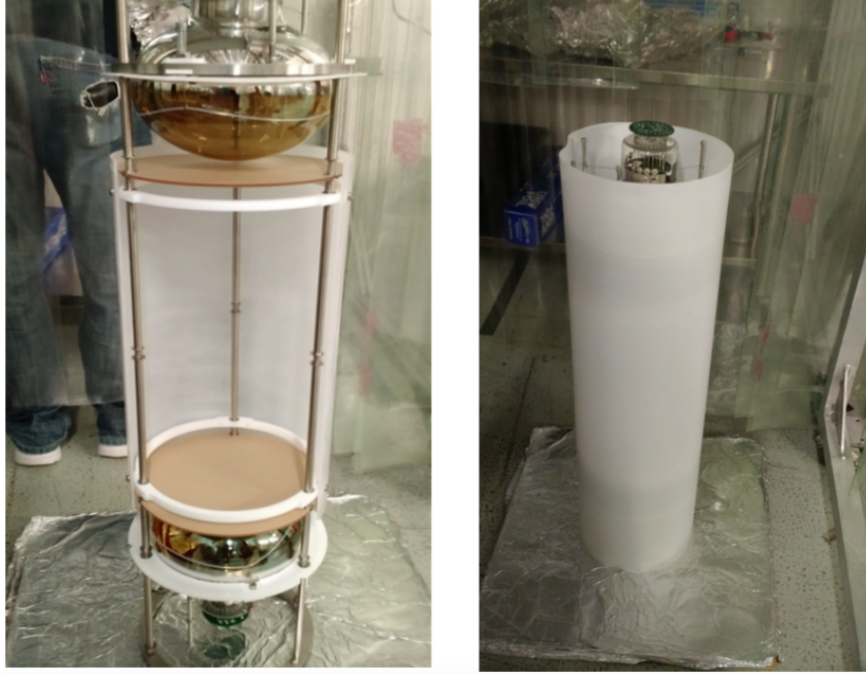


Figure 4.3: A mockup of the acrylic cylinder defining the CENNS-10 active volume prior to installation. Seen in the left image are the PMT support structure, the PMTs, the acrylic cylinder and the Teflon backing the PMTs. On the right, the Teflon wrap surrounds everything.

This TPB-coated acrylic cylinder was composed of three cylindrical sections on the side of the detector, as well as an acrylic disk in front of each PMT face. The side acrylic panels were painted in-house at Indiana University to a nominal TPB thickness of 0.24 mg cm^{-2} with an uncertainty of 30 %. The disks were evaporatively coated at Oak Ridge National Lab to a nominal thickness of 0.2 mg cm^{-2} . This TPB coating is the first material surface seen by any scintillation light produced in the active volume. The acrylic cylinder and the PMTs were backed by a thin sheet of Teflon to maximize the light collection efficiency.

The argon level in CENNS-10 is monitored by two complementary methods. Throughout the detector volume are a series of PT-100 resistance temperature detectors (RTDs) which monitor the temperature in a given location. They are located at various heights to monitor the liquid argon level. When an RTD temperature stabilizes at $\sim 87 \text{ K}$, it has been submerged as evidenced from slow control data from the initial CENNS-10 fill (Fig. 4.13). The highest RTD was located up the vent line pipe for liquid argon boiloff to ensure the entire detector volume is filled. A capacitive

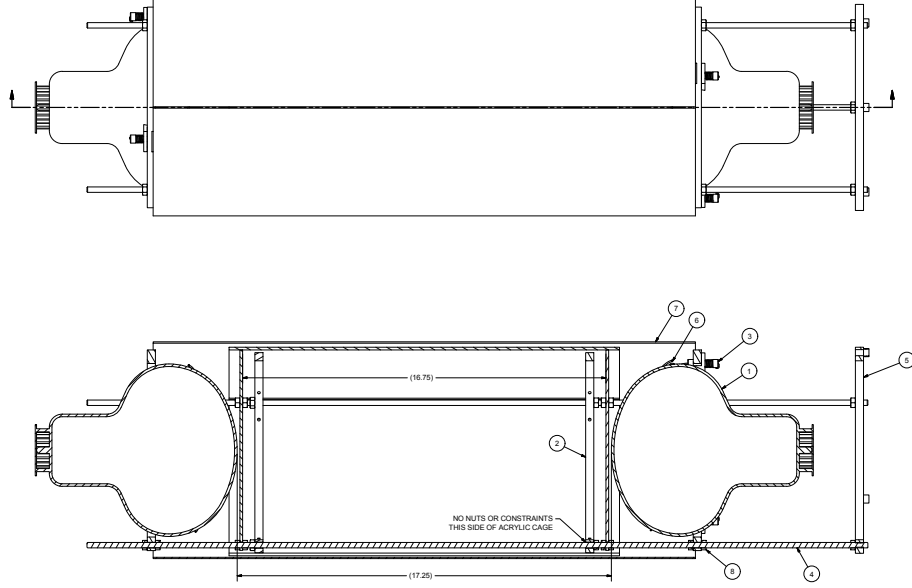


Figure 4.4: Engineering drawing of CENNS-10 inner detector volume for the Engineering Run. The readout consisted of 2 Hamamatsu R5912-02MOD photomultiplier tubes (1). Every surface of the fiducial volume was coated with tetraphenyl-butadiene (TPB) to wavelength shift the liquid argon scintillation light. A TPB coated acrylic cylinder covered the sides of the detector, and TPB-coated acrylic disks were located in front of each PMT. In addition, a sheet of Teflon (7) backed the acrylic cylinder to reflect as much wavelength-shifted light as possible. Remaining marked components made up the support structure for the readout/light-collecting volumes.

level gauge is used for more precise measurements of the liquid level near the top of the detector to ensure the top PMT base is submerged and prevent sparking.

4.2.2 VACUUM SYSTEM

Argon condenses at a temperature of 87 K. While warm in comparison to some other noble liquids, e.g. liquid helium, insulation of the detector volume is necessary to prevent boiling. The CENNS-10 cryogenic system is kept cold by an insulating vacuum, and is wrapped in super insulation for protection from infrared radiation.

Prior to filling the detector with liquid argon, the vacuum region is first purged with argon gas to eliminate water and then pumped to a 1×10^{-6} torr insulating vacuum. This level of vacuum is maintained at all times while CENNS-10 is running. During warmup, up to 1 torr of argon (or nitrogen) gas is backfilled into the insulating vacuum in order to improve thermal conductivity and

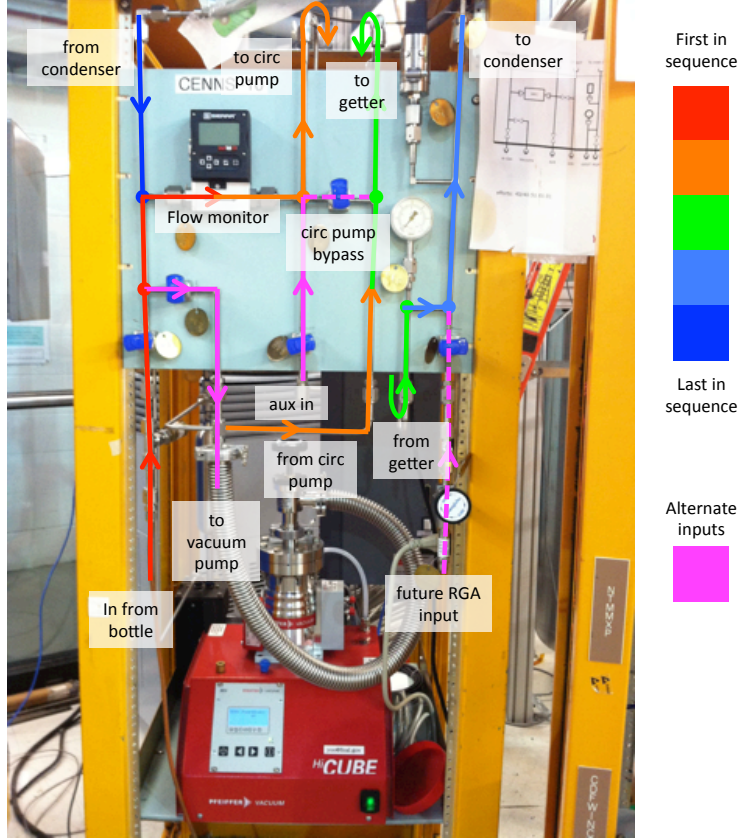


Figure 4.5: The CENNS-10 gas-handling rack is used to circulate argon gas after it boils off from the detector volume. The gas is circulated through a SAES getter to remove any impurities in the system which can harm the light output.

increase the warmup rate.

4.2.3 GAS-HANDLING SYSTEM

The CENNS-10 gas handling system serves to circulate and purify the argon in the system. The gas is continuously circulated through a Zr getter to remove any impurities that may be entering the system. A labelled photograph can be seen in Fig. 4.5, with additional details found in the plumbing diagram (Fig. 4.2). Flow rates are maintained by a Sierra Smart Trak 100 flow meter and are typically held between (5-10) slpm which is the optimal flow rate for the Zr getter. This SAES Zr getter (model PS4-MT3-R-1 [104]) is capable of reducing impurities in the LiqAr system down to ppb levels. The gas system is also kept at a slight overpressure relative to the atmosphere ($\sim(5-8)$ psig) to prevent any contaminants from entering the closed argon system.

high voltage, they are AC-coupled to the digitizer via a pair of signal pickoffs designed at Fermi National Accelerator Laboratory.

As seen in Fig. 4.6, after picking off the PMT signal, it is split. One signal proceeds straight to a Caen V1720 digitizer for fast timing. The other passes through a BBLP-39+ 23 MHz low-pass filter to slow the PMT signal down and is then sent to a separate channel on the digitizer. The V1720 is a 12 bit 250 MS/s 2 V peak-to-peak digitizer commercially produced by Caen with a programmable onboard FPGA providing flexible trigger options. The digitizer is then read out via optical link by a Caen A2818 PCI card on a linux computer.

In addition, various signals from the SNS accelerator (for details see Sec. 3.3.2) are monitored and used to trigger the CENNS-10 DAQ. An SRS 535 Gate/Delay generator [105] is used to apply the appropriate delays to these signals before triggering the DAQ. For details, see Sec. 4.4.1.

SLOW MONITORING The CENNS-10 Slow Monitoring system allows researchers to monitor the status of the detector remotely and removes the requirement for someone to be present at all times. Throughout the Engineering Run, a Windows Remote Desktop Window (Fig. 4.7) was used to monitor various temperatures and pressures of the detector system. It also provided the capability to modify the heat load on the cold head to prevent freezing.

In addition, there was a simple fast DAQ monitoring system which would quickly process run files and save simple information (total events, channel baselines etc.).

Alarms were implemented (with different priorities) to alert shift takers if any parameter fell out of range. These ranged from urgent (system pressure spiking) to more relaxed (DAQ crash in the middle of the night). The DAQ alarms proved particularly useful as at times, particularly near the beginning of the Engineering Run while parameters were being tuned, the DAQ would crash and require a restart.

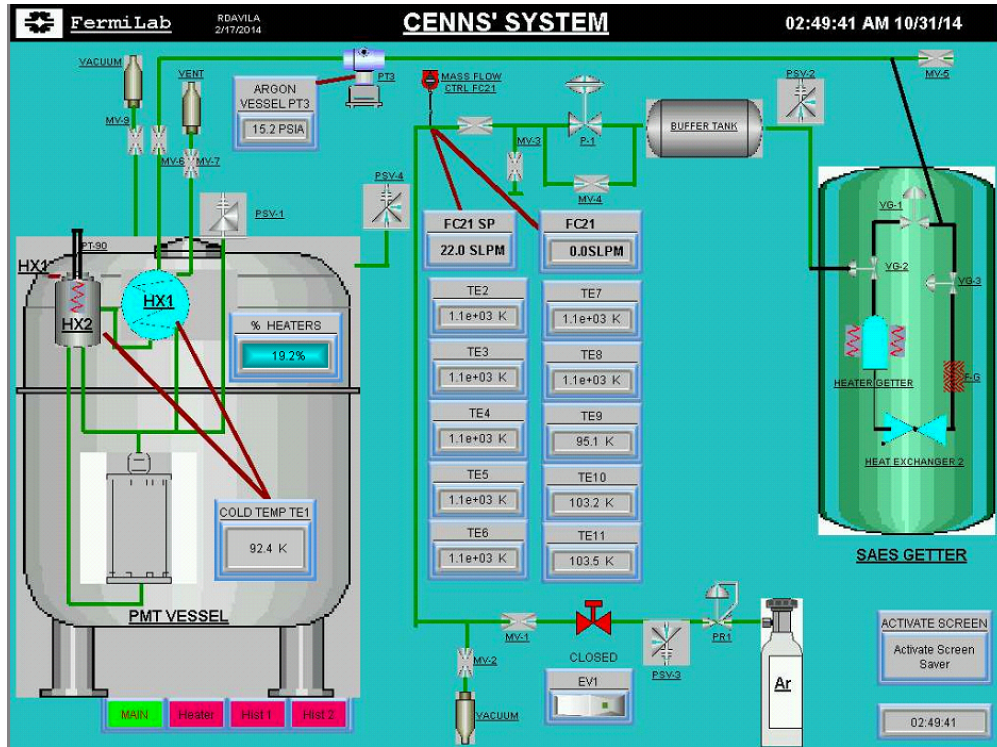


Figure 4.7: Snapshot of CENNS-10 Slow Monitoring Display. Note that at this time the detector was not filled.

4.2.5 EXTERNAL RADIATION SHIELD

To protect against external gamma rays and neutrons a multi-layered radiation shield was built around the detector. The shielding design requirements were based on the background measurements described in Chapter 3.

As seen in Fig. 4.1, the innermost layer is a water tank that surrounds the entire detector vacuum vessel and provides 23 cm of water to attenuate neutrons. The water tank did not quite cover the entire top of the vacuum vessel so water bags were installed on top of the vessel to provide ~7.6 cm of water shielding above the detector. A 1.27 cm thick box of copper is placed outside of the water tank. This box again did not completely cover the top of the detector. This copper box was placed on 10.16 cm of Pb shielding.

Following the conclusion of the Engineering Run, and prior to the start of the Production Run, additional Pb shielding was added to cover the remaining sides of the detector. The layout of the

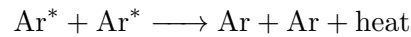


Figure 4.8: Siting and layout of CENNS-10 in Neutrino Alley.

CENNS-10 system in Neutrino Alley can be seen in Fig. 4.8.

4.3 LIQUID ARGON SCINTILLATION

The scintillation process of liquid argon, like the other noble liquids, is well understood. When energy is deposited in the liquid, it can both excite and ionize the Ar atoms with an ionization/excitation ratio of ~ 0.21 [90]. While the processes are different, both the excited and ionized atoms ultimately form dimer states [106] which then scintillate, in the case of liquid argon producing 128 nm light as seen in Fig. 4.9. It has also been proposed that the excited atoms can undergo non-radiative biexcitonic quenching [106, 107]:



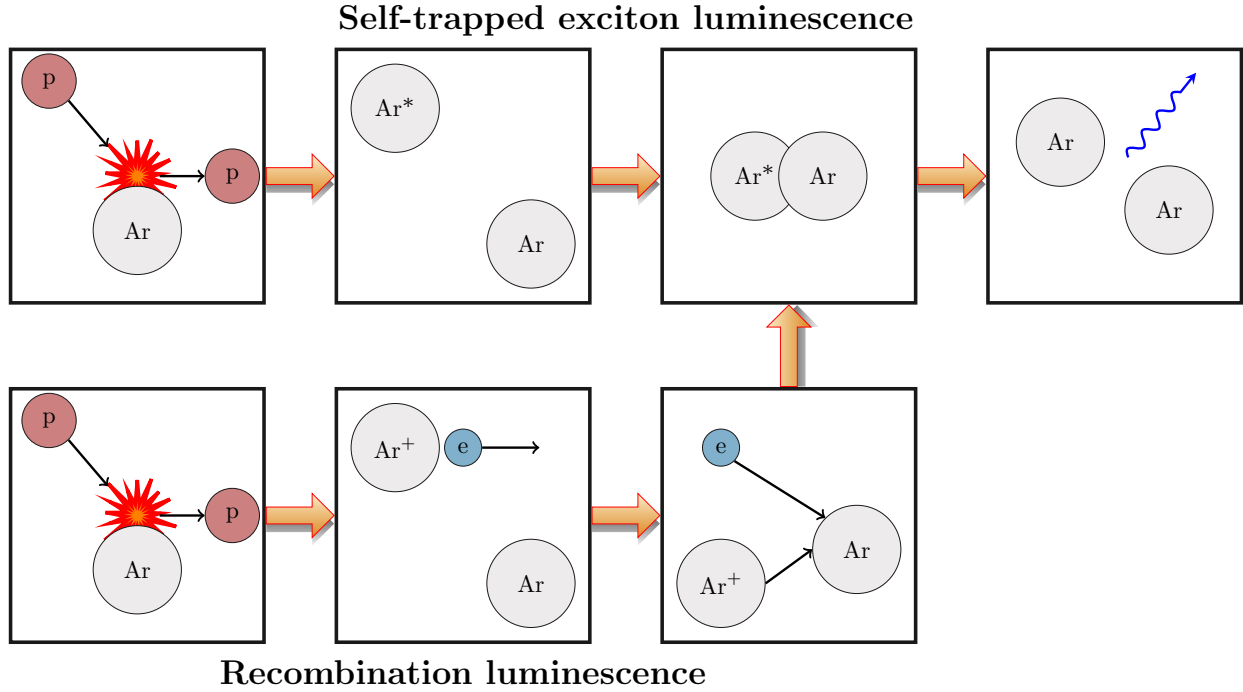


Figure 4.9: A schematic of the liquid argon scintillation process. Energy deposit in noble liquids will excite some atoms and ionize others. The excited ions will form a weakly-bound dimer state (self-trapped exciton) with an unexcited atom. This excited state then decays and emits a photon (top panel). Alternatively, an ionized nucleus can capture a free electron and again form a dimer state which decays via scintillation (bottom panel). Figure based on [108].

The stopping power dE/dx for nuclear recoils is higher than for electrons, resulting in a higher density of excited states. This may result in a larger fraction of de-excitations via biexcitonic quenching rather than dimerization, leading to the quenched light yield for nuclear recoils relative to electronic recoils.

The Ar dimers can form into either singlet or triplet states of approximately the same energy. In the case of liquid argon, the singlet state lifetime is ~ 6 ns while the triplet state lifetime is ~ 1600 ns, with some evidence of an intermediate lifetime [106]. The ratio of dimers formed into either the singlet or triplet state depends on the ionization density, but the mechanism is not well understood. The singlet to triplet ratio for electronic recoils (ER) is ~ 0.3 , whereas for nuclear recoils (NR) the ratio is closer to 0.7 providing the opportunity for pulse-shape discrimination (PSD) as seen in Fig. 4.10. This ratio of singlet to triplet states is particularly powerful at differentiating ER from NR events in liquid argon because the lifetimes of the singlet and triplet states are so drastically

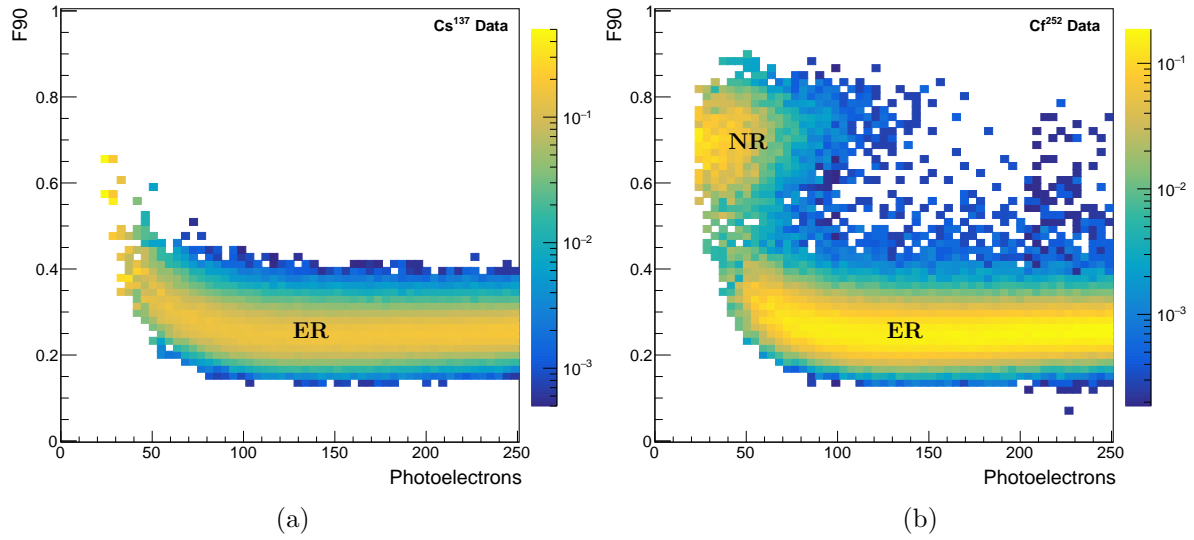


Figure 4.10: Data from CENNS-10 calibrations showing pulse-shape discrimination capabilities of liquid argon. Electronic recoil (ER) events have a much larger component of triplet state scintillation light compared to nuclear recoil (NR) events which contain mostly singlet light. (a) ^{137}Cs dataset. ^{137}Cs decays with a mono-energetic 662 keV gamma ray producing purely ER events in the detector. (b) Data from a ^{252}Cf fission source. NR events from neutron scatters can be seen as the ‘blob’ around $F_{90} \sim 0.7$.

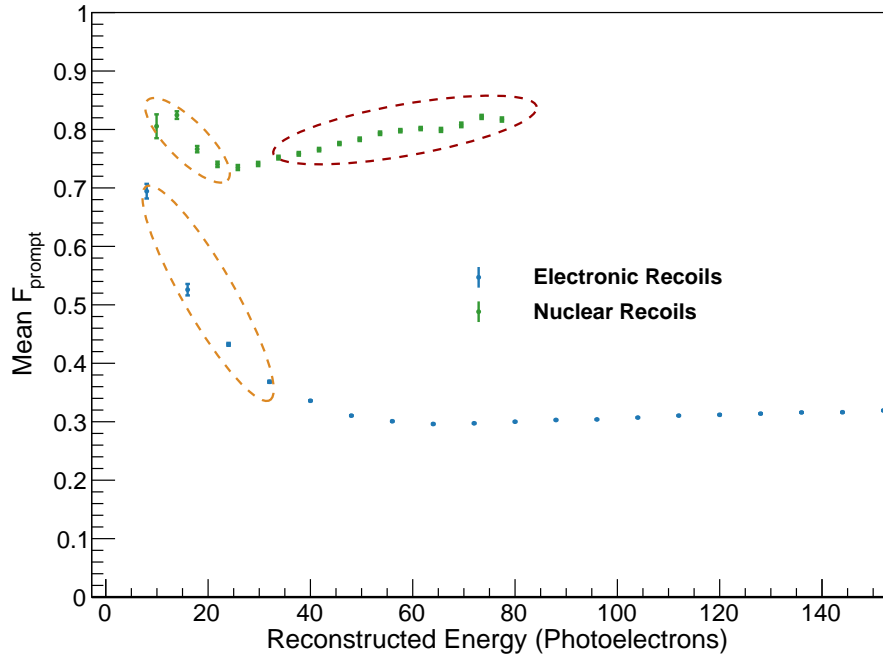


Figure 4.11: Behavior of the means of the electronic and nuclear recoil (ER and NR respectively) bands as a function of energy. The low energy behavior is due to a combination of a hardware threshold on the dataset (gold circles) as well as an energy dependence of the pulse shape (crimson circle).

different. A commonly used quantity to demonstrate this behavior is the F90 parameter [95, 97]:

$$F_{90} = \frac{LY_{90\text{ ns}}}{LY_{\infty}} \quad (4.1)$$

In other words, the F_{90} value is the fraction of the light in the first 90 ns of an event divided by the total amount of light in the event. F_{90} has been observed to be dependent on the energy deposit [109], with larger ionisation densities (lower energy particles) producing a larger fraction of singlet states. As seen in Fig. 4.11, this is also observed in CENNS-10 calibration datasets.

4.3.1 N₂ CONTAMINATION

The presence of N₂ contamination in a liquid argon detector will lead to quenching of the scintillation light. The most important reaction leading to the quenching of the Ar scintillation is the collision of the Ar₂^{*} excimers with N₂ impurities [110, 111]:



Essentially, the N₂ contamination causes the Ar excimers to give up their energy in a way other than scintillation.

The largest effect from the N₂ quenching is seen on the triplet light state, as, with the longer lifetime, the dimers have more opportunities to transfer energy to N₂ molecules. The most noticeable effect from this is that the ER band in F_{90} PSD plots moves to higher values and overlaps with the NR band. N₂ contamination is clearly important both with regards to the total light yield as well as with regards to PSD capabilities.

For scintillation-only LiqAr detectors, N₂ levels $\lesssim 1$ ppm are all that is required for sufficient scintillation [111]. To ensure the liquid argon in CENNS-10 is at least this pure, the detector boiloff is circulated through a gas handling rack with a SAES Zr getter [104].

Due to N₂ contamination quenching the argon triplet scintillation light, a measurement of

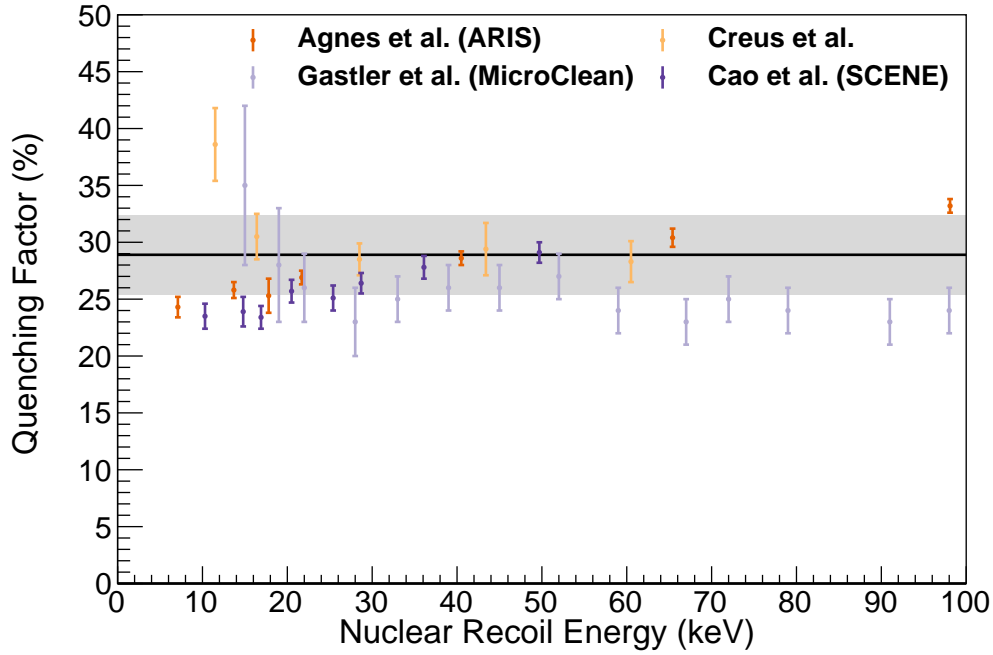


Figure 4.12: Global quenching factor (QF) data for liquid argon. At energies relevant for CEvNS, the QF can be modeled as energy independent with a value of $(28.9 \pm 3.5) \%$. Data from [91–94].

the triplet lifetime can give some indication of the level of N_2 in the system. At the end of the Engineering Run, an examination of the N_2 contamination level was performed by doping the system with nitrogen. Details of this test can be found in App. B. In this test, N_2 was added to the system to a level of 25 ppm by mass. The effect of the nitrogen contamination was evaluated with both a measurement of the triplet lifetime, as well as an independent measurement using an LDetek LD8000 N_2 monitor [112]. Good agreement was found between both methods. CENNS-10 was found to have a triplet lifetime of $1.2 \mu s$ prior to N_2 doping with a negligible triplet component after doping. With comparison to [111], this indicates a N_2 contamination of $\mathcal{O}(1 \text{ ppm})$ during the Engineering Run.

4.3.2 NUCLEAR RECOIL QUENCHING

As mentioned in Chapter 1, the light output from nuclear recoils is quenched relative to electronic recoils of the same energy. This is largely due to the increased dE/dx for nuclear recoils resulting in the energy being dispersed in ways other than scintillation. This relative light output difference

between nuclear and electronic recoils of the same energy is typically called the quenching factor (QF). A precise understanding of the QF is necessary for a CEvNS search as the understanding of a detector threshold is dependent on the QF, and any energy dependence of the QF can distort the CEvNS recoil spectrum.

These measurements are of particular interest to the dark matter community [113]. As seen in Fig. 4.12, multiple measurements of the liquid argon quenching factor have been carried out [91–94]. Within the COHERENT collaboration, an analysis of the global liquid argon QF data was performed by B. Suh. This fit introduced correlated errors between data points within a given measurement. With the introduction of these correlations, an energy-independent fit of the QF data over the CEvNS region of interest ($\sim(20\text{--}100)$ keV) adequately models the data and results in a quenching factor value of $(28.9 \pm 3.5)\%$.

4.4 CENNS-10 ENGINEERING RUN

CENNS-10 was installed in Neutrino Alley late in December 2016. As seen in Fig. 2.4, it is located in an alcove near the end of the hallway where there is enough space for all of the supporting hardware (cryogenics in particular). This location is roughly 28 m from the SNS target.

CENNS-10 was filled using boiloff gas from a liquid argon dewar from AirGas. During testing of the CENNS-10 system at IU, an AirGas representative stated that the boiloff gas from liquid argon dewars was as pure as 99.999% UHP gas cylinders. A comparison of gas from dewars and a UHP cylinder was performed at IU using an SRS UGA [114] which confirmed this was the case. Therefore, the decision was made to fill CENNS-10 with liquid argon boiloff from a dewar. We began filling in early December, and the detector was filled with liquid argon by December 11 as seen in Fig. 4.13. The argon gas was continuously circulated through a SAES getter [104], both during the fill and throughout the data run.

Shortly after completing the fill, the SNS turned off for a winter shutdown. The SNS turned back on February 23, 2017. The PMT signals were finalized on the 24th, and CENNS-10 ran in

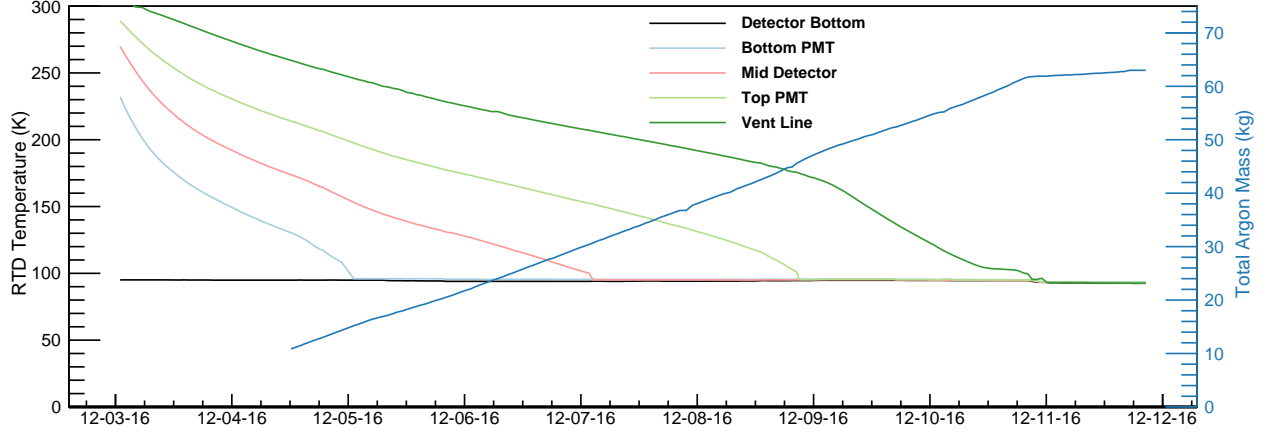


Figure 4.13: Slow control data from the CENNS-10 fill in Neutrino Alley. Shown here are temperature readings from Pt-100 RTDs located at various heights in the detector. Boiloff gas from a liquid argon dewar was used for this fill after confirmation of the purity during testing at IU. Filling the detector takes about 9 days.

that final configuration until the SNS shutdown on May 28, 2017. During this time, the beam ran more or less non-stop with the exception of a shutdown for minor maintenance and repairs every Tuesday. These minor shutdowns were used to acquire calibration data.

The run can be broken up into three different periods. CENNS-10 initially ran with no neutron shielding to make an in-situ measurement of the beam-related neutron flux. On March 8, the water shielding was installed. CENNS-10 ran in this configuration for two days, and the copper shielding was installed on March 10. CENNS-10 remained in this configuration for the remainder of the Engineering Run.

As seen in Fig. 4.14, a total of 1.8 GWhr of beam was delivered throughout the Engineering Run corresponding to a total of 4.2×10^{22} pot assuming a beam energy of 973 MeV. Of that, 1.5 GWhr was delivered in the fully-shielded configuration. The Engineering Run timeline, integrated power delivered, and the average beam power for each run period are all summarized in Table. 4.1.

4.4.1 TRIGGERING SCHEME

A trigger scheme that allowed CENNS-10 to run in a variety of different configurations was implemented for the Engineering Run and can be seen in Fig. 4.6. This was necessary for the different

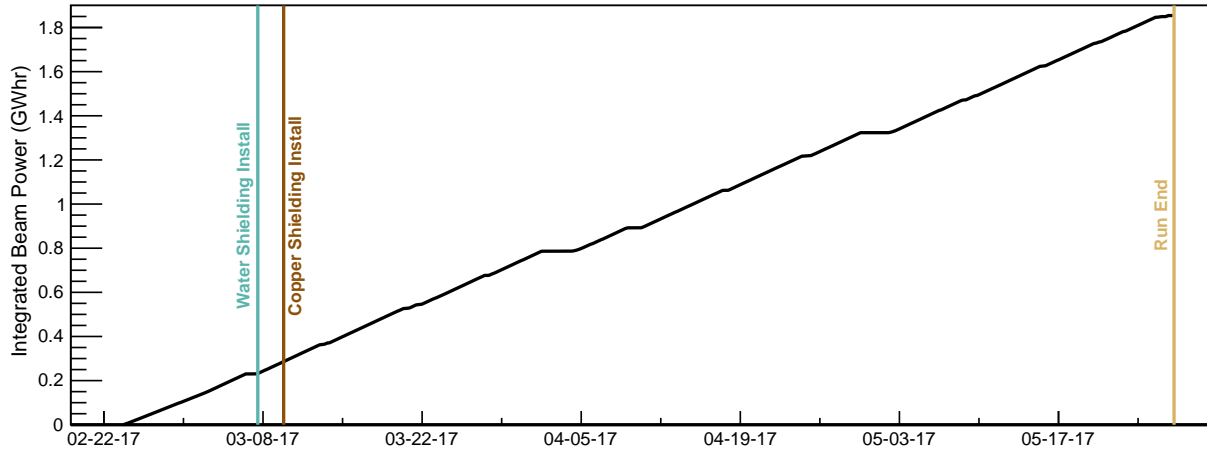


Figure 4.14: Integrated beam power over the course of the Engineering Run. Marked above are significant events during the run. The run began on February 24 and lasted until May 28, 2017.

types of data taken by CENNS-10 .

CALIBRATION TRIGGERS Every Tuesday maintenance day was used to take calibration data. To characterize the single photoelectron response, a pulsed low-light LED system was used. For these calibration runs, the LED was pulsed with a Rigol DG4162 waveform generator [115]. The ‘Sync Out’ output of the waveform generator was used as a thresholdless external trigger for these LED datasets.

In addition, a variety of radioactive sources were used to characterize the detected photon yield of CENNS-10. The most useful source was ^{137}Cs which provided a mono-energetic 662 keV gamma ray. Monthly data with a ^{252}Cf fission source was taken to characterize the PSD capabilities of CENNS-10. For these calibration source runs, an internal trigger based on the OR of the unfiltered

	Start Date	End Date	Integrated Power (GWhr)	Avg. Power (MW)
No Shielding	Feb. 24, 2017	Mar. 8, 2017	0.24	0.91
+ Water	Mar. 8, 2017	Mar. 10, 2017	0.04	0.99
+ Copper	Mar. 10, 2017	May 28, 2017	1.50	0.97

Table 4.1: Timeline of CENNS-10 engineering run. Protons were delivered on target at an energy of 973 MeV.

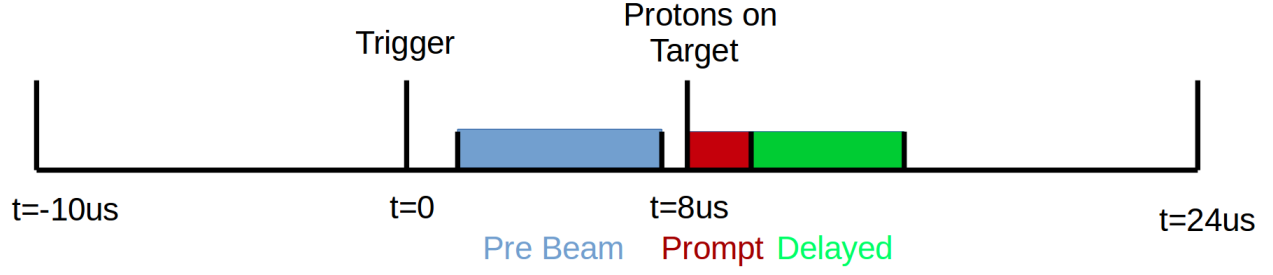


Figure 4.15: Schematic of the CENNS-10 beam trigger. The pre-beam window was used to characterize beam-unrelated backgrounds, the prompt window to search for beam-related fast neutrons and prompt ν_μ from pion decay, and the delayed window to search for delayed neutrinos from muon decay. Every beam trigger was preceded by an identical strobe trigger to further characterize the beam-unrelated backgrounds.

PMT signals (with a threshold of ~ 10 PEs) was used.

BEAM TRIGGER The same trigger used in the earlier SciBath run (Sec. 3.3.2) was used as a beam trigger during the Engineering Run. An SRS 535 Gate/Delay generator [105] was triggered externally on Event 61. This Gate/Delay generator then output a NIM pulse with no delay to produce a ‘Strobe’ trigger. These strobe windows with NO BEAM were used to characterize the beam-unrelated backgrounds (BUB) in Neutrino Alley.

The gate/delay generator also produced a delayed NIM pulse ($\mathcal{O}(2.1\text{ ms})$ later) that came in time with the beam (marked by Event 39) to trigger the fast DAQ. For a given trigger, a total of $33\mu\text{s}$ was read out: $10\mu\text{s}$ pre-trigger and $23\mu\text{s}$ post-trigger. Protons hit the target (tagged with Event 39) roughly $8\mu\text{s}$ after the trigger. A given beam (or strobe) waveform was also broken down further as seen in Fig. 4.15. An $\mathcal{O}(6\mu\text{s})$ pre beam window before the nominal beam-on-target time was used to further characterize the BUB. A prompt $1\mu\text{s}$ region centered on the beam pulse was used to look for fast neutrons and prompt neutrinos, and finally a delayed $\mathcal{O}(3\mu\text{s})$ window was defined to search for delayed neutrinos from muon decay.

CHAPTER 5

CENNS-10 WAVEFORM ANALYSIS AND CALIBRATION

In this chapter I discuss the waveform analysis methodology used in the Engineering Run. I then review the detector calibration procedure and the tuning of the detector Monte Carlo simulation. I finish with detector inefficiencies that are not directly simulated.

5.1 `daqman`

The `daqman` [116, 117] software package was used for both running the CENNS-10 fast DAQ, and for subsequent data analysis. Developed by B. Loer, `daqman` is an analysis framework capable of running the Caen V172X family of digitizers and was used for the data acquisition and analysis software for DarkSide 10. ‘`daqman`’ is both the software executable for running the Caen DAQ, and the software package as a whole.

5.1.1 TERMINOLOGY

Before discussing the waveform analysis procedure, I want to go over some terminology I will use (which may differ from the `daqman` terminology). Where there are differences I will point them out.

- **Waveform:** ADC values vs time. A waveform is collected for every live channel when a trigger is recorded.
- **Scintillation Event:** Any particle interaction in the detector
 - In `daqman` terminology, an ‘Event’ is the collection of waveforms for each trigger.

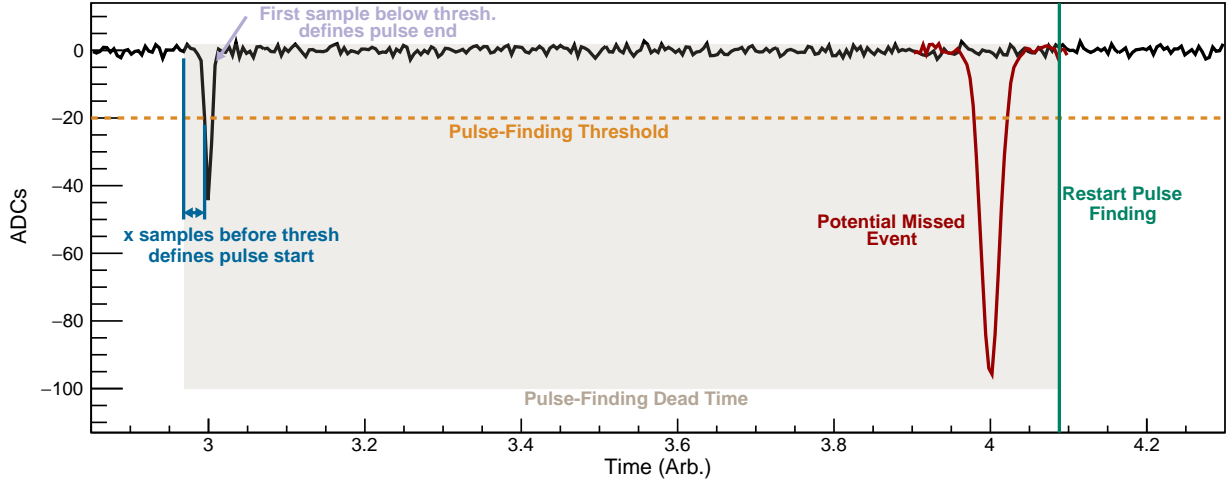


Figure 5.1: Pulse-finding algorithm schematic. Waveforms are stepped through sample-by-sample until a sample is below threshold. x samples before is the pulse start (marked by dark blue lines). The waveform is then stepped through again until a sample above threshold is found. The pulse end is y samples later. Pulse finding resumes some time later (marked by the green line). In CENNS-10 analysis this time is $6\text{ }\mu\text{s}$ later. This introduces a dead time (gray box) where events may be missed (crimson pulse).

- Pulse: particle events are made of individual photoelectron pulses (due to the detection of singlet and triplet light).
 - In `daqman` terminology, a ‘Pulse’ is what I am calling a ‘Scintillation Event’

5.1.2 EVENT BUILDING

`daqman` was designed as the DAQ for a dark matter experiment which relied on internal detector triggers to detect an event. As such, it was not set up to easily find events across channels when externally triggered. Each of the algorithms below run on each channel individually.

The first event-building-related module run by `daqman` is the `BaselineFinder` module which finds the baseline of a given waveform. For the Engineering Run, a fixed baseline was used. This means that `daqman` found the average baseline value over the first $1\text{ }\mu\text{s}$ of each waveform and applied that baseline value for the rest of the waveform. This baseline is only used for pulse finding. A separate local baseline value is later found in the pulse-fitting procedure (see Sec. 5.2).

The `PulseFinder` module is run next. A ‘DiscriminatorSearch’ method (schematic in Fig. 5.1)

Variable	Value	Description
T	20 ADCs	ADC threshold
x	5 samples	Samples before threshold crossing for event start
y	2 samples	Samples to skip ahead to search for pulse end
z	6 μ s	Time to jump forward to restart pulse finding

Table 5.1: Summary of pulse-finding settings.

is used to find pulses on each channel separately. In this algorithm, each waveform is stepped through sample-by-sample. When a sample s_0 falls below a user-defined threshold T (in the case of beam triggers 20 ADCs), a pulse is ‘found.’ The pulse start is defined as $s_0 - x$, where x is a user defined value (5 samples in the case of beam data). Then, the waveform is stepped through beginning at the samples $s_1 = s_0 + 1$ and $s_2 = s_0 + y + 1$ until a sample is found that is back above threshold. The pulse end is defined as s_2 .

In the case of the Engineering Run, y was defined to be 2 samples to ensure only the singlet peak is found. The algorithm then jumps forward some amount of time z (6 μ s for the Engineering Run to capture most triplet scintillation light) and the search is resumed. For beam triggers, the same procedure is applied to find the rising edge of the Event 39 TTL pulse. Relevant pulse-finding variables are summarized in Tab. 5.1.

This final pulse finding step was implemented to make fitting the singlet peak easier. It has the downside of missing some potential events if, e.g. one channel sees a small pulse from an earlier event that is not seen by the other PMT immediately before another event. These events would not be included in a CEvNS search anyway as the early pulse could be from, e.g. the triplet light of an earlier event which would contaminate the reconstructed pulse shape of both events. This event ‘loss’ rate is considered as an efficiency loss for the CEvNS analysis.

The `ScinEvtFinder` was implemented to group pulses across channels and identify actual events. This algorithm grabs the start times of every pulse from each channel. It then requires a coincidence across channels within 20 ns to define a ‘Scintillation Event.’ The event start time is defined as the start time of the first ‘Pulse’ making up the event and the event ends 6 μ s later.

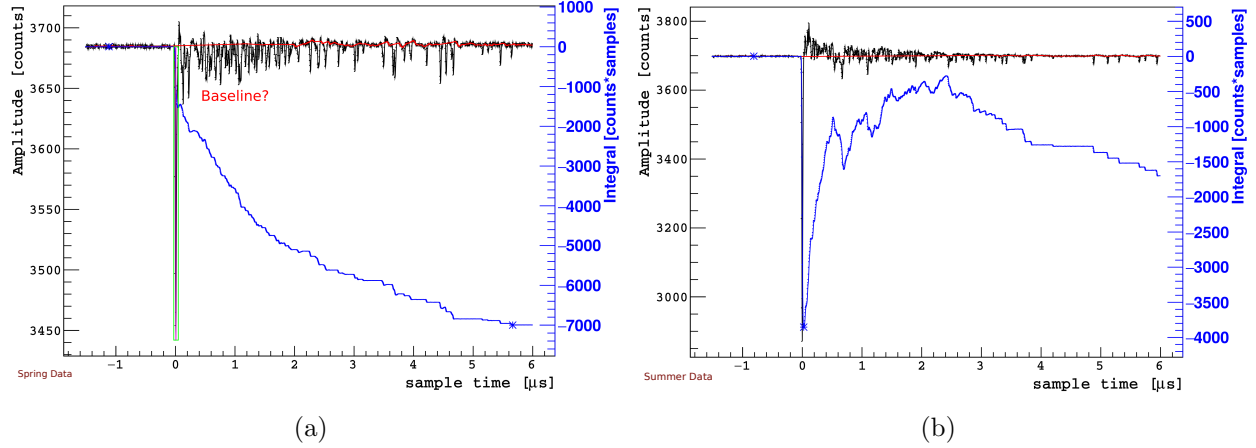


Figure 5.2: Main motivations for implementing the pulse fitting algorithm. (a) Waveform demonstrating the length of an Ar event and the difficulty of finding the baseline amongst the triplet light. In this event display, a moving-average baseline algorithm was implemented to alleviate some of the concern of the baseline drifting throughout the event. (b) Waveform from the Production Run dataset demonstrating the issues with finding a valid baseline after the singlet pulse even with the moving-average baseline algorithm. Overshooting due to AC coupling of the PMTs means the average baseline before an event can not be applied after the event without some sort of correction.

5.2 PULSE FITTING

While `daqman` has many built-in analysis capabilities, for the CENNS-10 Engineering Run, a pulse fitting algorithm was implemented to handle two main problems: (1) Uncertainty of the appropriate baseline to use when evaluating the amount of triplet light and (2) Remove the ‘overshooting’ effect caused by AC-coupling the PMTs to the ADC.

TRIPLET LIGHT As seen in Fig. 5.2a, an event in liquid argon takes place over several microseconds. This is due to the long triplet lifetime ($1.6\ \mu\text{s}$) of Ar scintillation light [106]. Typically, the baseline can be fit immediately before an event, and then assumed to be unchanging throughout the event. Due to the timescales of Ar scintillation light, this may not be a valid assumption. There is no guarantee that, e.g., the baseline at $t = 6\ \mu\text{s}$ is the same as the baseline at $t = 0.5\ \mu\text{s}$. The pulse-fitting procedure is meant to alleviate some of that concern.

NEW PRODUCTION RUN PMT CIRCUIT New PMT bases were designed, manufactured, and installed during the Summer 2017 SNS shutdown. This new circuit was designed to

remove the large initial overshoot of PMT pulses seen in the Engineering Run data (Fig. 5.2a at $\sim 0.1 \mu\text{s}$). The new PMT circuit created a longer recovery time (due to recharging capacitors) than the original circuit. This overshooting of the signals is unavoidable for an AC-coupled PMT [118]. The particular time constant of the RC-circuit in the Production Run PMT circuit causes the triplet light pulses to ride on the recovery back to baseline of the singlet pulse (and earlier triplet pulses) making an evaluation of the amount of triplet light difficult.

5.2.1 FITTING PROCEDURE

The fitting procedure is (with details to follow):

1. Form a single photoelectron (SPE) template shape
2. Perform an analytic least-squares (LS) parabola fit on the SPE template peak to find the peak time / amplitude
3. Find the singlet peak of an event as described above
4. Perform an analytic LS parabola fit to the singlet peak
5. ‘Fit’ the SPE template to a given event in the data
 - The scale factor applied to the template shape to match the singlet height indicates the number of PEs in the singlet state
 - The fit peak time gives a time shift to apply to the template
6. Form a residual between the data and the scaled/shifted template
 - The amount of triplet light is defined as the max integral value of the residual
 - Comparison to the template shape integral gives the number of photoelectrons in the triplet

5.3 SINGLE PHOTOELECTRON ANALYSIS

SINGLE PE TEMPLATE SHAPES Data was taken once a week with a pulsed low-light LED to characterize the single photoelectron (SPE) response of the photomultiplier tubes. LED

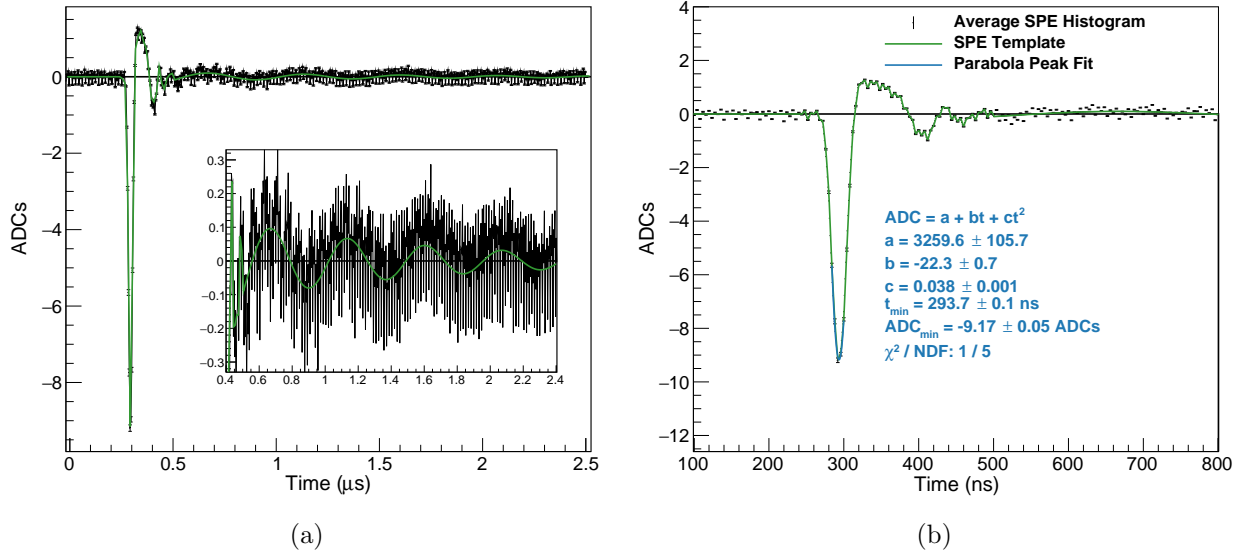


Figure 5.3: The average single photoelectron shape. (a) The template function fit to the average shape. This template shape is later applied to actual ‘Scintillation Event’ waveforms as a measure of the number of photoelectrons seen in the Scintillation Event. (b) Least-squares parabola fit to the single photoelectron template. Comparison to the pulse height and time of the SPE template provides a time shift and scale factor to apply to the template when fitting singlet pulses.

runs were externally triggered on the Sync Out of a Rigol DG4162 waveform generator (see Fig. 4.6) meaning that all LED pulses should occur at the same time in every waveform.

The first step in the fitting process is to form a single photoelectron (SPE) template shape. This is the only step that uses the TMinuit fitting class in ROOT as Minuit is relatively slow. The template shapes are formed by creating the average histogram of all the waveforms in a given LED run. Both a low and high ADC threshold cut ($5 < ADC < 20 \text{ ADCs}$) are applied to make sure only SPE pulses are included in the average.

Once the average SPE histogram has been formed, it can be fit with a function to help minimize any statistical fluctuations. This function consists of three separate time regions. Prior to the pulse, a flat baseline b calculated at the beginning of the waveform is used. Over the pulse and the initial overshoot, a ROOT TSpline3 of the average histogram is used. Finally, for the tail of the SPE pulse, the sum of a damped oscillator and an exponential decay were used. The fit function is

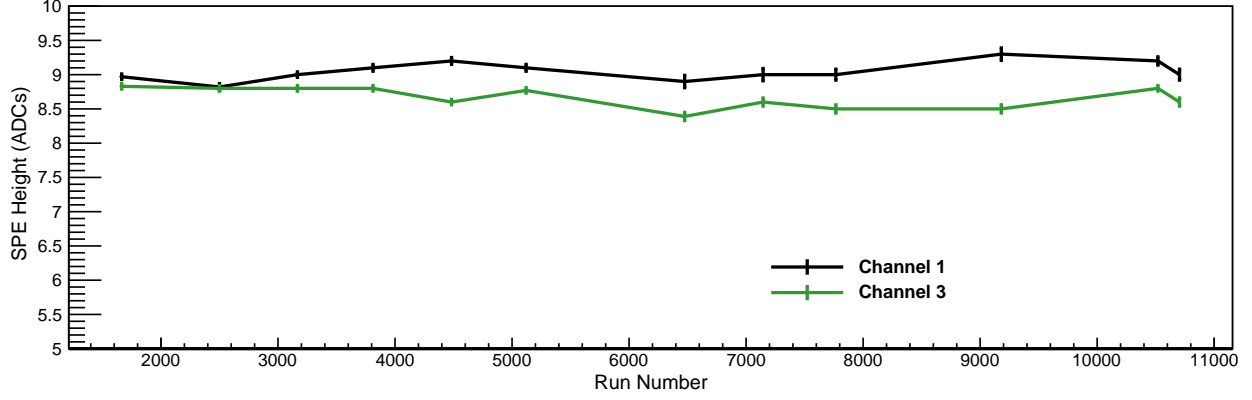


Figure 5.4: The single photoelectron response throughout the engineering run. The SPE peak height is stable to within $\pm 5\%$ throughout the course of the run.

summarized in Eq. 5.1:

$$f(t) = \begin{cases} b & -\infty < t \leq t_{start}^{pulse} \\ TSpline3 & t_{start}^{pulse} < t \leq t_{end}^{pulse} \\ Ae^{-(t-t_{start}^{pulse})/\tau_1} \cos(\omega t + \phi) + Be^{-(t-t_{start}^{pulse})/\tau_2} & t_{end}^{pulse} < t < \infty \end{cases} \quad (5.1)$$

An example SPE template shape can be seen in Fig. 5.3. The initial overshooting behavior and the ringing present in the tail of the SPE pulses led to the re-design of the PMT base prior to the Production Run mentioned in Sec. 5.2.

SPE LEAST SQUARES FIT Once the SPE templates have been formed, an analytical least-squares (LS) parabola fit is done to the peak of the average histogram (Fig. 5.3). The fit range is $\pm 8\text{ ns}$ ($\pm 2\text{ samples}$) on either side of the minimum ADC time of the average histogram. This fit gives both the time of the minimum, as well as the SPE height in ADCs. In this LS fit, the baseline value used is the average histogram value at the beginning of the waveform. From this procedure, the SPE template shape, the minimum ADC time, and the minimum ADC height are all stored for later application to scintillation events in the detector as discussed in the next section.

This SPE analysis is performed every week to monitor the stability of the PMT SPE response

throughout the run as seen in Fig. 5.4. The SPE response is stable to within 5 % throughout the course of the Engineering Run. For more information on the least squares fit, see App. C.

5.4 WAVEFORM ANALYSIS

5.4.1 SHIFT AND SCALE

After the single photoelectron characterization, the next step is to fit the template shape to a given event. To do this, a LS parabola fit is performed on the singlet pulse of an event. From the `daqman` pulse finder, the singlet pulse start, end, and minimum sample times are all known. The minimum ADC value and 2 samples on each side are fit with a parabola to find both the peak ADC height and time of the minimum.

The singlet pulse height with respect to the baseline is then compared to the pulse height of the average SPE pulse to find the number of photoelectrons in the singlet pulse. The baseline for the pulse is assumed to be the average value of the 15 samples (60 ns) before the pulse start index. Based on the minimum fit time of the singlet pulse, the SPE template is shifted in time to line up with the given event. This time shift and scaling is used to ‘fit’ the SPE template to the singlet pulse.

5.4.2 SUBTRACT

After scaling and shifting the SPE template shape, the residual of the template and the waveform being considered can be taken to analyze the triplet light.

$$r(t) = F(t) - D(t) \tag{5.2}$$

where $r(t)$ is the residual, $F(t)$ is the scaled/shifted template, and $D(t)$ is the data waveform. The integral waveform of the residual is then used for the triplet light analysis:

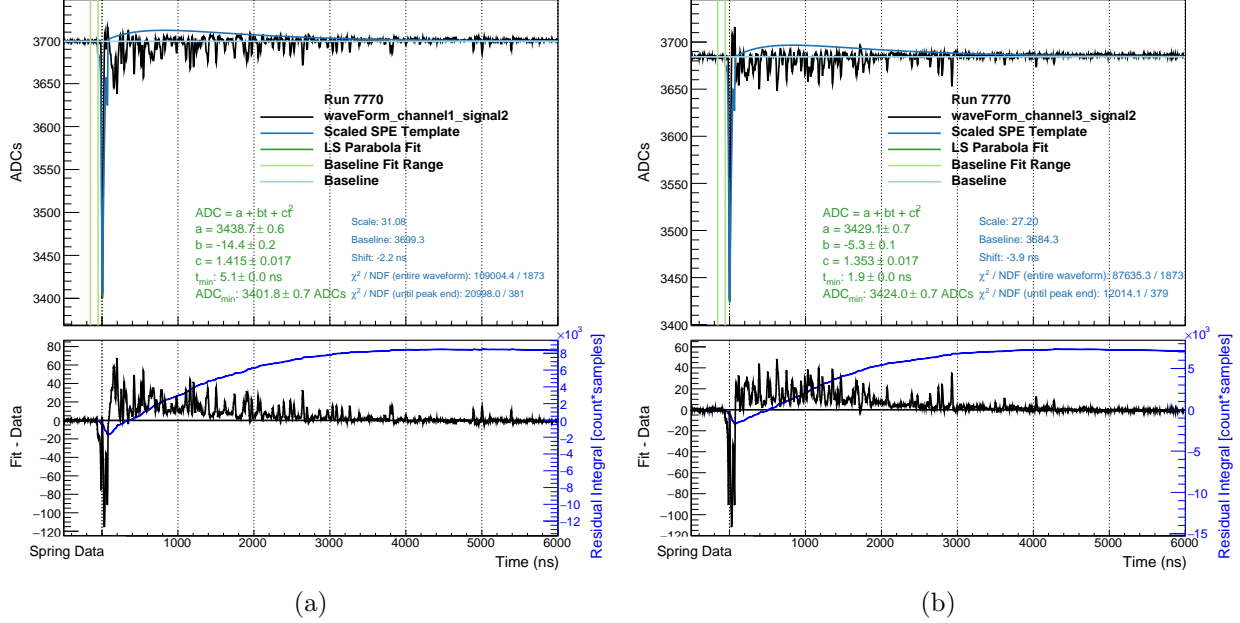


Figure 5.5: An example waveform fit taken from a ^{137}Cs calibration dataset in the Engineering Run. (a) Channel 1 and (b) Channel 3. The scale factor corresponds to the number of PEs in the singlet peak.

$$I(t_n) = \sum_i^n r(t_i) \quad (5.3)$$

where the sum runs over all samples in the event up to the time t_n found during the event building procedure (Sec. 5.1.2). This integral skips the first 240 ns of the residual to remove any statistical fluctuations remaining in the SPE template shape TSpline3 region. The integral of the residual corresponds to the amount of light in the triplet state observed. Comparison to the integral of the SPE template shape gives a conversion to photoelectrons.

A threshold of 2 ADCs was placed on this integration to improve energy resolution and pulse shape reconstruction as discussed in Sec. 5.5 and 5.6. A fixed integral time was considered, but using the maximum integral value was determined to give better results in energy resolution and pulse-shape discrimination. An example waveform fit can be seen in Fig. 5.5.

A NOTE ON THE FITTING ERRORS: When fitting individual waveform peaks, the errors on the ADC value were set to the maximum of 1.0 or the square root of the difference from baseline.

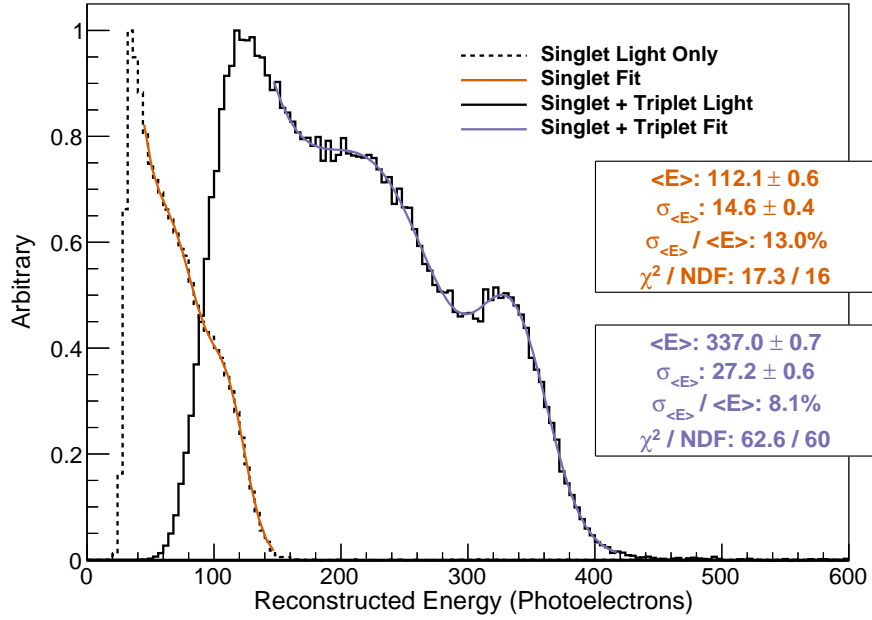


Figure 5.6: Reconstructed ^{137}Cs energy spectrum. The photopeak at ~ 335 photoelectrons corresponds to a detected photon yield of 0.55 photoelectrons/keVee. The importance of including the triplet light in the energy reconstruction is evident as it increases the energy resolution at the photopeak by a factor of two. Incorporating the quenching factor for nuclear recoils (see Sec. 4.3.2), gives an energy threshold for CEvNS events of ~ 80 keVnr.

5.5 ENERGY CALIBRATION

Every week during the Engineering Run, calibration data was taken with a ^{137}Cs source. ^{137}Cs provides a mono-energetic 662 keV gamma ray to characterize the detected photon yield and light-yield uniformity of CENNS-10. Lower energy calibration sources were considered, but there were no other readily available sources in Neutrino Alley with an activity high enough to be seen by CENNS-10.

As seen in Fig. 4.6, calibration runs were taken with an internal trigger based on the OR of either PMT with an ADC threshold of roughly 10 photoelectrons. Lower thresholds were attempted, but dead time issues due to the data throughput complicated the interpretation of those datasets.

Five minute runs were taken with the ^{137}Cs source at three points: near the center of the detector and at ± 17.8 cm to characterize the z-dependence of the light yield. A one-off ‘z-scan’ with smaller ~ 2.5 cm steps was taken once to help tune the CENNS-10 Monte Carlo optical properties.

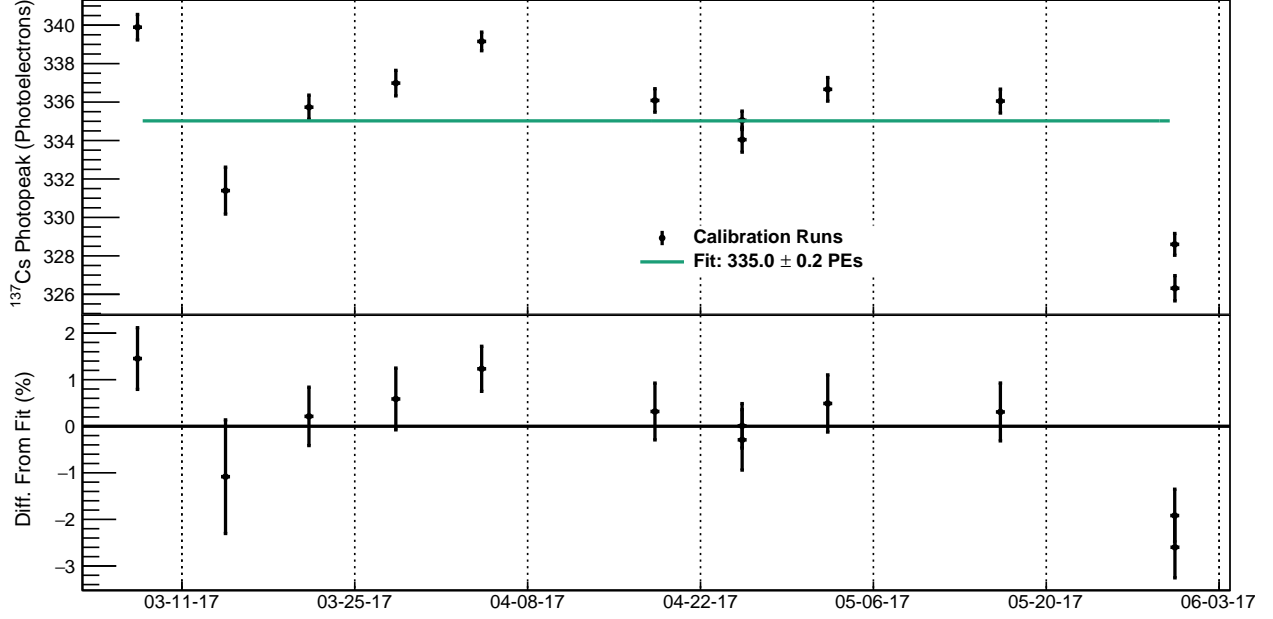


Figure 5.7: Monitoring the ^{137}Cs photopeak stability over the run. The photopeak was stable to within $\pm 2\%$ over the course of the run. Error bars shown are the errors on the mean of a gaussian fit to the photopeak.

In addition, a ten minute source-less calibration dataset was taken at the beginning and end of each calibration run to be used for background subtraction.

The photopeak at 662 keV from ^{137}Cs datasets was used to characterize the detected photon yield. An effective fiducial-volume cut was imposed to only select events happening near the center of the detector by requiring the fraction of light seen by the top PMT to be from (40-60) % in a given event. A fit to the ^{137}Cs photopeak from a typical calibration run can be seen in Fig. 5.6.

The light output of CENNS-10 was monitored throughout the run by taking calibration datasets every week. As seen in Fig. 5.7, the light yield was constant to within $\pm 2\%$ over the course of the run.

The light uniformity of the detector response as a function of position was examined with the combination of two different methods: (1) changing the location of the calibration source and (2) changing the cut on the fraction of light seen by the top PMT. Method 1 by itself was not adequate to localize events in the detector as there was no collimation of the source. Nevertheless, moving the source can give some insight into the height-dependence of the detector response. As seen in

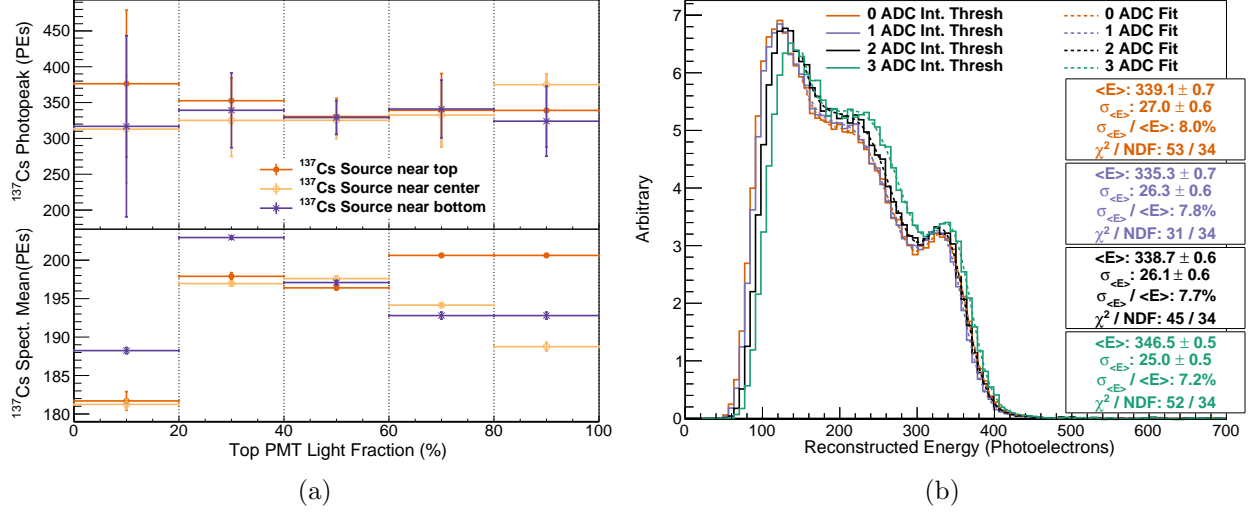


Figure 5.8: (a) The ^{137}Cs photopeak as a function of position in the detector. Cutting on the fraction of light seen by the top PMT is an effective fiducial-volume cut with fractions near 100 % selecting events near the top of the detector. Changing marker style and color corresponds to changing the calibration source location. The detected photon yield is seen to be independent of location in CENNS-10 (to within 7 %) (b) ^{137}Cs photopeak as a function of the threshold placed on the integration of the triplet light. The peak location is relatively unaffected by the threshold, although the resolution improves with larger thresholds. An integration threshold of 2 ADCs was used for the Engineering Run analysis.

Fig. 5.8a, the response is fairly independent of the interaction location in the detector.

The light yield for the Engineering Run was (0.55 ± 0.05) photoelectrons/keVee and is relatively unaffected by the triplet-light integration threshold. As summarized in Tab. 5.2, the uncertainty is driven by the slight non-uniformity of the detector response (7 %) with contributions from effects due to the integration threshold (2 % seen in Fig. 5.8b), the movement of the photopeak during the run (2 %), and the uncertainty on the SPE response (5 %). The threshold for a CEvNS search with this detected photon yield, assuming a quenching factor of 28.9 % (Sec. 4.3.2), is ~ 80 keVnr.

5.6 PULSE SHAPE DISCRIMINATION

As discussed in Sec. 4.3, the properties of liquid argon scintillation light provide pulse-shape discrimination (PSD) capabilities. The typical parameter used for PSD in liquid argon is F_{90} which is defined as the fraction of the total light that arrives in the first 90 ns. With the pulse-fitting procedure used here however, a slightly different PSD parameter is used. F_{prompt} is defined as the

	Value	Uncertainty (%)
Detected Photon Yield	0.55 PEs/keVee	9 %
Light Yield Uniformity		7 %
Single PE Response		5 %
Integration Threshold		2 %
Stability in Time		2 %
Photopeak		0.1 %

Table 5.2: Detected photon yield calculation. Sources of uncertainty are discussed in more detail in Sec. 5.5.

ratio of the amount of light in the singlet (given by the sum of the SPE template scale factors S) and the total amount of light (sum of the SPE template scale factors and triplet integrals T):

$$F_{prompt} = \frac{\sum_{chans} S}{\sum_{chans} (S + T)}. \quad (5.4)$$

The monthly ^{252}Cf datasets were used to characterize the pulse-shape response of CENNS-10. When considering events in reconstructed PSD space (Fig. 5.9), the importance of the integration threshold on the triplet light becomes clear. With no threshold, the distribution of low energy nuclear recoil events is a ‘blob’ in PSD space. Placing a threshold on the integration removes much of the baseline noise from the integration and minimizes the effect from any imperfections in the modeled shape of the SPE template tail. This both improves the effectiveness of PSD cuts in separating electronic and nuclear recoil events, as well as simplifies the modeling of nuclear recoil events in Monte Carlo simulations.

5.7 CENNS-10 SIMULATIONS

To fully understand and characterize the particle interactions in the CENNS-10 detector, a **Geant4** [46, 47] optical simulation was developed [119]. All simulations run used **Geant4** version geant4-10-02-p02. Details of the physics settings can be found in [119].

The **Geant4** simulation outputs a vector of photon hit times for each PMT, as well as truth

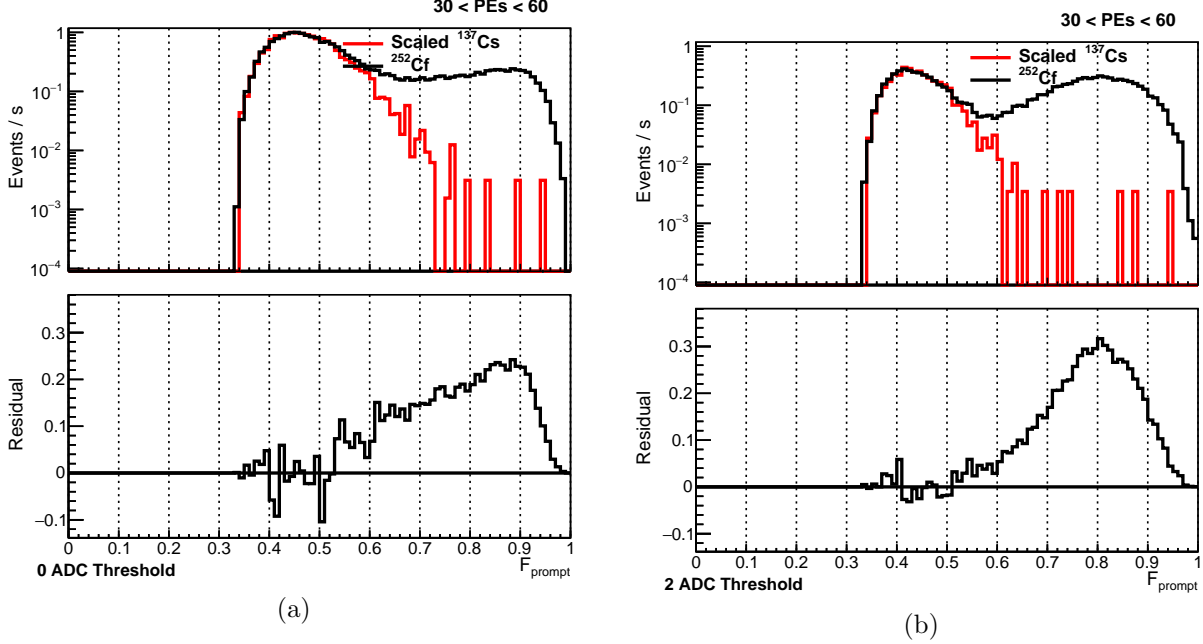


Figure 5.9: Low energy nuclear recoil pulse-shape distributions without (a) and with (b) a threshold in the triplet-light integration. The introduction of the threshold is seen to clean up the reconstructed pulse shape considerably, improving pulse shape discrimination between electronic and nuclear recoils as well as simplifying the pulse shape modeling in Monte Carlo simulations.

information about energy deposition, particle type etc.

5.7.1 GEOMETRY

As seen in Fig. 5.10, the full CENNS-10 detector geometry is modeled in the simulation. CENNS-10 is represented as a cylinder of liquid argon. The fiducial volume is defined by a TPB-coated acrylic cylinder 42.5 cm tall and 24.8 cm wide. **Geant4** can only handle wavelength shifting in bulk materials, so the TPB coatings are represented as 2 μm thick coatings on the acrylic. To handle the wavelength shifting within the TPB, 100 % of incident VUV light is transmitted and then wavelength shifted in the bulk.

The shielding geometry (not pictured in Fig. 5.10) is modeled as a cylinder of water surrounding the vacuum vessel with a thickness of 20.3 cm and a copper box outside the water with a thickness of 1.3 cm. The shielding can be turned on or off depending on the situation being simulated.

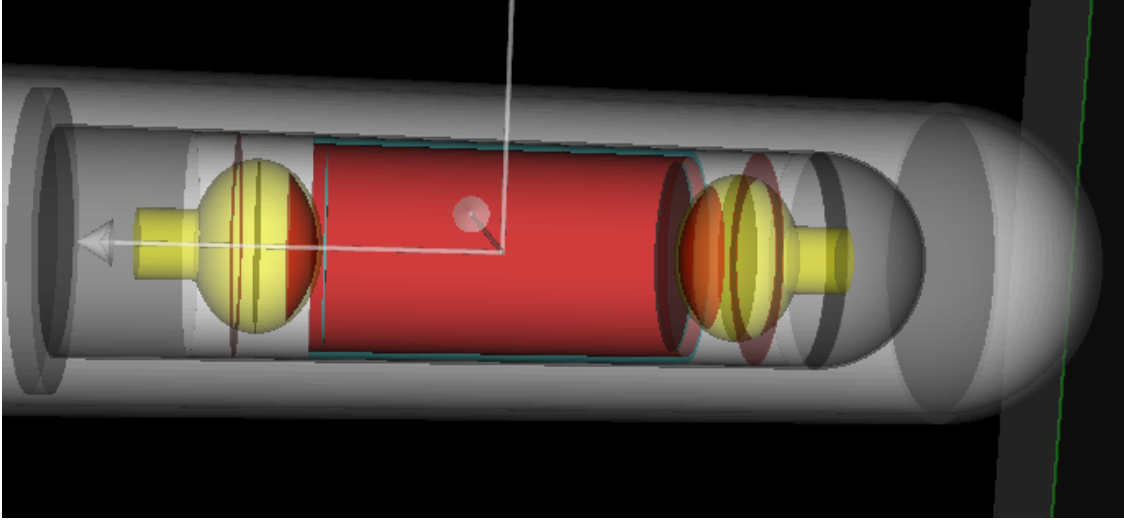


Figure 5.10: CENNS-10 **Geant4** simulation detector geometry. Visible are the vacuum vessel (outer gray vessel), cryostat (inner gray vessel), photomultiplier tubes (yellow), TPB-coated acrylic cylinder (red) and Teflon reflector (white). The rest of the volume in the cryostat is filled with liquid argon.

5.7.2 SIMULATION TUNING

A chain of parameter tuning is required to make the simulation results match the calibration data. The tuning required can roughly be broken down into three areas: effective photon yield, light detection z-dependence, and pulse-shape discrimination.

EFFECTIVE PHOTON YIELD

The liquid argon volume scintillation properties can be defined separately depending on the interacting particle and are summarized in Tab. D.01. To minimize computation time, photons are thrown away at the generation step rather than when they reach a PMT. Therefore an ‘effective scintillation yield’ of $6\gamma/\text{keV}$ is defined that is the product of the expected scintillation yield, the PMT quantum efficiency, and the expected TPB wavelength-shifting efficiency. This yield was tuned to match the photopeak of a simulated ^{137}Cs source with that seen in calibration data (Fig. 5.11).

At low energies, electron quenching is handled by Birks’ law [85]. Quenching of nuclear recoil events on the other hand is handled by a separate quenching factor (see Sec. 4.3.2).

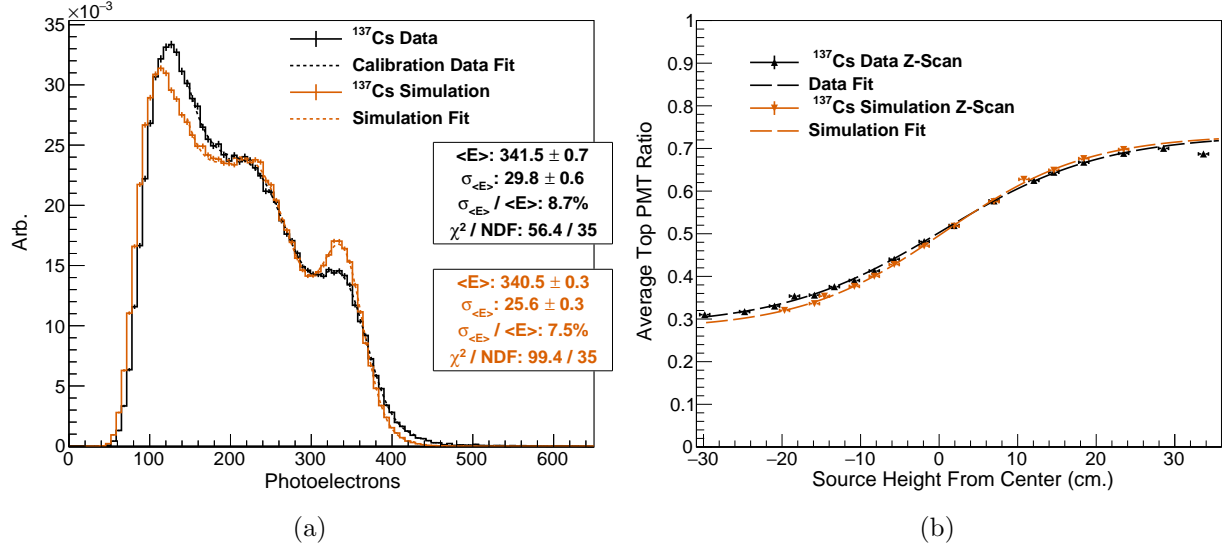


Figure 5.11: Tuning the CENNS-10 **Geant4** simulation optical properties. (a) Tuning the simulation photon yield to match the ^{137}Cs calibration data photopeak. The ^{137}Cs photopeaks match up quite well. There are some minor shape differences due to, e.g., small pileup contamination remaining in the calibration dataset. (b) Tuning the z-dependence of the detector response. Shown here is the average fraction of light for all events seen by the top PMT as a function of ^{137}Cs calibration source location. The MC response is seen to reproduce the data response after introducing reflections from the side TPB coatings.

LIGHT DETECTION Z-DEPENDENCE

Tuning of some optical properties is required to match calibration data. These properties are applied to the handling of ‘optical photons’ in **Geant4**. Optical photons are used when the wavelength of the photon is \gg the atomic spacing. Within the simulation, material-dependent optical properties are defined. These properties are energy-dependent and can be applied to both bulk and surface materials.

Relevant properties can be seen in Fig. 5.12 (surface absorption, transmission, and reflection and bulk absorption) and the tuned surface property parameters are summarized in Tab. D.02. In the simulation, all optical surfaces are assumed to be dielectric_dielectric with a ground finish and the surface model used is the unified model. To tune these properties, the average fraction of light seen by the top PMT was considered as a function of the ^{137}Cs calibration source height as seen in Fig. 5.11. The implementation of 95% reflectivity of visible light from the side TPB cylinder

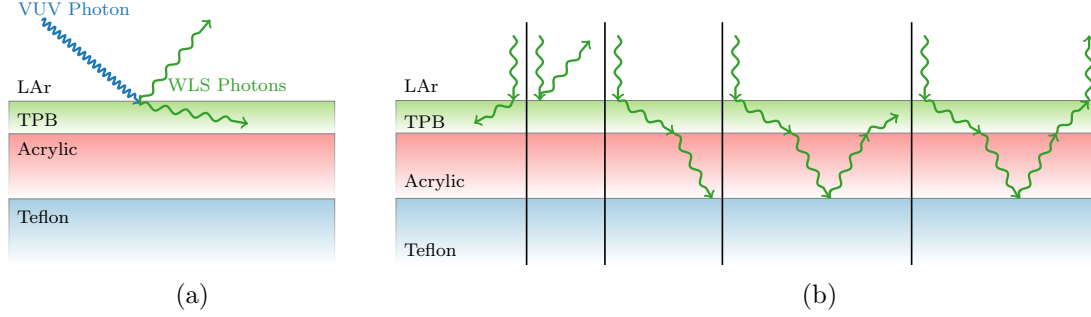


Figure 5.12: Relevant surface optical properties in the CENNS-10 simulation. (a) Wavelength shifting of VUV photons in CENNS-10 **Geant4** simulation. Any VUV photon incident on the TPB layer is immediately absorbed and re-emitted in 4π with a wavelength sampled from the TPB emission spectrum. (b) Relevant optical properties, both surface and bulk, for visible photons to tune in the CENNS-10 **Geant4** simulation to match calibration data include transmission, reflection, and absorption.

surface was used to match the ^{137}Cs calibration data behavior.

PULSE SHAPE DISCRIMINATION

Finally, the pulse shape behavior in the simulation is tuned to match the behavior of ^{137}Cs and ^{252}Cf calibration data (for ER and NR events respectively). This is implemented by changing the YIELDFACTOR for the fast and slow scintillation components of the liquid argon scintillation process. An energy-independent YIELDFACTOR was found to be sufficient to replicate the ER PSD behavior in CENNS-10 as seen in Fig. 5.13a.

For NR events, an energy-dependent PSD behavior was observed in calibration data which needs to be reproduced in the **Geant4** simulations. In simulations of ^{40}Ar recoils (used for CEvNS predictions) the YIELDFACTOR can be made energy-dependent by splitting up the simulated energy range into energy slices, each with its own singlet:triplet ratio as seen in Fig. 5.13b. For neutron simulations on the other hand, the YIELDFACTOR is treated as energy-independent within the **Geant4** simulation with the setting taken from the 50 keV setting for tuned ^{40}Ar simulations. The NR PSD band can then be made energy-dependent in post-processing to match calibration data, although this correction was not implemented until the full-shielded beam analysis.

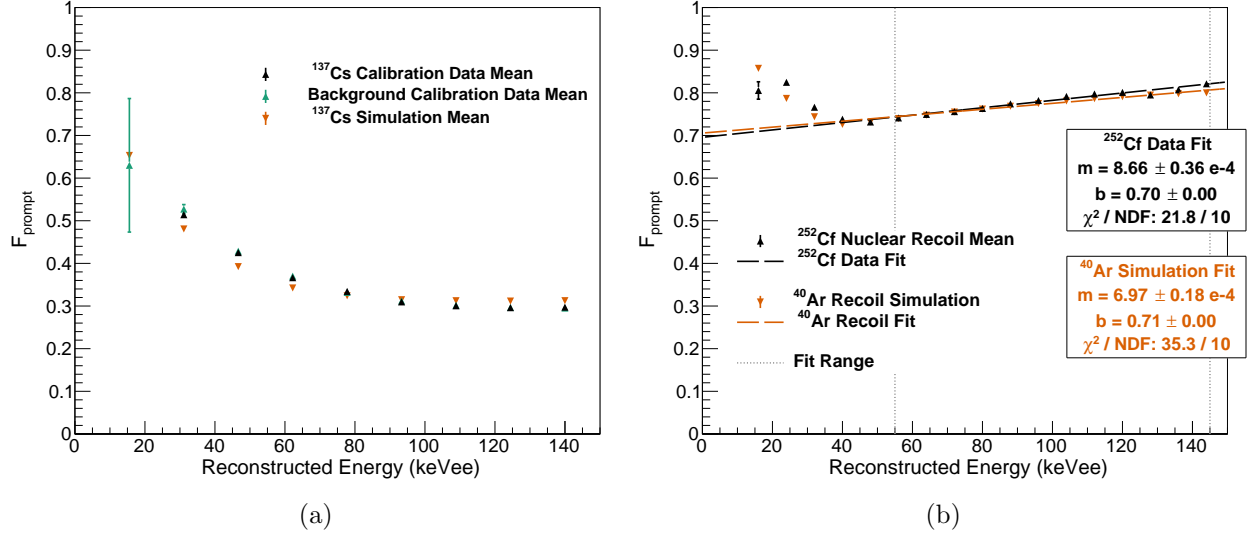


Figure 5.13: Tuning CENNS-10 **Geant4** pulse shape behavior to match calibration data. (a) Comparison of ^{137}Cs and background calibration data to a ^{137}Cs simulation. For ER events, an energy-independent singlet:triplet ratio matches the data well. (b) Comparison of ^{252}Cf data to simulations of ^{40}Ar recoils. For nuclear recoil events at lower energies, an energy-dependent singlet:triplet ratio is required.

5.7.3 DETECTOR SIMULATION

Some elements of detector simulations are easier to handle outside of the **Geant4** framework. For this reason, a separate detector simulation step was implemented to perform some post-processing of the **Geant4** simulation output. In particular, integer number of photons detected in the **Geant4** simulation were smeared with photomultiplier tube dependent smearing factors to match the single photoelectron response seen in the data.

In addition, the quenching factor applied to nuclear recoil events was finalized at this stage to make investigations of the effect from the quenching factor on predicted spectra more easily performed.

5.7.4 BEAM-UNRELATED BACKGROUND SIMULATIONS

While these simulations were not used in any beam analysis (these background sources were well measured by CENNS-10), the expected beam-unrelated background (BUB) sources were simulated to verify there were no unexpected background sources in Neutrino Alley. The sources simulated

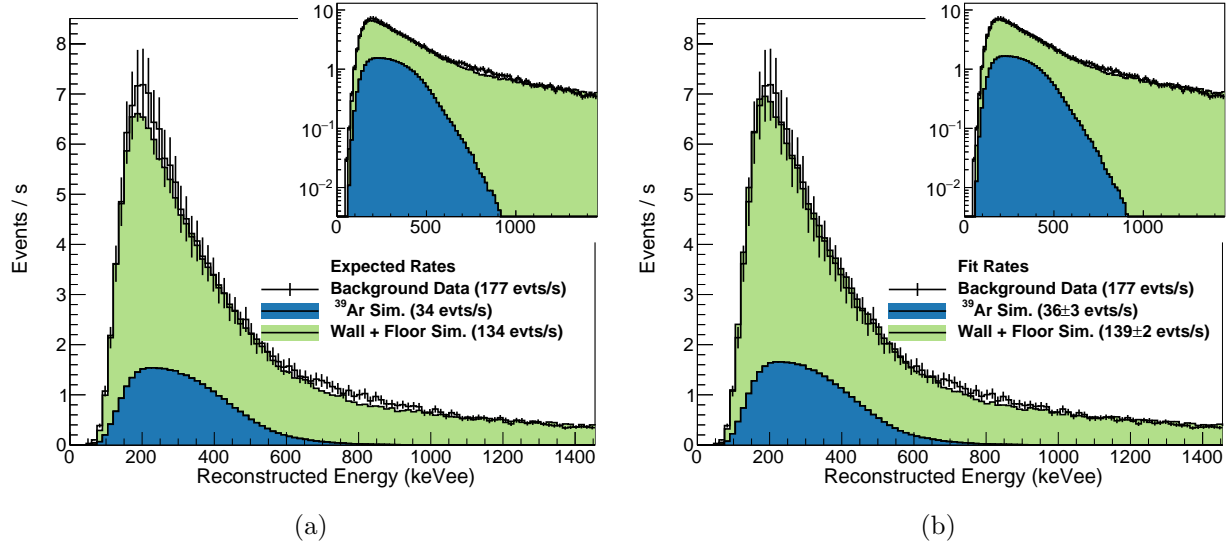


Figure 5.14: Comparison of measured beam-off backgrounds taken from calibration datasets to Monte Carlo predicted rates. (a) Expected rates based on prior measurements made in Neutrino Alley (see Sec. 3.1) and (b) A fit allowing the normalization of the background sources to float independently.

are the same as discussed in Sec. 3.1. These beam-unrelated backgrounds can be separated into two categories: beam-off and beam-on. To remove the effects from pileup due to high rates, only the full-shielded configuration (water + copper installed) was simulated.

BEAM-OFF BEAM-UNRELATED BACKGROUNDS

Beam-off beam-unrelated backgrounds are backgrounds present even when the SNS is not running. The dominant backgrounds are due to ³⁹Ar and the concrete making up Neutrino Alley.

These backgrounds were simulated with the CENNS-10 **Geant4** simulation, and a predicted spectrum was made based upon the expected rate of each source. ³⁹Ar was simulated throughout the liquid argon volume in the simulation. The wall and floor gammas were generated uniformly from planar sources. The floor gammas were generated just below the Pb shielding from a (2 × 2) m² source. The wall gammas were also generated from a planar source perpendicular to side of the Cu shielding, again from a (2 × 2) m² source, 0.6 m from the center of the detector.

A comparison of the expected rates in CENNS-10 to the measured rates taken from a back-

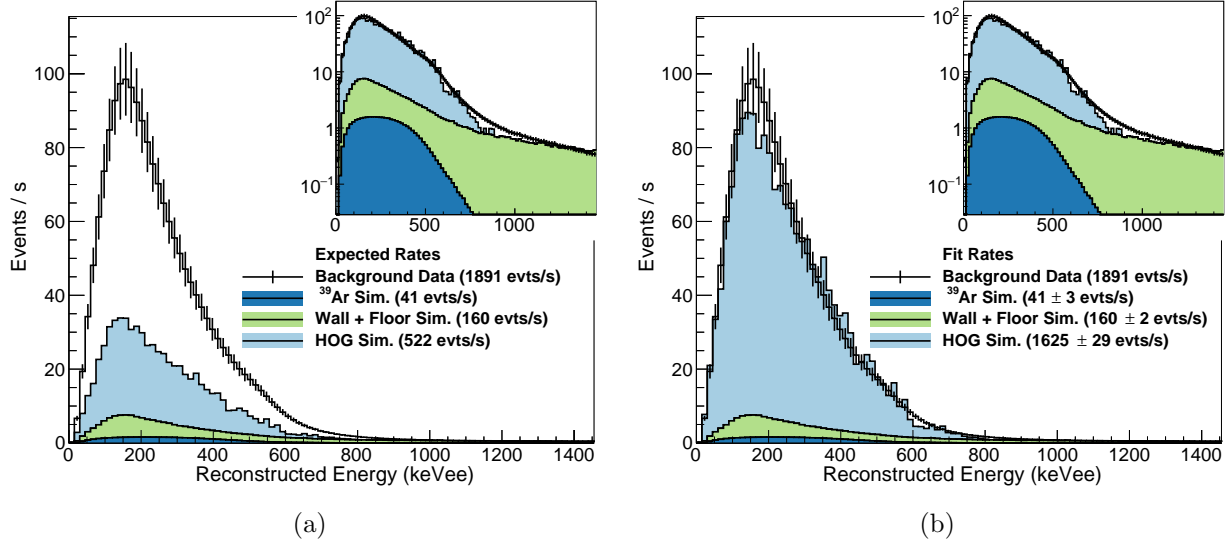


Figure 5.15: Comparison of measured beam-unrelated backgrounds while the beam is running to Monte Carlo predicted rates. The contribution of the HOG is significant. (a) Expected rates based on prior measurements made in Neutrino Alley (see Sec. 3.1). At first look the predicted HOG rate appears low, but the expected rate came from a single measurement. The rate is known to vary in time by up to a factor of ~ 3 (Fig 3.1). (b) A fit fixing the ^{39}Ar and Wall+Floor rates to those found in Fig 5.14. The rates appear different due to different thresholds.

ground calibration dataset can be seen in Fig. 5.14. The expected rates are almost exactly what is observed. This gives us confidence that the Monte Carlo is accurately representing the interactions in the radiation shielding. The generated background spectra can also be fit to the measured data by allowing the normalizations to float individually, and with the introduction of an energy scaling factor. The observed rates are found to agree with the expected ones to within 9%, and the best fit modification to the energy scaling is sub-1%.

BEAM-ON BEAM-UNRELATED BACKGROUNDS

When the beam is running, there is an additional contribution to the beam-unrelated backgrounds from the HOG (Sec. 3.1.1). The HOG was simulated as a uniform cylindrical source ($r = 0.05$ m, $l = 2$ m) roughly 2.5 m from the detector center.

Using the measured flux discussed in Sec. 3.1, and the simulation of the HOG, the expected event rate due to the 511 keV gamma rays can be found as seen in Fig. 5.15. At first glance, the

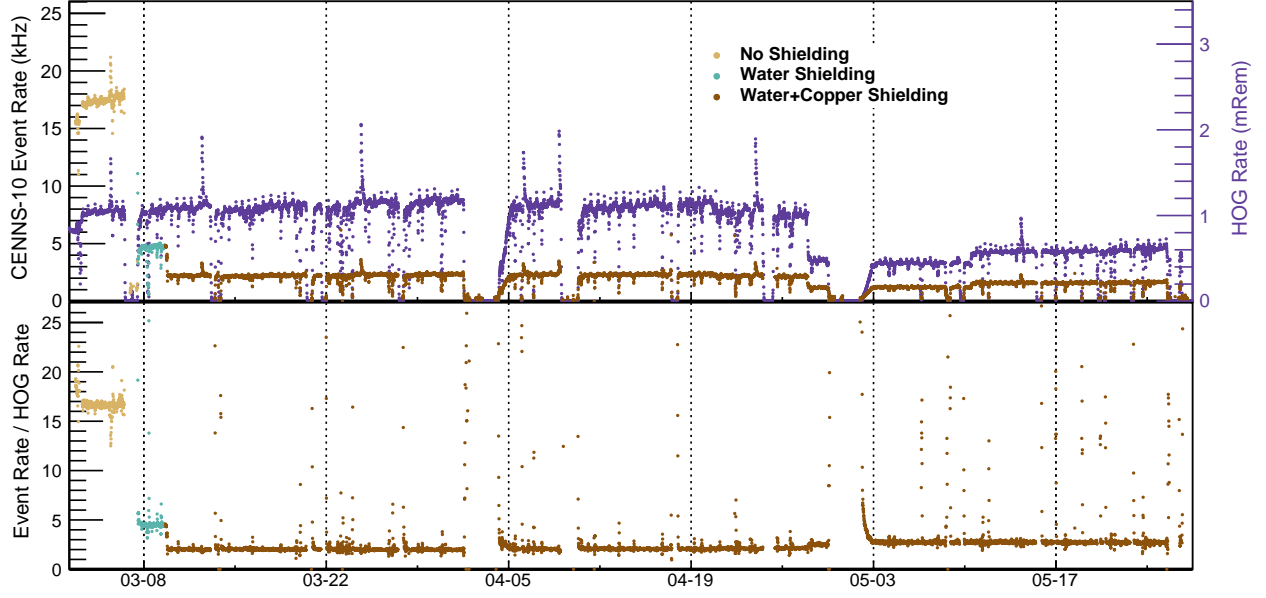


Figure 5.16: Comparison of the measured CENNS-10 event rates with the HOG rate. The HOG activity is measured by the SNS with dosimeters, and logged every second. Top panel shows how the event rates change with the addition of shielding. Bottom panel shows the ratio of the measured event rate to the HOG rate. CENNS-10 event rates are seen to be correlated with the 511 rates from the HOG pipe running down Neutrino Alley. No PSD cuts are applied.

simulation seems to severely under-predict the event rate due to the hot off-gas. However, recall that the HOG measurement was taken on a single day in 2014, and the HOG rate can change by a factor for ~ 3 . The measured rate in Fig. 5.15 on the other hand is the average rate for the entire Engineering Run.

The average event rate due to the HOG can be found by allowing the HOG rate to float (and holding the ^{39}Ar and wall+floor rates constant). This gives an event rate of (1585 ± 27) Hz BEFORE any pulse shape discrimination cut. The event rate in CENNS-10 when the beam is on seems to be driven by the 511 rate from the HOG, and that is indeed what is observed in Fig. 5.16, demonstrating the importance of the additional Pb shielding installed for the Production Run over the Summer of 2017.

5.7.5 BEAM-RELATED NEUTRON SIMULATIONS

Simulations of beam-related neutrons (BRNs) were performed for both the no-shielding configu-

ration as well as the full-shielded (water+copper) configuration of the Engineering Run. In these simulations, 2×10^7 neutrons were generated from (0-300) MeV from a (2×2) m planar source 0.6 m from the detector with a cosine angular distribution. An energy-independent quenching factor with a central value of 28.9% was assumed, along with systematic excursions using the $\pm 1\sigma$ from the energy independent fit in Sec. 4.3.2.

Energy deposit by MeV-scale neutrons is not strongly correlated with the incident neutron energy making it difficult to apply the correct singlet:triplet ratio event-by-event in the **Geant4** simulation. Therefore an energy-independent PSD setting was used in the **Geant4** simulation that is corrected in post-processing. The correction consists of a re-weighting depending on the reconstructed energy of nuclear recoil events to match the tuning to ^{252}Cf calibration data.

These simulations were then re-weighted to the measured SciBath flux to form a predicted beam-related neutron rate. From (5-30) MeV, the weights used came from the SciBath measurement. Above 30 MeV the one-sigma limit on the high energy flux measured by SciBath was assumed, and the flux from (0-5) MeV came from a linear fit to the SciBath measurement from (5-30) MeV and extrapolating to 0 MeV. An additional weighting factor of ~ 2.1 is required to convert the SciBath flux (which assumed an inward spherical flux) to that simulated for CENNS-10 (a plane looks roughly like half a sphere with some small geometric corrections needed).

The no-shielding dataset was used to find a scaling to apply to future beam-related neutron predictions in CENNS-10 based on the SciBath measurement to account for differences in location and beam energy between runs.

5.7.6 CEVNS SIMULATION

To form a CEvNS prediction, 4×10^6 ^{40}Ar recoils were simulated uniformly throughout the detector volume from (0-128) keV. These simulations were separated into 32 keV energy slices to follow the measured F_{prompt} curve from ^{252}Cf calibration data (Fig. 5.13). Again, an energy-independent quenching factor was assumed, with central value of 28.9% with systematic excursions using the

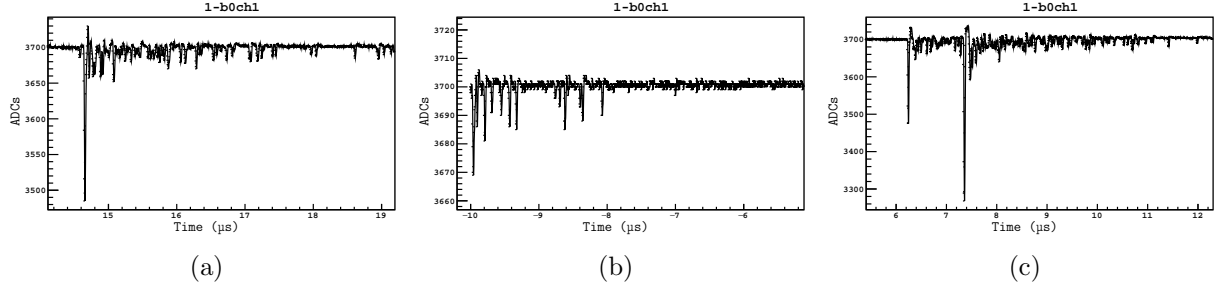


Figure 5.17: Example events failing quality cuts. (a) ‘Bad Baseline’ cut removes events with a large variance on the mean baseline value right before the singlet peak. (b) Typically events failing the ‘Successful Fit’ cut occurred too close to the waveform start to calculate an average baseline and have already failed the baseline cut. (c) The ‘Bad Peak’ cut removes pileup by cutting events where the minimum ADC value does not occur during the singlet peak.

$\pm 1\sigma$ from the energy independent fit in Sec. 4.3.2. These simulations were then re-weighted to the expected nuclear recoil spectra for each neutrino species (ν_μ , ν_e , $\bar{\nu}_\mu$) to form CEvNS predictions.

5.8 EFFICIENCIES

An energy-dependent efficiency loss due to the event building threshold (2 PE coincidence in the singlet as discussed in Sec. 5.1.2) can be accurately modeled in the CENNS-10 `Geant4` simulation by requiring > 2 PE in each PMT during a 90 ns window at the start of an event.

However, there are some inefficiencies in the data that are not modeled in the Monte Carlo and need to be evaluated with beam-off data and folded-in with the Monte Carlo predictions. These efficiency losses can be split into two categories: data quality cuts and losses due to PMT dark rates.

5.8.1 DATA QUALITY CUTS

Quality cuts are applied to the data to ensure only ‘good’ waveforms and events are included in the analysis.

WAVEFORM QUALITY CUTS These cuts are applied to individual PMT waveforms and reject entire DAQ triggers. They consist of the requirement that a valid baseline is found at

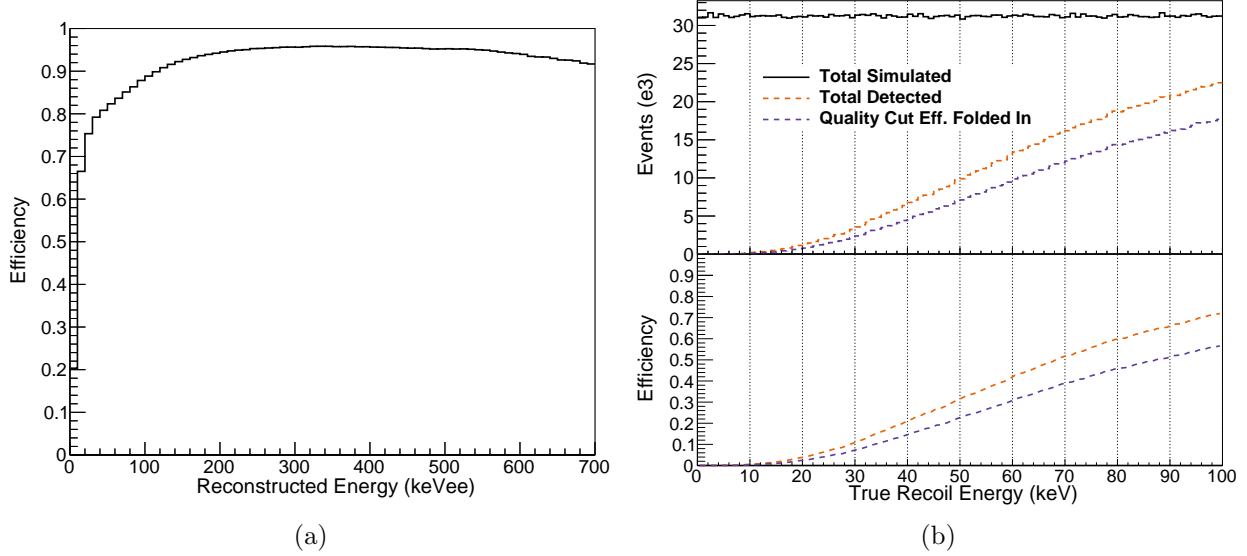


Figure 5.18: Energy-dependent event detection efficiency. (a) Efficiency loss due to quality cuts in the data. These are not included in the CENNS-10 simulation and are calculated with the use of beam-off data. The efficiency is defined as the fraction of identified events passing the cut. (b) Efficiency for nuclear-recoil events to pass event-building cuts. This efficiency is evaluated in the CENNS-10 *Geant4* simulation. Events are required to have > 2 PEs in the singlet on both PMT channels. The red curve shows the total events passing the 2 PE threshold cut. In blue shows the effect of folding in the efficiency curve shown in (a).

the beginning of the window (required for pulse finding), that no PMT channel was saturated throughout the waveform, and that the trigger occurred after the first second but before the last second of the run (to ensure, e.g., that no digitizer registers were in the process of being written). For beam data, an additional cut that there were fewer than 3 PMT coincidences within a given DAQ window was imposed to help remove any effects from pileup contamination on PSD reconstruction. The efficiency loss from these waveform cuts ranges from 7% for the no-shielding dataset to sub-1% after the water and copper shielding was installed.

EVENT QUALITY CUTS After events were identified, various quality cuts were imposed to ensure the event analysis and reconstruction was accurate. The first requirement was that a valid baseline was found before the singlet pulse with a variance of < 3 ADCs. This ‘Good Baseline’ cut was necessary to ensure an accurate pulse fit to the singlet peak. The next requirement was that a successful parabola fit was made to the singlet peak. Again, this was required to ensure

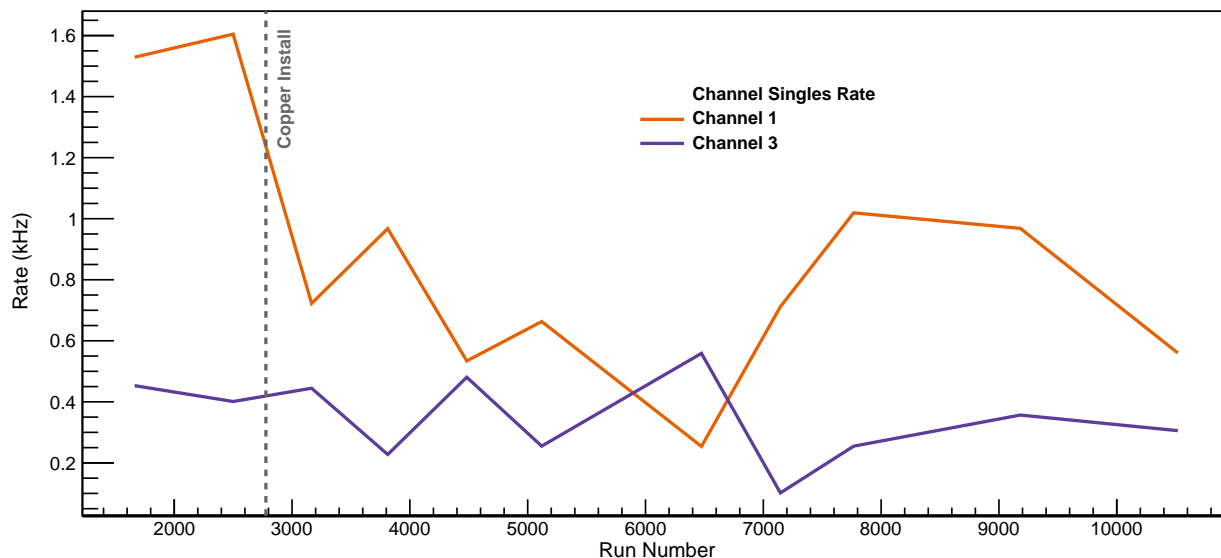


Figure 5.19: PMT singles rate throughout the run. Rates were monitored to evaluate an efficiency loss due to PMT dark noise. LED calibration runs were used to evaluate the pulse rate above the pulse-finding threshold of each PMT independent of the other PMT.

an accurate measurement of the singlet peak height was made. A hard 2 PE threshold was then imposed for each channel.

To minimize pileup effects, a ‘Bad Peak’ cut which required the minimum ADC value for a given event occurred during the singlet was included. Finally, a ‘Pre Trace’ cut which required that the previous event occurred $> 7 \mu\text{s}$ before was imposed to minimize contamination from triplet light due to an earlier event. Example waveforms that failed these cuts can be found in Fig. 5.17. The overall efficiency loss from these cuts is summarized in Table 5.3, and the energy dependence can be seen in Fig. 5.18. The apparent efficiency hit at high energy is largely due to the pile-up cut, and does not have a large effect on the beam-data analysis. Note that no efficiency loss due to PSD cuts is shown here.

5.8.2 DARK RATE INEFFICIENCIES

Due to the way the pulse finding algorithm works (Sec. 5.1.2), there is a potential for dark noise, or a low energy signal only seen by a single PMT, to introduce a $6 \mu\text{s}$ dead time. The PMT dark

	Waveform Quality	Dark Rate	Good Baseline	Successful Parabola Fit	Bad Peak	Pre Trace
Efficiency	> 99 %	97 %	> 99 %	> 99 %	95 %	95 %

Table 5.3: Event efficiencies not included in the CENNS-10 **Geant4** simulation. These are folded in when making event rate predictions. With the exception of the waveform quality and dark rate cuts, all of the above cuts are energy dependent. The values listed above are the fraction of ALL events that pass the respective cut. Energy-dependent efficiencies can be seen in Fig. 5.18. Cuts are discussed in more detail in the text.

rate could also potentially cause an actual event to fail a PSD cut during the beam analysis. Note that this effect will be largest for low energy events (with small numbers of photoelectrons).

To quantify the efficiency loss due to low-energy signals only seen by a single PMT (or due to the PMT dark rate), the ‘singles rate’ of each PMT, that is the pulse rate above the pulse finding threshold (20 ADCs) INDEPENDENT of the other PMT, was monitored from LED calibration datasets (from time windows when the LED was not flashing). From this rate, the probability that either PMT could have a random pulse within a $6\text{ }\mu\text{s}$ window was calculated to be 0.9 %.

For the possibility that pileup will cause an event to fail a PSD cut, the sum of the PMT singles rates (in Fig. 5.19) and the coincidence rate (taken from beam-off triggers during beam running) can give the probability that either case can happen during an actual event. This rate is 3 kHz giving a probability of either a PMT dark pulse OR an event in a $6\text{ }\mu\text{s}$ window of 2 %. This is a conservative estimate and assumes that anytime there is a dark pulse or event in the tail of an earlier event it will cause the event to fail a PSD cut. This gives a conservative measure of the efficiency loss of 3 %.

The efficiency curve of CENNS-10 is summarized in Table 5.3 and Fig. 5.18. These efficiencies are folded into the Monte Carlo predictions of the expected beam signals.

CHAPTER 6

CENNS-10 SHIELDING STUDIES

CENNS-10 originally ran in Neutrino Alley with no neutron shielding installed to verify the beam-related neutron rate measured by SciBath (Sec. 3.3). This no-shielding run was used to constrain beam-related neutron (BRN) predictions for the full-shielded CEvNS analysis. Comparison of the BRN prediction with the observed rate in CENNS-10 supplies a scale factor to apply to future BRN predictions in CENNS-10 to account for differences of location and beam energy between the SciBath and CENNS-10 runs and possible neutron interaction rate differences between the Monte Carlo predictions and data.

6.1 RUN SUMMARY

The no-shielding run is summarized in Table 4.1. CENNS-10 ran with no shielding for two weeks and amassed a total of 0.24 GWhr of beam. Protons were delivered on target with an energy of 973 MeV.

The no-shielding run beam-trigger setup is discussed in more detail in Sec. 4.4.1. The specific waveform time regions (relative to protons-on-target) for the no-shielding dataset are summarized in Table 6.1. Because the expected CEvNS rate in the no-shielding run was expected to be small (< 1 event even with no PSD cut), both the pre-beam and delayed windows were used to verify the validity of the background subtraction.

	Pre-Beam	Prompt	Delayed
Time Window	$(-6.5-0.5) \mu\text{s}$	$(0.5-1.5) \mu\text{s}$	$(1.5-8.5) \mu\text{s}$

Table 6.1: Timing regions used for no-shielding beam analysis. Times are relative to beam-on-target as marked by the SNS Event 39 timing signal. For strobe triggers the ‘beam’ time is marked by the Event 39 time within the previous beam trigger.

6.2 PSD CUT OPTIMIZATION

Liquid argon provides the opportunity to separate electronic and nuclear-recoil events through the use of pulse-shape discrimination (Sec. 4.3). An energy-dependent pulse-shape discrimination (PSD) cut based on F_{prompt} (Sec. 5.6) was found to minimize the fractional error on the background subtraction. In the case of the no-shielding analysis, a 1:1 background subtraction was performed. I.e. the beam-unrelated background (BUB) measurement came from the same time region in strobe triggers that the beam-related measurement came from in the beam triggers. In the full-shielded analysis, the BUB measurement came from a larger strobe window to minimize the statistical uncertainty of the BUB spectrum.

6.2.1 FIGURE OF MERIT

The fractional error on the background subtraction was minimized to find an optimal PSD cut for beam data. In other words, the figure of merit $\mathcal{F} \equiv \frac{N_{sig}}{\sigma_{sig}}$ was maximized. Here, N_{sig} is the number of signal events, and σ_{sig} is the error on the number of signal events.

To maximize \mathcal{F} , the error on the number of signal events needs to be known. The first thing to note is that the number of beam events measured (N_{Beam}) is a combination of both the desired signal events, as well as contamination from BUB events (N_{BUB}). Therefore any background events need to be subtracted out.

$$N_{sig} = N_{Beam} - N_{BUB} \tag{6.1}$$

Note that with strobe data, the statistical fluctuations on the beam-unrelated background rate

can be reduced by considering a larger time window than for beam data. If this larger dataset is used, $N_{BUB} \equiv f N_{Strobe}$ where $f = 1$ if the time considered from beam data and BUB data is equal. The statistical error on N_{sig} follows from simple propagation of errors:

$$\begin{aligned}
\sigma_{sig}^2 &= \sigma_{Beam}^2 + \sigma_{BUB}^2 \\
&= N_{Beam} + f^2 N_{Strobe} \\
&= N_{Beam} + f N_{BUB}
\end{aligned} \tag{6.2}$$

Eq. 6.1 can be used to replace N_{Beam} in Eq. 6.2:

$$\begin{aligned}
\sigma_{sig}^2 &= N_{sig} + N_{BUB} + f N_{BUB} \\
&= N_{sig} + (1 + f) N_{BUB}
\end{aligned} \tag{6.3}$$

Therefore, the quantity to maximize is

$$\mathcal{F} \equiv \frac{N_{sig}}{\sigma_{sig}} \equiv \frac{N_{sig}}{\sqrt{N_{sig} + (1 + f) N_{BUB}}} \tag{6.4}$$

Using this FOM, an optimal energy-dependent pulse shape discrimination (PSD) cut can be found.

6.2.2 BEAM-RELATED NEUTRON PREDICTIONS

The beam-related neutron prediction used the **Geant4** neutron simulation discussed in Sec. 5.7.5. To find the expected neutron rate in the no-shielding dataset, the simulation results were re-weighted to the expected incoming neutron flux as measured by SciBath (Sec. 3.3). For this re-weighting, the average beam power during the run period (0.91 MW), the total number of beam spills (4.9×10^7), and the area of the neutron generating plane (4 m^2) are needed to normalize to the expected neutron flux.

With this beam-related neutron prediction in hand, an optimal energy-dependent PSD cut can be found using the figure of merit defined in Eq. 6.4. This cut can be seen in Fig. 6.1 overlaid on both

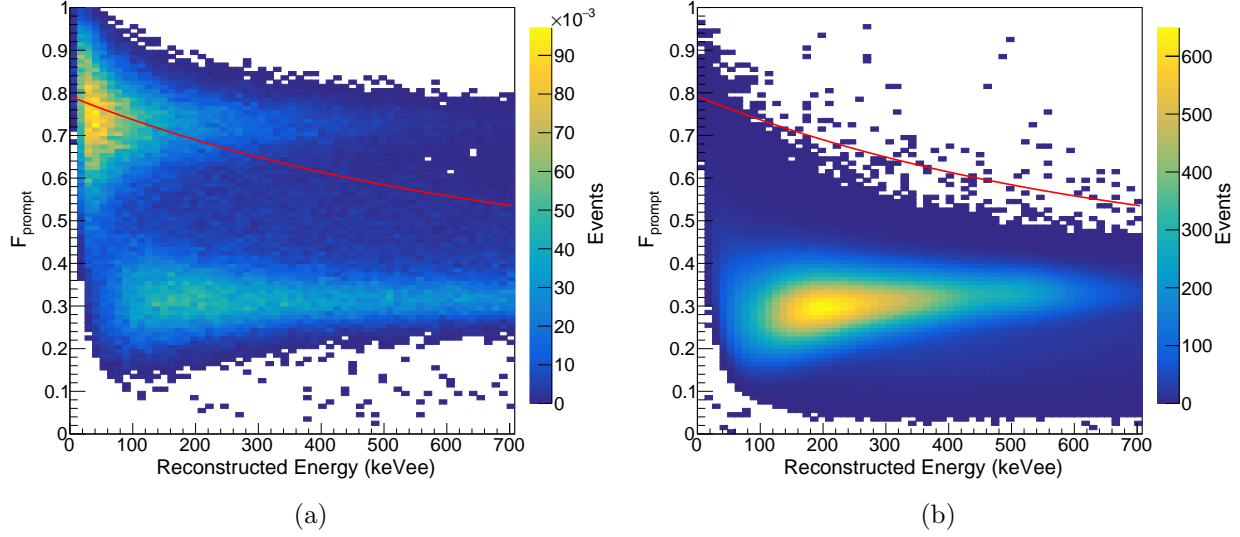


Figure 6.1: Optimized no-shielding PSD cut (red). Cut was optimized to minimize the fractional uncertainty on the beam residual. (a) Beam-related neutron prediction from `Geant4`. ER events are present due to inelastic neutron scatters in the liquid argon. (b) Distribution of beam-unrelated background events as measured with strobe triggers.

the predicted neutron signal, and the predicted BUB signal in energy:PSD space. Predictions were made both with and without the high energy neutron flux limit from the SciBath measurement, but the PSD cut was optimized assuming no high energy neutrons.

The predicted spectra both with and without a PSD cut can be seen in Fig. 6.2. The background rates are too high for any noticeable excess with no PSD cut, but there should be a beam-related neutron excess after the PSD cut is applied. The PSD cut reduces the background rate by a factor of $\mathcal{O}(5 \times 10^{-5})$. After the PSD cut, the signal:bkg should be about 1:1 with $\mathcal{O}(40)$ signal events predicted on a background of 45 events as summarized in Tab. 6.3. Note that while the rates predicted with and without the SciBath limit > 30 MeV are different, the predicted spectral shapes are quite similar. At the time of the initial no-shielding analysis, a correction for the energy-independent PSD setting in the simulation had not been developed. As the no-shielding analysis was mainly used to normalize future beam-related neutron predictions, this has a small effect on the final result. An efficiency correction due to the F_{prompt} shape was later applied to examine the effects on the predicted BRN spectrum.

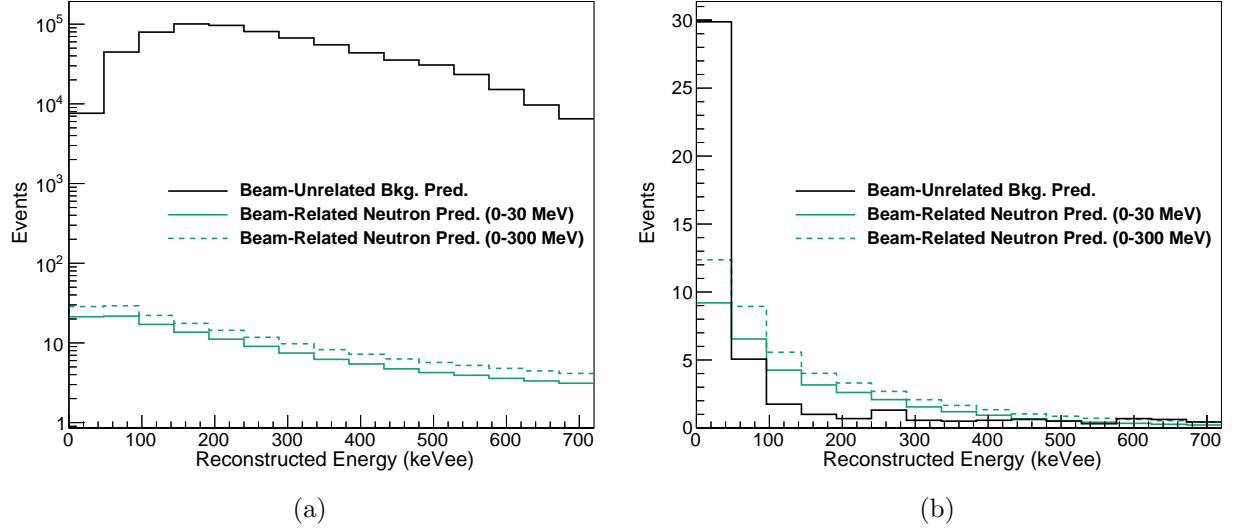


Figure 6.2: Predicted beam-unrelated background and beam-related neutron spectra for the no-shielding dataset without (a) and with (b) the signal:bkg optimized PSD cut.

6.3 PRE-BEAM AND DELAYED TIME REGIONS

The pre-beam and delayed time regions were considered first to verify the beam-unrelated rates are the same in both strobe and beam triggers. Energy spectra for the pre-beam and delayed windows were made both with and without the PSD cut shown in Fig. 6.1. While the background subtraction is quite large when no PSD cut is applied, the residuals agree with zero within two-sigma as seen in Table 6.2. The rates are greatly reduced after implementing a PSD cut, and again, the background subtraction is consistent with zero as seen in Fig. 6.3.

With this verification that the beam-unrelated background rates in the strobe and beam triggers are the same, the beam window can be investigated.

	Pre-Beam		Delayed	
	No PSD	PSD	No PSD	PSD
Strobe	4.9×10^6	259	4.9×10^6	272
Beam	4.9×10^6	304	4.9×10^6	254
Residual	-4664 ± 3135	45 ± 24	3278 ± 3131	-18 ± 23

Table 6.2: Summary of pre and post-beam event rates for the no-shielding dataset. Residuals agree with zero within two-sigma.

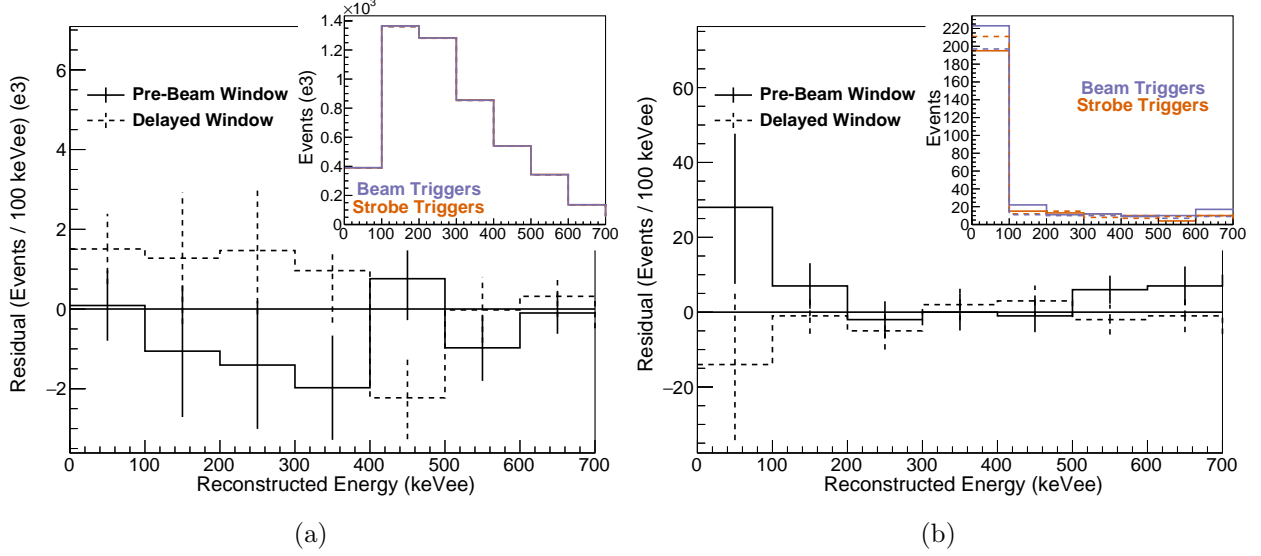


Figure 6.3: Beam residuals before and after beam on target. Solid lines correspond to the pre-beam window. Dashed lines correspond to the delayed region. Raw spectra are shown in the inlay with beam (strobe) spectra shown in blue (red). (a) No PSD cut applied. (b) Optimized PSD cut for beam-related neutron signal applied.

6.4 BEAM-RELATED NEUTRON SIGNAL

After the out-of-beam time regions were considered, the prompt $1\ \mu\text{s}$ beam window was investigated.

The observed and predicted rates are summarized in Table 6.3.

6.4.1 NO PSD CUT

As with the pre-beam and delayed windows, even making use of the beam duty factor to reduce the effect of any BUB, the event rate is too high to see any beam excess with no PSD cut. The errors on the background subtraction are $\mathcal{O}(1 \times 10^3)$ events, with a predicted beam-related neutron signal of 122 (159) events without (with) the high energy neutron limit from SciBath as seen in Fig. 6.4 and summarized in Table 6.3.

6.4.2 PSD CUT

As seen in Fig. 6.5, imposing a PSD cut removes much of the BUB contamination from the beam signal and allows a clear beam-related-signal to appear. An observed excess of (61 ± 12) events is

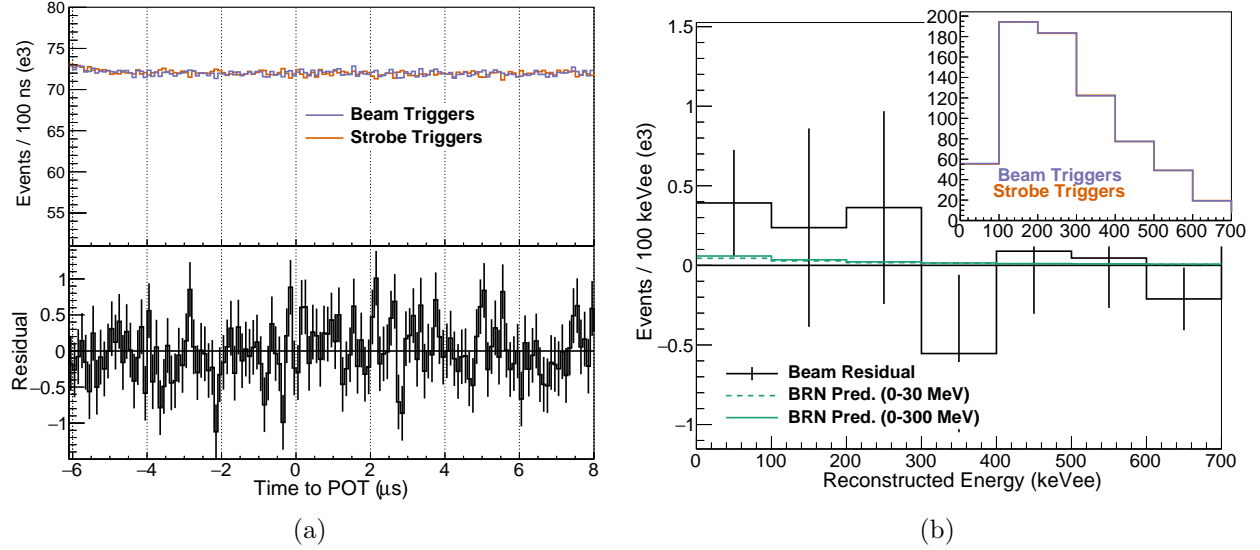


Figure 6.4: No-shielding energy and time spectra with no PSD cut. (a) Timing spectra relative to protons-on-target. (b) Prompt energy spectra centered on the expected beam timing window. Inlaid plot shows un-subtracted beam and strobe spectra. The BUB rates are too high to observe a beam excess with no PSD cut.

in good agreement with the prediction using the SciBath measurement of 35 (47) events without (with) the high energy neutron flux limit.

NEUTRON FIT

A likelihood fit of the neutron prediction to the beam residual can be performed to inform the BRN prediction of the full-shielded CEvNS search. In the fit, the normalization of the neutron prediction is allowed to float to find the best match to the beam data. The fit provides a scaling to apply to the neutron prediction in the full-shielded dataset which corrects for, e.g. different beam

	Predicted Rates		Observed Rates	
	No PSD	PSD	No PSD	PSD
Beam-Unrelated Background	7.0×10^5	44	7.0×10^5	44
Beam-Related Neutrons	122 (159)	35 (47)		
Beam Residual			362 ± 1184	61 ± 12

Table 6.3: Predicted and observed no-shielding dataset ‘prompt’ event rates. Less than one CEvNS event is expected to be in the no-shielding dataset. Neutron predictions are assuming an incoming flux from (0-30) MeV. Numbers in parenthesis include the SciBath limit > 30 MeV. A total of 105 events were seen in the beam window after the PSD cut.

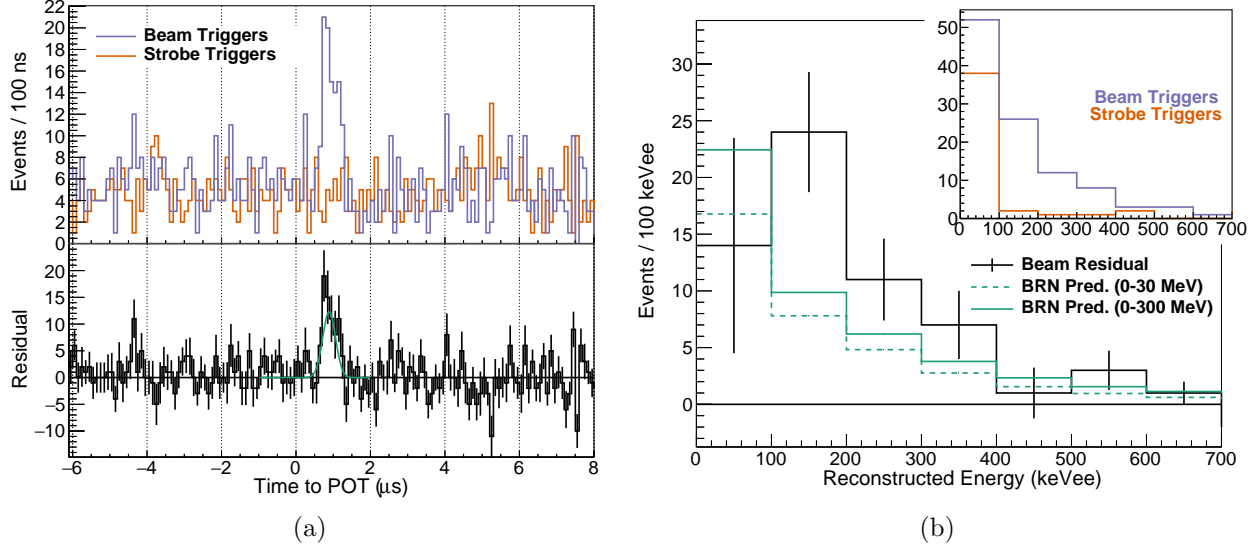


Figure 6.5: No-shielding energy and time spectra with PSD cut imposed. (a) Timing spectra. Overlaid on the bottom panel in green is the prompt beam-related neutron peak from the SciBath measurement normalized to the predicted number of events in CENNS-10. (b) Prompt energy spectrum. The observed beam excess is in good agreement with the predicted rate from the SciBath measurement. Inlay plot shows un-subtracted spectra.

energies and different locations from the SciBath to the CENNS-10 run.

The results of the fit can be seen in Fig. 6.6 and suggest that the predicted BRN rate should be increased by 70 % (30 %) if the high energy neutron flux is not (is) considered. The $\chi^2/N.D.F.$ of the fit is 8.7 / 6 (9.6 / 6) without (with) the high energy flux, to be compared to the χ^2_{null} value of 41.7. Alternative incident neutron spectral shapes were investigated (e.g. power law behavior), but were not found to match the data as well as the SciBath flux.

A shape correction to the BRN prediction was later implemented due to the energy-dependence of the F_{prompt} parameter improving the χ^2 to 6.3. This correction is necessary as the singlet:triplet ratio in the **Geant4** simulation is an energy-independent value for neutron simulations. Due to the observed decrease in the singlet:triplet ratio in calibration data (see Fig. 5.13), this shape correction serves to decrease the rate at low energy and pull up the rate at higher energies, making the predicted neutron shape better match the observed beam-related excess. This correction was applied to the full-shielding predictions.

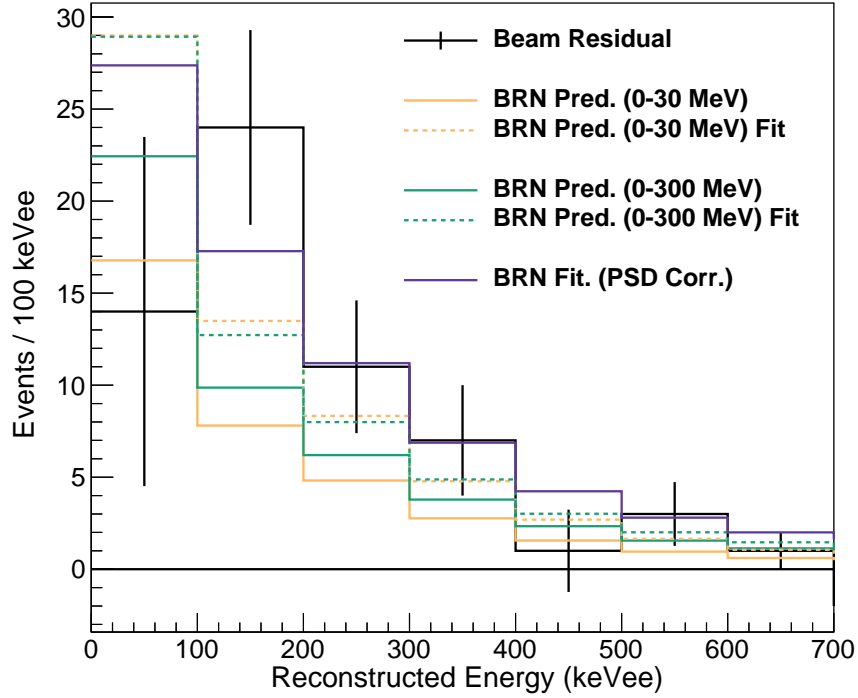


Figure 6.6: Fit of the beam-related neutron predictions to the no-shielding beam-related excess. According to the fit, the neutron prediction for the full-shielded dataset should be increased by 30 % (70 %) relative to the prediction using the SciBath measurement with (without) the high energy flux limit. An efficiency correction due to the energy dependence of F_{prompt} was later applied resulting in better agreement between the beam residual and the MC predicted shape. The effect on the predicted BRN shape can be seen in the dark blue curve.

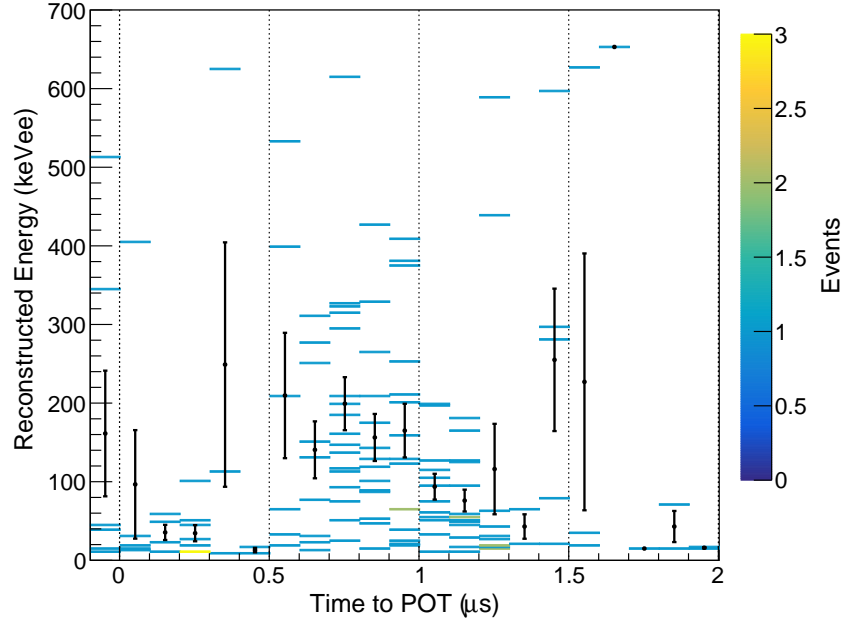


Figure 6.7: Beam-related neutron mean energy vs arrival time. Neutrons arriving earlier seem to have higher energies than those detected later consistent with higher energy neutrons travelling faster.

BRN ARRIVAL TIMES

Another question about the beam-related neutron flux is whether there is any time dependence. To look into this, the two-dimensional spectrum of arrival time (relative to beam-on-target) vs. reconstructed energy for events passing the PSD cut was created. For each time bin, the average energy of the events passing cuts was found.

As seen in Fig. 6.7, there appears to be a correlation with the reconstructed energy of a beam-related event and the arrival time relative to beam-on-target. Higher energy events tend to occur closer to beam-on-target, consistent with higher energy neutrons travelling at a higher rate of speed.

CHAPTER 7

A CEVNS SEARCH WITH CENNS-10

In this chapter I discuss two analyses performed as part of a CEvNS search in the Engineering Run dataset: a counting experiment (Sec. 7.3) and a full 3D likelihood analysis including energy, time, and PSD information (Sec. 7.4). I finish by examining the implications on non-standard neutrino interactions as a result of the likelihood fit results.

7.1 RUN SUMMARY

The CEvNS search covered the full-shielded section of the Engineering Run summarized in Table 4.1. A total of 1.5 GWh ($\sim 3.5 \times 10^{22}$ POT) of beam was delivered over the course of the full-shielded dataset at an average power of 0.97 MW.

7.1.1 ANALYSIS SUMMARY

Two analyses were performed on the full-shielded dataset: a counting experiment after optimizing a PSD cut, and a full likelihood fit.

The counting experiment, followed the same procedure as the no-shielding run: the waveform was split into three time regions (summarized in Tab. 7.1) and a PSD cut was applied to search for beam-related events. In this case, the prompt and delayed windows were used to search for a beam-related neutron excess and an alternative energy range in the delayed window was considered to search for CEvNS events.

	Counting Analysis			Likelihood
	Prompt	Delayed BRN	Delayed CEvNS	Analysis
Energy (keVee)	(0-700)	(0-700)	(0-30)	(0-300)
F_{prompt}	Opt. E Dep.	Opt. E Dep.	Opt. E Dep.	(0.55-0.95)
Time (μs)	(0.4-1.4)	(1.4-4.4)	(1.4-4.4)	(0.4-4.4)

Table 7.1: Summary of analysis-specific cuts used for the full-shielded analysis. Details are found in the text. ‘Opt. E Dep.’ F_{prompt} cut is an energy-dependent cut to minimize the statistical uncertainty of the background-subtracted beam signal. Time cuts are only placed on beam windows and are measured relative to Event 39. A 16 μ s window from strobe triggers is used to characterize beam-unrelated backgrounds.

In the likelihood analysis, the prompt and delayed time regions were combined, and a three-dimensional reconstructed energy/PSD/time likelihood analysis of the beam data was performed. The full-shielded-specific analysis cuts are summarized in Table 7.1 and cut optimizations are discussed in more detail in later sections.

One major difference from the no-shielding neutron run: after extensive study, it was determined that a larger (16 μ s) time window from strobe triggers could be used to better characterize the beam-unrelated backgrounds (BUB) and minimize statistical fluctuations on the BUB predictions.

7.1.2 STROBE TRIGGER INVESTIGATIONS

Before a larger time window from the strobe triggers can be used to characterize the beam-unrelated backgrounds, it first needs to be verified that there is no time dependence in the strobe triggers. As a first check, the strobe time spectrum can be considered after all quality cuts are imposed. To verify that there is no time dependence, the spectrum was fit with a 0th-order polynomial over the time range of interest (some time at the beginning of each waveform is skipped to remove effects due to events happening before the waveform readout began). This fit is seen in Fig. 7.1, and the strobe time spectrum is indeed seen to be flat in time.

The strobe trigger can also be split into two time regions to investigate whether anything is changing from the beginning to the end of the waveform. For this study, both energy and PSD

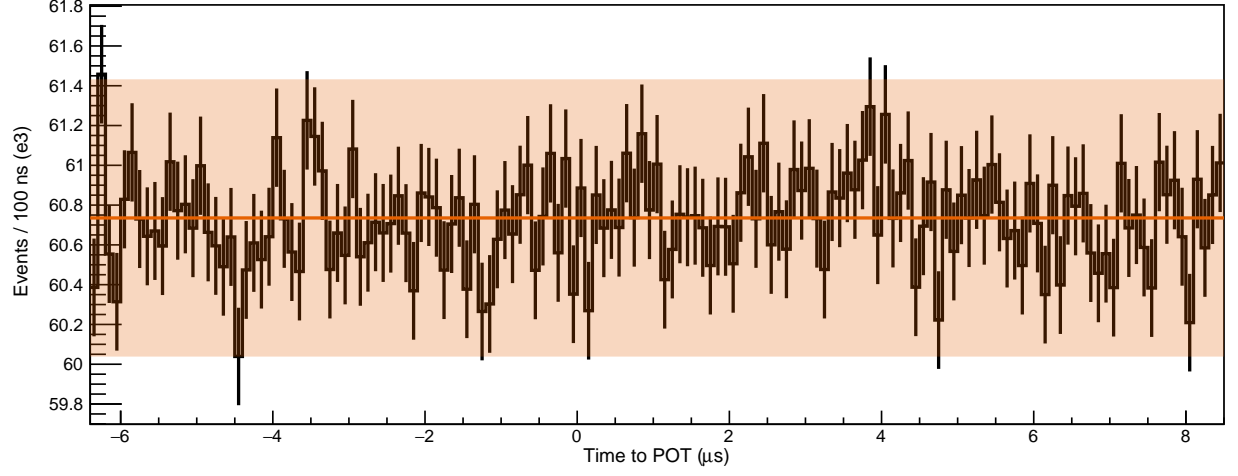


Figure 7.1: Strobe time spectrum fit. A good fit of a horizontal line gives confidence that the BUB rate is not changing in time. The best-fit line is shown in orange, with the $\pm 1\sigma$ error bars shown in the orange shaded region. The best fit is $(60.7 \pm 0.7) \times 10^3$ events/100 ns with a $\chi^2/N.D.F$ of 109 / 124 and a p-value of 0.83.

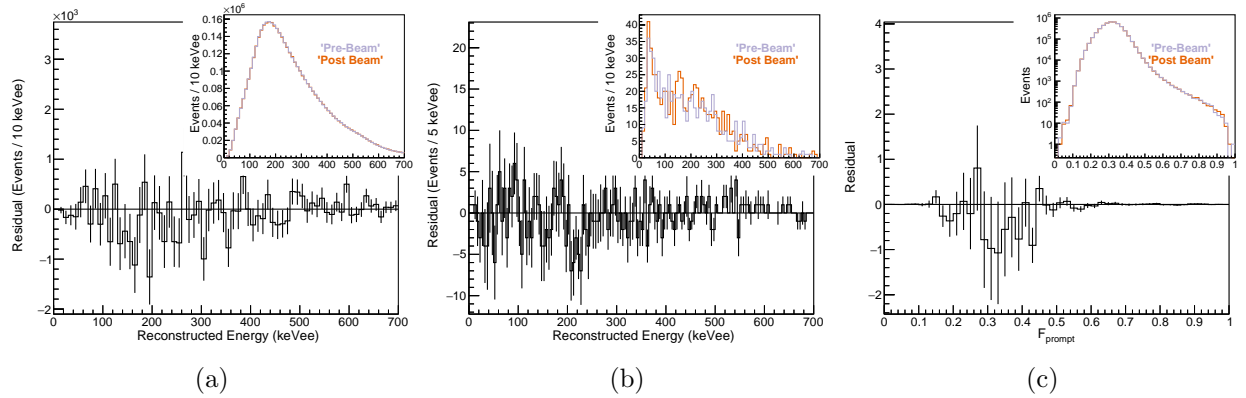


Figure 7.2: Comparison of energy and PSD spectra for different time windows within strobe triggers. Inlaid plots show un-subtracted spectra. (a) Energy spectra with no PSD cut. (b) Energy spectra with PSD cut. (c) PSD spectra. The good agreement allows the full strobe window to be used to characterize the beam-unrelated backgrounds.

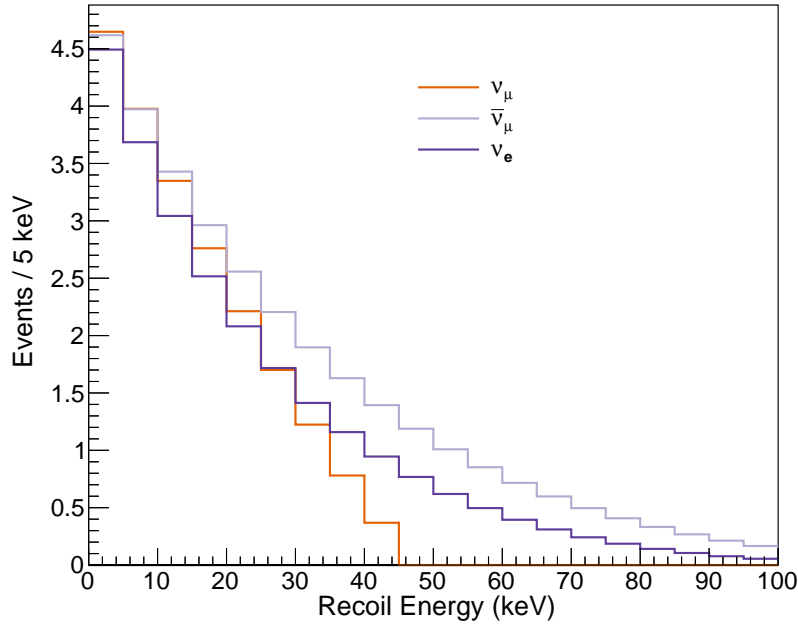


Figure 7.3: Expected CEvNS recoil spectra due to prompt ν_μ and delayed $\bar{\nu}_\mu$ and ν_e accounting for the CENNS-10 detector mass (29 kg) and total integrated beam power (1.5 GWh). No detector efficiencies are included here.

spectra were formed for an ‘early’ and a ‘late’ time window within each strobe trigger ($-8.0 < t < 0.0 \mu\text{s}$ and $0.0 < t < 8.0 \mu\text{s}$ respectively). Then the residual between the early and late spectra can be taken to verify that it agrees with zero as it should. These residual spectra can be seen in Fig. 7.2, and the residuals do, in fact, agree with zero.

As a final check, tests of statistical compatibility can be run between the ‘early’ and ‘late’ spectra. Both a χ^2 and a Kolmogorov-Smirnov test were performed to compare the spectra from ‘early’ strobe events to those from ‘late’ strobe events. The smallest p-value found was 0.21. Based on these results, the decision was made to use a larger strobe time window to characterize the beam-unrelated backgrounds of the full-shielded dataset.

7.2 SIGNAL PREDICTIONS

Due to the lack of Pb shielding and the low NIN rate observed in [3], NINs were not considered in the analysis of this dataset.

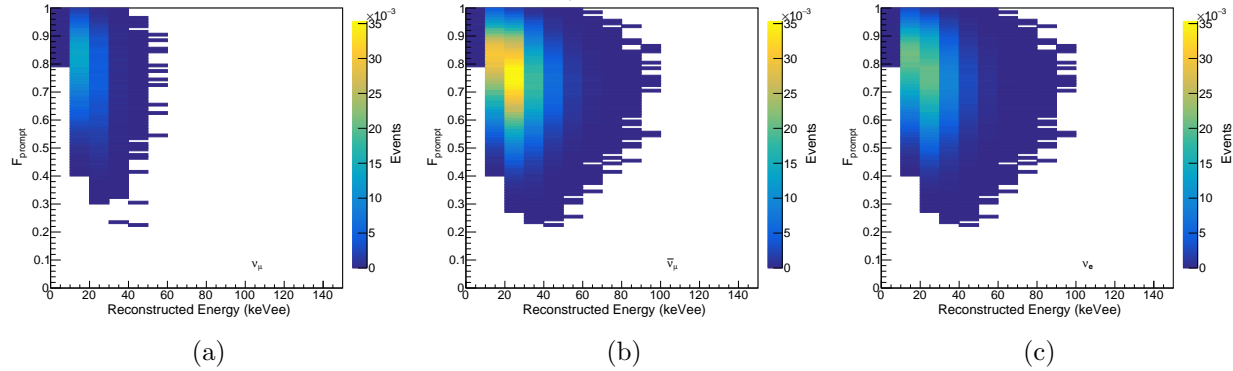


Figure 7.4: Two-dimensional CEvNS energy:PSD pdfs. (a) ν_μ (b) $\bar{\nu}_\mu$ and (c) ν_e . These are convolved with the appropriate neutrino timing distribution (Fig. 2.2) to form pdfs for the likelihood analysis. They are combined with the predicted beam-related neutron spectra to optimize cuts in the counting experiment analysis.

7.2.1 CEVNS SIGNAL

A **Geant4** simulation (Sec. 5.7.6) was used to form the predicted shape in energy:PSD space from CEvNS events. The results from this simulation were then be re-weighted to the expected recoil energy spectra for each neutrino species (ν_μ , $\bar{\nu}_\mu$, and ν_e), taking into account the total integrated power over the course of the run and the detector mass. These recoil spectra can be found by convolving the π -DAR neutrino energy spectrum with the CEvNS cross section and can be seen in Fig. 7.3. The predicted CEvNS spectra were then be combined with the beam-related neutron prediction to optimize the cuts used in the counting analysis.

Finally, the predicted energy:PSD distributions for each neutrino flavor (Fig. 7.4) were convolved with the expected neutrino timing distributions to form three-dimensional pdfs for use in the likelihood analysis. These timing distributions come from convolving the average POT trace with the appropriate particle lifetimes as seen in Fig. 2.2. An additional 25 ns offset from the BRN arrival time is included to account for time-of-flight differences.

7.2.2 BEAM-RELATED NEUTRON SIGNAL

Similar to the no-shielding analysis, **Geant4** simulations were run using the simulation discussed in Sec. 5.7.5. The only modification to the procedure was the addition of the scaling factor applied to

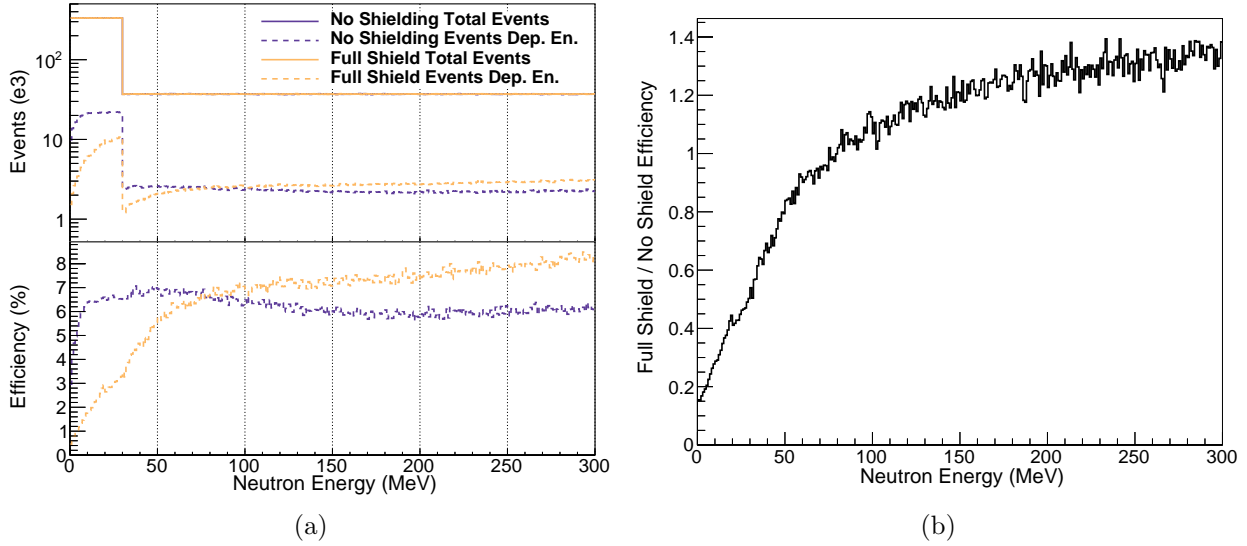


Figure 7.5: Efficiency of fast neutrons to reach (deposit energy in) the CENNS-10 detector. (a) Efficiency as a function of neutron energy comparing CENNS-10 with (blue) and without (peach) neutron shielding. (b) The ratio of the efficiency for fast neutrons to reach the detector with and without the water shielding. The neutron shielding is seen to reduce the probability that lower energy neutrons reach CENNS-10, but it actually increases the probability that higher energy neutrons reach the detector.

the prediction, found in Sec. 6.4.2, and the additional water and copper shielding were modeled.

The addition of the water shielding causes a large difference in the predicted rate depending on whether or not the high energy limit from the SciBath measurement is included. As seen in Fig. 7.5, the water does an excellent job of preventing low energy neutrons from interacting in CENNS-10, but it only moderates the higher energy neutron flux, and many high energy neutrons still reach the detector.

The **Geant4** simulations were used to characterize the two-dimensional reconstructed energy:PSD spectrum from BRNs. This two-dimensional spectrum was used, similar to the no-shielding analysis, to form an energy-dependent PSD cut for the counting analysis. It was also convolved with the expected timing distribution of BRNs to form a three-dimensional BRN pdf for the likelihood analysis. A gaussian fit to the fast-neutron peak from the no-shielding analysis was used for the expected timing shape of the beam-related neutrons.

For the PSD cut optimization, only the (0-30) MeV simulation was considered. A summary

	Total	Counting Analysis			Likelihood
		Prompt	Delayed BRN	Delayed CEvNS	Analysis
BUB	5.7×10^5	88	261	10.3	5.2×10^3
BRN	350 (700)	23 (123)	< 1	< 1	143
CEvNS	5.0	0.2	0.7	0.5	3.9

Table 7.2: Expected rates in the full-shielded dataset. Total event rates, as well as predicted rates for the counting and likelihood analyses are shown. Energy/time/PSD cuts are given in Table. 7.1. ‘Total BUB’ rate is the number of events expected in a given 1 μ s window. The difference between the ‘Delayed BRN’ and ‘Delayed CEvNS’ rates are due to different energy ranges.

of the predicted rates for the two analyses can be found in Table 7.2. Due to the high energy threshold during the energy run (of ~ 80 keVnr), the expected CEvNS signal was quite small.

7.2.3 SYSTEMATICS

A variety of systematic excursions about the central-value predictions were run to quantify the systematic uncertainty on the CEvNS and BRN expected rates and shapes.

PULSE SHAPE DISCRIMINATION

The tuned PSD setting in the CEvNS and neutron predictions came from identifying the nuclear recoil band in ^{252}Cf calibration data. With a variety of uncertainties entering into this calculation, largely driven by the separation of nuclear recoil events from electronic recoil contamination in the calibration dataset, a conservative approach to the PSD systematic was taken. While a correction for the energy-dependence of the NR band was ultimately applied, the initial choice of the singlet:triplet ratio in the beam-related neutron simulations was chosen to be representative of the wide range of energies considered ((0-700) keVee). It was set to the NR band value from the calibration curve at 50 keVee. As a one-sigma uncertainty on the PSD behavior, the difference from the lowest F_{prompt} value relevant for the CEvNS predictions to this value was considered.

For examination of systematic effects PSD could have on the predicted spectra, three alternative CEvNS and BRN pdfs were generated with energy-independent PSD settings: the original BRN simulation value, and $\pm 1\sigma$ as defined above.

	PSD	Quenching Factor	PE Threshold	Neutron Flux
CEvNS	×		×	
Neutrons	×	×	×	×

Table 7.3: Systematics on the signal predictions considered for the CEvNS search at the SNS. Relevant systematics for a given prediction are marked with an ‘×.’

QUENCHING FACTOR

From the quenching factor (QF) analysis, an energy-independent value of 28.9% in the energy region of interest for CEvNS was found to fit the LiqAr QF data well. The statistical uncertainty on this value was $\pm 3.5\%$ and this uncertainty was used to generate alternative PDFs of the CEvNS and BRN spectra for later analysis.

PE THRESHOLD

During the waveform analysis, a hard 2PE cut is imposed after the pulse fitting. However, during event building a separate 20 ADC value is used to identify pulses. To represent the possibility that this ADC threshold could at times be a harder cut than the later 2PE threshold, in the MC predictions, a 3PE threshold was used in the MC to generate alternative pdfs to be used for systematic studies.

LOW ENERGY NEUTRON FLUX

The extrapolation of the incident neutron flux below 5 MeV introduces some uncertainty to the BRN prediction. This low energy flux came from extrapolating a linear fit to the observed (5-30) MeV flux measured by SciBath. A conservative one-sigma uncertainty on this low energy flux was defined as the difference between the low energy extrapolated value and the measured flux from (5-10) MeV. With the neutron shielding present during the full-shielding run, this uncertainty has a small effect on the predicted BRN signal.

A summary of the systematics considered for each beam-related source can be found in Table 7.3.

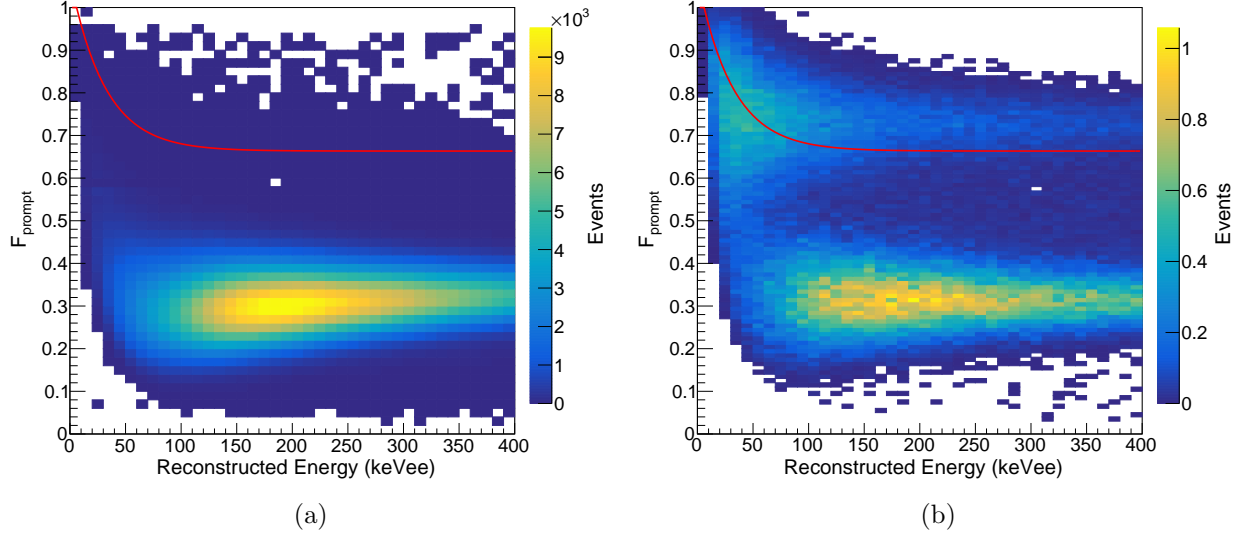


Figure 7.6: Overlaying the optimized PSD cut for the full-shielded Counting Experiment analysis on (a) predicted beam-unrelated background spectrum and (b) predicted signal spectrum. Signal is defined as the combined BRN and CEvNS signals. The optimal PSD cut was formed before a beam-related neutron PSD shape correction was developed.

7.3 COUNTING EXPERIMENT

For the counting experiment, much like in the no-shielding analysis, a PSD cut was optimized to minimize the statistical uncertainty on the number of background-subtracted beam events. The same figure-of-merit (\mathcal{F}) was used (see Eq. 6.4), but in this case, a wider strobe time window was considered to reduce the statistical uncertainty on the beam-unrelated background characterization resulting in a value for f less than one.

7.3.1 MAXIMIZING \mathcal{F}

The same procedure used to optimize the PSD cut for the no-shielding run was used to optimize the PSD cut for the full-shielding run. However, in this case, the ‘signal’ was the sum of the CEvNS and beam-related neutron (BRN) predictions. For the BRN prediction, the expected rate assuming ONLY the (0-30) MeV incident flux was used. The optimal PSD cut is driven by the BRN signal as the expected CEvNS signal is so small. The cut is shown in red in Fig. 7.6. The predicted energy spectra with and without a PSD cut can be seen in Fig. 7.7.

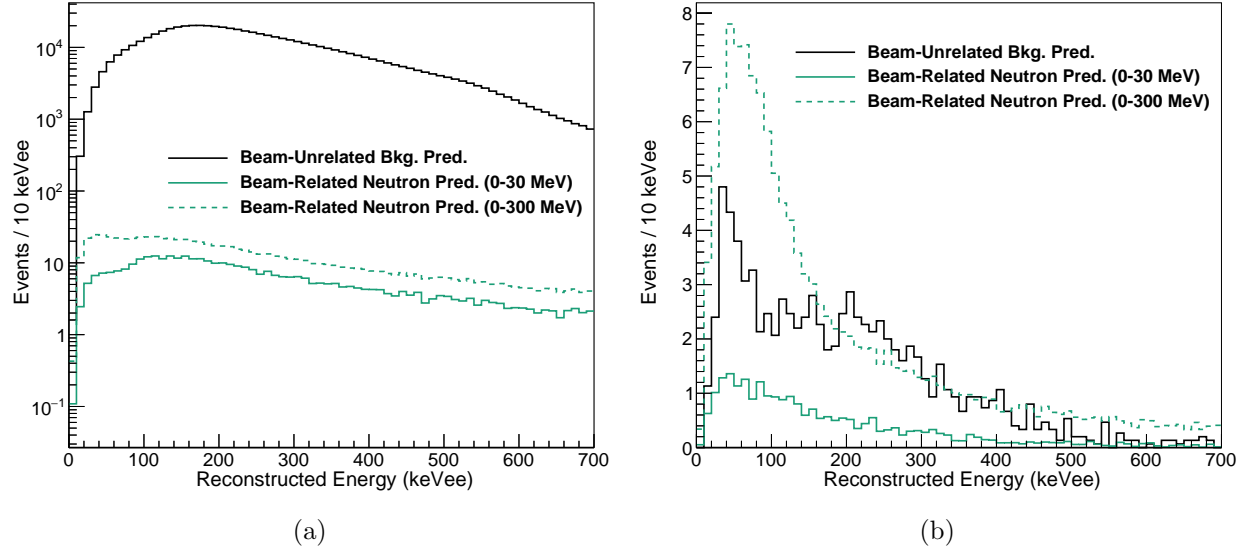


Figure 7.7: Predicted beam-unrelated background and beam-related neutron spectra for the full-shielded dataset without (a) and with (b) an optimized PSD cut.

Figure 7.8 shows the efficiency loss for nuclear recoil events with the addition of the counting experiment PSD cut. The large efficiency loss at low energies was a driving factor prompting the full three-dimensional likelihood fit in which PSD space was opened up to maximize the amount of CEvNS signal included. A similar optimization procedure was used to find the optimal time and energy cuts for the delayed CEvNS analysis, with the t_0 for beam events coming from a gaussian fit to the fast neutron peak in the no-shielding neutron run. The counting experiment cuts are summarized in Table 7.1.

For these optimization studies, no PSD shape correction to the BRN prediction was performed. When ultimately comparing to beam data, the BRN prediction was corrected based on the predicted energy-dependent PSD shape (a simple efficiency correction for the counting experiment, and a full shape correction to the BRN pdf for the likelihood analysis).

7.3.2 PRE-BEAM SUBTRACTION

Before proceeding to the beam time window, the pre-beam window ($-6.0 < t_{POT} < 0.0 \mu\text{s}$) background subtraction was performed to check that there are no long-lived beam-related back-

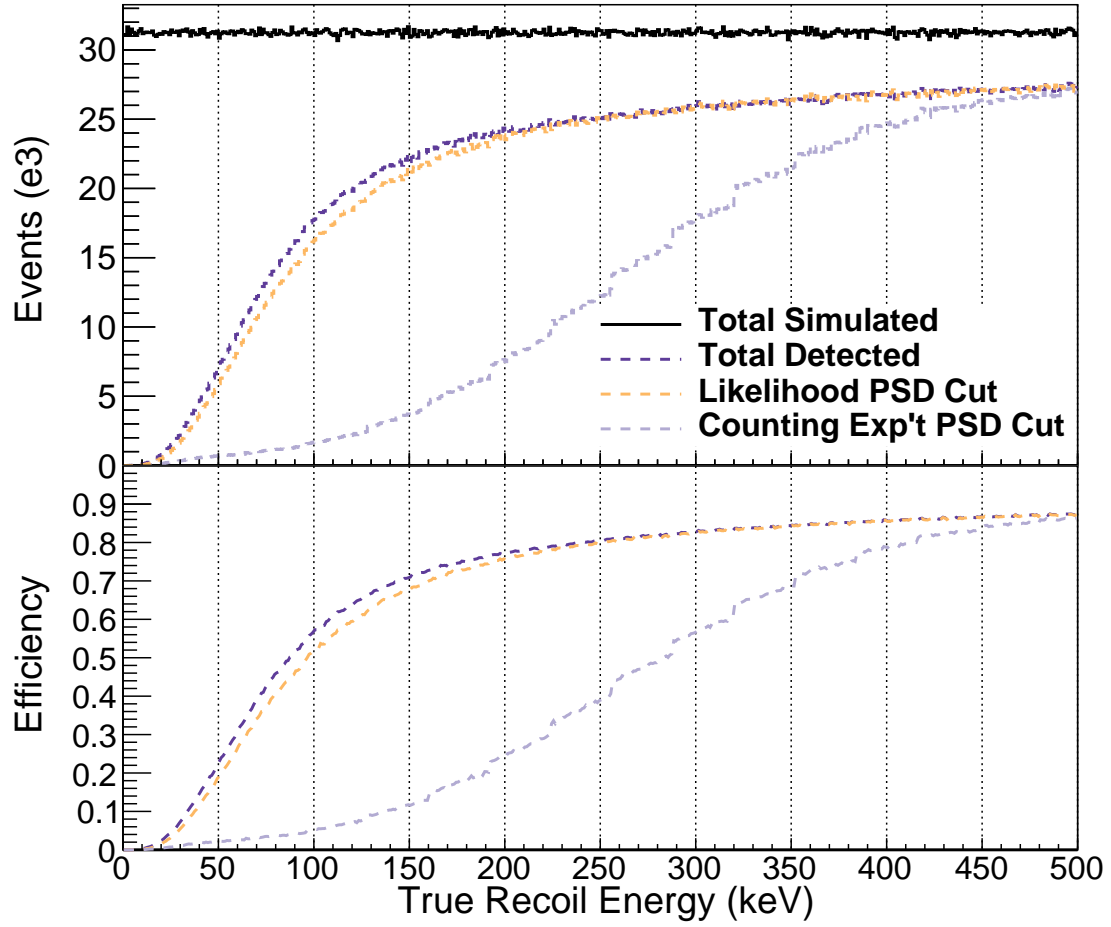


Figure 7.8: Nuclear recoil detection efficiency from ^{40}Ar recoil simulations with all cuts applied. The detection efficiency plateaus at < 1 because events were generated outside of the fiducial volume where the probability of detection is small. Step behavior in the counting experiment efficiency curve is due to finite binning used when generating energy-dependent singlet:triplet simulations.

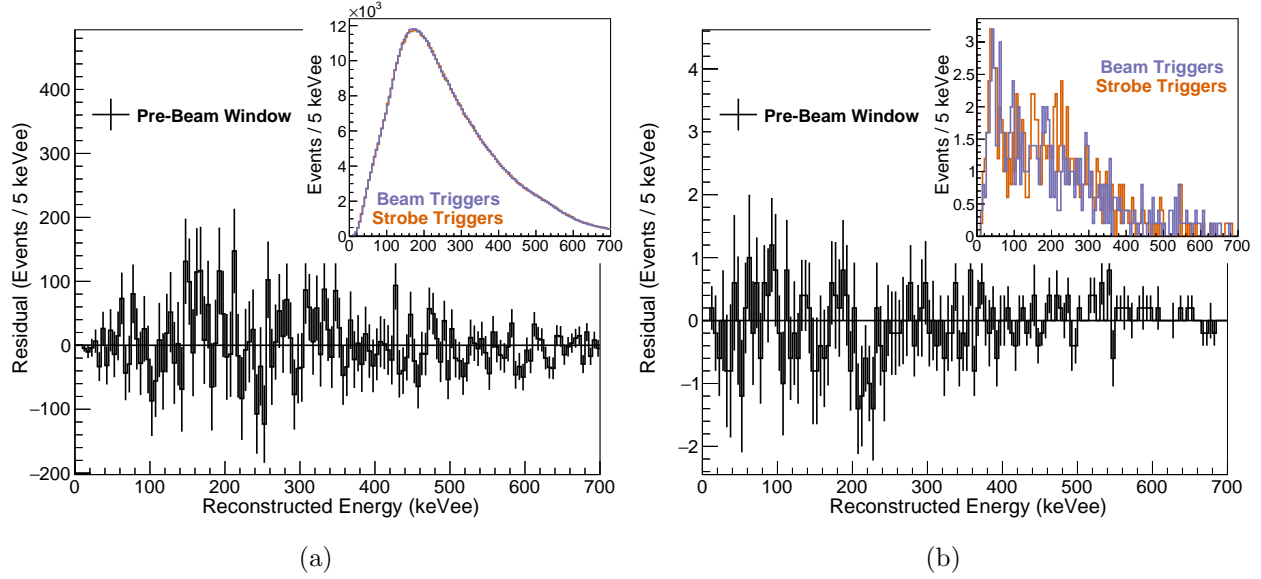


Figure 7.9: Full-shielded dataset pre-beam subtraction without (a) and with (b) a PSD cut. The pre-beam subtraction agrees with zero within one-sigma indicating no long-lived beam-related backgrounds in the full-shielded dataset. Insets show the un-subtracted spectra.

grounds present in the strobe triggers. The background-subtracted pre-beam energy spectra can be seen in Fig. 7.9. The beam-trigger residuals agree with zero within one-sigma both without $((1331 \pm 2611)$ events) and with $((-27 \pm 32)$ events) a PSD cut. Statistical compatibility tests were also performed between the beam and strobe trigger pre-beam energy, time, and PSD spectra for various sections of the run. The pre-beam spectra are statistically compatible with a lowest p-value of 0.11.

7.3.3 PROMPT BEAM EVENTS

With the verification that the strobe data accurately represents the beam-unrelated backgrounds expected during the beam window, the prompt beam window $((0.4-1.4) \mu\text{s})$ was considered. As seen in Fig. 7.10, even with the additional water and copper shielding, the beam-unrelated background rates were too high to observe any sort of beam-related excess before imposing a PSD cut.

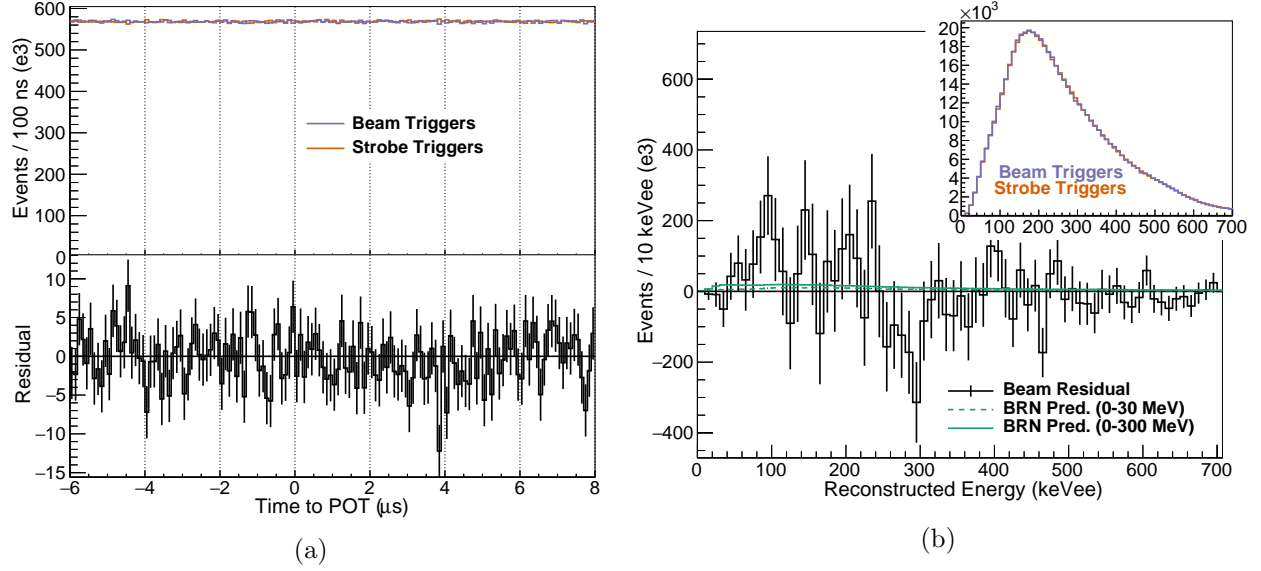


Figure 7.10: Full-shielded time and prompt energy spectra with no PSD cut. (a) Residual time spectrum. (b) Prompt energy spectra. Plot inlay shows the un-subtracted spectra. The beam-unrelated background rates are too high to observe any beam-related excess before a PSD cut.

PSD CUT

The beam-related neutron prediction was corrected for the energy-dependent F_{prompt} shape in the full-shielded analysis. To do this, the ^{40}Ar simulations with an energy-dependent singlet:triplet ratio setting were compared to a similar set of simulations with an energy-independent singlet:triplet setting. The energy-dependent efficiency for events to pass the PSD cut were considered for each case, with the ratio of efficiencies giving an energy-dependent weighting factor to apply to the BRN prediction. This correction serves to pull down the low energy component of the BRN prediction (by $\sim 20\%$ at the lowest energies), while increasing the predicted rate at higher energies by $\sim 10\%$ above 100 keVee. A similar weighting method was considered for the predictions with no PSD cut, but ultimately determined to be unnecessary.

The beam-related excess after imposing a PSD cut can be seen in Fig. 7.11. The observed rate of (126 ± 15) events is in excellent agreement with the BRN prediction, including the high energy limit from the SciBath measurement, of 123 events as discussed in the next section.

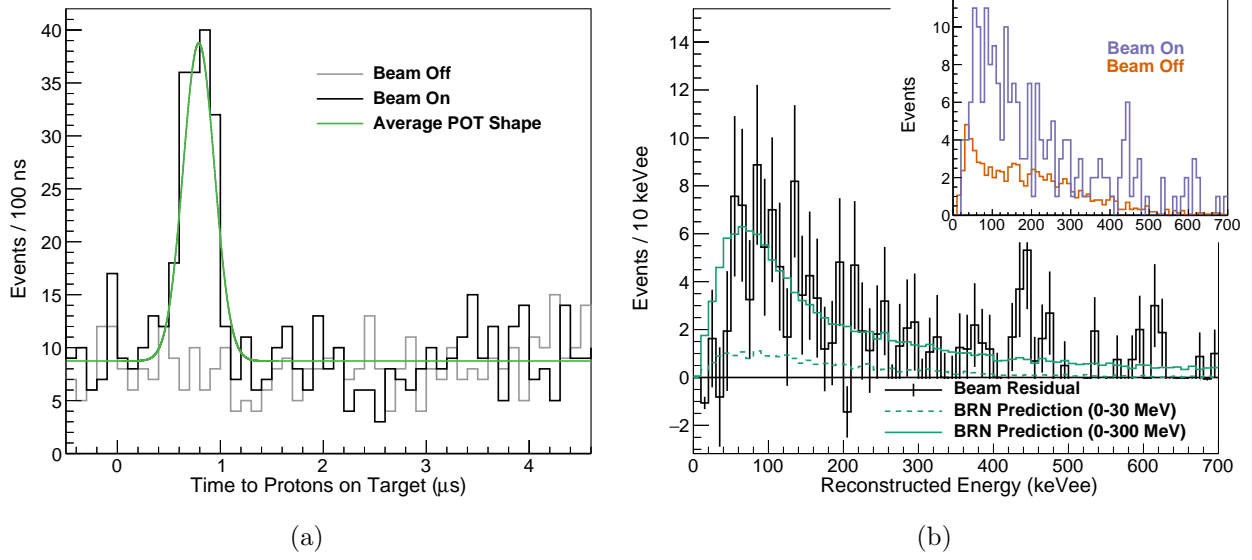


Figure 7.11: Full-shielded energy and time spectra after optimized PSD cut. (a) Time spectrum relative to beam-on-target. No indication of a delayed fast-neutron flux is seen. (b) ‘Prompt’ energy spectra occurring within 1 μ s of beam-on-target for beam-on and beam-off triggers. A noticeable excess of (126 ± 15) events is seen. Plot inlay shows the un-subtracted spectra. Note that the beam-off prediction used a 16 μ s strobe window scaled to the appropriate amount of integrated time.

SYSTEMATIC ERRORS

A full chi-square analysis of the prompt beam-related excess was performed, with the predicted neutron spectrum representing the expected signal. Including correlated errors, the chi-square value between two distributions can be defined as

$$\chi^2 \equiv \sum_{i,j=1}^N (d_i - \mu_i) V_{ij}^{-1} (d_j - \mu_j) \quad (7.1)$$

where the sum over i and j runs over the bins considered, d is the measured data, μ is the expected value, and V is the full covariance matrix defined in Eq. 3.8.

If there are no correlations, Eq. 7.1 simplifies to the more familiar

$$\chi^2 \equiv \sum_{i=1}^N \frac{(d_i - \mu_i)^2}{\sigma_i^2}. \quad (7.2)$$

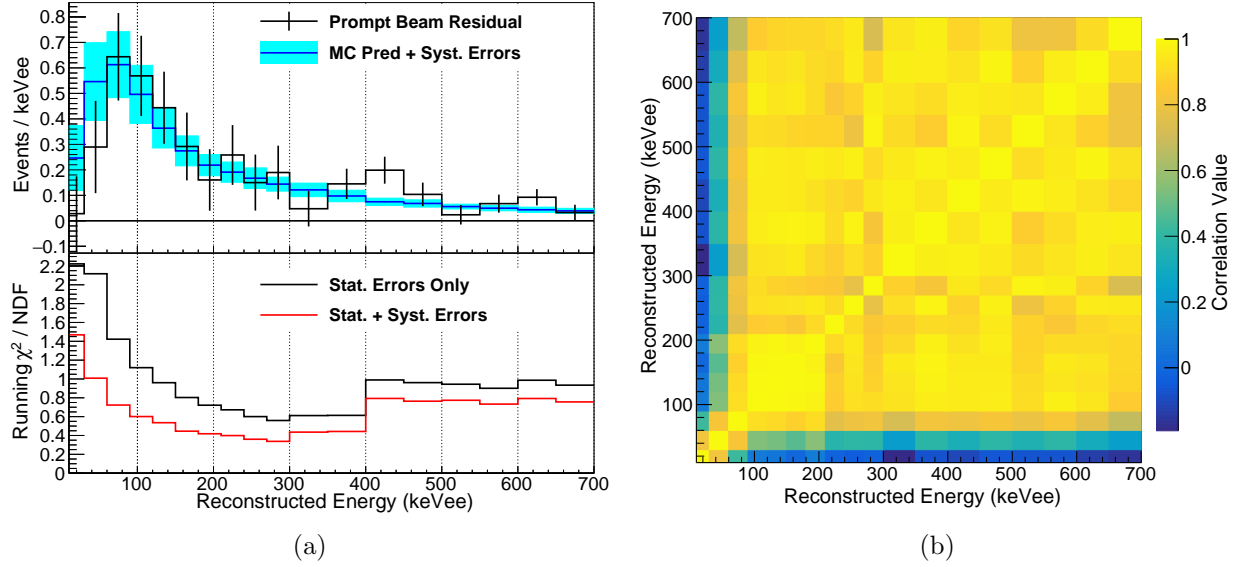


Figure 7.12: (a) Running χ^2 (statistical only and full χ^2 with correlations due to systematic effects) between the full-shielded beam excess and the predicted beam-related-neutron spectrum. Good agreement between the data and prediction is seen. (b) Correlation matrix of beam-related-neutron prediction. Most bins are positively correlated, but some low energy bins are anticorrelated with higher energy bins.

In order to better account for low statistics signal regions in the data, the assumed statistical errors on the signal come from the predicted number of events.

A covariance matrix incorporating all systematic excursions covered in Sec. 7.2.3 was formed, allowing the chi-square calculation in Eq. 7.1 to be performed. By considering the correlation matrix (found in Fig. 7.12), we can examine how correlated energy bins are with each other. While most bins are positively correlated with each other (if one increases so does the other), there are some anticorrelated bins (on the order of 10%). I.e. if the bin content of one increases, the other would be expected to decrease. This is most noticeable between low energy and high energy bins.

As seen in Fig. 7.12, this χ^2 comparison shows the MC prediction is a good match for the data with a final χ^2/NDF of 13.6/18. A full χ^2 fit to the beam residual, allowing the BRN normalization to float relative to the central value prediction, gives a best-fit value of 1.02 ± 0.23 with a minimum χ^2 of 13.6. This analysis validates the technique of using the no-shielded dataset to normalize the BRN prediction in future datasets.

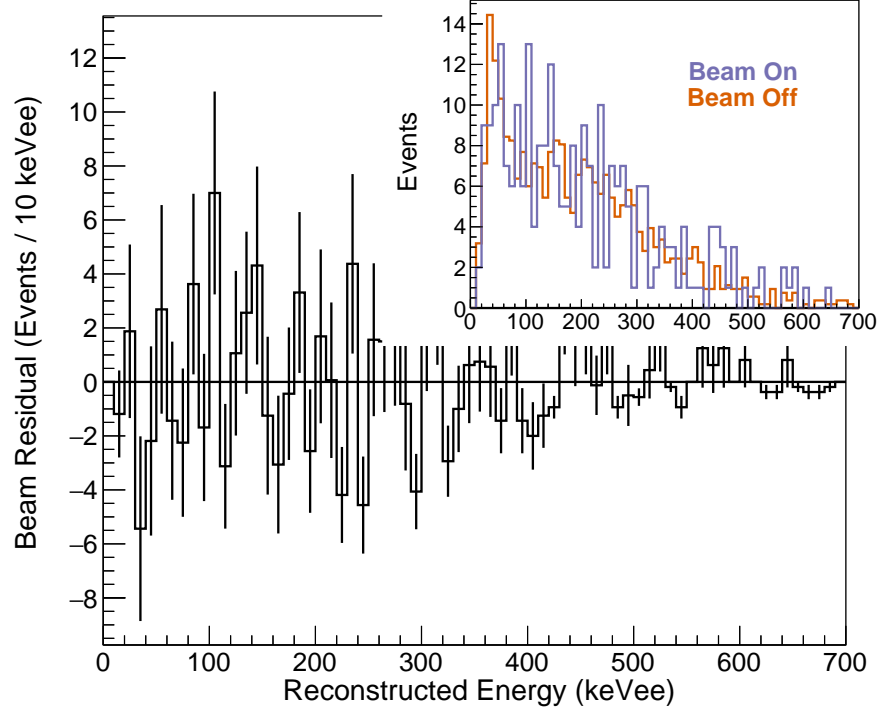


Figure 7.13: Full-shielded delayed energy spectrum with PSD cut. The residual is consistent with zero indicating no delayed beam-related fast neutron flux. The errors on the background subtraction can be used to place a first limit on the CEvNS cross section on argon as discussed in the text. Plot inlay shows un-subtracted spectra.

7.3.4 DELAYED EVENTS

The same PSD cut used for the analysis of prompt beam-related events was used in the analysis of the delayed time window. Recall that a time window from $(1.4-4.4) \mu\text{s}$ was considered to maximize \mathcal{F} in Eq. 6.4 for CEvNS events. For a CEvNS search, an optimal energy range of $(0-30) \text{ keVee}$ was found to be optimal. To characterize any sort of beam-related neutron flux, the energy range $(0-700)$ was also investigated.

The delayed energy spectrum after implementing a PSD cut can be found in Fig. 7.13. There is no noticeable excess in the beam-on spectrum consistent with previous measurements showing no evidence of a delayed beam-related fast neutron flux.

The errors on the background subtraction can be used to put a first limit on the CEvNS cross section on argon (although a more powerful limit will come from the full likelihood analysis).

	Total Events	Prompt Cuts	Delayed BRN Cuts	Delayed CEvNS Cuts
Observed (Beam On)	5.7×10^5	210	261	11
Observed (Beam Off)	5.7×10^5	84	252	10.3
Observed (Residual)	300 ± 780	126 ± 15	9 ± 18	0.7 ± 3.6

Table 7.4: Observed event rates from the counting experiment. Cuts are summarized in Tab. 7.1. The difference between ‘Delayed BRN’ and ‘Delayed CEvNS’ is the energy range considered. The beam residual from the delayed CEvNS analysis cuts can be used to place a one-sigma limit on the CEvNS cross section of $< 150 \times 10^{-40} \text{ cm}^2$, roughly $8.5\times$ the Standard Model prediction.

Within the optimized energy range, the beam residual is (0.7 ± 3.6) events. The combination of the one-sigma limit on the background subtraction of (4.3 events) and the SM prediction of 0.5 events can be used to place a one-sigma limit on the CEvNS cross section. The flux averaged Standard Model CEvNS cross section on argon is $18 \times 10^{-40} \text{ cm}^2$. Therefore, the counting experiment can place a limit of

$$\sigma_{CEvNS}^{\text{Ar}} < \frac{4.3}{0.5} \cdot 18 \times 10^{-40} \text{ cm}^2 < 150 \times 10^{-40} \text{ cm}^2$$

on the CEvNS cross section for argon.

Observed event rates for the Counting Experiment are summarized in Table 7.4.

7.4 3D LIKELIHOOD ANALYSIS

To maximize the sensitivity to the CEvNS signal, a 3D-binned likelihood analysis in energy/PSD/time space was performed. This likelihood analysis allowed us to open up the available space to maximize the sensitivity to a CEvNS signal.

The formation of the signal pdfs (CEvNS and BRNs) was discussed in Sec. 7.2. The beam-unrelated background (BUB) energy:PSD shape was characterized by using the $16 \mu\text{s}$ strobe window. This shape was then convolved with the expected BUB time distribution to form a BUB pdf for the likelihood fit. A time-independent shape was assumed with the normalization coming from a fit to the strobe time spectrum to remove any statistical fluctuations from time bin to time bin.

Ideally the entire PSD space could be considered in the likelihood fit. However, due to uncer-

tainties in the inelastic neutron cross sections on Ar (which tend to produce electronic recoil events), a minimal PSD cut to remove most electronic recoil events was imposed. A cut of $F_{prompt} > 0.55$ ($\sim 2\sigma$ from the mean of the reconstructed F_{prompt}^{NR} distribution) allowed 97.5 % of elastic BRNs and CEvNS events to still remain within the fitting range. An upper cut of $F_{prompt} < 0.95$ was also imposed due to statistical limitations in the BUB dataset and the lack of predicted signal events at high PSD values.

A time window of (0.4-1.4) μs in 1 μs time bins relative to protons on target was considered. This allowed for 1 μs centered on the beam for prompt neutrinos and BRNs, as well as the optimized 3 μs delayed window found from the counting experiment analysis.

In energy space, the region from (0-300) keVee was considered in three 100 keVee bins. All CEvNS events fell into the first energy bin, while the two higher energy bins helped to separate the CEvNS/BRN signals in energy space. Above 300 keVee, the BUB pdf began to suffer from statistical limitations at the higher F_{prompt} values.

The likelihood fit provides a best fit combined prompt+delayed CEvNS rate as well as a best fit BRN rate which can be used to further constrain the predicted BRN rate in future analyses. In light of the counting experiment results, only a BRN pdf including the high energy limit from SciBath was used.

7.4.1 NEUTRON PDF PSD SHAPE CORRECTION

Before proceeding to the likelihood fit, a shape correction to the BRN pdf in the two-dimensional energy:PSD space was performed. This was not necessary in the counting experiment as a simple efficiency correction was capable of replicating the energy-dependent behavior of the nuclear recoil F_{prompt} band. However, for the likelihood fit, the actual shape in PSD space is quite important. Therefore, an energy-dependent re-weighting was applied to the BRN energy:PSD component of the pdf. The weighting factors were based on the energy-dependent F_{prompt} behavior from the CEvNS predictions. Recall that this behavior was tuned to match the ^{252}Cf calibration datasets.

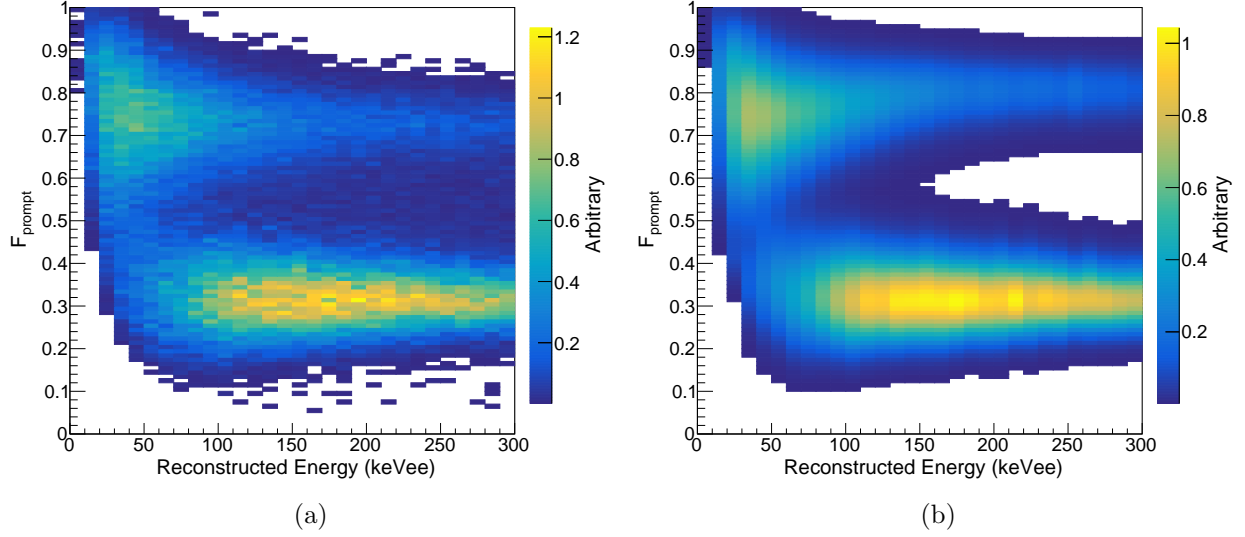


Figure 7.14: PSD shape correction for beam-related neutron likelihood pdf. (a) Original two-dimensional energy:PSD component of the pdf from the output of the **Geant4** simulation. (b) Energy:PSD shape of beam-related neutron pdf after applying a shape correction based on the ^{252}Cf calibration datasets. In prior analyses a simple efficiency correction was performed. For the likelihood analysis, PSD shape information is required.

The result of this shape correction can be seen in Fig. 7.14. With this final correction in hand, the likelihood analysis could be performed.

The predicted event rates in the likelihood analysis are summarized in Tab. 7.2.

7.4.2 LIKELIHOOD FITTING

The likelihood fit made use of the **Roofit** analysis framework [120,121] which minimizes the log-likelihood test statistic. As we are interested in the actual number of events, the extended likelihood formalism is used with

$$-\ln(L(\boldsymbol{\theta})) = \nu(\boldsymbol{\theta}) - \sum_{i=1}^n \ln(\nu(\boldsymbol{\theta})f(x_i; \boldsymbol{\theta})) \quad (7.3)$$

the test statistic being minimized [122]. Here, ν is the expected number of events, f is the assumed underlying pdf, and $\boldsymbol{\theta}$ are the parameters being minimized (in this case, the number of CEvNS and BRN events). A likelihood fit is more general than a standard chi-square fit, especially in the case of small statistics, as it does not require any assumptions about the gaussian nature of the

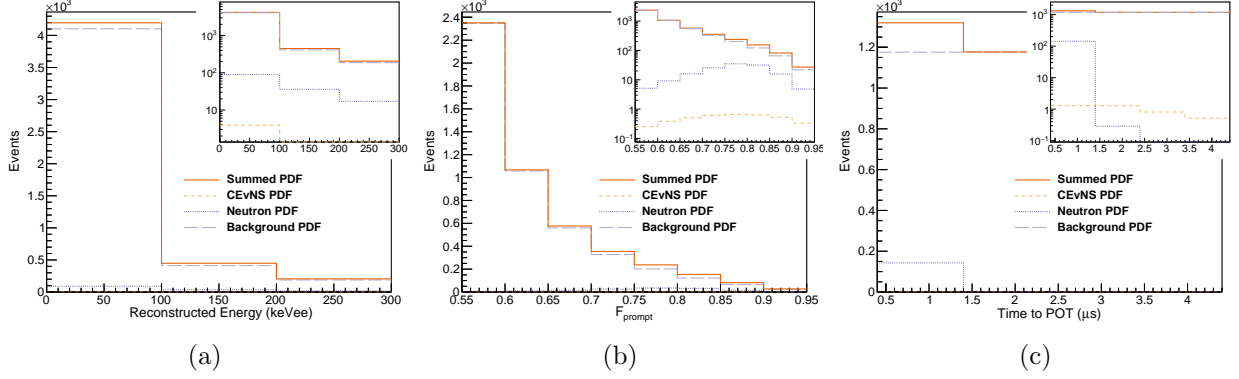


Figure 7.15: Likelihood pdfs in (a) energy, (b) PSD and (c) time normalized to the expected rates. While the pdfs have been projected to a specific axis here, the actual likelihood fit takes into account the full three-dimensional shape of the distributions. Inlaid plots show the pdfs on a log-scale making the CEvNS distribution more clear.

underlying errors.

For this analysis, a profile-likelihood fit was performed for both the BRN and the CEvNS signals. With the large statistics available to characterize the beam-unrelated background shape and rate, N_{BUB} was held constant during the fit. The underlying pdfs for each source (beam-unrelated background, beam-related neutrons, and CEvNS), normalized to the expected rates, are shown in Fig. 7.15. Note that these projections are just for visualization purposes. The likelihood fit takes into account information from the complete three-dimensional shape of the pdfs. The best-fit result, projected to time, energy, and PSD space, can be seen in Fig. 7.16.

Statistical errors on the best fit CEvNS and BRN rates come from the likelihood curves. In the case of the beam-related neutrons, Wilks' Theorem [123] is used to estimate the one-sigma statistical error on the best-fit value. The Feldman-Cousins prescription [124] was used to analyze the CEvNS signal due to small number of expected events.

In both cases, systematic errors were handled the same way. Alternative pdfs for each systematic covered in Sec. 7.2.3 were formed and fit to the beam data. The spread of the results using these alternative pdfs was used as an estimate of the systematic uncertainty on the result.

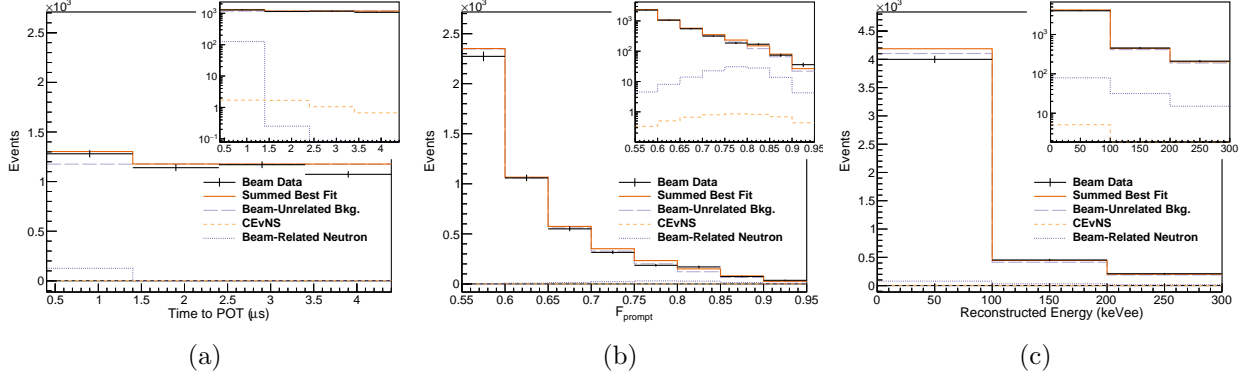


Figure 7.16: One-dimensional projections of global best-fit to Engineering Run data. (a) Time, (b) PSD, and (c) Reconstructed Energy. The CEvNS curve shown is from the 68.3 % confidence limit found. Inlaid plots show the spectra in log-scale to make the CEvNS distributions more clear.

7.4.3 BEAM-RELATED NEUTRON RESULT

To find the beam-related neutron rate, the CEvNS normalization was profiled over (although the best fit BRN value is fairly uncorrelated with the best fit CEvNS value due to the small CEvNS signal size). The likelihood function L as a function of the BRN rate was mapped out, with the best fit value where the minimum of the $-2 \ln L$ occurs as seen in Fig. 7.17.

In the case of a likelihood fit, the actual value of the log-likelihood function is unimportant. What is more important in the likelihood ratio taken relative to another point on the curve:

$$-2 \ln L = (-2 \ln L)_{BF} - (-2 \ln L) \quad (7.4)$$

In the limit of large sample sizes, Wilks' Theorem [123] can be used to approximate the log-likelihood ratio as a chi-square distribution with n degrees of freedom. Using Wilks' theorem, the one-sigma statistical errors on the BRN rate can be found from the intersection of the log-likelihood ratio curve (Fig. 7.17a) with a value of one (the $\Delta\chi^2$ corresponding to a one-sigma uncertainty for a distribution with one degree of freedom).

As a measure of the systematic error on the result, alternative pdfs based on the one-sigma systematic excursions discussed in Sec. 7.2.3 are fit to the beam data. The standard deviation from these results then gives the systematic uncertainty on the best-fit neutron rate as seen in Fig. 7.17.

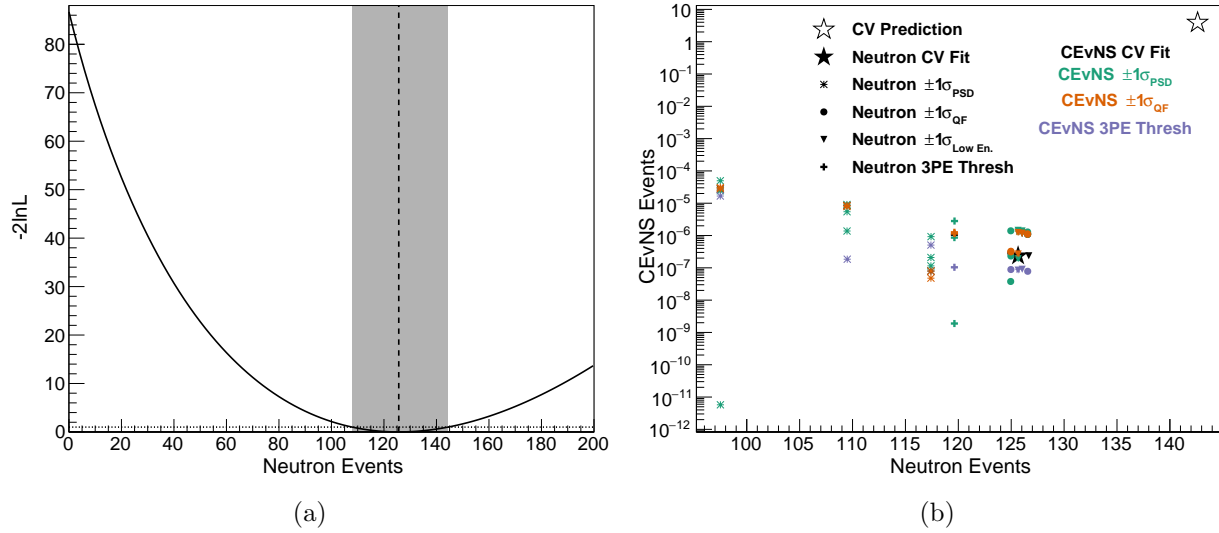


Figure 7.17: Beam-related neutron profile-likelihood fit results. (a) Log-likelihood ratio curve as a function of the number of neutron events. The gray band represents the one-sigma statistical uncertainty on the best fit value (given by the vertical dashed line) following Wilks' Theorem [123]. (b) The spread of the best fit neutron values with alternative BRN pdfs gives the systematic uncertainty on the fit. Changing marker colors represent the effect of changing the CEvNS pdf on the global best-fit value. Changing marker styles represents the effects of changing the neutron pdf. The hollow star shows the central value prediction.

This procedure gives the best fit beam-related neutron rate as $126 \pm 18(\text{stat}) \pm 11(\text{syst})$ events which agrees with the prediction (143 events) within one-sigma.

7.4.4 CEVNS ANALYSIS

For the CEvNS analysis, the Feldman-Cousins (FC) [124] procedure was used due to the small expected signal from CEvNS events. FC prescribes a frequentist approach for setting confidence limits based on the log-likelihood test statistic. The analysis here follows the procedure covered in [125] which is a fully frequentist approach using fake datasets to generate both the experimental sensitivity as well as the ultimate confidence limit (CL).

SENSITIVITY

Feldman and Cousins noted in their initial paper that downward fluctuations in the expected background can cause a better CL than might be expected. For that reason, the experimental

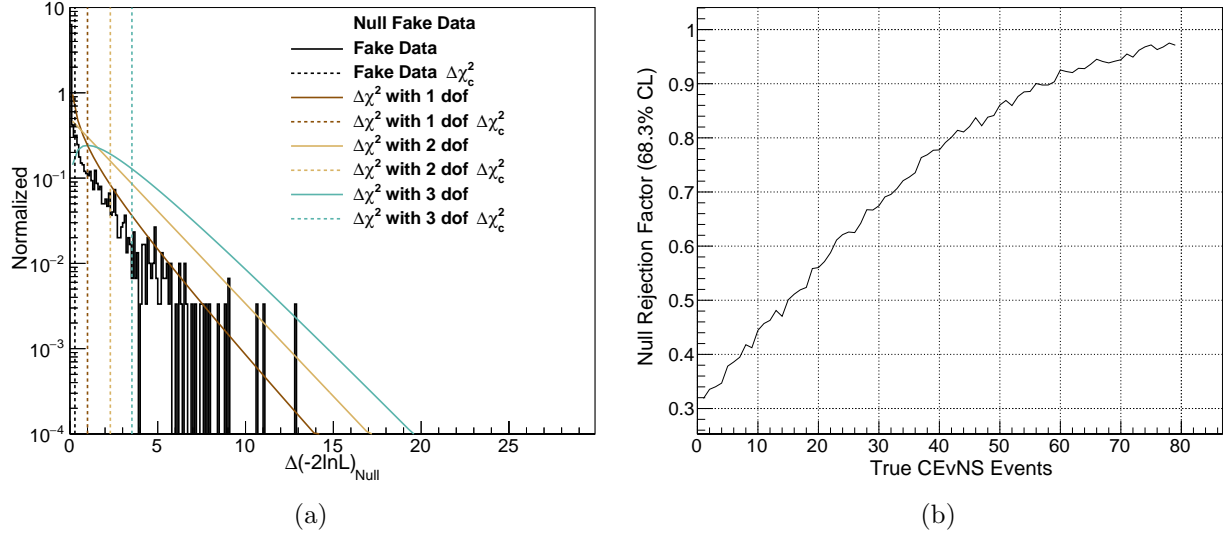


Figure 7.18: Sensitivity calculation following **SensMethod1**. (a) Null fake data delta log-likelihood distribution. Overlaid are χ^2 distributions with different degrees of freedom. The $\Delta\chi^2_c$ values shown here are the one-sigma values. (b) Fraction of fake datasets for varying the true N_{CEvNS} with $\Delta(-2\ln L)_{Null}$ greater than $\Delta\chi^2_c$. The experimental sensitivity is the number of CEvNS events for which this fraction is 50 %.

sensitivity is typically quoted along with the CL. The sensitivity was found in two different ways: **SensMethod1** and **SensMethod2**.

The sensitivity is the predicted confidence limit from an experiment based on background studies only. In other words it is the expected confidence limit that would be set from an ensemble of null experiments and represents the amount of signal necessary to cause a change in the experimental result at a given CL.

SENSMETHOD1 To find the sensitivity, 3000 null fake datasets (no signal) were generated. For each fake dataset, the likelihood ratio

$$\Delta(-2\ln L)_{Null} \equiv (-2\ln L)_{Null} - (-2\ln L)_{BF} \quad (7.5)$$

was calculated where $(-2\ln L)_{Null}$ is the value of the log-likelihood curve under the assumption of 0 events and $(-2\ln L)_{BF}$ is the best fit physically allowed log-likelihood value. A pdf based on the distribution of $\Delta(-2\ln L)_{Null}$ was formed and a critical χ^2 value, $\Delta\chi^2_c$, was found. $\Delta\chi^2_c$ is the

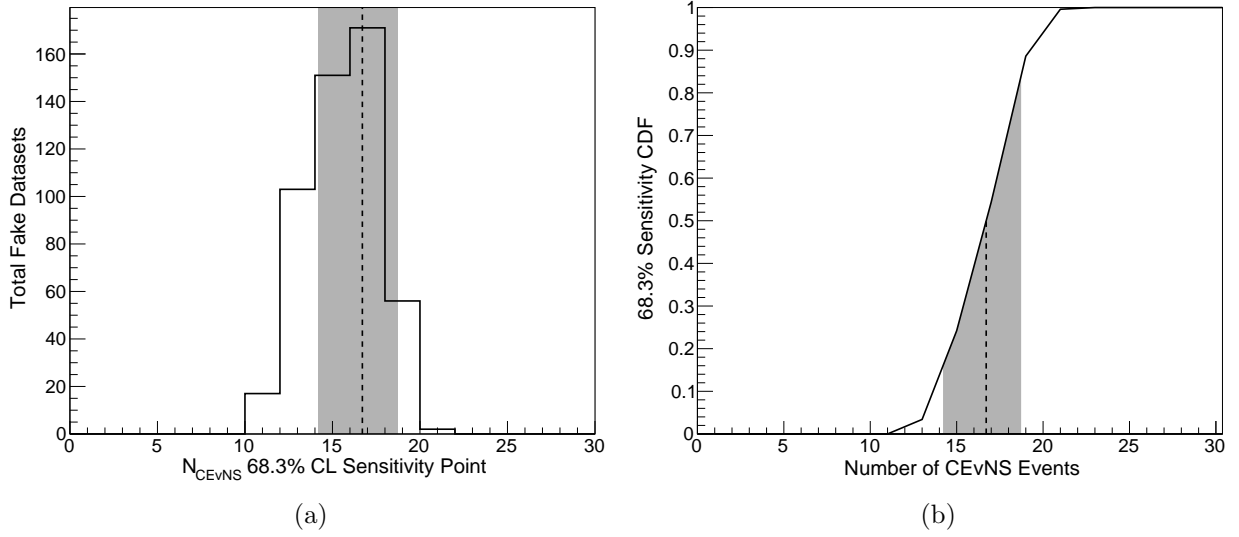


Figure 7.19: Sensitivity calculation following **SensMethod2**. (a) Distribution of sensitivities found for the fake datasets. (b) The cdf of the distribution found in (a). The $\pm 1\sigma$ uncertainty on the sensitivity is shown as the gray band with the central value shown as the dashed line.

value of $\Delta(-2\ln L)_{\text{Null}}$ where $x\%$ of the fake datasets have a smaller delta log-likelihood. In the case of a one-sigma limit, $x \equiv 68.3\%$. The pdf of these delta log-likelihood values for the central value pdfs can be seen in Fig. 7.18a along with χ^2 distributions for different numbers of degrees of freedom.

Then, to find the sensitivity, 1000 fake datasets for each true number of CEvNS events were generated and the fraction of the datasets with $(-2\ln L)_{\text{Null}} > \Delta\chi_c^2$ was found as seen in Fig. 7.18b. The experimental sensitivity is the true number of CEvNS events for which 50% of the fake datasets have $\Delta(-2\ln L)_{\text{Null}}$ greater than $\Delta\chi_c^2$. In the engineering run, this was found to be 15.2 events.

SENSMETHOD2 **SensMethod2** is an alternative method to calculate the experimental sensitivity following the CLs technique [126–128] that allows for an uncertainty on the sensitivity. This method makes use of the $\Delta(-2\ln L)_{\text{Null}}$ pdfs from **SensMethod1**. Here, an alternative $\Delta(-2\ln L)_{\text{Null}}$ pdf is generated by sampling from the original pdf 1000 times for each true N_{CEvNS} . A sensitivity is then found following the method of **SensMethod1** with these alternative pdfs. This is repeated 500 times. Each of these sensitivity values is histogrammed and the cdf of this histogram

is formed as seen in Fig. 7.19.

The sensitivity following this method is the value of N_{CEvNS} for which the cdf is 0.5. The cdf can also be used to find an uncertainty in the sensitivity. In the case of a one-sigma uncertainty, the $\pm 1\sigma$ values are the values of N_{CEvNS} for which the cdf is 0.50 ± 0.34 . **SensMethod2** gives a sensitivity of $16.7^{+2.0}_{-2.5}$. **SensMethod2** gives a weaker sensitivity than **SensMethod1**, but they do agree within 1σ .

SYSTEMATICS To incorporate systematic effects on the sensitivity, fake datasets were generated using one of the alternative systematic pdfs and the sensitivities were calculated as discussed above. Systematics were then incorporated into the **SensMethod1** result by finding the average sensitivity following this method for the CV pdf and all excursions. This gives a sensitivity S_1 of 15.3 events.

Systematic effects on the sensitivity following **SensMethod2** were considered as additional sources of uncertainty on the result S_2 . Following the same method as in the BRN result, the spread about the central-value sensitivity was found to be 1.6 events giving a final sensitivity of $16.7 + 2.0(stat.) - 2.5(stat) \pm 1.6(syst.)$ events.

7.4.5 CEVNS CROSS SECTION LIMIT

To place a limit on the CEvNS cross-section a fully frequentist version of the Feldman-Cousins prescription was followed [125]. This limit is based on the likelihood ratio test statistic $\Delta(-2 \ln L)_{true}$ defined as

$$\Delta(-2 \ln L)_{true} \equiv (-2 \ln L)_{BF} - (-2 \ln L)_{true} \quad (7.6)$$

where BF indicates the likelihood value at the physically allowed best-fit point, and $true$ indicates the likelihood value at the true number of CEvNS events.

All of the fake datasets necessary to generate the confidence limit (CL) on the number of CEvNS events were generated for the sensitivity calculation. To find the desired confidence limit

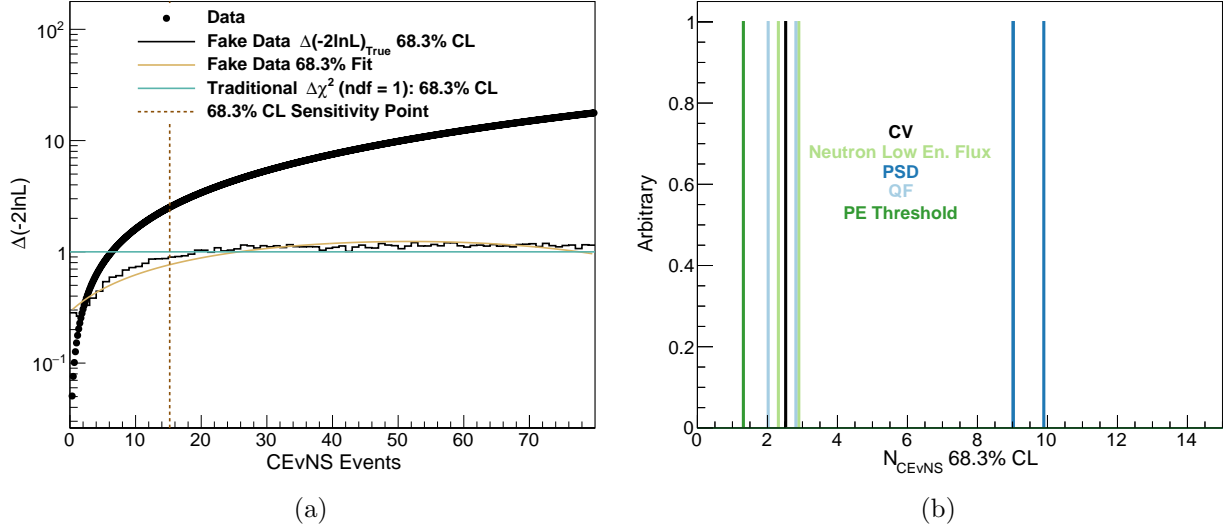


Figure 7.20: Placing a limit on the CEvNS cross section. (a) Illustration of the confidence limit procedure. The data log-likelihood curve is given by the black points. The one-sigma $\Delta\chi_c^2$ values from frequentist fake data are given by the black curve and the traditional one-sigma limit is given by the teal curve. The statistical limit is given by the intersection of the data points with the fake data $\Delta\chi_c^2$ curve. A stronger limit than would be expected is placed because the measured number of signal events was smaller than the predicted number of background events. For this reason, the sensitivity (vertical dashed curve from **SensMethod1**) is also quoted. (b) One-sigma limits on the number of CEvNS events for alternative systematic pdfs. The spread around the central value result gives the systematic uncertainty on the CEvNS limit.

on the number of CEvNS events, $\Delta(-2\ln L)_{true}$ was found for each fake dataset thrown. For each true N_{CEvNS} , the pdf of these likelihood ratios was formed, and a critical $\Delta\chi_c^2$ value is found. In this case, $\Delta\chi_c^2$ value is the $\Delta(-2\ln L)_{true}$ where x% of the fake datasets have a $\Delta(-2\ln L)_{true} < \Delta\chi_c^2$. A 2nd-degree polynomial fit to the $\Delta\chi_c^2$ curve was performed to smooth out any statistical fluctuations as seen in Fig. 7.20a.

The likelihood curve $\Delta(-2\ln L)$ relative to the best fit number of CEvNS events from beam data is then calculated. The statistical confidence limit is then defined as the intersection of the data curve with the fake data $\Delta\chi_c^2$ curve.

Following this method gives a one-sigma CL on the number of CEvNS events of fewer than 2.5 events. The non-chi-square behavior of the data likelihood curve is largely due to the relatively high levels of background and the small signal size of the Engineering Run. This is a better limit than might be expected from Wilks' theorem (the teal curve in Fig. 7.20a giving a limit

	Events	σ_{CEvNS}
CL	< 5.1	$< 24 \times 10^{-40} \text{ cm}^2$
S₁	15.3	$71 \times 10^{-40} \text{ cm}^2$
S₂	$16.7^{+2.0}_{-2.5}(\text{stat.}) \pm 1.6(\text{syst.})$	$\left(77^{+9}_{-12}(\text{stat.}) \pm 7(\text{syst.})\right) \times 10^{-40} \text{ cm}^2$
BRN	$126 \pm 18(\text{stat}) \pm 11(\text{syst})$	

Table 7.5: Summary of likelihood fit results. CEvNS results are from the one-sigma CL analysis. 3.9 CEvNS events and 143 BRN events were predicted.

of < 6.3 events) because the measured number of signal events was smaller than the predicted number of background events. Monte Carlo studies indicate that the downward fluctuation in the beam-unrelated background rate is consistent with expected statistical fluctuations.

SYSTEMATICS To incorporate systematic effects on the CL, the same procedure was performed for each alternative pdf. The spread of these one-sigma limits can be seen in Fig. 7.20b. The spread about the central value result is 4.5 events. Combining this in quadrature with the statistical limit of 2.5 events gives a one-sigma confidence limit of < 5.1 events. From this result and the Standard Model prediction, a one-sigma limit on the CEvNS cross section on Ar can be found:

$$\sigma_{CEvNS}^{\text{Ar}} < \frac{5.1}{3.9} 18 \times 10^{-40} \text{ cm}^2 < 24 \times 10^{-40} \text{ cm}^2 \quad (7.7)$$

The results from the likelihood analysis are summarized in Table. 7.5.

7.5 IMPLICATIONS FOR NON-STANDARD NEUTRINO INTERACTIONS

An interesting physics study from the Engineering Run result is to investigate implications on non-standard neutrino-quark interactions (see Sec. 1.2), in particular, the non-standard couplings ϵ_{ee}^{uV} and ϵ_{ee}^{dV} . Due to the small recoil energies induced by CEvNS, the introduction of these non-standard couplings to the CEvNS cross section results in an overall scaling relative to the Standard Model predicted cross section. The χ^2 analysis used for the CsI result [3] is not applicable to the liquid argon Engineering Run result as the liquid argon cross section was found following the FC

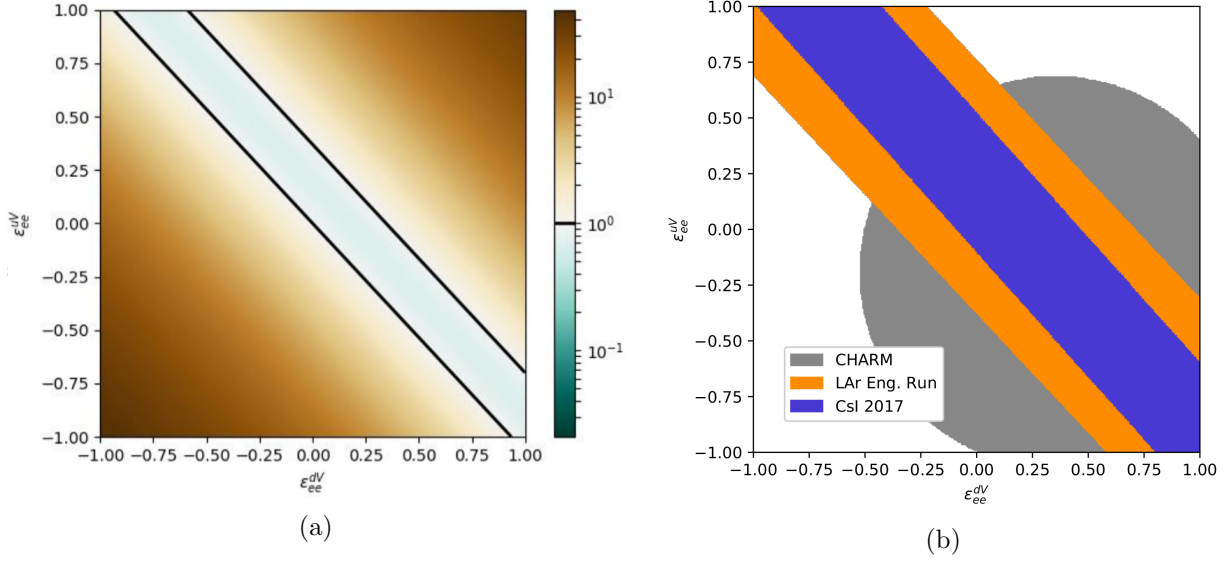


Figure 7.21: Constraints on non-standard neutrino interactions. (a) Change in the argon CEvNS cross section relative to the Standard Model prediction as the NSI parameters are varied. Points along the black lines have non-zero NSI couplings but result in the same cross section as the Standard Model prediction. (b) Limit on ϵ_{ee} parameters based on the Engineering Run results. While not competitive with the CsI result [3], we confirm that previous result and rule out much of the pre-COHERENT phase space. Plots courtesy of G. Sinev.

prescription.

To constrain the NSI couplings with the CENNS-10 Engineering Run result, a 90% confidence limit on the argon CEvNS cross section was found following the method outlined in Sec. 7.4.5. This limit was found to be $\sigma_{CEvNS}^{\text{Ar}} < 67 \times 10^{-40} \text{ cm}^2$.

Then, the flux-averaged CEvNS cross section relative to the Standard Model prediction can be calculated as a function of the NSI parameters ϵ_{ee}^{dV} and ϵ_{ee}^{uV} as seen in Fig. 7.21a. Finally, a band in $\epsilon_{ee}^{uV} : \epsilon_{ee}^{dV}$ space allowing modifications to the CEvNS cross section up to $\frac{67 \times 10^{-40} \text{ cm}^2}{18 \times 10^{-40} \text{ cm}^2} = 3.72$ can be mapped out. This result is shown in Fig. 7.21b. While the limit on the NSI couplings is not as stringent as the CsI result [3], this result confirms the CsI limits and is still capable of excluding much of the pre-COHERENT phase space.

CHAPTER 8

CONCLUSIONS

The COHERENT experiment is intending to measure the N^2 dependence of the CEvNS cross section. After the initial observation with 14.6 kg of CsI[Na], a liquid argon detector, CENNS-10, was installed to provide a low N nucleus for a CEvNS observation.

Prior to the installation of CENNS-10, a measurement of the beam-related neutron flux in the planned CENNS-10 location was made with the SciBath detector. This measurement was used to inform the shielding design for CENNS-10 and predict the expected beam-related neutron rate seen by CENNS-10.

CENNS-10 was installed in winter of 2016, and an Engineering Run was completed in the spring of 2017. This run provides a valuable constraint on the beam-related neutron (BRN) flux, in addition to the SciBath measurement, with an in-situ measurement inside the neutron shielding installed for the CEvNS measurement. The prompt BRN flux is non-negligible and it will remain an ongoing challenge to separate the prompt CEvNS signal from the BRNs. Investigations are underway regarding the most-efficient way to reduce this prompt-neutron flux. This measurement confirmed that the delayed BRN flux in Neutrino Alley is negligible.

Due to the lower than expected light output of 0.5 PEs/keVee, and the relatively short run time (only 1.5 GWh of integrated beam power) the Engineering Run was only able to place a limit on the CEvNS cross section on argon of $< 24 \times 10^{-40} \text{ cm}^2$ (68.3 % confidence limit) in agreement with the Standard Model prediction as seen in Fig. 8.1. Even with the limited signal statistics, low

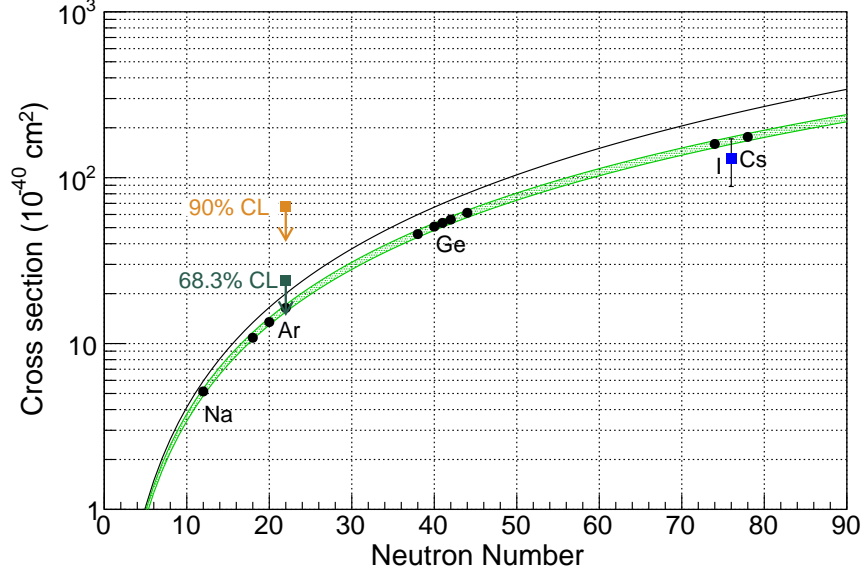


Figure 8.1: CEvNS cross section as a function of neutron number including the 68.3% and 90% confidence-limit values from the Engineering Run likelihood analysis.

light levels, and relatively high background rates present during the Engineering Run, constraints were set on non-standard neutrino interactions that rule out much of the pre-COHERENT phase space and confirm the earlier CsI[Na] result.

An extremely successful light collection upgrade was made to CENNS-10 in the summer of 2017, increasing the detected photon yield to ~ 4.3 PEs/keVee, and the CENNS-10 Production Run began in the fall of 2017. CENNS-10 is still running in this mode, collecting > 6 GWh and should see $\mathcal{O}(100)$ events) providing confirmation of the CsI[Na] observation of CEvNS.

COHERENT is working towards additional CEvNS detectors (NaI and Ge) to further map out the N^2 dependence of the cross section and developing tonne-scale detectors which will allow precision CEvNS measurements. This next generation of detectors will provide opportunities to investigate physics beyond the standard model, search for accelerator-produced dark matter, and look for nuclear structure in the CEvNS recoil spectra.

BIBLIOGRAPHY

- [1] F. J. Hasert et. al. Observation of neutrino-like interactions without muon or electron in the Gargamelle neutrino experiment. *Physics Letters B*, 46(1):138 – 140, 1973.
- [2] D. Z. Freedman. Coherent effects of a weak neutral current. *Phys. Rev. D*, 9:1389–1392, Mar 1974.
- [3] D. Akimov et al. Observation of coherent elastic neutrino-nucleus scattering. *Science*, 357(6356):1123–1126, 2017.
- [4] D. Akimov et al. COHERENT 2018 at the Spallation Neutron Source. 2018.
- [5] R. H. Helm. Inelastic and elastic scattering of 187-MeV electrons from selected even-even nuclei. *Phys. Rev.*, 104:1466–1475, Dec 1956.
- [6] R. Hofstadter. Electron scattering and nuclear structure. *Rev. Mod. Phys.*, 28:214–254, Jul 1956.
- [7] S. R. Klein and J. Nystrand. Exclusive vector meson production in relativistic heavy ion collisions. *Phys. Rev. C*, 60:014903, Jun 1999.
- [8] J. Barranco et al. Probing new physics with coherent neutrino scattering off nuclei. *Journal of High Energy Physics*, 2005(12):021, 2005.
- [9] K. A. Olive et al. Review of Particle Physics. *Chin. Phys.*, C38:090001, 2014.
- [10] S. J. Brice et al. A method for measuring coherent elastic neutrino-nucleus scattering at a far off-axis high-energy neutrino beam target. *Phys. Rev. D*, 89:072004, Apr 2014.
- [11] J. Erler et al. Weak mixing angle at low energies. *Phys. Rev. D*, 72:073003, Oct 2005.
- [12] M. Cadeddu et al. Average CsI neutron density distribution from COHERENT data. *Phys. Rev. Lett.*, 120:072501, Feb 2018.

- [13] M. Cadeddu and F. Dordei. Reinterpreting the weak mixing angle from atomic parity violation in view of the Cs neutron rms radius measurement from COHERENT. *Phys. Rev. D*, 99:033010, Feb 2019.
- [14] J. Barranco et al. Sensitivity of low energy neutrino experiments to physics beyond the standard model. *Phys. Rev. D*, 76:073008, Oct 2007.
- [15] B. Dutta et al. Sensitivity to z -prime and nonstandard neutrino interactions from ultralow threshold neutrino-nucleus coherent scattering. *Phys. Rev. D*, 93:013015, Jan 2016.
- [16] D. K. Papoulias and T. S. Kosmas. COHERENT constraints to conventional and exotic neutrino physics. *Phys. Rev. D*, 97:033003, Feb 2018.
- [17] L. M. Krauss. Low-energy neutrino detection and precision tests of the standard model. *Physics Letters B*, 269(3):407 – 411, 1991.
- [18] P. Coloma and T. Schwetz. Generalized mass ordering degeneracy in neutrino oscillation experiments. *Phys. Rev. D*, 94:055005, Sep 2016.
- [19] P. Coloma et al. Curtailing the dark side in non-standard neutrino interactions. *Journal of High Energy Physics*, 2017(4):116, Apr 2017.
- [20] S. Davidson et al. Present and future bounds on non-standard neutrino interactions. *Journal of High Energy Physics*, 2003(03):011, 2003.
- [21] J. Dorenbosch et al. Experimental verification of the universality of ν_e and ν_μ coupling to the neutral weak current. *Phys. Lett.*, B180:303–307, 1986.
- [22] K. Scholberg. Prospects for measuring coherent neutrino-nucleus elastic scattering at a stopped-pion neutrino source. *Phys. Rev. D*, 73:033005, Feb 2006.
- [23] D. Akimov et al. The COHERENT experiment at the Spallation Neutron Source. 2015.

- [24] P. Coloma et al. COHERENT enlightenment of the neutrino dark side. *Phys. Rev. D*, 96:115007, Dec 2017.
- [25] J. Billard et. al. Implication of neutrino backgrounds on the reach of next generation dark matter direct detection experiments. *Phys. Rev. D*, 89:023524, Jan 2014.
- [26] R. J. Gaitskell. Direct detection of dark matter. *Annual Review of Nuclear and Particle Science*, 54(1):315–359, 2004.
- [27] C.D. Ott et. al. Core-collapse supernovae, neutrinos, and gravitational waves. *Nuclear Physics B - Proceedings Supplements*, 235-236:381 – 387, 2013. The XXV International Conference on Neutrino Physics and Astrophysics.
- [28] H.-T. Janka. *Neutrino Emission from Supernovae*, pages 1–30. Springer International Publishing, Cham, 2016.
- [29] C. J. Horowitz et. al. Supernova observation via neutrino-nucleus elastic scattering in the CLEAN detector. *Phys. Rev. D*, 68:023005, Jul 2003.
- [30] H. De Vries et. al. Nuclear charge-density-distribution parameters from elastic electron scattering. *Atomic Data and Nuclear Data Tables*, 36(3):495 – 536, 1987.
- [31] K. Patton et al. Neutrino-nucleus coherent scattering as a probe of neutron density distributions. *Phys. Rev. C*, 86:024612, Aug 2012.
- [32] A. B. Brown. Neutron radii in nuclei and the neutron equation of state. *Phys. Rev. Lett.*, 85:5296–5299, Dec 2000.
- [33] C. J. Horowitz and J. Piekarewicz. Neutron star structure and the neutron radius of ^{208}Pb . *Phys. Rev. Lett.*, 86:5647–5650, Jun 2001.

- [34] P. S. Amanik and G. C. McLaughlin. Nuclear neutron form factor from neutrino-nucleus coherent elastic scattering. *Journal of Physics G: Nuclear and Particle Physics*, 36(1):015105, 2009.
- [35] S. Abrahamyan et al. Measurement of the neutron radius of ^{208}Pb through parity violation in electron scattering. *Phys. Rev. Lett.*, 108:112502, Mar 2012.
- [36] A. Drukier and L. Stodolsky. Principles and applications of a neutral-current detector for neutrino physics and astronomy. *Phys. Rev. D*, 30:2295–2309, Dec 1984.
- [37] J. Billard et al. Coherent neutrino scattering with low temperature bolometers at Chooz reactor complex. *Journal of Physics G: Nuclear and Particle Physics*, 44(10):105101, 2017.
- [38] A. Aguilar-Arevalo et al. The CONNIE experiment. *Journal of Physics: Conference Series*, 761(1):012057, 2016.
- [39] G. Agnolet et al. Background studies for the MINER coherent neutrino scattering reactor experiment. *Nuclear Instruments and Methods in Physics Research Section A: Accelerators, Spectrometers, Detectors and Associated Equipment*, 853:53 – 60, 2017.
- [40] R. Strauss et al. The ν -cleus experiment: a gram-scale fiducial-volume cryogenic detector for the first detection of coherent neutrino–nucleus scattering. *The European Physical Journal C*, 77(8):506, Jul 2017.
- [41] F. Moroni et al. Charge coupled devices for detection of coherent neutrino-nucleus scattering. *Phys. Rev. D*, 91:072001, Apr 2015.
- [42] A. Aguilar-Arevalo et al. Results of the engineering run of the coherent neutrino nucleus interaction experiment (CONNIE). *Journal of Instrumentation*, 11(07):P07024–P07024, jul 2016.
- [43] W. Maneschg. The status of CONUS, June 2018.

- [44] T.E. Mason et al. The Spallation Neutron Source in Oak Ridge: A powerful tool for materials research. *Physica B: Condensed Matter*, 385-386:955 – 960, 2006.
- [45] Spallation Neutron Source. <https://neutrons.ornl.gov/sns>. Accessed: 1/15/2019.
- [46] S. Agostinelli et al. Geant4: A simulation toolkit. *Nucl. Instrum. Meth.*, A506:250–303, 2003.
- [47] J. Allison et al. Geant4 developments and applications. *IEEE Transactions on Nuclear Science*, 53(1):270–278, Feb 2006.
- [48] M. Harada et al. Proposal: A search for sterile neutrino at J-PARC Materials and Life Science Experimental Facility. 2013.
- [49] S. Axani et al. Decisive disappearance search at high Δm^2 with monoenergetic muon neutrinos. *Phys. Rev. D*, 92:092010, Nov 2015.
- [50] O. Moreno and T. W. Donnelly. A unified approach to electron and neutrino elastic scattering off nuclei with an application to the study of the axial structure. *Phys. Rev. C*, 92:055504, Nov 2015.
- [51] F. T. Avignone III and Y. V. Efremenko. Neutrino-nucleus cross-section measurements at intense, pulsed spallation sources. *Journal of Physics G: Nuclear and Particle Physics*, 29(11):2615, 2003.
- [52] J. A. Formaggio and G. P. Zeller. From eV to EeV: neutrino cross sections across energy scales. *Rev. Mod. Phys.*, 84:1307–1341, Sep 2012.
- [53] S. Nakamura et al. Neutrino-deuteron reactions at solar neutrino energies. *Nuclear Physics A*, 707(3):561 – 576, 2002.
- [54] N. Mascarenhas et al. Results with the Neutron Scatter Camera. *IEEE Transactions on Nuclear Science*, 56(3):1269–1273, June 2009.

- [55] R. Tayloe et al. A large-volume detector capable of charged-particle tracking. *Nucl. Instrum. Meth.*, 562:198, June 2006.
- [56] L. Garrison. *Measurement of Neutron and Muon Fluxes 100m Underground with the SciBath Detector*. PhD thesis, Indiana University, Bloomington, 2014.
- [57] P. deNiverville et al. Light new physics in coherent neutrino-nucleus scattering experiments. *Phys. Rev. D*, 92:095005, Nov 2015.
- [58] P. deNiverville et al. Light dark matter in neutrino beams: Production modeling and scattering signatures at MiniBooNE, T2K, and SHiP. *Phys. Rev. D*, 95:035006, Feb 2017.
- [59] S. Ge and I. M. Shoemaker. Constraining photon portal dark matter with TEXONO and COHERENT data. *Journal of High Energy Physics*, 2018(11):66, Nov 2018.
- [60] A. Aguilar-Arevalo et al. Dark matter search in a proton beam dump with MiniBooNE. *Phys. Rev. Lett.*, 118:221803, May 2017.
- [61] E. Kolbe and K. Langanke. The role of ν -induced reactions on lead and iron in neutrino detectors. *Phys. Rev. C*, 63:025208, 2001.
- [62] J. Engel et al. What can be learned from a lead-based supernova neutrino detector. *Phys. Rev. D*, 67:013005, 2003.
- [63] J. I. Collar et al. Coherent neutrino-nucleus scattering detection with a CsI[Na] scintillator at the SNS spallation source. *Nucl. Instrum. Meth.*, A773:56–65, 2015.
- [64] Detective-100t hpge-based hand-held radioisotope identifier. <https://www.ortec-online.com/products/nuclear-security-and-safeguards/hand-held-radioisotope-identifiers-riids/detective-100t>. Accessed 1/9/2017.

- [65] Tech. Rep. SNS 102030102-ES0016-R03. Spallation Neutron Source final safety assessment document for neutron facilities. Technical report, Spallation Neutron Source, Oak Ridge National Lab, 2011.
- [66] X-5 Monte Carlo Team. MCNP-version 5, vol. i: Overview and theory, 2003.
- [67] M. R. Heath et al. Flux measurements and background simulation results for the CENNS-10 liquid argon detector at the SNS. Technical report, Indiana University, New Mexico State University, 2017. COHERENT Technical Note 4.
- [68] P. Benetti et al. Measurement of the specific activity of ^{39}Ar in natural argon. *Nuclear Instruments and Methods in Physics Research Section A: Accelerators, Spectrometers, Detectors and Associated Equipment*, 574(1):83 – 88, 2007.
- [69] H.O. Back et al. Depleted argon from underground sources. *Physics Procedia*, 37:1105 – 1112, 2012. Proceedings of the 2nd International Conference on Technology and Instrumentation in Particle Physics (TIPP 2011).
- [70] H. O. Back et al. First large scale production of low radioactivity argon from underground sources. 2012. arXiv:1206.6024 [astro-ph.IM].
- [71] P. Agnes et al. Results from the first use of low radioactivity argon in a dark matter search. *Phys. Rev. D*, 93:081101, Apr 2016.
- [72] R. Lazauskas and C. Volpe. Low-energy neutrino scattering measurements at future spallation source facilities. *Journal of Physics G: Nuclear and Particle Physics*, 37(12):125101, Nov 2010.
- [73] R. Lazauskas and C. Volpe. Corrigendum: Low-energy neutrino scattering measurements at future spallation source facilities (2010 J. Phys. G: Nucl. Part. Phys. 37(12):125101). *Journal of Physics G: Nuclear and Particle Physics*, 42(5):059501, Mar 2015.

- [74] G. M. Fuller et al. Prospects for detecting supernova neutrino flavor oscillations. *Phys. Rev. D*, 59:085005, Mar 1999.
- [75] E. Kolbe and K. Langanke. Role of ν -induced reactions on lead and iron in neutrino detectors. *Phys. Rev. C*, 63:025802, Jan 2001.
- [76] J. Engel et al. What can be learned with a lead-based supernova-neutrino detector? *Phys. Rev. D*, 67:013005, Jan 2003.
- [77] C. A. Duba et al. HALO – the helium and lead observatory for supernova neutrinos. *Journal of Physics: Conference Series*, 136(4):042077, Nov 2008.
- [78] D. Väänänen and C. Volpe. The neutrino signal at HALO: learning about the primary supernova neutrino fluxes and neutrino properties. *Journal of Cosmology and Astroparticle Physics*, 2011(10):019–019, Oct 2011.
- [79] S. E. Woosley et al. The nu-process. *APJ*, 356:272–301, June 1990.
- [80] Y.-Z. Qian et al. Neutrino-induced neutron spallation and supernova r -process nucleosynthesis. *Phys. Rev. C*, 55:1532–1544, Mar 1997.
- [81] Eljen technology. www.eljentechnology.com. Accessed 1/30/2019.
- [82] Saint-Gobain crystals. <https://www.crystals.saint-gobain.com>. Accessed 1/30/2019.
- [83] R00 SSNS 1090200200-TD00006. SNS timing master functional system description. Technical report, ORNL SNS, 2011.
- [84] E. Padovani et al. MCNPX-PoliMi users manual.
- [85] J. B. Birks. Scintillations from organic crystals: Specific fluorescence and relative response to different radiations. *Proceedings of the Physical Society. Section A*, 64(10):874–877, Oct 1951.

- [86] S. Miyake. Rapporteur paper on muons and neutrinos. *International Cosmic Ray Conference*, 5:3638–3655, 1973. Denver 1973.
- [87] A. Höcker et al. SVD approach to data unfolding. *Nucl. Instrum. Meth.*, A372:469–481, 1996.
- [88] B. Braizinha et al. Determination of the proton and alpha-particle light-response functions for the KamLAND, BC-501A and BC-517H liquid scintillators. *Nucl. Instrum. Meth.*, 623:1046–1049, Nov 2010.
- [89] L. N. Bogdanova et al. Cosmic muon flux at shallow depths underground. *Phys. Atom Nucl.*, 69:1293–1298, 2006.
- [90] T. Doke et al. Estimation of absolute photon yields in liquid argon and xenon for relativistic (1 MeV) electrons. *Nucl. Instrum. Meth.*, A291:617–620, 1990.
- [91] D. Gastler et al. Measurement of scintillation efficiency for nuclear recoils in liquid argon. *Phys. Rev. C*, 85:065811, Jun 2012.
- [92] P. Agnes et al. Measurement of the liquid argon energy response to nuclear and electronic recoils. *Phys. Rev. D*, 97:112005, Jun 2018.
- [93] H. Cao et al. Measurement of scintillation and ionization yield and scintillation pulse shape from nuclear recoils in liquid argon. *Phys. Rev. D*, 91:092007, May 2015.
- [94] W. Creus et al. Scintillation efficiency of liquid argon in low energy neutron-argon scattering. *Journal of Instrumentation*, 10(08):P08002–P08002, aug 2015.
- [95] P.-A. Amaudruz et al. Measurement of the scintillation time spectra and pulse-shape discrimination of low-energy β and nuclear recoils in liquid argon with DEAP-1. *Astroparticle Physics*, 85:1 – 23, 2016.

- [96] P. Benetti et al. First results from a dark matter search with liquid argon at 87K in the Gran Sasso underground laboratory. *Astroparticle Physics*, 28(6):495 – 507, 2008.
- [97] W. H. Lippincott et al. Scintillation time dependence and pulse shape discrimination in liquid argon. *Phys. Rev. C*, 78:035801, Sep 2008.
- [98] Cryomech PT90 Cryocoolers. <https://www.cryomech.com/products/pt90/>. Accessed 2/13/2019.
- [99] V. M. Gehman et al. Fluorescence efficiency and visible re-emission spectrum of tetraphenyl butadiene films at extreme ultraviolet wavelengths. *Nucl. Instrum. Meth.*, A654:116–121, 2011.
- [100] C. Benson et al. Measurements of the intrinsic quantum efficiency and absorption length of tetraphenyl butadiene thin films in the vacuum ultraviolet regime. *The European Physical Journal C*, 78(4):329, Apr 2018.
- [101] C.H. Lally et al. UV quantum efficiencies of organic fluors. *Nuclear Instruments and Methods in Physics Research Section B: Beam Interactions with Materials and Atoms*, 117(4):421 – 427, 1996.
- [102] D. N. McKinsey et al. Fluorescence efficiencies of thin scintillating films in the extreme ultraviolet spectral region. *Nuclear Instruments and Methods in Physics Research Section B: Beam Interactions with Materials and Atoms*, 132(3):351 – 358, 1997.
- [103] P. Agnes et al. First results from the DarkSide-50 dark matter experiment at Laboratori Nazionali del Gran Sasso. *Physics Letters B*, 743:456 – 466, 2015.
- [104] <http://www.saespuregas.com/Products/Gas-Purifier/PS4-MT315.html>. Accessed 4/1/2018.

- [105] Digital delay generator DG535. <https://www.thinksrs.com/products/dg535.html>. Accessed 2/15/19.
- [106] A. Hitachi et al. Effect of ionization density on the time dependence of luminescence from liquid argon and xenon. *Phys. Rev. B*, 27:5279–5285, May 1983.
- [107] A. Hitachi et al. Luminescence quenching in liquid argon under charged-particle impact: relative scintillation yield at different linear energy transfers. *Phys. Rev. B*, 46:11463–11470, Nov 1992.
- [108] B. Jones. Introduction to scintillation light in liquid argon. Slide 6, 2014.
- [109] C. Regenfus et al. Study of nuclear recoils in liquid argon with monoenergetic neutrons. *Journal of Physics: Conference Series*, 375(1):012019, jul 2012.
- [110] S. Himi et al. Liquid and solid argon, and nitrogen doped liquid and solid argon scintillators. *Nucl. Instrum. Meth.*, 203:153–157, 1982.
- [111] R. Acciarri et al. Effects of nitrogen contamination in liquid argon. *JINST*, 5:P06003, June 2010.
- [112] <http://www.lldetek.com/our-products/ld8000/>. Accessed 4/1/2018.
- [113] T. Marrodán Undagoitia and L. Rauch. Dark matter direct-detection experiments. *Journal of Physics G: Nuclear and Particle Physics*, 43(1):013001, dec 2015.
- [114] <http://www.thinksrs.com/products/UGA.htm>. Accessed 4/1/2018.
- [115] <https://www.rigolna.com/products/waveform-generators/dg4162/>. Accessed 3/29/2019.
- [116] B. Loer. *Towards a Depleted Argon Time Projection Chamber WIMP Search: DarkSide Prototype Analysis and Predicted Sensitivity*. PhD thesis, Princeton University, 2011.

- [117] B. Loer. daqman. <https://github.com/bloer/daqman/tree/master>, 2016.
- [118] A. G. Wright. *The Photomultiplier Handbook*. Oxford University Press, 2017.
- [119] M. R. Heath and J. Zettlemoyer. CENNS-10 simulation readme. Technical report, Indiana University, 2018.
- [120] W. Verkerke and D. Kirkby. The RooFit toolkit for data modeling. Technical Report physics/0306116, SLAC, Stanford, CA, Jun 2003.
- [121] W. Verkerke and D. Kirkby. RooFit Users Manual v2.91. Technical report, SLAC, Stanford, CA, Oct 2008.
- [122] G. Cowan. Statistical data analysis stat 3: p -values, parameter estimation, 2018. Lecture notes set 3. www.pp.rhul.ac.uk/~cowan/stat_course.html.
- [123] S. S. Wilks. The large-sample distribution of the likelihood ratio for testing composite hypotheses. *Ann. Math. Statist.*, 9(1):60–62, 03 1938.
- [124] G. J. Feldman and R. D. Cousins. Unified approach to the classical statistical analysis of small signals. *Phys. Rev. D*, 57:3873–3889, Apr 1998.
- [125] R. T. Thornton. *Search for Light Dark Matter Produced in a Proton Beam Dump*. PhD thesis, Indiana University, Bloomington, 2017.
- [126] D. S. Akerib et al. Results from a search for dark matter in the complete LUX exposure. *Phys. Rev. Lett.*, 118:021303, Jan 2017.
- [127] A. L. Read. Presentation of search results: The CL(s) technique. *J. Phys.*, G28:2693–2704, 2002.
- [128] G. Cowan et al. Asymptotic formulae for likelihood-based tests of new physics. *The European Physical Journal C*, 71(2):1554, Feb 2011.

- [129] R. L. Cooper. Extracting thermal flux with SciBath. Tech note on re-weighting SciBath capture gamma simulation, September 2015.
- [130] M. R. Heath. Effects of induced N₂ contamination of the CENNS-10 detector. Technical report, 2017. COHERENT Technical Note 10.
- [131] E. Morikawa et al. Argon, krypton, and xenon excimer luminescence: From the dilute gas to the condensed phase. *The Journal of Chemical Physics*, 91(3):1469–1477, 1989.
- [132] M. Kase et al. Fano factor in pure argon. *Nuclear Instruments and Methods in Physics Research Section A: Accelerators, Spectrometers, Detectors and Associated Equipment*, 227(2):311 – 317, 1984.
- [133] E. L. Snider and G. Petrillo. LArSoft: Toolkit for simulation, reconstruction and analysis of liquid argon tpc neutrino detectors. *J. Phys. Conf. Ser.*, 898(4):042057, 2017.

APPENDIX A

SCIBATH CAPTURE SIMULATION RE-WEIGHTING

Courtesy of R. L. Cooper (from [129]). Reprinted here for ease of access:

Suppose N_0 neutrons are generated from a spherical source of radius r and emitted inward with a $\cos \theta$ distribution. Then the flux ϕ_0 is

$$\phi_0 = \frac{N_0}{(4\pi r^2) \left(\int_0^{2\pi} d\phi \int_{-1}^0 d(\cos \theta) \cos \theta \right)} = \frac{N_0}{4\pi^2 r^2} \quad (\text{A.1})$$

MCNP is used to simulate these neutrons and determine the capture position within SciBath. To accomplish this, SciBath is binned (or voxelized) in 3D. The simulation tells us the fraction f_i of generated neutrons that capture in bin i . Note, $\sum_i f_i < 1$ because many neutrons will escape without capturing. Here $f_i = n_{ci}/N_0$ where n_{ci} is the integer number of captures in bin i from the MCNP simulations with N_0 generated neutrons.

Of the n_{ci} captures in bin i , a fraction ϵ_i will emit a 2.2 MeV gamma ray that passes analysis cuts (e.g., PEs, fiducial, etc.). ϵ_i is calculated from the **Geant4** simulation. It is the ratio of m_i events generated in bin i AND pass analysis cuts to the total number of events M_i generated in bin i , i.e., $\epsilon_i = m_i/M_i$.

Finally, we are in position to calculate the total number of captures expected when N_0 are generated. Each bin contributes $N_0 f_i \epsilon_i$ captures. The total number of detected events $m_d =$

$N_0 \sum_i f_i \epsilon_i$. Furthermore, the initial flux ϕ_0 is now connected to the number of detected events

$$\frac{m_d}{\phi_0} = (4\pi^2 r^2) \frac{m_d}{N_0} = (4\pi^2 r^2) \frac{N_0 \sum_i f_i \epsilon_i}{N_0} = (4\pi^2 r^2) \sum_i f_i \epsilon_i. \quad (\text{A.2})$$

Suppose SciBath takes data and collects n_d detected events after cuts. The ratio of the detected events to the flux should be the same in data as simulation, i.e.. $m_d/\phi_0 = n_d/\phi$. Using simulations to calculate ϵ_i and f_i with the same cuts, the flux ϕ is

$$\phi = n_d \left(\frac{\phi_0}{m_d} \right) = n_d \left(\frac{m_d}{\phi_0} \right)^{-1} = \frac{n_d}{(4\pi^2 r^2) (\sum_i f_i \epsilon_i)}. \quad (\text{A.3})$$

APPENDIX B

CENNS-10 N₂ DOPING TEST

This appendix is a summary of the N₂ doping tests performed with CENNS-10. Further details can be found in [130].

B.1 MOTIVATION

To ensure the quality of the liquid argon (LiqAr) in CENNS-10, the detector boiloff is circulated through a gas handling rack with a SAES PS4-MT3-R-1 Zr getter [104]. For a reasonable getter lifetime, a starting purity of 5-nines (99.999%) Ar is necessary. A single getter cartridge allows ~20 fills of a ~60 kg detector with 5-nines Ar. An Airgas representative unofficially informed us that the boiloff from their LiqAr dewars is the same quality as the 5-nines UHP cylinders they sell. Therefore, CENNS-10 was filled with LiqAr boiloff as it is more cost effective than purchasing 5-nines UHP cylinders.

Before the initial fill of CENNS-10 at IU, a significant amount of effort was spent on ensuring that the boiloff Ar was the same quality as an example 5-nines cylinder through the use of an SRS UGA [114] and an LDetek LD8000 N₂ monitor [112]. In addition, when CENNS-10 was filled at IU during the summer of 2016, the getter was not used until the detector was full. This allowed the change in the electronic recoil (ER) PSD band as the Ar was purified to be seen (see Fig B.11). Note that there are no data quality cuts (pileup etc) placed on these plots. As these are from a high-rate ⁶⁰Co dataset, there is likely a lot of pileup present.

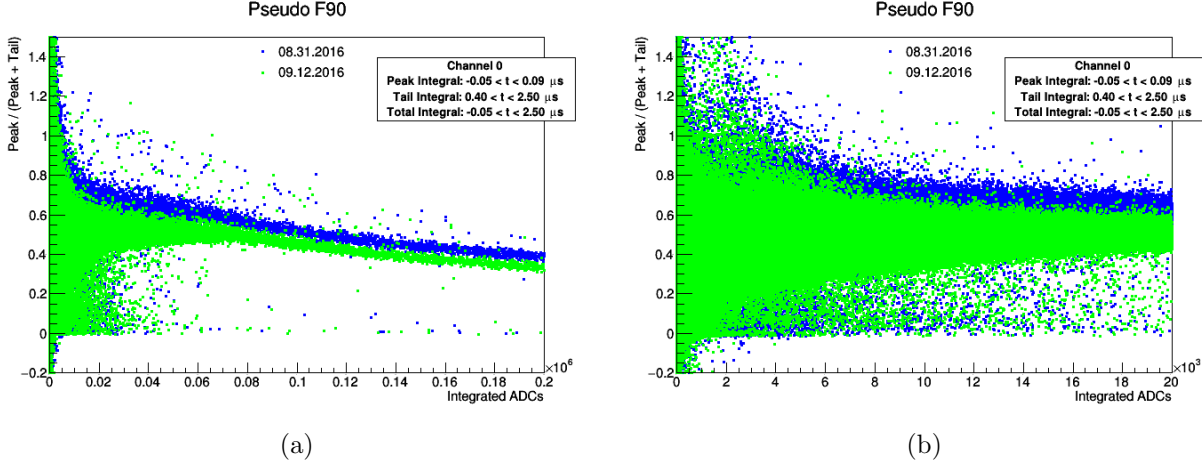


Figure B.11: Illustration of the shift of electronic recoil (ER) PSD band while purifying during summer 2016 CENNS-10 system testing at Indiana University. (a) Full energy range. (b) Zoom to low energies. There are no data quality cuts on these plots. After purification, the ER band is seen to drift to lower PSD values indicating a larger component of triplet scintillation light and therefore lower levels of N_2 contamination.

Although checked with an SRS UGA before filling, the boiloff of the liquid argon dewar at the SNS was never systematically checked. The argon gas also passed through the getter as CENNS-10 was filled at the SNS, so no change in the ER PSD band was observed. To make sure the light yield issues in the Engineering Run were not due to N_2 contamination, the decision was made to introduce ~ 25 ppm of N_2 to the detector after the beam shutoff in June 2017. To characterize the amount of N_2 contamination in CENNS-10, the detector boiloff gas was monitored with the UGA and N_2 monitor and the triplet lifetime measured both before and after introducing N_2 into the system.

B.2 PROCEDURE

B.2.1 N_2 LEVELS

Based on the results of [111], it was decided to add ~ 25 ppm by mass of N_2 into the system. Under the assumption that 68 kg of argon were in the system, 1.2 g (0.04 mol) of N_2 gives 25 ppm. To introduce the N_2 into the system, a Cu fill tube with an inner volume of $\sim 9 \times 10^{-5} \text{ m}^3$ was used. The tube was filled to 8 psi ($1.56 \times 10^5 \text{ Pa}$) for each ‘fill,’ requiring a total of seven tubes of N_2 to

reach 25 ppm of N_2 in the system.

B.2.2 TEST PREPARATION

The plumbing used for the gas quality tests can be seen in Fig. B.22.

Prior to any sort of gas tests, the UGA was baked out to remove any contamination and had an internal pressure of 6×10^{-9} Torr.

Before any valid readings from the LD8000, it must be purged with 99.999% pure Ar for a minimum of 24 h. Following a 24 h purge from the UHP cylinder in Neutrino Alley, (which was used to top off the detector following the power shutdown in January 2017), the LD8000 gave a reading of 39 ppm. A 5-nines cylinder should contain less than 1 ppm of N_2 contamination indicating this cylinder had become contaminated with N_2 at some point. This cylinder was replaced with a new UHP cylinder, and the purge repeated. ~20 h later, the LD8000 read 9.6 ppm. When valve GQV-6 was opened to allow UGA tests of the gas, the N_2 level dropped to 1.5 ppm. This is still an unresolved issue. For the remainder of the tests, N_2 readings with valve GQV-6 closed and open were taken. Gas from the UHP Ar cylinder was allowed to flow through the LD8000 while the N_2 contamination was mixing in the detector volume.

The LD8000 requires at least 4 psi input gas (10 psi is optimal). While the LD8000 was being purged, the pressure in CENNS-10 was brought up to 5 psi.

B.2.3 TESTS PERFORMED

Multiple tests were taken both before and after adding the N_2 contamination: (1) direct N_2 measurements with the LD8000 and (2) measurements of the triplet lifetime.

N_2 TESTS N_2 tests were taken both before and after adding the N_2 doping. Following the LD8000 detector purge, these consisted of allowing gas to flow through the LD8000 for ~5 min until the reading stabilized. Readings were taken of both a UHP cylinder (as a control), and of the gas circulating in CENNS-10. In both cases, data was taken with the valve to the UGA (GQV-6)

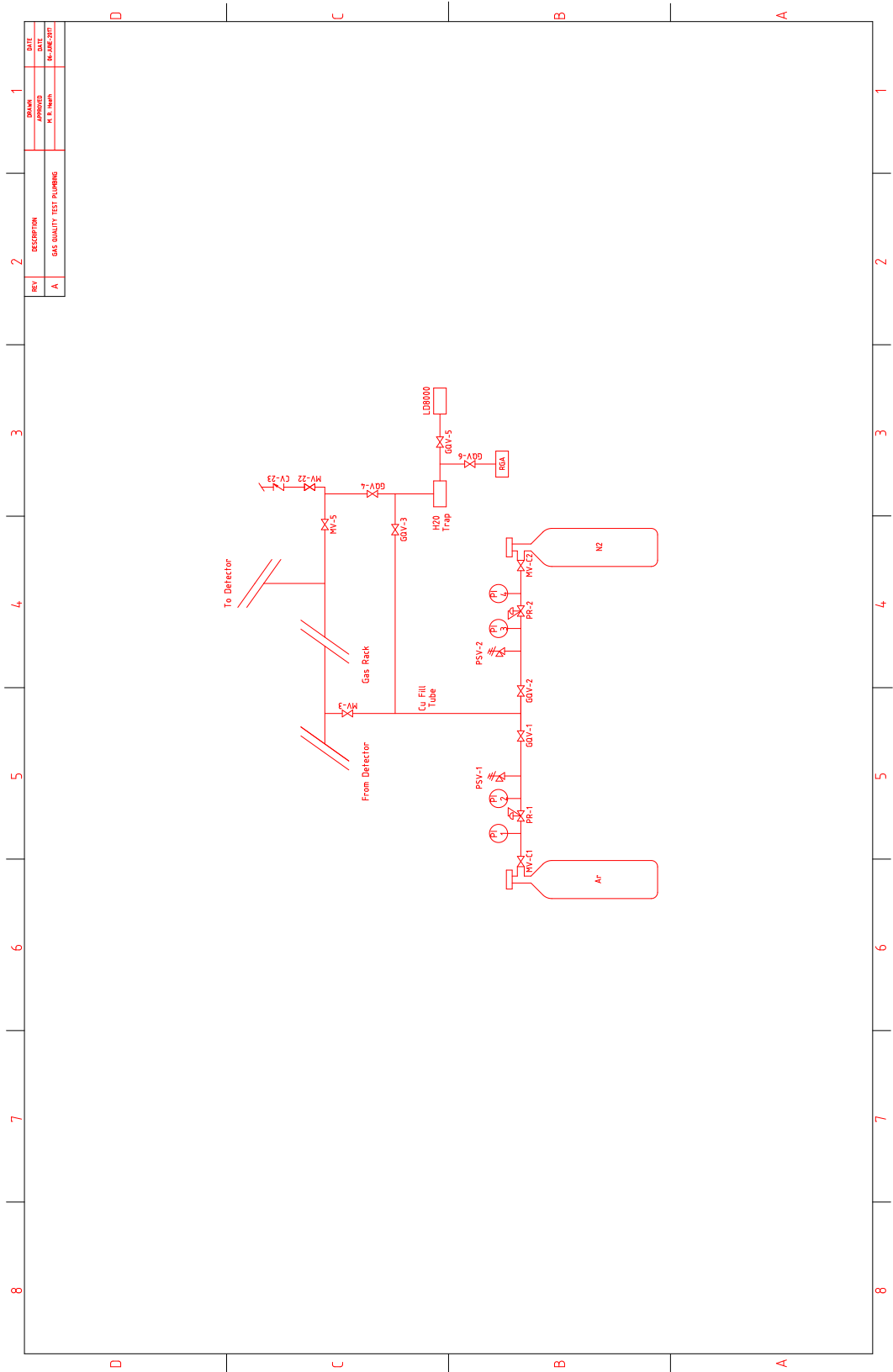


Figure B.22: Plumbing used for the gas quality tests.

Table B.21: Summary of LD8000 readings before and after N₂ doping.

	Pre-Doping		Post-Doping	
	GQV-6 Closed	GQV-6 Open	GQV-6 Closed	GQV-6 Open
UHP Ar	10 ppm	1.5 ppm	9 ppm	1 ppm
Detector Gas	8 ppm	1.3 ppm	30 ppm	22 ppm

both open and closed. For these tests, the gas from the cylinder and detector system were both at 5 psi.

CALIBRATION RUNS As N₂ contamination has the largest effect on the triplet scintillation light, data was taken with a 1 μ Ci ¹³⁷Cs source both before and after the N₂ doping to examine the change in pulse shapes after the introduction of N₂ into the system.

B.2.4 N₂ INTRODUCTION

Only 6 tubes of N₂ were added to allow for any volumes not accounted for (there was some extra tubing etc). The N₂ was allowed to mix overnight before any tests were taken.

B.3 RESULTS

B.3.1 PRE N₂ DOPING

N₂ MONITOR As stated above, there were 2 different N₂ readings depending on if the valve to the UGA was open or closed. The LD8000 readings are summarized in Table B.21 For the UHP cylinder, the reading was 10 ppm with the valve closed and 1.5 ppm with the valve open. For the detector gas system, the reading was 8 ppm with the valve closed, and 1.3 ppm with the valve open.

CALIBRATION RUNS The triplet lifetime from a background run taken on June 30, was fit in Fig. B.33. To be included in the average waveform, an individual waveform must have a minimum pulse height of 100 ADCs, and a maximum pulse height of 3000 ADCs. The triplet light was fit with the sum of a decaying exponential, a ringing oscillator, and a constant offset to account

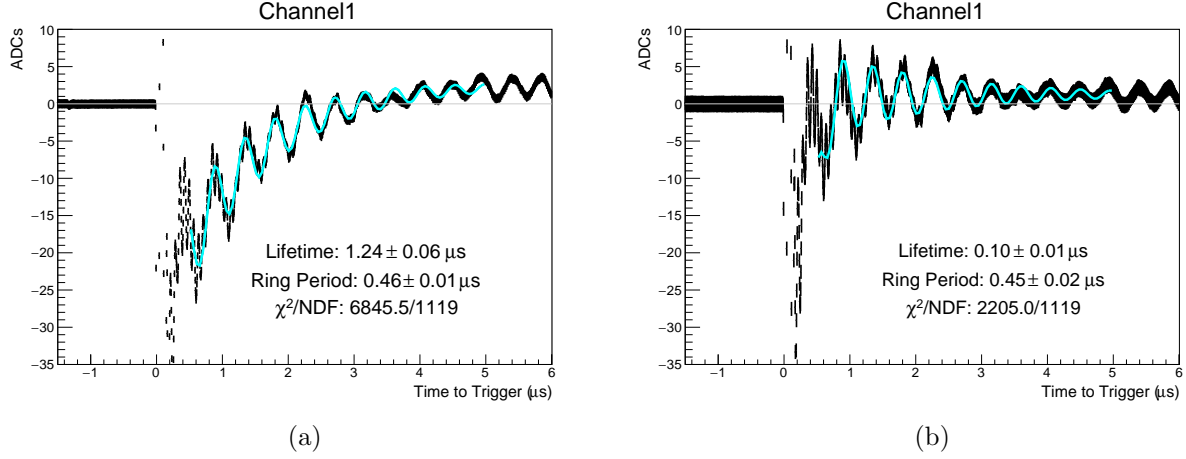


Figure B.33: Comparison of average waveforms from a ^{137}Cs dataset (a) before and (b) after N_2 doping. The nitrogen contamination is seen to quench the scintillation light from dimers in the triplet state. These lifetimes are consistent with a N_2 level of 1 ppm before and 25 ppm after the nitrogen doping.

for the overshooting beginning at $\sim 3.5 \mu\text{s}$:

$$f(t) = A \cdot e^{-t/\tau_{trip}} + B \cdot \sin((t + t_0) * \omega) \cdot e^{-t/\tau_{osc}} + C \quad (\text{B.1})$$

The average waveform for channel 1 has a triplet lifetime of $1.24 \mu\text{s}$. The lifetime for channel 3 is $1.20 \mu\text{s}$. This corresponds to a N_2 contamination of ~ 1 ppm [111].

B.3.2 POST N_2 DOPING

N_2 MONITOR Again, readings were taken with the UGA valve open and closed for both the detector gas as well as the UHP cylinder. For the UHP cylinder, the N_2 reading was 9 ppm with the valve to the UGA closed. With the valve open, the reading was 1 ppm. For the detector gas, the N_2 reading was 30 ppm with the valve closed. The reading was 23 ppm with the valve open. These results are summarized in Table B.21.

CALIBRATION RUNS Average waveforms after N_2 doping can be found in Fig. B.33. The triplet lifetime has again been fit using Eq. B.1. The triplet lifetime for channel 1 changed to

Table B.42: Measured triplet lifetimes during N₂ doping tests.

	Channel 1	Channel 3	N ₂ Level
Before Doping	1.28 μ s	1.20 μ s	1 ppm
After Doping	0.30 μ s	0.27 μ s	23 ppm

0.10 μ s. For channel 3 it decreased to 0.27 μ s. This corresponds to a N₂ level of ~23 ppm [111]. A summary of the fits to the triplet lifetime (both before and after N₂ doping) can be found in Table B.42.

B.4 CONCLUSIONS

Both the results from the LD8000, and the fits to the triplet lifetime showed that the level of N₂ contamination in the detector changed from ~1 ppm to ~23 ppm after doping with N₂. This exercise helped demonstrate that the light collection issues in the Engineering Run most likely are not due to contamination of the Ar, and are likely due to issues with the TPB/acrylic, as expected from the simulations.

APPENDIX C

LEAST SQUARES FITTING

NOTATION: A summary of the notation used in this section can be found in Table C.21.

C.1 LEAST SQUARES METHOD

Suppose a variable $\mathbf{y} = \{y_1, y_2, \dots, y_N\}$ is measured at the corresponding times $\mathbf{t} = \{t_1, t_2, \dots, t_N\}$.

The variable $\boldsymbol{\eta} = \{\eta_1, \eta_2, \dots, \eta_N\}$ represents the true values of \mathbf{y} and is unknown. We assume that there is some underlying model

$$\mathbf{f} = \mathbf{f}(\theta_1, \dots, \theta_L; \mathbf{t}) = \sum_{j=1}^L a_{ij} \theta_j, L \leq N$$

that relates \mathbf{y} and $\boldsymbol{\eta}$ and a given value of \mathbf{t} . According the Least Squares Principle, the best model \mathbf{f} is that which minimizes

$$\chi^2 \equiv \sum_{i=1}^N w_i \cdot (y_i - f_i)^2 \tag{C.1}$$

Here, w_i is the weight applied to each equation. The set of parameters $\boldsymbol{\theta}$ that minimizes the χ^2 is called the Least Squares Estimate of the parameters. The weight represents the accuracy of the measurement y_i .

In the case that the errors on each observation in \mathbf{y} are different but known this is known as a Weighted Least Squares Estimate. Here, the weight is set to the inverse of the square of the

measurement error, ie, $w_i \equiv 1/\sigma_i^2$. In this case, the quantity to be minimized is:

$$\chi^2 \equiv \sum_{i=1}^N \left(\frac{y_i - f_i}{\sigma_i^2} \right)^2 \quad (\text{C.2})$$

While assumed not to be the case in the peak fitting procedure here, if the measurements are correlated, the full covariance matrix \mathbf{V} must be used. In the case of uncorrelated measurements, $\mathbf{V} = \text{diag}(\sigma_1, \dots, \sigma_N)$. The resulting (and most general) matrix equation is then

$$\chi^2 \equiv (\mathbf{y} - \mathbf{A} \cdot \boldsymbol{\theta})^T \mathbf{V}^{-1} (\mathbf{y} - \mathbf{A} \cdot \boldsymbol{\theta}) \quad (\text{C.3})$$

where $\mathbf{f} \equiv \mathbf{A} \cdot \boldsymbol{\theta}$.

To minimize the χ^2 , its derivatives with respect to the $\boldsymbol{\theta}$ values should be zero. Ie:

$$\nabla \chi^2 = -2 \left(\mathbf{A}^T \mathbf{V}^{-1} \mathbf{y} - \mathbf{A}^T \mathbf{V}^{-1} \mathbf{A} \boldsymbol{\theta} \right) = 0 \quad (\text{C.4})$$

Assuming $(\mathbf{A}^T \mathbf{V}^{-1} \mathbf{A})$ is non-singular, it can be inverted and we can solve for $\boldsymbol{\theta}$.

$$\boldsymbol{\theta} = \left(\mathbf{A}^T \mathbf{V}^{-1} \mathbf{A} \right)^{-1} \mathbf{A}^T \mathbf{V}^{-1} \mathbf{y} \quad (\text{C.5})$$

Another quantity of interest is what the errors of the $\boldsymbol{\theta}$ parameters are. That is, we would like the covariance matrix of $\boldsymbol{\theta}$. Note that here, the only errors involved are those on the measured variable \mathbf{y} . Following the standard propagation of errors formula:

$$\mathbf{V}(\phi) = \mathbf{S} \mathbf{V}(\rho) \mathbf{S}^T$$

where $\phi = \mathbf{c} + \mathbf{S} \rho$ and \mathbf{c} is a constant term. This implies

$$\mathbf{V}(\boldsymbol{\theta}) = \left(\left(\mathbf{A}^T \mathbf{V}^{-1} \mathbf{A} \right)^{-1} \mathbf{A}^T \mathbf{V}^{-1} \right) \mathbf{V} \left(\left(\mathbf{A}^T \mathbf{V}^{-1} \mathbf{A} \right)^{-1} \mathbf{A}^T \mathbf{V}^{-1} \right)^T$$

Variable	Meaning	Dimensions
\mathbf{t}	Observational points (ie time)	N dimensional column vector
\mathbf{y}	Measured points (ie ADC charge)	N dimensional column vector
$\boldsymbol{\sigma}$	Errors on the measured values \mathbf{y}	N dimensional column vector
\mathbf{V}	Covariance matrix of \mathbf{y}	$N * N$ dimensional matrix
$\boldsymbol{\eta}$	True values	N dimensional column vector
\mathbf{f}	Underlying model relating $\boldsymbol{\eta}$ and \mathbf{y}	N dimensional vector
\mathbf{A}	The coefficients of the $\boldsymbol{\theta}$ parameters	$N * L$ dimensional matrix
$\boldsymbol{\theta}$	The parameters of \mathbf{f}	L dimensional vector
χ^2	Measurement of the goodness of fit	NA

Table C.21: Summary of notation used in the Least Squares Fit

This simplifies to

$$\mathbf{V}(\boldsymbol{\theta}) = \left(\mathbf{A}^T \mathbf{V}(\mathbf{y})^{-1} \mathbf{A} \right)^{-1} \quad (\text{C.6})$$

C.2 PARABOLA FIT

The waveform is simply a time ordered pair of ADC values. For the waveform fitting, we assume that the peak can be fit with a parabola as a function of time. In this case,

$$\mathbf{f}(\boldsymbol{\theta}; \mathbf{t}) = \theta_1 + t\theta_2 + t^2\theta_3 \quad (\text{C.7})$$

To perform the fitting, we use the minimum ADC index, and 2 on either side. We are therefore performing a fit with 3 parameters and 5 degrees of freedom. For the parabola fit, the matrix \mathbf{A} is of the form

$$\mathbf{A} = \begin{pmatrix} 1 & t_1 & t_1^2 \\ 1 & t_2 & t_2^2 \\ 1 & t_3 & t_3^2 \\ 1 & t_4 & t_4^2 \\ 1 & t_5 & t_5^2 \end{pmatrix} \quad (\text{C.8})$$

We assume each ADC sample measurement is uncorrelated with the rest. Therefore, the covariance matrix is

$$\mathbf{V}(\mathbf{y}) = \begin{pmatrix} \sigma_1^2 & 0 & 0 & 0 & 0 \\ 0 & \sigma_2^2 & 0 & 0 & 0 \\ 0 & 0 & \sigma_3^2 & 0 & 0 \\ 0 & 0 & 0 & \sigma_4^2 & 0 \\ 0 & 0 & 0 & 0 & \sigma_5^2 \end{pmatrix} \quad (\text{C.9})$$

The knowledge of these 2 matrices lets us easily solve for $\boldsymbol{\theta}$, using Eq. C.5 and its associated error matrix using Eq. C.6.

In the case of fitting pulses, what we are most interested in is finding the minimum ADC value and its corresponding time. To find these, we make use of Eq. C.7. To find the time when the minimum (or maximum) ADC value occurs, we simply take the derivative of \mathbf{f} with respect to time.

$$\partial_t \mathbf{f}(\boldsymbol{\theta}; t) = \theta_2 + 2\theta_3 t = 0 \implies t_{min} = -\frac{\theta_2}{2\theta_3} \quad (\text{C.10})$$

Plugging this value back into Eq. C.7 gives the minimum ADC value

$$ADC_{min} \equiv \mathbf{f}(\boldsymbol{\theta}; t_{min}) = \theta_1 + \theta_2 t_{min} + \theta_3 t_{min}^2 \quad (\text{C.11})$$

ERRORS

We would also like to know the errors on these values. These values of simply found with error propogation. I will go through in detail for the errors on t_{min} , and then give the result for $\sigma_{ADC_{min}}$.

We know that $t_{min} = -\frac{\theta_2}{2\theta_3}$. Therefore, the error on the minimum time is given by:

$$\sigma_{t_{min}}^2 = \sum_{ij} \left[\frac{\partial t}{\partial \theta_i} \frac{\partial t}{\partial \theta_j} \right] V_{ij}(\boldsymbol{\theta}) \quad (\text{C.12})$$

Working through this step-by-step:

$$\begin{aligned}\sigma_{t_{min}}^2 = & \cancel{\frac{\partial t}{\partial \theta_1} \frac{\partial t}{\partial \theta_1} V_{11}} + \cancel{\frac{\partial t}{\partial \theta_1} \frac{\partial t}{\partial \theta_2} V_{12}} + \cancel{\frac{\partial t}{\partial \theta_1} \frac{\partial t}{\partial \theta_3} V_{13}} + \\ & \cancel{\frac{\partial t}{\partial \theta_2} \frac{\partial t}{\partial \theta_1} V_{21}} + \frac{\partial t}{\partial \theta_2} \frac{\partial t}{\partial \theta_2} V_{22} + \frac{\partial t}{\partial \theta_2} \frac{\partial t}{\partial \theta_3} V_{23} + \\ & \cancel{\frac{\partial t}{\partial \theta_3} \frac{\partial t}{\partial \theta_1} V_{31}} + \frac{\partial t}{\partial \theta_3} \frac{\partial t}{\partial \theta_2} V_{32} + \frac{\partial t}{\partial \theta_3} \frac{\partial t}{\partial \theta_3} V_{33}\end{aligned}$$

Using the fact that \mathbf{V} is symmetric gives

$$\begin{aligned}\sigma_{t_{min}}^2 &= \frac{\partial t}{\partial \theta_2} \frac{\partial t}{\partial \theta_2} V_{22} + 2 \frac{\partial t}{\partial \theta_2} \frac{\partial t}{\partial \theta_3} V_{23} + \frac{\partial t}{\partial \theta_3} \frac{\partial t}{\partial \theta_3} V_{33} \\ &= -\frac{1}{2\theta_3} V_{22} + 2 \frac{1}{2\theta_3} \frac{\theta_2 - 1}{2} \frac{1}{\theta_3^2} V_{23} + \left[\frac{\theta_2 - 1}{2} \frac{1}{\theta_3^2} \right]^2 V_{33} \\ &= \frac{V_{22}}{4\theta_3^2} - \frac{\theta_2 V_{23}}{\theta_3^3} + \left(\frac{\theta_2}{2\theta_3^2} \right)^2 V_{33}\end{aligned}$$

Therefore, the error on the minimum time is

$$\sigma_{t_{min}} = \sqrt{\frac{V(\boldsymbol{\theta})_{22}}{4\theta_3^2} - \frac{\theta_2 V(\boldsymbol{\theta})_{23}}{\theta_3^3} + \left(\frac{\theta_2}{2\theta_3^2} \right)^2 V(\boldsymbol{\theta})_{33}} \quad (\text{C.13})$$

Following a similar method and noting that

$$\begin{aligned}\sigma_{ADC_{min}}^2 &\equiv \sigma_{f_{min}} = \sum_{ij} \left[\frac{\partial f}{\partial \theta_i} \frac{\partial f}{\partial \theta_j} \right] V_{ij}(\boldsymbol{\theta}) \\ \partial_{\theta_1} f|_{t_{min}} &= 1 \quad \partial_{\theta_2} f|_{t_{min}} = t_{min} \quad \partial_{\theta_3} f|_{t_{min}} = 2\theta_3 t_{min}^2\end{aligned}$$

gives the error on the minimum ADC value as

$$\sigma_{ADC_{min}}^2 = V_{11} + 2t_{min}V_{12} + 2t_{min}^2V_{13} + t_{min}^2V_{22} + 2t_{min}^3V_{23} + t_{min}^4V_{33} \quad (\text{C.14})$$

APPENDIX D

MONTE CARLO TUNED OPTICAL PARAMETERS

Light Yield	40 γ /keV [90]
PMT Quantum Efficiency	15 %
TPB Efficiency	1 $\gamma_{\text{vis}}/\gamma_{\text{VUV}}$
Effective Scintillation Yield	6 γ /keV
Scintillation Spectrum	From [131]
RESOLUTIONSCALE	0.11 [132]
Fast Time Constant	6 ns [106]
Slow Time Constant	1590 ns [106]
Yield Ratio (~Quenching Factor)	1.00 ER (0.35 NR)
Excitation Ratio (PSD)	0.25 ER (0.69 NR)

Table D.01: Summary of liquid argon scintillation properties in the CENNS-10 **Geant4** simulation. The effective scintillation yield takes into account the actual light yield, the PMT quantum efficiency, and the TPB efficiency ($SY \equiv LY \cdot QE \cdot \epsilon_{TPB}$). Unless otherwise noted, parameters were tuned to match calibration data. PSD values are energy independent values tuned in post-processing. Quenching factor is also finalized in post-processing.

Material	Reflection	Transmission
Teflon	95 %	5 %
Acrylic	100 %	0 %
Side TPB	95 %	5 %
Disk TPB	0 %	72 %

Table D.02: A summary of surface optical properties applied to visible wavelengths in the CENNS-10 **Geant4** simulation. These parameters were tuned to match calibration data. TPB is assumed to transmit 100 % of VUV light where it is wavelength shifted in the bulk. TPB emission spectrum from [133].

Matthew R. Heath
Curriculum Vitae

EDUCATION

Ph. D. Physics,

Indiana University, Bloomington, IN, Sept. 2013 - May 2019

Thesis Title: A First Search for Coherent Elastic Neutrino-Nucleus Scattering with
Liquid Argon

Advisor: Dr. Rex Tayloe

B.S. Astronomy/Astrophysics,

University of Michigan, Ann Arbor, MI, Sept. 2009 - May 2013

B.S. Interdisciplinary Physics,

University of Michigan, Ann Arbor, MI, Sept. 2009 - May 2013

APPLIED RESEARCH EXPERIENCE

Research Assistant,

Indiana University, Bloomington, IN, 2013 - Present

- Performed statistical analysis of first CEvNS data taken with a liquid argon detector
- Installed and configured multiple detector and DAQ systems using both VME and NIM electronics
- Characterized detector systems with Geant4 simulations and radioactive sources
- Constructed and redesigned the liquid argon scintillation detector CENNS-10
- Optimized and mixed multiple organic liquid scintillator batches for various neutron measurements
- Developed waveform fitting and analysis algorithms to de-convolve AC-coupling effects on PMT signals
- Defined project priorities and goals by working closely with project management and R&D teams

ATLAS Collaboration Undergraduate Researcher,

Bellarmino University, Louisville, KY, 2012

- Identified and grouped relevant events using event topologies and visual representations of structured data
- Analyzed statistical significance of identified events using ROOT data analysis framework

Undergraduate Researcher,

University of Michigan, Ann Arbor, MI, 2011 - 2012

- Identified x-ray binary candidates by studying current research papers
- Extracted observational data of identified sources from the Chandra Source Catalog to analyze using CIAO software
- Informed theories of accretion disk dynamics by characterizing x-ray luminosity of black hole and neutron star x-ray binary candidates

TEACHING EXPERIENCE

Teaching Assistant,

Indiana University, Bloomington, IN, 2013 - 2014

- Taught over 60 major and non-major students in 3 laboratory sections
- Evaluated student performance via lab reports and papers

Indiana University Department of Physics Open House Volunteer,

Indiana University, Bloomington, IN, 2013 - 2014

- Collaborated with colleagues, and peers from other fields, to demonstrate physics principles to a non-technical audience
- Fostered an interest in physics and other STEM fields in local elementary to high school aged children

CONFERENCE TALKS

2015

Third International Workshop on Low Energy Particle Physics Moscow, Russia
Measuring Neutrons with SciBath

Indiana University High Energy Physics Seminar Bloomington, IN
Coherent Elastic Neutrino-Nucleus Scattering at the SNS with COHERENT

2016

APS Division of Nuclear Physics (DNP) Meeting Vancouver, BC, Canada
Background Studies at the Spallation Neutron Source for the COHERENT Experiment

2018

APS April Meeting Columbus, OH
Status of CEvNS Search with the CENNS-10 Liquid Argon Detector

Joint Meeting of APS DNP and Physical Society of Japan Waikoloa, HI
First Results from a CEvNS Search with the CENNS-10 Liquid Argon Detector

2019

APS April Meeting Denver, CO
Results from a CEvNS Search with the CENNS-10 Liquid Argon Detector

PUBLICATIONS

D. Akimov et al. *The COHERENT Experiment at the Spallation Neutron Source* (2015)
arXiv:1509.08702 [physics.ins-det]

D. Akimov et al. *Observation of Coherent Elastic Neutrino-Nucleus Scattering* (2017)
10.1126/science.aao0990 (arXiv:1708.01294 [nucl-ex])

D. Akimov et al. *COHERENT 2018 at the Spallation Neutron Source* (2018)
arXiv:1803.09183 [physics.ins-det]

SELECTED AWARDS

2019: John R. Pruett Award from Indiana University Department of Physics for outstanding graduate student

2019: Travel award from APS Division of Nuclear Physics for 2019 April Meeting

SELECTED SKILLS

Programming Proficiency: C/C++ , git, L^AT_EX, GNU Make, Python, Shell Scripting

Mathematics: Linear Algebra, Monte Carlo techniques, Multi-variate calculus,
Probability, Statistics

Radiation Detectors: Cryogenics, DAQ systems, Liquid noble gas detectors, Organic
liquid scintillators, Shielding design, Vacuum Technology

Programs: AutoCAD, CERN ROOT, FLUKA, Geant4, Maple, Mathematica